Bound States in the Continuum in Planar Anisotropic Structures

Samyobrata Mukherjee

Supervisors: Dr. David Artigas and Dr. Lluis Torner

A thesis presented for the award of the degree of
Doctor of Philosophy

Universitat Politècnica de Catalunya
Spain
June 2021

To the memory of my late grandmother,

and to Jhijhi.

Contents

Acknowledgements vii

Abstract xi

Resumen xiii

1 Introduction 1
- 1.1 Modes in Waveguides . . . 2
- 1.2 Bound States in the Continuum . . . 5
- 1.3 Leaky Modes in Anisotropic Planar Waveguides . . . 13
- 1.4 Anisotropy-induced BICs . . . 18
- 1.5 Unidirectional Guided Resonances . . . 22
- 1.6 Structure of the Thesis . . . 23

2 Methods 25
- 2.1 The Berreman Transfer Matrix Method . . . 26
- 2.2 Complex Root Finding Method . . . 36
- 2.3 The Finite Difference Time Domain Method . . . 38
  - 2.3.1 Derivative as Finite Difference . . . 38
  - 2.3.2 The FDTD algorithm . . . 39

3 BICs in Anisotropic Waveguides with a Single Radiation Channel 45
- 3.1 Theory . . . 46
  - 3.1.1 Ordinary and Extraordinary Basis Waves . . . 46
  - 3.1.2 Dispersion Equation . . . 50
  - 3.1.3 Auxiliary Condition . . . 54
- 3.2 Variation of Optic Axis Orientation . . . 56
  - 3.2.1 Anisotropy-symmetry . . . 57

3.2.2 Positive Uniaxial Core, Negative Uniaxial Substrate . . . 58
3.2.3 Negative Uniaxial Core, Positive Uniaxial Substrate . . . 69
3.2.4 Existence Loci of BICs under Continuous Variation of Optic Axes Orientation . . . 79
3.2.5 Impact of the Auxiliary Condition . . . 84
3.3 Variation of the Refractive Indices of Waveguide Materials 91
3.3.1 Positive Uniaxial Core, Negative Uniaxial Substrate . . . 91
3.3.2 Negative Uniaxial Core, Positive Uniaxial Substrate . . . 96
3.3.3 Bands of INT BICs . . . 102
3.3.4 Refractive Index Sensing . . . 106

4 BICs and UGRs in Anisotropic Waveguides with Two Radiation Channels 109
4.1 Theory . . . 111
4.1.1 Dispersion Equation . . . 112
4.1.2 Auxiliary Condition . . . 114
4.2 Waveguide with Negative Uniaxial Materials . . . 116
4.2.1 Azimuthal Anisotropy-Symmetry Breaking . . . 119
4.2.2 Polar Anisotropy-Symmetry Breaking . . . 127
4.2.3 Both Polar and Azimuthal Anisotropy-Symmetry Breaking . . . 140
4.2.4 Impact of the Auxiliary Condition . . . 142
4.3 Other Waveguide Structures . . . 146
4.3.1 Positive Uniaxial Film, Substrate and Cover . . . 147
4.3.2 Positive Uniaxial Film, Negative Uniaxial Substrate and Cover . . . 149

5 Leaky D'yakanov Surface Waves and DSW BICs 153
5.1 Theory . . . 156
5.2 Guided DSWs and Leaky DSWs . . . 160
5.3 DSW BICs . . . 164
5.4 Variation of the Offset between Optic Axes . . . 166

6 Summary and Conclusions 171

Acknowledgements

At the very outset, I must thank my supervisors David and Lluis for giving me the opportunity to pursue my PhD at ICFO. They have been exemplary supervisors and mentors. While they checked in regularly, they never suffocated me, thereby achieving a delicate but extremely important balance. David was always available to suggest new calculations, to act as a bouncing board for ideas, or to provide feedback on my work. Lluis provided direction whenever needed and taught me a fair bit when it comes to writing papers. In addition to my professional development, I have felt at different times that both of them were also invested in me as a person. That was particularly helpful in managing to work through a pandemic while far from home. I must also acknowledge the contribution of Jordi, who was a post doctoral researcher in our group when I joined and was the person I worked with every day for the first two and a half years of my PhD. He smoothed my entry into life at ICFO, and taught me several techniques. Without his guidance, the research presented in this thesis would simply not have materialised. My thanks are also due to Pili and Carles and Te with whom I had the pleasure of sharing offices and working and learning. The support services at ICFO are excellent and life as a PhD student would have been much harder without them. I am particularly grateful to the Human Resources department and especially to Ingrid and Anne (and Manuela) for helping out with everything from getting a visa and relocation to residence card renewal and finding flatmates. I must also thank the IT team at ICFO for the prompt resolution of most issues that came up over the course of my work.

I am grateful to the open science movement that aspires towards the unfettered flow of knowledge. This movement has started an important conversation within the academic community and even changed a few publication policies. However, these are minor victories and a lot remains to be done. Having worked in institutions with vast dif-

ferences in terms of available resources, I appreciate even more the importance of open science in the face of the stark inequalities that plague our world. I must therefore acknowledge the debt I owe to services allied with the open science movement, such as SciHub, run by Alexandra Elbakyan, and Library Genesis, that have permitted me to follow this academic trajectory. In the future I hope to work with the academic community to build consensus against the monopolisation of knowledge for the sake of profit, and to work towards a more equitable model that does not restrict access to knowledge.

It is important to have a strong support system in life. The need for a support system is felt even more acutely at various points in the PhD given how it is structured. I have been extremely fortunate to have had an unwavering support system comprising many different groups of people over the course of my PhD. The first among these are my family - my parents, my sister and my late grandmother who passed during the course of my PhD. They have, at different times, encouraged me, consoled me, scolded me and celebrated with me. They got me to the start of this PhD and then, despite the separation of a few time zones, carried me through to the end.

In addition to my family, several groups of friends have also played starring roles in my life over the course of my PhD. And while it is inevitable that I might miss a few of them, I shall attempt to list all of their names here. In Barcelona I could always count on Patrick, Daniel, Jessica, Hara, Vindhiya and Amelia (and for a time, Sascha and Nazie) to talk about life, politics and the PhD experience over delicious food and drinks. I am thankful to Mika, Jaime and Gabriel for their friendship, Uruguayan lunch on Thursdays, and their patience in helping me practice my Spanish. The group of people who play football at ICFO on Thursdays have been a great community of sorts and I must thank them for indulging my awful football for these four and a half years. I am also grateful to the community of Indian researchers at ICFO (and other institutes in Barcelona) for their help in adapting to life in Barcelona and then initiating various social and political initiatives and participating in them. I must mention Manu, Avijit, Chandan, Debraj, Banhirup (all "Da"-s), Mallika di, Madhu, Chaitanya, Sukeert, Aamir, Mohit, Varun, Parmeshwar, Mamatha and Ipsita who have been constant friends. Some of these people have often cooked incredible Indian food - the very best that can be found in Barcelona. I have also had the pleasure of travelling with some of the

aforementioned groups of people and I cannot overstate the value of those trips. Here's looking forward to more trips in the future.

Away from Barcelona, I have had the constant support of friends from earlier stages in my life. And once the pandemic struck, forcing us all to interact remotely, their support became even more invaluable. I am particularly grateful to Debo and Akshit for their invaluable advice given that they have recently traversed similar trajectories. I am also grateful to Debo, Apoorv, Esther, Akshit, Soutik, Sudhir, Vatsal, Dhruva, Adi, Raghu, Arjuna for the video calls, the football conversations, the gaming sessions, the numerous recipes and all the conversations that helped make sense of the world. Tirthankar, Kaustav, Swarnendu, Samudra, Hridam and Shrutakirti are friends from my school life and I am grateful to them for keeping me grounded and helping me with timely advice during our conversations.

This thesis would never have seen the light of day without the input and support of these very many incredibly kind people. I owe them a lot more than I could possibly convey in writing. This, then, is poor thanks, but, for now, will have to suffice.

Abstract

Bound states in the continuum (BICs) are modes that remain radiationless though they exist in the part of the spectrum that corresponds to radiating waves. They are a general wave phenomenon and following initial theoretical predictions and subsequent landmark experimental demonstrations of the existence of BICs in photonic systems, there has been an explosion of interest in photonic BICs. Planar anisotropic waveguides containing uniaxial materials support the existence of full vector BICs.

In this thesis we study the properties of these full vector BICs using the leaky mode formalism. We start by studying a structure with an isotropic cover, a uniaxial core/film and a uniaxial substrate, where one of the basis waves in the substrate provides the radiation channel. We find that the orientation of the optic axes of the two materials has substantial impact on BIC existence. This allows us to define regimes of anisotropy-symmetry based on the orientation of the optic axes relative to the direction of propagation and the interface plane. Varying the offset between the film and substrate optic axes in the interface plane, or azimuthal anisotropy-symmetry breaking, leads to the distortion of the BIC lines of existence on the leaky mode. Moving either optic axis out of the interface plane, or polar anisotropy-symmetry breaking, leads to the BIC lines of existence collapsing to points. The collapse of the BIC lines of existence to discrete points when polar anisotropy-symmetry is broken also leads to a transformation from lines of phase discontinuity to phase singularities in the radiation channel amplitude which can be assigned winding numbers. The BICs are robust and cease to exist only when two BICs with opposite winding numbers merge in the parameter space or the BIC moves beyond the leaky mode cutoff.

We also study the impact of the variation of the constitutive parameters of this waveguide on the existence of BICs. We find that varying the refractive indices of the different components of the waveg-

uide have varying degrees of impact on the BIC lines of existence but in all cases results in their continuous transformation, allowing us to construct bands of BIC existence. The sensitivity of BICs to changes of the refractive index also suggest possible applications in sensing.

We then move on to studying structures where the cover, the film and the substrate are all uniaxial with radiation channels available in the cover and the substrate. The structure supports lines of BIC existence when the structure is mirror symmetric and therefore the radiation channels are equivalent. Breaking the mirror symmetry of the structure in any way leads to distinct radiation channels and the added constraint of a second radiation channel also having to be zero leads to the lines of BIC existence collapsing to discrete points. These discrete BIC points are robust and tunable and characterised by phase singularities in both radiation channels. Breaking polar anisotropy-symmetry in addition to the mirror symmetry leads to the formation of unidirectional guided resonances, which are unbound modes that radiate only via one radiation channel even when other channels are available. UGRs are characterised by phase singularities in the amplitude of the radiation channel where they do not radiate.

Finally, we study the surface modes at an interface between a positive uniaxial material and a negative uniaxial material. We find that this interface can support standard, guided D'yakonov surface waves (DSWs). Moreover, it can also support leaky DSWs and even a surface D'yakonov BIC when coupling of the leaky DSW to the radiation channel is cancelled.

We have thus improved the understanding of the hybrid leaky modes and full vector BICs supported by such structures and developed the concept of anisotropy-symmetry which has substantial impact on the existence of BICs and UGRs in these structures.

Resumen

Los estados ligados en el continuo (BIC) son modos que permanecen sin radiación aunque existen en la parte del espectro que corresponde a las ondas radiantes. Son un fenómeno ondulatorio general y, tras las predicciones teóricas iniciales y las demostraciones experimentales históricas posteriores de la existencia de BIC en sistemas fotónicos, ha habido una explosión de interés en los BIC fotónicos. Las guías de ondas planas anisotrópicas que contienen materiales uniaxiales respaldan la existencia de los BIC que tienen todos los componentes de los campos.

En esta tesis estudiamos las propiedades de estos BIC utilizando el formalismo de modo con fugas. Comenzamos estudiando una estructura con una cubierta isotrópica, un núcleo / capa uniaxial y un sustrato uniaxial, donde una de las ondas base en el sustrato proporciona el canal de radiación. Encontramos que la orientación de los ejes ópticos de los dos materiales tiene un impacto sustancial en la existencia de BIC. Esto nos permite definir regímenes de anisotropía-simetría basados en la orientación de los ejes ópticos en relación con la dirección de propagación y el plano de interfaz. La variación del desplazamiento entre los ejes ópticos de la capa y el sustrato en el plano de la interfaz, o la ruptura de la simetría de anisotropía azimutal, conduce a la distorsión de las líneas de existencia BIC en el modo con fugas. Mover el eje óptico fuera del plano de la interfaz, o la ruptura de la simetría de anisotropía polar, lleva a que las líneas de existencia de los BIC colapsen en puntos. El colapso de las líneas de existencia BIC a puntos discretos cuando se rompe la simetría de anisotropía polar también conduce a una transformación de líneas de discontinuidad de fase a singularidades de fase en la amplitud del canal de radiación a las que se les pueden asignar números de devanado. Los BIC son robustos y dejan de existir solo cuando dos BIC con números de devanados opuestos se fusionan en el espacio de parámetros o el BIC se mueve más

allá del corte del modo de fugas.

También estudiamos el impacto de la variación de los parámetros constitutivos de esta guía de ondas sobre la existencia de BIC. Encontramos que la variación de los índices de refracción de los diferentes componentes de la guía de ondas tiene diversos grados de impacto en las líneas de existencia BIC pero en todos los casos da como resultado su transformación continua, lo que nos permite construir bandas de existencia BIC. La sensibilidad de los BIC a los cambios del índice de refracción también sugiere posibles aplicaciones en la detección.

Luego pasamos al estudio de estructuras donde la cubierta, la capa y el sustrato son todos uniaxiales con canales de radiación disponibles en la cubierta y el sustrato. La estructura admite líneas de existencia de los BIC cuando la estructura es simétrica de espejo y, por lo tanto, los canales de radiación son equivalentes. Romper la simetría especular de la estructura de cualquier manera conduce a canales de radiación distintos y la restricción adicional de un segundo canal de radiación, que también debe ser cero, conduce a que las líneas de existencia BIC colapsen en puntos discretos. Estos puntos de BIC discretos son robustos y sintonizables y se caracterizan por singularidades de fase en ambos canales de radiación. La ruptura de la anisotropía-simetría polar además de la simetría especular conduce a la formación de resonancias guiadas unidireccionales, que son modos libres que irradian solo a través de un canal de radiación incluso cuando hay otros canales disponibles. Los UGR se caracterizan por singularidades de fase en la amplitud del canal de radiación donde no irradian.

Finalmente, estudiamos los modos de superficie en una interfaz entre un material uniaxial positivo y un material uniaxial negativo. Descubrimos que esta interfaz puede admitir ondas de superficie D'yakonov (DSW) guiadas y estándar. Además, también puede admitir DSW con fugas e incluso un BIC D'yakonov de superficie cuando se cancela el acoplamiento del DSW con fugas al canal de radiación.

Por lo tanto, hemos mejorado la comprensión de los modos híbridos con fugas y los BIC de vector completo respaldados por estas estructuras y hemos desarrollado el concepto de anisotropía-simetría que tiene un impacto sustancial en la existencia de BIC y UGR en estas estructuras.

Chapter 1

Introduction

The localisation of light has been one of the most studied areas of optics and photonics for a long time. Research has been carried out to understand the processes that lead to the localisation of light. This knowledge has then been harnessed to create diverse photonic systems that localise or confine light and has been applied to various applications ranging from lasers to optical fibres. The linear photonic systems used most commonly to confine light are optical cavities and waveguides and they typically use either standard reflection, or total internal reflection, to confine light to the desired space.

We will study bound states in the continuum in anisotropic planar structures in this thesis. Bound states in the continuum involve localisation of light that is somewhat counter intuitive, and different from the ordinary guided modes of waveguides. In this introductory chapter we will provide a concise introduction to the concepts that will be used and elaborated upon later in this thesis. We will also situate our research in the broader context of research being done in this field. We will start by discussing the localisation of light in waveguides and ordinary guided modes. We shall then explain the concept of bound states in the continuum and provide a concise survey of the various photonic systems where they may be found. We shall then elaborate on the concept of leaky modes, particularly in the context of anisotropic planar structures. We shall end this chapter with brief discussions on anisotropy induced bound states in the continuum in these planar structures and on unidirectional guided resonances. At the very end of this chapter we shall briefly outline the structure of this thesis and the contents of the subsequent chapters.

1.1 Modes in Waveguides

Maxwell's equations and the wave equation provide an adequate model to study the propagation of light in different materials in the classical regime [1–3]. The macroscopic response of an isotropic, dielectric material can be characterised by a real, positive, scalar value of the relative dielectric permittivity, ϵ_r [1]. The application of Maxwell's equations to a homogeneous continuum of such a material results in harmonic solutions of the form $\mathbf{A}(\mathbf{r})e^{i(\mathbf{k}\cdot\mathbf{r}-\omega t)}$ which tells us that light with any free space wavelength, λ_0, can travel in this medium with the wave momentum $\mathbf{k}$ and angular frequency $\omega = 2\pi c/\lambda_0$, and the wave has an amplitude given by $\mathbf{A}(\mathbf{r})$. The magnitude of the propagation constant is

$$k = \frac{2\pi}{\lambda_0}\sqrt{\epsilon_r} = k_0 n, \tag{1.1}$$

where $k_0 = 2\pi/\lambda_0$ is the free space propagation constant and $n = \sqrt{\epsilon_r}$ is the refractive index of the dielectric material. However, light cannot be localised in a homogeneous material and therefore, inhomogeneous structures must be introduced. A simple method of introducing inhomogeneity is to have different materials in the structure with different relative permittivities.

We shall confine ourselves in this thesis to the study of planar structures comprising dielectric materials. The confinement of light in dielectric waveguides was first studied more than a century ago [4]. Dielectric waveguides typically harness total internal reflection to confine light [5]. Since total internal reflection occurs when light moves from a medium with higher refractive index to a medium with lower refractive index, light in dielectric waveguides is typically confined in the material with the higher index. The light that is confined propagates with a fixed field profile that remains unchanged. These are called the eigenmodes of the structure which are characterised by the field profile and the mode propagation constant [6].

The magnitude of the propagation constant for a wave in a bulk medium is given in eq. 1.1. In a planar structure it is convenient to resolve the vector wave momentum in components along the direction of propagation and components in the transverse direction. We will consider propagation in the y direction throughout this thesis. We will also consider that different materials are placed along the x direction, meaning that x is the direction perpendicular to the interfaces of the

planar structures. The planar structures will be constant in the z direction and we will therefore ignore it and restrict ourselves to the $x-y$ plane. We can thus resolve the momentum of the waves travelling in the medium as

$$\mathbf{k} = k_x\hat{\mathbf{x}} + k_y\hat{\mathbf{y}}, \tag{1.2}$$

where $\hat{\mathbf{x}}$ and $\hat{\mathbf{y}}$ are the unit vectors along the x and y directions. Since the wave momentum is directly proportional to the refractive index, the highest wave momentum will be obtained in the material with the highest refractive index. We define this material as the core/film and consider that it is surrounded by cladding materials, that are known as the substrate and the cover, that have lower refractive indices. The fields that make up the waves must obey appropriate boundary conditions at the interfaces of materials with two different refractive indices [1]. A consequence of the boundary conditions is that the tangential component of the wave vector must be continuous across the interface. Therefore, for a mode propagating along the y direction, which is a direction tangential to the interfaces of the planar structure, all the waves in the cover, core and substrate materials that make up the mode must have the same value of k_y.

If we define, $\kappa_x = k_x/k_0$ and $\kappa_y = k_y/k_0$, we can combine eqs. 1.1 and 1.2, for the core/film material to get

$$\left(\kappa_x^f\right)^2 + \left(\kappa_y^f\right)^2 = n_f^2, \tag{1.3}$$

where n_f is the film refractive index. The cover refractive index (n_c) and the substrate refractive index (n_s) are lesser than the film refractive index ($n_c < n_f$ and $n_s < n_f$). Since κ_y has to be constant for all the waves making up the mode, if we select a value of κ_y that is real and is greater than n_c and n_s, we would obtain values of $\kappa_x^{c/s} = \sqrt{n_{c/s}^2 - \kappa_y^2}$ in the cover and the substrate that are imaginary. Conservation of energy requires that we select the sign of $\kappa_x^{c/s}$ that leads to exponential decay, as we move away from the interface into the cover or the substrate. This, therefore, leads to solutions for modes where the field is confined in the core and the field decays exponentially as we move away from the core with only evanescent waves in the substrate and the cover.

However, while solutions of Maxwell's equations exist for any value of $\kappa_y < n$ for a single, infinite homogeneous material, boundary conditions come into play when multiple materials are involved [1, 2]. The waves that can travel in a structure containing multiple different

materials must satisfy these boundary conditions and this results in solutions of Maxwell's equations existing only for specific values of κ_y. These solutions are the aforementioned eigenmodes of the structure and the permitted values of κ_y are known as the mode propagation constants [6]. We shall hereafter refer to κ_y as the normalised mode propagation constant N. The boundary conditions and the specific values of N that can propagate unchanged as eigenmodes of the structure also mean that those values of N can only propagate at specific wavelengths or angular frequencies ω. The link between the wavevectors and wavelengths is given by the dispersion relation for the mode which is typically plotted in the $k - \omega$ space. The wavelengths that can propagate in a structure are determined by the dependence of the refractive indices on wavelength (material dispersion) as well as the dimensions of the structure (geometric dispersion).

From the definition of $\omega(= 2\pi c/\lambda_0)$ and eq. 1.1, we can write $\omega = ck_0$, where c is the speed of light in vacuum. This is known as the light line of vacuum in the $k-\omega$ space. For a material, the light line is defined as $\omega = ck_0/n$, where n is the refractive index of the material. Waves with frequencies above the light line can propagate in the material while waves with frequencies below the light line are evanescent and cannot propagate in the material. For a waveguide, the light line is defined by the cladding materials, the cover and/or the substrate, and is given by $\omega = ck_0/max(n_s, n_c)$. Modes that have frequencies below the light line ($N > max(n_s, n_c)$) are evanescent in the cover and the substrate and therefore remain confined in the core/film [6, 7]. These are known as guided modes of the waveguide. A symmetric planar waveguide, where $n_c = n_s$, and which satisfies the condition $n_f > n_s$, always supports at least one guided mode for any wavelength of light [8]. Otherwise, the condition $n_f > max(n_s, n_c)$ is a necessary condition but not sufficient for the existence of guided modes for any wavelength. On the other hand, modes with frequencies above the light line ($N < max(n_s, n_c)$) can propagate radiatively in either the cover or the substrate or both. Therefore the mode in the core/film can couple to a radiating wave in the cover and/or the substrate and this leads to energy being radiated away from the mode. We define the wave which radiates energy away from the mode as the radiation channel. The radiation channel becomes accessible only when the mode propagation constant N is lesser than the refractive index of one of the cladding materials. Even when access to the radiation channel is available,

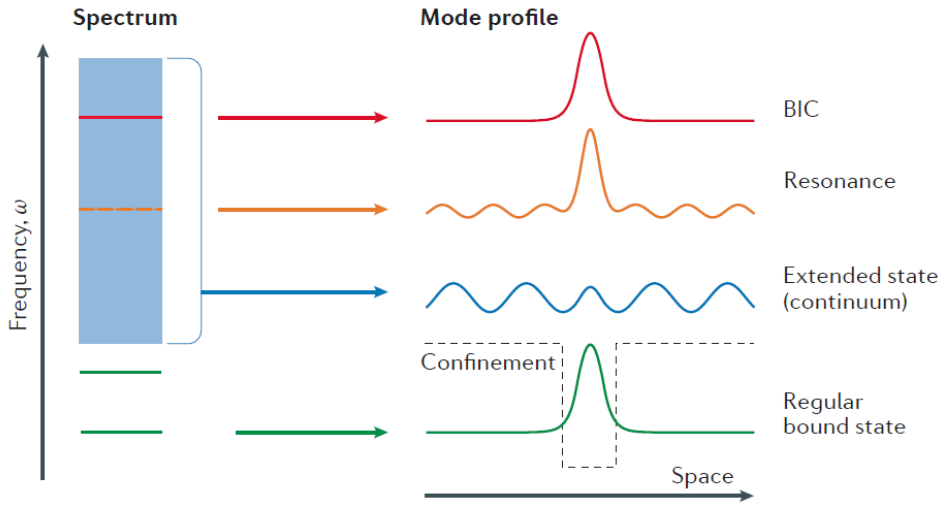

Fig. 1.1: Schematic showing the locations of the various kinds of modes that a waveguide can support in the spectrum on the left as well as the associated mode profile on the right. The dashed black line shows the confining potential which typically supports guided (green) and continuum (blue) modes. Modes inside the continuous part of the spectrum typically radiate by coupling to the continuum (orange). BICs, while located in the continuum, do not radiate and remain confined. Image adapted from Ref. [9].

temporary localisation of the fields in the waveguide is possible via resonances with limited lifetimes (see Fig. 1.1).

1.2 Bound States in the Continuum

The modes with frequencies above the light line can couple to the continuum of radiation modes in the cladding materials. Therefore, the fields are not confined in the waveguide and energy is radiated away from the waveguide via a radiation channel. These modes are variously called leaky modes [8] or radiation/resonant modes [9], depending on how they are treated, but their characteristic feature is the loss of energy from the mode to the surroundings. It is however possible to obtain a mode above the light line, in the part of the spectrum that corresponds to radiating modes, which remains localised within the waveguide. In this mode, the coupling to the radiative modes in

the cladding materials via the radiation channel is somehow avoided. Such a mode, that remains radiationless despite coexisting with the continuum of radiation modes of the structure, is called a bound state in the continuum (BIC). Fig. 1.1 shows a schematic representation of BICs, radiating modes and guided modes.

BICs were first predicted in the field of quantum mechanics by von Neumann and Wigner [10]. They artificially designed an oscillating three dimensional potential that extended to infinity and could theoretically support an electron with energy higher than the potential barrier, i.e., a bound state in the continuum. Such a potential was difficult to realise in an experiment and research into quantum mechanical BICs remained dormant for a long time till Stillinger and Herrick published their study of other artificially designed local potentials that could also support BICs [11]. Subsequently, Friedrich and Wintgen theoretically demonstrated that BICs could arise in a structure where multiple resonances were coupled to a single channel and destructive interference between the two resonances in the channel leads to radiation being cancelled [12]. Though the genesis of the concept of BICs lies in quantum mechanics, there have never been any definitive experimental demonstrations of the concept of BICs in quantum mechanics [9]. This is due to the difficulty of engineering the required potentials and the relative lack of tunable parameters in these systems. However, BICs have since been found to be general wave phenomenon and exist in various systems that support wave propagation. Acoustic BICs, for example, were observed in air flow over a cascade of parallel plates [13]. BICs have also been predicted in spin orbit coupled atomic systems [14].

More recently, there has been an explosion of interest in BICs in photonic structures. The first theoretical predictions of BICs in photonic structures involved two parallel arrays of dielectric gratings or dielectric cylinders and the interaction between the trapped modes giving rise to BICs [15]. Another theoretical scheme that was proposed around the same time showed that a defect layer in a photonic crystal with local defect rod could also support a BIC [16]. These proposals were soon followed by landmark experimental demonstrations of BICs in photonic systems. The first report of the experimental demonstration of photonic BICs was in 2011 when Plotnik, et. al. studied the modes supported by a one dimensional array of waveguides but with two additional waveguides, one placed above and one below the array

[17]. It was found that one of the bound modes of the vertical waveguides, despite being placed within the band of modes of the waveguide array, did not couple to the modes of the array due to a symmetry mismatch. This was therefore a BIC that existed due to a mismatch of the symmetry of the mode and the radiation channel. It was found that breaking the symmetry led to the mode becoming radiative, i.e., the BIC ceased to exist. Soon after, Hsu et. al. reported the experimental observation of a different kind of BIC in a dielectric photonic crystal slab [18]. They found that it was possible to have a BIC located on a band of radiating modes located above the light line supported by a dielectric slab with a rectangular array of holes drilled into it. This BIC does not exist due to a symmetry mismatch between the BIC and the radiating modes, but due to destructive interference that leads to the radiation being cancelled in the radiation channel and is obtained by parameter tuning. Therefore we can broadly classify photonic BICs into two categories depending on their underlying mechanism:

- Symmetry protected BICs that arise due to a mismatch between the symmetry of the BIC and the radiation channel. The BIC ceases to exist and starts radiating if the relevant symmetry is broken [17].

- BICs obtained by parameter tuning that arise due to destructive interference cancelling the radiation into the radiation channel. Variation of parameters typically leads to the BIC shifting its position in the parameter space. While not being instrumental in terms of the mechanism underlying the existence of these BICs, certain symmetries are still typically required and the BIC turns into a radiating mode if those are broken [18].

Subsequently, BICs have been predicted in various photonic systems. It was found that a periodic array of dielectric rods can support both symmetry protected and parameter tuned BICs [22]. It was reported that a micro cavity made up of four defect rods embedded in a photonic crystal waveguide could support a BIC [23]. BICs were also predicted in other periodic structures such as a one dimensional array of dielectric spheres [24]. BICs with high orbital angular momentum were predicted in a dielectric rod with periodically modulated permittivity [25]. The experimental detection of a symmetry protected BIC with zero orbital angular momentum [26] and also a BIC with

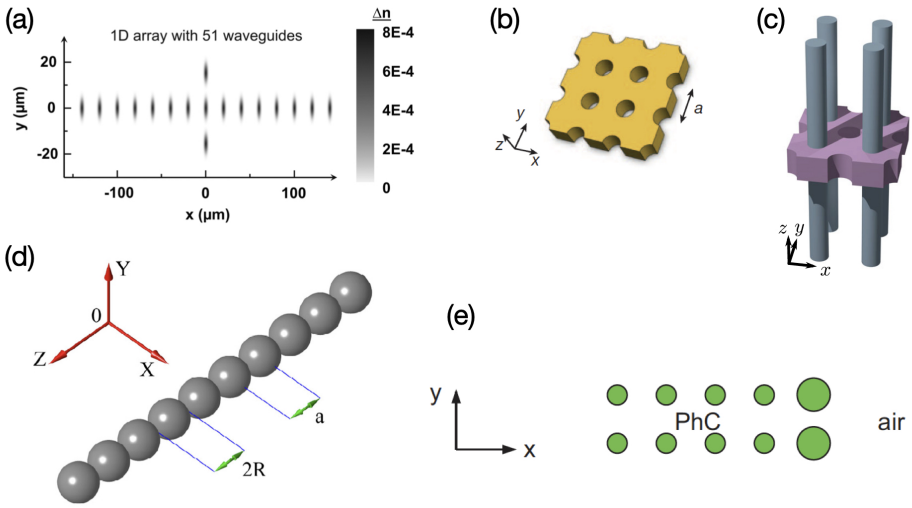

Fig. 1.2: Some photonic geometries that can support BICs. (a) One dimensional array of waveguides with additional waveguides above and below the array that support symmetry protected BICs. Image taken from Ref. [17]. (b) Dielectric photonic crystal structure that supports an off axis BIC obtained by parameter tuning. Image taken from Ref. [18]. (c) A photonic crystal slab placed within a photonic crystal environment that supports lines of BICs. Image taken from Ref. [19]. (d) An array of dielectric spheres that can support topologically protected BICs. Image taken from Ref. [20]. (e) Photonic crystal made up of cylindrical dielectric rods terminated by surface rods with increased radii that can support surface BICs. Image taken from Ref. [21].

zero orbital angular momentum obtained by parameter tuning [27] has been reported in a chain of dielectric disks. Experimental detection of BICs arising from parameter tuning by embedding a photodetector in a photonic crystal slab have been reported [28]. One photonic crystal stacked on top of another photonic crystal to form a double layer can support BICs [29]. It has been shown that BICs can be engineered by environmental design, i.e, by breaking the homogeneity of the environment and placing the photonic crystal core within a photonic crystal environment [19]. Experimental demonstration of BICs in the symmetry band gap of a crystal, in a system where the environment is also a photonic crystal has been reported [30]. It has been theoretically predicted and experimentally demonstrated using a 2D array of waveguides that the topological corner-localized modes

in higher order topological materials can be symmetry protected BICs [31, 32]. BICs arising due to the interaction of leaky modes and diffraction orders in gratings were predicted [33]. It was also found that fibers with periodic Bragg gratings could support BICs [34]. Both symmetry protected and parameter tuned BICs have been predicted to exist in hybrid structures comprising a plasmonic grating on a dielectric waveguide [35]. BICs that arise from the destructive interference of interfering resonances have also been predicted to exist in dielectric waveguides with a metal grating on top and a metal substrate underneath [36, 37]. BICs have also been predicted in silicon nanowire superlattices with sub-wavelength diameter [38] and have been used to obtain confinement of light in sub-wavelength resonators [39]. It has also been predicted that all-dielectric metasurfaces can support BICs and various applications have been proposed [40–42].

Parity-time (PT) symmetric systems feature balanced loss and gain. It has been shown that a one dimensional array of waveguides with PT-symmetric defects can support BICs with both exponential and sub-exponential confinement [43]. It has also been predicted that a PT-symmetric array of coupled optical waveguides can support an unstable BIC that coincides with an exceptional point and can grow with an infinitesimal perturbation [44]. It has also been predicted that a one dimensional binary array of waveguides, comprising alternate waveguides with loss and gain can also support BICs [45]. Following these studies of one dimensional PT-symmetric systems, our group has shown that even two dimensional PT-symmetric systems can support BICs [46]. More recently, it has been shown that the introduction of PT-symmetric perturbation into a photonic system that supports BICs leads to that BIC splitting into a lasing threshold mode and a new kind of BIC that has been termed a pt-BIC [47].

BICs are known to exist in systems in which at least one spatial dimension is infinitely extended. This property is due to considerations arising from the boundary conditions at the interface of a structure that is confined in all three dimensions. These considerations would be avoided if the structure were to have permittivity or permeability equal to zero or $\pm\infty$ at some point. However, it is extremely difficult to realise these compact BICs given that the points where the real part of the permittivity is near zero, the imaginary part of the permittivity, which gives material loss, is typically very high [9]. In fact, the theoretical papers that predict the existence of BICs in compact structures

that are finite in all three dimensions involve a dielectric sphere surrounded by a shell with zero permittivity [48] or a layered nanosphere where at least one of the constituent layers has to have zero permittivity [49]. It has also been predicted that a slab of material with zero refractive index, either due to permittivity being equal to zero or permeability being equal to zero or both, can also support the existence of BICs [50]. An all-dielectric photonic crystal structure has also been proposed which supports zero index modes that are also symmetry protected BICs, thereby serving to solve the issue of radiation from zero index modes [51].

So far we have discussed structures where light is confined in the core of a waveguide or a resonator. However, it has been known for some time that surfaces can support BICs in the context of surface acoustic waves [52, 53]. More recently, bound surface modes have been predicted at the interface of a finite, one dimensional array of waveguides which remain localised near the region where the array ends and a homogeneous bulk material begins [54]. The existence of such bound surface modes has been experimentally demonstrated in such systems with algebraic [55] and sub-exponential localisation [56]. The existence of Bloch surface waves at the interface of photonic crystals that are below the light line have been known for some time. The existence of surface BICs that are above the light line but still remain localised at the interface have also been predicted and studied at the interface of a two dimensional array of waveguides with a slightly modified surface layer [21, 57].

By definition, BICs correspond to zeroes of radiation and can therefore correspond to polarisation or phase singularities in the radiation channel. This property was first shown for BICs in photonic crystals which act as vortex centers in the polarisation direction of far field radiation, which are robust, and whose winding numbers determine their evolution, generation and annihilation [58]. Subsequently, it was shown that BICs supported by an array of dielectric spheres correspond to phase singularities in the complex coupling strength [20]. These BICs were robust under variation of parameters and could only be destroyed by annihilation of the topological charge or by moving them to the part of the parameter space where an extra radiation channel opened up. More recently, BICs that are characterised by phase singularities in the coupling coefficient between incident light and the eigenmode of a slab waveguide terminated with a ridge have been reported [59]. The

experimental observation of the existence of the polarisation vortices corresponding to BICs were reported in a one dimensional grating [60] and in periodic plasmonic structures [61]. The topological properties of BICs have been used to tune structures in order to merge multiple BICs so that we end up with a single BIC which has even better localisation of light in the areas of the parameter space around the BIC [62, 63]. The resulting BIC could either be symmetry protected [62] or obtained by parameter tuning [63]. The polarization vortices occurring at BICs have also been used to generate optical vortex beams [64]. It has also been shown that breaking of certain symmetries in photonic crystals can lead to the creation of circularly polarised states characterised by half integer charges [65, 66] and can even transform a symmetry protected BIC to a BIC arising from parameter tuning [66]. On the other hand, it has been shown that the tuning of parameters can also lead to pairs of circularly polarised states merging to from a BIC in a photonic crystal [67].

Perfectly localised BICs can exist above the light line under idealised conditions in extended, lossless systems that maintain certain necessary symmetries. However, these conditions cannot be realised in reality. This leads to the deformation of the BIC mode leading to the formation of quasi BICs that are radiatively coupled to the continuum but still retain signatures of the BIC and are resonances with very long lifetimes [18, 42]. The material of the substrate and its roughness can turn a BIC into a resonance with finite lifetime [68]. The finite size of real structures can also result in BICs turning into quasi BICs [69, 70]. It has been found that BICs can turn into quasi BICs due to small perturbations [71] or small distortions in the geometry, such as slightly non-circular cylinders in an array which would support BICs if the cylinders were all perfectly circular [72]. The breaking of symmetries that are essential for the existence of BICs that arise from parameter tuning can lead to the formation of quasi BICs [18, 73]. Interestingly, it has been shown using a silicon metasurface that BICs turn into quasi BICs upon symmetry breaking but then at even greater asymmetry, topologically protected extended BIC states, arising due to interfering resonances, are recovered [74]. In addition to all of these, material losses can lead to BICs turning into quasi BICs [26, 68, 75]. While quasi BICs are not perfectly confined modes, they also have several interesting properties. It has been found that the sharp, high Q-factor (quality factor, which is related to the resonance lifetime) resonances

in asymmetric metasurfaces arise from the distortion of symmetry protected BICs into quasi BICs due to the breaking of symmetry [73]. The same principle was applied to nonlinear metasurfaces to enhance their nonlinear response [76]. It has also been shown that metasurfaces can support chiral quasi BICs [77] and Brewster quasi BICs that are transparent at a particular angle of incidence [78]. The selection rules that determine the polarisation to which the BIC couples upon the breaking of symmetry in a photonic crystal slab have also been studied [79].

BICs are interesting due to their very existence as confined or localised modes above the light line and their features are worth studying. However, the existence of BICs in various structures has also been harnessed for various real world applications. BICs have possible applications in acoustics [80], and as spin filters [81] and spin polarisers [82] in spintronics. In photonics, it has been shown that the high lifetime of modes in the vicinity of BICs in the parameter space can lead to critical field enhancement [83]. It has also been shown that quasi BICs can be supported in a single sub-wavelength high index dielectric nanoresonator and this helps create high Q-factor supercavity modes in them [84]. It was found that nanoantennae tuned to the BIC regime could have a huge nonlinear response with high conversion efficiency for second harmonic generation [85]. Sub-wavelength dielectric nanostructure resonators with high Q-factor modes have been used for nonlinear optics [39]. Quasi BICs have been used to design nonlinear metasurfaces for second and third harmonic generation [86]. BICs have been used to design photonic crystal cavities that are doubly resonant for efficient second harmonic generation [87] and the second harmonic generation of a vortex beam [88].

The position of BICs in the parameter space depends on the parameters of the system and this property has been exploited to develop sensors based on BICs. BICs have been used to develop sensors on photonic crystal platforms [89]. BICs supported by all-dielectric metasurfaces have been used for biosensing [90, 91] and to sense ultralow-weight molecules [92]. It has also been shown that the exponential sensitivity of these BIC based sensors on metasurfaces can be tuned [93], and that BICs supported by dielectric gratings can be used for sensing [94, 95].

BICs have also been used to design photonic crystal surface emitting lasers [96]. Tunable lasing from BIC cavities built using arrays of cylindrical nanoresonators has also been reported even when the ar-

ray is scaled down to just 8×8 nanoresonators [97]. BICs have also been used to design lasers that emit vortex beams [64, 98]. It has also been predicted that a BIC in a rectangular dielectric waveguide with an active layer can allow for both coherent perfect absorption and lasing [99]. BICs have also been used for broadband light capture [100]. Quasi BICs have also been found in photonic integrated circuit platforms based on lithium niobate [101] and been used for communication [102].

We have provided a cursory introduction to the various kinds of photonic structures that support BICs, the properties of those BICs and their applications. A more detailed overview can be found in the review articles in Refs. [9, 103, 104].

1.3 Leaky Modes in Anisotropic Planar Waveguides

BICs are modes with frequencies above the light line of the structure in which they exist. Since we are interested in studying BICs in anisotropic planar waveguides, we must first determine a method to study the solutions of Maxwell's equations above the light line in these structures. To this end, we employ the leaky mode formalism in our studies [8].

For any given transverse planar waveguide profile, the modes supported by the structure can be decomposed into a finite number of guided modes and a continuum of radiation modes which are the eigenmodes of the structure, typically forming an orthogonal basis set. The guided modes propagate without any changes in shape while the radiation modes result in the diffractive spread of energy away from the core. The guided modes exist below the light line or when the mode propagation constant, also known as the mode effective index, is greater than the refractive index of the cover and substrate material ($N > max(n_c, n_s)$), leading to evanescent waves in the cladding materials. The continuum of radiation modes exist above the light line or when $N < max(n_c, n_s)$. When $N < max(n_c, n_s)$, light in the core/film couples to the continuum in the cover if $N < n_c$ and in the substrate if $N < n_s$ and energy is radiated away from the core/film.

Fig. 1.3(a) shows the transverse refractive index profile of an anti-guiding structure where the refractive indices of the cover (n_c) and

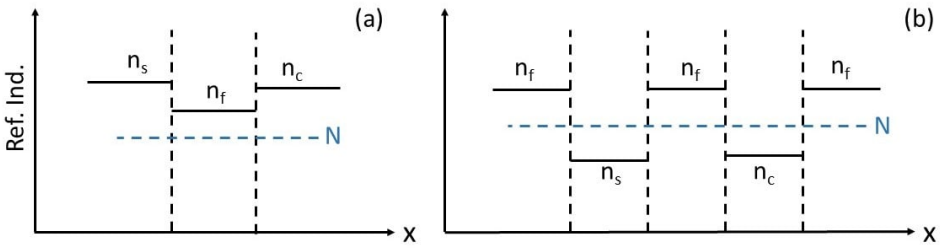

Fig. 1.3: Schematic showing the transverse profiles for structures where (a) the core/film with refractive index n_f is surrounded by cover (n_c) and substrate (n_s) materials with higher refractive indices, and (b) where the core is surrounded with finite layers of materials with lower refractive index but then the final, semi-infinite layers have the same index as the core. The dashed blue lines indicate the mode propagation index N. The dashed black lines show the interfaces between the layers.

the substrate (n_s) are higher than the index of the film (n_f). Light incident on this profile would only couple to radiation modes since no guided modes are supported and it would diffract. This is because the maximum value of N is limited by n_f (see eq. 1.3) and since $n_f < n_c$ and $n_f < n_s$, we have N always satisfying the condition for radiation modes ($N < max(n_c, n_s)$) and never the condition for guided modes ($N > max(n_c, n_s)$). Fig. 1.3(b) shows a W-shaped profile where the cladding materials just around the film have a lower refractive index ($n_f > n_c$ and $n_f > n_s$) but these layers are finite and there are semi-infinte blocks of the same material as the film placed at the points where the cladding materials end. This structure, also known as a depressed cladding waveguide, does not support any guided modes. However, when the thickness of the cover and the substrate is large enough, the structure supports a beam that resembles a guided mode with localisation in the film which attenuates exponentially as it propagates [8, 105]. This is a leaky mode.

Leaky modes exist above the light line of the waveguide where $N < max(n_c, n_s)$ but they are improper modes in that they are not a part of the complete set of orthogonal eigenmodes of the waveguide [106]. They exist in structures where there is some confinement of the light in the core/film even though the light can couple to the continuum modes in the cladding materials. Leaky modes attenuate exponentially as they propagate. Thus, leaky modes have a complex propagation

constant N whose imaginary part approximates the loss of energy to the surroundings. Since the leaky mode attenuates exponentially in the propagation direction, flux considerations require that the leaky mode must then grow exponentially in the transverse direction as we move away from the waveguide [8, 107]. Since an infintely growing wave at $x \to \pm\infty$ is clearly unphysical, we conclude that the leaky mode formalism is accurate only in the vicinity of the waveguide. Leaky modes were first reported in the context of microwave waveguides [106, 108, 109] and later experimentally verified [110].

We are interested in anisotropic waveguides which support leaky modes. Anisotropic materials have different properties when light propagates in different directions. We will restrict ourselves to uniaxial materials in this thesis. These are birefringent materials which cannot be defined by a scalar dielectric permittivity value and require a 3×3 permittivity tensor, meaning that light propagating in the structure with different polarisations experiences different dielectric responses. In natural materials this anisotropy can be seen in certain classes of crystals and the axis of symmetry of these crystals coincides with one of the principal axes of the permittivity tensor. This axis is defined as the optic axis [3]. The behaviour of a uniaxial material can be understood using a single optic axis. The principal value ϵ_e of the tensor occurs for the principal axis that corresponds to the optic axis. The principal values corresponding to the two other principal axes are identical (ϵ_o). When light propagates along one of the principal axes of the uniaxial material, the dielectric tensor is diagonal, and when it makes some angle with the principal axes, we can obtain the appropriate permittivity tensor by applying rotation matrices to the diagonal tensor containing only the principal values. A uniform plane wave propagating parallel to the optic axis, with polarisation perpendicular to the optic axis is only affected by the ordinary permittivty ϵ_o and therefore it is governed by a ordinary refractive index ($n_o = \sqrt{\epsilon_o}$). However, for a plane wave propagating in any other direction, we can resolve it into a component with polarisation perpendicular to the optic axis (governed by n_o) and another component with polarisation along the optic axis and this second component is then governed by an extraordinary refractive index that is dependent on the direction ($n_e(\theta, \phi)$, where θ and ϕ are the angles used to specify direction). The value of $n_e(\theta, \phi)$ is bounded by n_o and $n_e = \sqrt{\epsilon_e}$. Note that when we write n_e we only mean $\sqrt{\epsilon_e}$ whereas we will refer to the extraordinary index

that varies as a function of direction as $n_e(\theta, \phi)$, explicitly referring to it as a function. We will give an expression for $n_e(\theta, \phi)$ in a later section, but for now it suffices to note that a uniaxial material has two refractive indices, an ordinary refractive index that is independent of direction and a direction dependent extraordinary refractive index and thus, any light propagating in an infinite block of a uniaxial material can be resolved into ordinary and extraordinary basis waves.

It has been known for some time that planar waveguide structures comprising uniaxial materials can support both fully guided and leaky modes [111–114]. For propagation directions that coincide with the principal axes of the dielectric tensor, these waveguides support pure transverse electric (TE) or transverse magnetic (TM) modes. For other propagation directions, the modes are hybrid [111, 112]. It is also important to note that while a bulk uniaxial material can support ordinary and extraordinary waves, the modes supported by planar uniaxial waveguides are generally hybrid [112, 114]. This is due to the boundary conditions at the interfaces between the materials which lead to the mixing of the ordinary and extraordinary waves in the materials on the two sides of the interface.

For a structure where at least one of the cladding materials is uniaxial, it is possible to have a transition from guided to leaky modes by the variation of the orientation of the optic axis [111, 112, 114]. This can occur because the extraordinary refractive index varies as the optic axis orientation is changed. Besides, the mode propagation constant N can also vary as a function of the optic axis orientation and depending on the interplay of these values, a radiation channel may or may not be available. We consider that the substrate is a uniaxial material with refractive indices n_{os} and $n_{es}(\theta, \phi)$. Then the mode in the waveguide can couple radiatively to the ordinary wave in the substrate if $N < n_{os}$ and the ordinary wave acts as the radiation channel. If $N < n_{es}(\theta, \phi)$ then the mode can couple radiatively to the extraordinary wave in the substrate and the extraordinary wave acts as the radiation channel. If $N > n_{os}$ and $N > n_{es}(\theta, \phi)$, then the mode cannot access any radiation channel and the mode would be a purely guided wave. On the other hand, if $N < n_{os}$ and $N < n_{es}(\theta, \phi)$, then the mode can access both radiation channels in the substrate.

In this thesis we are interested in studying leaky modes where the mode propagation constant is situated between the indices of the substrate so that only one of the ordinary or extraordinary waves in the

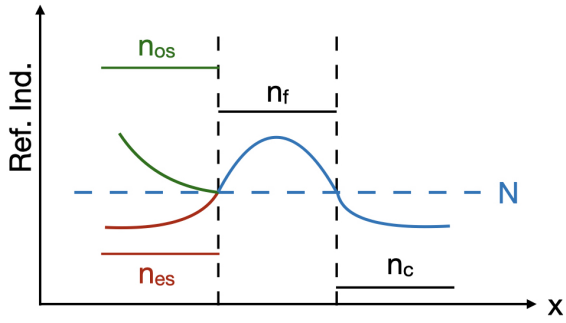

Fig. 1.4: Schematic showing the transverse mode profile of a leaky mode in a structure where the substrate is a negative uniaxial material. The wave corresponding to the radiation channel, shown in green, grows exponentially. The dashed blue line indicates the mode propagation index N. The dashed black lines show the interfaces between the layers.

substrate serves as the radiation channel while the other wave is evanescent and serves as a confinement channel, i.e., either $N > n_{os}$ and $N < n_{es}(\theta, \phi)$ OR $N < n_{os}$ and $N > n_{es}(\theta, \phi)$. Sometimes we refer to such modes as semi-leaky modes in our papers, but since these are the only kind of leaky modes we shall study in this thesis, in order to avoid confusion, we shall refer to them simply as leaky modes. Fig. 1.4 shows the schematic of a leaky mode in such a scenario where the substrate is a negative birefringent uniaxial material. Since the mode propagation constant is greater than the cover refractive index, the mode decays exponentially in the cover. In the substrate, $N > n_{es}(\theta, \phi)$ and therefore the extraordinary basis wave (brown) in the substrate decays exponentially. However, $N < n_{os}$ and therefore the ordinary basis wave (green) acts as the radiation channel via which the mode couples to the continuum and leaks energy to the substrate. As discussed previously, the wave corresponding to the radiation channel has to grow exponentially in the transverse direction due to flux considerations arising from the exponential attenuation of the leaky mode in the direction of propagation. If we had considered a wave guide with a positive birefringent uniaxial substrate, with ($n_{os} < n_{es}$), we would have had the extraordinary wave acting as the radiation channel and growing exponentially.

We will use this leaky mode formalism to first study structures where only the film and and the substrate are uniaxial and later apply

it to structures where both the cover and the substrate are uniaxial. In the second case we will study leaky modes which can access one radiation channel each in the cover and in the substrate, while the other basis wave is evanescent in both cladding materials.

1.4 Anisotropy-induced BICs

The radiative loss from leaky modes varies as a function of several parameters of the waveguide structure. The minima of the radiative losses of leaky modes in anisotropic waveguides and the spectrally embedded minima of layered anisotropic structures had been studied previously [111, 115, 116]. The existence of BICs in asymmetric planar waveguide structures containing anisotropic materials was first reported by our group in 2017 [117]. Subsequently, the existence of BICs in photonic crystal structures containing anisotropic defect layers has been theoretically predicted [118] and experimentally demonstrated [119]. The structures that were studied in Ref. [117] had an isotropic cover, air with $n_c = 1$ and a uniaxial substrate which provided a radiation channel. Cases with both isotropic and uniaxial materials in the core/film were studied. In all cases, the optic axes were parallel to the interface plane and in the cases where the film and substrate were both uniaxial, the optic axes were aligned. The leaky mode formalism discussed in the previous section was applied to these structures to find the leaky modes supported by these structures. The leaky modes could couple to the continuum via only one radiation channel in the substrate. BICs exist in these structures when the coupling of the leaky modes to the continuum of radiation modes in the substrate is cancelled due to some mechanism. It was found that these structures can support two classes of BICs based on the underlying mechanism - polarisation separable (PS) BICs and interferometric (INT) BICs.

PS BICs in anisotropic planar structures are the analogs of the more general class of symmetry protected BICs. The PS BIC arises because the mode is decoupled from the continuum due to orthogonal polarisations of the mode and the radiation channel. They can only occur when the propagation direction coincides with one of the principal axes of the permittivity tensor when the structure supports pure TE/TM modes [111]. For propagation along the y direction, when perpendicular to the optic axis, the ordinary and extraordinary waves

in the substrate reduce to TM and TE waves, respectively. Therefore, for a positive (negative) uniaxial substrate, a TM (TE) mode propagating along y, perpendicular to the optic axis cannot couple to the TE (TM) radiation channel in the substrate that is orthogonal to it despite meeting the requirement $N < n_{es}(\theta, \phi)(N < n_{os})$ for access to a radiation channel. PS BICs can occur both with an isotropic film or with a uniaxial film. For an isotropic film, it merely requires a guiding profile with respect to one of the refractive indices in the substrate, i.e., $n_f > min(n_{os}, n_{es})$. For a uniaxial core, either the set of ordinary indices or the set of extraordinary indices have to provide a guiding profile, i.e., $n_{of} > n_{os}$ OR $n_{ef} > n_{es}$. The existence of PS BICs was experimentally verified using reflection spectroscopy experiments [117]. Since PS BICs arise due to geometric considerations, they exist along a particular direction for all wavelengths at which the leaky mode exists. PS BICs cannot occur for propagation directions that are not along the principal axes because then the modes are hybrid and a hybrid mode is coupled to both the ordinary and extraordinary waves in the substrate. The PS BICs are standard TE/TM guided modes of standard integrated optics setups that have been known for a while but it was not appreciated earlier that they were BICs.

For off axis propagation, the only BICs that can exist are INT BICs. In anisotropic planar structures, they are the analogs of BICs obtained by parameter tuning. They can only exist when both the film and the substrate are uniaxial. An isotropic film and a uniaxial substrate cannot support INT BICs. In the case of INT BICs, the decoupling of the mode from the radiation channel does not rest on orthogonality but on the destructive interference of the radiation in that channel due to the mixing of waves at the interface upon the application of the appropriate boundary conditions. Unlike PS BICs which can only exist for certain specific propagation directions, INT BICs can exist for a broad range of propagation directions and it has been shown that their angular position can be tuned based on structure parameters. Besides, since INT BICs exist for propagation directions that are not along the principal axes, they are full vector hybrid modes and their polarization can be tuned by varying the waveguide parameters. The full vector nature of INT BICs in anisotropic planar structures is a key distinction since BICs in most other photonic structures are almost pure TE/TM modes [15, 17, 18, 54–56, 58]. In order to find INT BICs, an auxiliary condition was derived to find the points where the

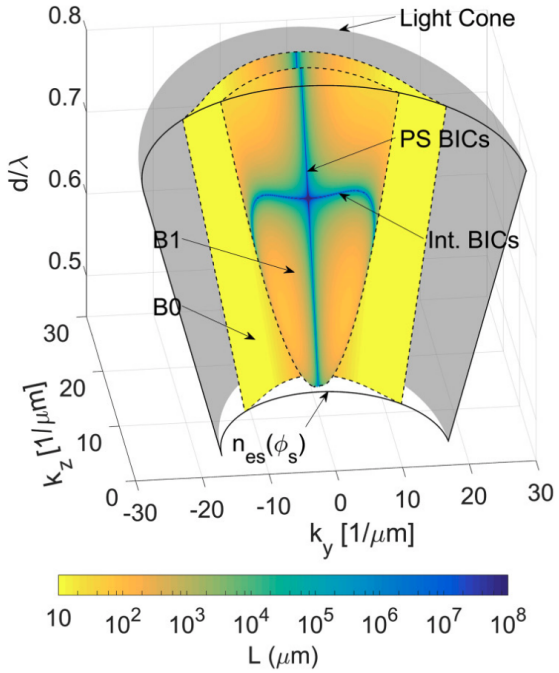

Fig. 1.5: Momentum-frequency dispersion diagram for the leaky modes of a structure comprising a uniaxial film with positive birefringence ($n_{of} = 1.5$, $n_{ef} = 1.75$), a uniaxial substrate with negative birefringence ($n_{os} = 2.00$, $n_{es} = 1.25$) and air as a cover ($n_c = 1$). The ratio d/λ is the normalized frequency and k_z and k_y are the mode momenta along the y and z direction. Two yellowish surfaces (B0 and B1) for the leaky modes are plotted, where dashed lines show the limits of the surface and the color indicates the $1/e$ decay length L (in μm). The blue lines stand for an infinite decay length, indicating the existence of BICs. The grey surface behind the leaky mode sheets is the light cone, given by $k_0 \cdot n_{os}$; the light grey-transparent surface limited by solid lines sets the leaky mode cutoff, given by $k_0 \cdot n_{es}(\phi)$. Here k_0 is the free-space wavenumber.

amplitude of the radiation channel was zero. INT BICs occur at the points where the solutions of the dispersion equation of the structure and the solutions of the auxiliary condition intersect.

We now select a concrete example to illustrate the concepts of PS and INT BICs in anisotropic planar structures. Fig. 1.5 shows the momentum-frequency dispersion diagram (k_y, k_z, d/λ) of an anti-guiding structure that was studied in Ref. [117] with an isotropic cover,

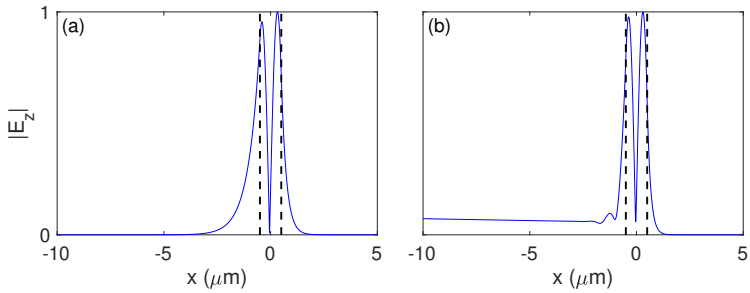

Fig. 1.6: The transverse profile of the absolute value of the tangential electric field component E_z of the first order leaky mode (B1) supported by the structure studied in Fig. 1.5 at (a) the BIC at $D/\lambda = 0.685$ and angle between optic axes and direction of propagation $\phi = 65.367°$, (b) a point on the leaky mode at the same value of ϕ but at $D/\lambda = 0.9$. The width of the film is set to $1\mu m$. The dashed black lines show the interfaces. The field is normalized with respect to the maximum value of $|E_z|$.

a positive uniaxial core and a negative uniaxial substrate. The interface between the materials is parallel to the $y-z$ plane. The structure supports two families of leaky modes, which are shown in the plot as two sheets marked B0 and B1 with color proportional to the decay length of the leaky mode. B0 is the fundamental leaky mode while B1 is the first order leaky mode. The dark grey surface marked as the light cone indicates the points below which no radiation channels are available and therefore only guided modes are allowed. However, since this is an anti-guiding structure with the highest index of the structure being the ordinary refractive index of the substrate, we do not find any guided solutions. The light grey transparent surface in the front indicates the points above which both the ordinary and the extraordinary waves in the substrate become available as radiation channels. Since we are only interested in leaky mode solutions with a single radiation channel, we restrict ourselves to the solutions between these two surfaces. BICs are given by pure real solutions of the mode propagation constant N, at which the leakage through the radiation channel vanishes. The solution for the BICs exist as lines in the dispersion diagram, in contrast to most other photonic systems where they exist as dots [18, 49]. The vertical line corresponds to PS BICs that exist when propagation is orthogonal to the optic axis and the TE mode propagating in that direction is decoupled from the TM radiation channel provided

by the ordinary wave in the substrate. The PS BICs exist at the same propagation direction on both B0 and B1. The curved horizontal line in the upper surface B1 corresponds to INT BICs where the radiating ordinary wave is cancelled by destructive interference. We see that the line of INT BICs exists for a continuous range of propagation directions making arbitrary angles with the principal axes of the uniaxial materials. Fig. 1.6(a) shows the transverse profile of the tangential field component E_z at a point on the line of INT BICs. We see that despite being above the light line, the field at the BIC is confined to the film and decays exponentially away from the interface in the substrate and the cover. Fig. 1.6(b) shows the same field component but at a point on the leaky mode, away from the BIC lines, with non-zero losses and we see that there is leakage from the film to the substrate. Note that BICs are the only non-radiating states of this anti-guiding structure.

Thus, to summarize, we have learnt that anisotropic planar structures can support PS BICs for propagation along the principal axes, and INT BICs when operated off axis. We will subsequently use this structure and the BICs supported by it as the starting point of our investigations in later chapters.

1.5 Unidirectional Guided Resonances

So far we have considered leaky modes where energy can be radiated away from the mode via only one radiation channel. However, it is also possible to obtain leaky mode solutions where two or more radiation channels are available. We have learnt that is possible to cancel radiation into one radiation channel to form BICs. Using the mechanisms underlying BICs, it might also be possible to cancel the radiation into multiple channels. That would of course lead to the formation of BICs in a structure with two radiation channels. It has been shown that it is also possible to cancel the radiation into all but one channel, leading to the radiation escaping from the mode via only that channel. Such a mode has been defined as a unidirectional guided resonance (UGR) [120]. Thus, while a leaky mode would simple radiate via all available radiation channels, a UGR radiates via only one radiation channel and radiation is cancelled in all the other channels.

Control of the proportion of radiation escaping from a structure

via each radiation channel is desirable for various applications, such as photonic crystal surface emitting lasers [96], vertical grating couplers [121, 122] or light detection and ranging devices [123], among others. Various schemes have been proposed to obtain unidirectional radiation by directing all radiation into a single radiation channel. Some of these schemes propose using stacked reflectors [124, 125], others propose leveraging interference from radiating antennae [126], or using asymmetric photonic crystal structures [127–129]. However, the aim of perfectly unidirectional radiation was only recently achieved using the concept of topologically enabled radiation cancellation that is typical of bound states in the continuum (BICs) [120]. The insight into the mechanism of radiation cancellation gained from BICs had previously been harnessed in structures with multiple radiation channels to create directional resonances [130].

The existence of UGRs has been recently proposed and experimentally observed in a photonic crystal structure where up-down mirror symmetry is broken [120]. The UGR is understood by starting from a BIC in a mirror symmetric photonic crystal structure. Then, the BIC is split into opposite circularly polarised resonances, characterised by half integer charges, as the up-down mirror symmetry is broken. The value of the symmetry breaking parameter is then tuned till at one point in the parameter space, the opposite circularly polarised resonances merge and there is no radiation into one of the channels and a UGR is obtained. Since then there has been another report on the existence of UGRs in photonic crystal structures [131].

In this thesis we will study leaky modes in anisotropic planar structures that can couple to two radiation channels and then explore the cancellation of radiation in all available channels to form BICs and in all but one channel to form UGRs.

1.6 Structure of the Thesis

We have provided a brief introduction to the concepts that we will employ later in this thesis. In Chapter 2, we provide an introduction to the techniques that we have used to solve Maxwell's equations in the structures that we study such as the Berreman transfer matrix method [132] and the FDTD method [133].

Chapter 3 presents the results of our study of BICs in anisotropic

planar structures with a single radiation channel. At the very beginning of this chapter we present the theoretical framework necessary to study the leaky modes and BICs in this class of structures. This framework was developed in collaboration with Jordi Gomis Bresco and Pilar Pujol Closa with the input of my supervisors. The next section of Chapter 3 presents our study of the impact of the variation of the orientation of the optic axes of the uniaxial materials on the existence of BICs. An account of the essential results from this section can be found in Ref. [134]. The subsequent section of Chapter 3 deals with the impact of the variation of the constitutive parameters of the waveguide on the existence of BICs. A summary of the results of this study can be found in Ref. [135].

Chapter 4 deals with structures that support leaky modes with two radiation channels. At the beginning of the chapter we present the minor modifications to the framework developed in Chapter 3 that are needed so that it is suitable for application to this class of structures. Then we study the impact of the variation of optic axis orientation on the existence of BICs and UGRs in this structure. The results presented in this chapter can be found in Refs. [136, 137].

In Chapter 5 we apply our understanding of leaky modes and the existence of BICs to a structure without a core, i.e., instead of a waveguide, we study a single interface between two uniaxial materials with opposite signs of birefringence. We study the existence of D'yakonov surface waves at this interface, their transition to leaky surface waves and the existence of surface BICs embedded in the leaky part. Finally, in Chapter 6 we summarize the main findings of this thesis and outline possible lines of research that could be pursued in the future.

Chapter 2

Methods

Maxwell's equations describe the behaviour of electromagnetic waves at a macroscopic scale. Since in our work we investigate the behaviour of light when interacting with materials whose volume is much larger compared to that of a single atom, Maxwell's equations suffice for our purposes and we use the Maxwell-ian model exclusively. Maxwell's equations comprise two divergence and two curl equations and in a vacuum without charges and currents are

$$\begin{aligned} \nabla \cdot \mathbf{E} &= 0, \\ \nabla \cdot \mathbf{H} &= 0, \\ \nabla \times \mathbf{E} &= -\mu_0 \frac{\partial \mathbf{H}}{\partial t}, \\ \nabla \times \mathbf{H} &= \epsilon_0 \frac{\partial \mathbf{E}}{\partial t}, \end{aligned} \tag{2.1}$$

where $\mathbf{E}$ and $\mathbf{H}$ are the electric and magnetic fields respectively, ϵ_0 is the vacuum permittivity, and μ_0 is the vacuum permeability [1, 2]. Taking the curl of both sides of the curl equations, and then using the divergence equations and the vector identity $\nabla \times \nabla \times \mathbf{A} = \nabla(\nabla \cdot \mathbf{A}) - \nabla^2 \mathbf{A}$ we get two differential wave equations

$$\begin{aligned} \nabla^2 \mathbf{E} &= \mu_0 \epsilon_0 \frac{\partial^2 \mathbf{E}}{\partial t^2}, \\ \nabla^2 \mathbf{H} &= \mu_0 \epsilon_0 \frac{\partial^2 \mathbf{H}}{\partial t^2}. \end{aligned} \tag{2.2}$$

These wave equations support harmonic wave solutions of the form

$$\begin{aligned} \mathbf{E}(\mathbf{r}, t) &= \mathbf{E_0} e^{i(\mathbf{k}\cdot\mathbf{r} - \omega t)}, \\ \mathbf{H}(\mathbf{r}, t) &= \mathbf{H_0} e^{i(\mathbf{k}\cdot\mathbf{r} - \omega t)}, \end{aligned} \tag{2.3}$$

where $\mathbf{k}$ is the wave vector with magnitude $k_0 = 2\pi/\lambda_0$ corresponding to vacuum wavelength λ_0, ω is the angular frequency of the waves, and $\mathbf{r}$ is a position vector. These solutions represent plane waves with surfaces of constant phase defined by

$$\mathbf{k} \cdot \mathbf{r} - \omega t = constant \tag{2.4}$$

travelling in the direction of $\mathbf{k}$ with a phase velocity $v_p = 1/\sqrt{\mu_0 \epsilon_0} = c$.

For light propagating in a material the permittivity and permeability change to reflect the presence of the material and the equations are

$$\begin{aligned} \nabla \cdot \mathbf{D} &= 0, \\ \nabla \cdot \mathbf{H} &= 0, \\ \nabla \times \mathbf{E} &= -\mu_0 \mu_r \frac{\partial \mathbf{H}}{\partial t}, \\ \nabla \times \mathbf{H} &= \epsilon_0 \epsilon_r \frac{\partial \mathbf{E}}{\partial t}, \end{aligned} \tag{2.5}$$

where ϵ_r and μ_r are the relative permittivity and permeability of the material in question and $\mathbf{D} = \epsilon_0 \epsilon_r \mathbf{E}$ is the electric displacement field. For non-magnetic materials the relative permeability is 1 and we shall set $\mu_r = 1$ in all our calculations.

We study the behaviour of light in structures containing uniaxial birefringent materials and to that end we solve Maxwell's equations given in eq. 2.5 in those structures. We make use of various methods to solve Maxwell's equations in them. Transfer matrix methods are typically used to calculate modes of planar structures. We employ the Berreman transfer matrix method [132] which is suitable for anisotropic planar waveguides to solve Maxwell's equations and calculate modes in the structures that we study. These planar structures are finite along one Cartesian axis while extending infinitely along the two other Cartesian axis. We use finite difference time domain (FDTD) methods to study propagation of light in structures of our interest [133]. We will introduce each method in this chapter.

2.1 The Berreman Transfer Matrix Method

D.W. Berreman outlined a method for calculating reflection and transmission in anisotropic media using 4×4 matrices in his seminal paper in

1972 [132]. This method can be easily programmed and we implement the Berreman Transfer Matrix method as described by Hodgkinson et. al. [138, 139] to solve Maxwell's equations in planar structures comprising birefringent materials. Applied to the plane wave solutions in eq. 2.3, the partial derivative operators can be written as $\nabla \rightarrow i\mathbf{k}, \frac{\partial}{\partial t} \rightarrow -i\omega$. Therefore, using the harmonic plane wave solutions from eq. 2.3 in Maxwell's equations in an infinite block of homogeneous material, given in 2.5, Maxwell's equations can be rewritten as

$$\begin{aligned} \mathbf{k} \cdot \mathbf{D} &= 0, \\ \mathbf{k} \cdot \mathbf{H} &= 0, \\ \mathbf{k} \times \mathbf{E} &= \mu_0 \omega \mathbf{H}, \\ \mathbf{k} \times \mathbf{H} &= -\epsilon_0 \epsilon_r \omega \mathbf{E}. \end{aligned} \tag{2.6}$$

The relative permittivity ϵ_r is typically a scalar magnitude for isotropic materials. However for the anisotropic materials of our interest, it is a symmetric 3×3 tensor and we will write it as $\hat{\epsilon}_r$ for the sake of clarity whenever discussing anisotropic materials. In general, any birefringent crystal has three principal axes with three refractive indices n_1, n_2, and n_3. Therefore the permittivity tensor in the material frame $\hat{\epsilon}_{123}$ (aligned along the material's principal axes) can be written as

$$\hat{\epsilon}_{123} = \begin{bmatrix} \epsilon_1 & 0 & 0 \\ 0 & \epsilon_2 & 0 \\ 0 & 0 & \epsilon_3 \end{bmatrix} \tag{2.7}$$

where $\epsilon_i = n_i^2$.

We assume a planar structure with modes *always* propagating along the y direction and the x direction *always* being perpendicular to the interfaces. The material orientation can be changed by rotations about the z-axis given by the angle θ and rotations about the x-axis given by the angle ϕ and we can thus compute the dielectric permittivity tensor $\hat{\epsilon_r}$ in the propagation frame using rotation matrices. These operations will result in a dielectric permittivity tensor in the propagation frame that is symmetric. So for now we assume the most general form for $\hat{\epsilon_r}$ without any additional restrictions

$$\hat{\epsilon}_r = \begin{bmatrix} \epsilon_{xx} & \epsilon_{xy} & \epsilon_{xz} \\ \epsilon_{xy} & \epsilon_{yy} & \epsilon_{yz} \\ \epsilon_{xz} & \epsilon_{yz} & \epsilon_{zz} \end{bmatrix}. \tag{2.8}$$

The wave vector $\mathbf{k}$ can be written as $\mathbf{k} = k_x\hat{\mathbf{x}} + k_y\hat{\mathbf{y}} + k_z\hat{\mathbf{z}}$ where $\hat{\mathbf{x}}, \hat{\mathbf{y}}$ and $\hat{\mathbf{z}}$ are the unit vectors along the Cartesian axes in the propagation frame. We can then normalize the wave vector to get

$$\kappa = \mathbf{k}/k_0 = (k_x\hat{\mathbf{x}} + k_y\hat{\mathbf{y}} + k_z\hat{\mathbf{z}})/k_0 = \kappa_x\hat{\mathbf{x}} + \kappa_y\hat{\mathbf{y}} + \kappa_z\hat{\mathbf{z}}. \tag{2.9}$$

Using this expression we can re-write the cross product equations from eq. 2.6 as

$$\begin{aligned} \kappa \times \mathbf{E} &= z_0\mathbf{H}, \\ \kappa \times \mathbf{H} &= -\frac{1}{z_0}\hat{\epsilon}_r\mathbf{E}, \end{aligned} \tag{2.10}$$

where we have used the relations $\omega = ck_0$, $c = 1/\sqrt{\mu_0\epsilon_0}$ and vacuum impedance $z_0 = \sqrt{\mu_0/\epsilon_0}$. The electric and magnetic field vectors can be written as 3×1 column vectors in the Cartesian propagation frame and therefore the vector cross product can be written as a 3×3 matrix operator such that

$$\kappa \times \mathbf{A} = \hat{\kappa}\vec{A} = \begin{bmatrix} 0 & -\kappa_z & \kappa_y \\ \kappa_z & 0 & -\kappa_x \\ -\kappa_y & \kappa_x & 0 \end{bmatrix} \begin{bmatrix} A_x \\ A_y \\ A_z \end{bmatrix}, \tag{2.11}$$

where $\vec{A}$ denotes the vector $\mathbf{A}$ written in the 3×1 column vector form. The expressions in eq. 2.10 can now be written in the matrix operator and column vector form as

$$\begin{aligned} \hat{\kappa}\vec{E} &= z_0\vec{H}, \\ \hat{\kappa}\vec{H} &= -\frac{1}{z_0}\hat{\epsilon}_r\vec{E}. \end{aligned} \tag{2.12}$$

Without loss of generality, we assume that light propagates in the $x-y$ plane for the planar structure shown in fig. 2.1. We can therefore set the z component of the wave vector to zero ($k_z = \kappa_z = 0$) [138]. Applying this in eq. 2.12, we get

$$\begin{aligned} \begin{bmatrix} 0 & 0 & \kappa_y \\ 0 & 0 & -\kappa_x \\ -\kappa_y & \kappa_x & 0 \end{bmatrix} \begin{bmatrix} E_x \\ E_y \\ E_z \end{bmatrix} &= z_0 \begin{bmatrix} H_x \\ H_y \\ H_z \end{bmatrix} \\ -z_0 \begin{bmatrix} 0 & 0 & \kappa_y \\ 0 & 0 & -\kappa_x \\ -\kappa_y & \kappa_x & 0 \end{bmatrix} \begin{bmatrix} H_x \\ H_y \\ H_z \end{bmatrix} &= \begin{bmatrix} \epsilon_{xx} & \epsilon_{xy} & \epsilon_{xz} \\ \epsilon_{xy} & \epsilon_{yy} & \epsilon_{yz} \\ \epsilon_{xz} & \epsilon_{yz} & \epsilon_{zz} \end{bmatrix} \begin{bmatrix} E_x \\ E_y \\ E_z \end{bmatrix} \end{aligned} \tag{2.13}$$

This gives us 6 equations

$$\kappa_y E_z = z_0 H_x, \tag{2.14}$$
$$-\kappa_x E_z = z_0 H_y, \tag{2.15}$$
$$-\kappa_y E_x + \kappa_x E_y = z_0 H_z, \tag{2.16}$$

$$-z_0 \kappa_y H_z = \epsilon_{xx} E_x + \epsilon_{xy} E_y + \epsilon_{xz} E_z, \tag{2.17}$$
$$z_0 \kappa_x H_z = \epsilon_{xy} E_x + \epsilon_{yy} E_y + \epsilon_{yz} E_z, \tag{2.18}$$
$$z_0(\kappa_y H_x - \kappa_x H_y) = \epsilon_{xz} E_x + \epsilon_{yz} E_y + \epsilon_{zz} E_z. \tag{2.19}$$

Since the magnetic field components H_i in the above equations always occur multiplied by z_0, we define $\tilde{H}_i = z_0 H_i$ and use $\tilde{H}_i$ going forward. We make use of eq. 2.14 and eq. 2.17 to obtain expressions for E_x and H_x in terms of the remaining components

$$\begin{aligned} E_x &= -\frac{1}{\epsilon_{xx}}(\kappa_y \tilde{H}_z + \epsilon_{xy} E_y + \epsilon_{xz} E_z), \\ \tilde{H}_x &= \kappa_y E_z. \end{aligned} \tag{2.20}$$

$\tilde{H}_x$ and E_x are the components of the magnetic and electric fields that are perpendicular to the interface, and as such are not necessary for boundary condition matching. They may be necessary to calculate power flow, but we can calculate $\tilde{H}_x$ and E_x using the relations given in eq. 2.20 if the remaining components are known. Therefore, we use the expressions derived in eq. 2.20 and apply them to eqs. 2.14, 2.15, 2.17 and 2.18 and obtain expressions for $E_y, E_z, \tilde{H}_y$ and $\tilde{H}_z$ that do not contain E_x and $\tilde{H}_x$

$$\begin{aligned} -\frac{\kappa_y \epsilon_{xy}}{\epsilon_{xx}} E_y + \left(1 - \frac{\kappa_y^2}{\epsilon_{xx}}\right) \tilde{H}_z - \frac{\kappa_y \epsilon_{xz}}{\epsilon_{xx}} Ez &= \kappa_x E_y, \\ \left(\epsilon_{yy} - \frac{\epsilon_{xy}^2}{\epsilon_{xx}}\right) E_y - \frac{\kappa_y \epsilon_{xy}}{\epsilon_{xz}} \tilde{H}_z + \left(\epsilon_{yz} - \frac{\epsilon_{xy}\epsilon_{xz}}{\epsilon_{xx}}\right) E_z &= \kappa_x \tilde{H}_z, \\ -\tilde{H}_y &= \kappa_x E_z, \\ \left(\frac{\epsilon_{xy}\epsilon_{xz}}{\epsilon_{xx}} - \epsilon_{yz}\right) E_y + \frac{\kappa_y \epsilon_{xz}}{\epsilon_{xx}} \tilde{H}_z + \left(\kappa_y^2 + \frac{\epsilon_{xz}^2}{\epsilon_{xx}} - \epsilon_{zz}\right) E_z &= \kappa_x \tilde{H}_y. \end{aligned} \tag{2.21}$$

The system of equations given in eq. 2.21 can be written in matrix

form as

$$\begin{bmatrix} -\frac{\kappa_y \epsilon_{xy}}{\epsilon_{xx}} & 1-\frac{\kappa_y^2}{\epsilon_{xx}} & -\frac{\kappa_y \epsilon_{xz}}{\epsilon_{xx}} & 0 \\ \epsilon_{yy}-\frac{\epsilon_{xy}^2}{\epsilon_{xx}} & -\frac{\kappa_y \epsilon_{xy}}{\epsilon_{xz}} & \epsilon_{yz}-\frac{\epsilon_{xy}\epsilon_{xz}}{\epsilon_{xx}} & 0 \\ 0 & 0 & 0 & -1 \\ \frac{\epsilon_{xy}\epsilon_{xz}}{\epsilon_{xx}}-\epsilon_{yz} & \frac{\kappa_y \epsilon_{xz}}{\epsilon_{xx}} & \kappa_y^2+\frac{\epsilon_{xz}^2}{\epsilon_{xx}}-\epsilon_{zz} & 0 \end{bmatrix} \begin{bmatrix} E_y \\ \tilde{H}_z \\ E_z \\ \tilde{H}_y \end{bmatrix} = \kappa_x \begin{bmatrix} E_y \\ \tilde{H}_z \\ E_z \\ \tilde{H}_y \end{bmatrix}. \tag{2.22}$$

Setting

$$\hat{L} = \begin{bmatrix} -\frac{\kappa_y \epsilon_{xy}}{\epsilon_{xx}} & 1-\frac{\kappa_y^2}{\epsilon_{xx}} & -\frac{\kappa_y \epsilon_{xz}}{\epsilon_{xx}} & 0 \\ \epsilon_{yy}-\frac{\epsilon_{xy}^2}{\epsilon_{xx}} & -\frac{\kappa_y \epsilon_{xy}}{\epsilon_{xz}} & \epsilon_{yz}-\frac{\epsilon_{xy}\epsilon_{xz}}{\epsilon_{xx}} & 0 \\ 0 & 0 & 0 & -1 \\ \frac{\epsilon_{xy}\epsilon_{xz}}{\epsilon_{xx}}-\epsilon_{yz} & \frac{\kappa_y \epsilon_{xz}}{\epsilon_{xx}} & \kappa_y^2+\frac{\epsilon_{xz}^2}{\epsilon_{xx}}-\epsilon_{zz} & 0 \end{bmatrix}, \vec{F} = \begin{bmatrix} E_y \\ \tilde{H}_z \\ E_z \\ \tilde{H}_y \end{bmatrix}, \tag{2.23}$$

we can write eq. 2.22 as

$$\hat{L}\vec{F} = \kappa_x \vec{F}. \tag{2.24}$$

Eq. 2.24 is an eigenvalue equation where $\hat{L}$ is the matrix for the eigenvalue problem, κ_x corresponds to the eigenvalues and $\vec{F}$ corresponds to the eigenvectors. Since $\hat{L}$ is a 4×4 matrix, there can be at most four distinct eigenvalues. The eigenvalue equation given in 2.24 can be solved numerically in Matlab. However, we solve this equation analytically for the systems of our interest. The analytic results improve both the speed and the accuracy of our code. These analytic results for specific structures are presented in the next chapter. For now, we continue presenting the method as applicable in the general case of any birefringent material.

These four values of κ_x correspond to the four basis waves that can propagate in the birefringent material for a given value of κ_y. As indicated by the arrows in fig. 2.1 there are two waves propagating forward in the x-direction ($\vec{F}_1^+, \vec{F}_2^+$) and two propagating backward in the x-direction ($\vec{F}_1^-, \vec{F}_2^-$). Corresponding to these four basis waves are the four eigenvalues $\kappa_{x1}^+, \kappa_{x2}^+, \kappa_{x1}^-$ and κ_{x2}^-, which give us the normalized wave vector component along the x-direction for the basis waves. Writing the four field vectors ($\vec{F}_{1/2}^{+/-}$) as the columns of a matrix, we can construct a 4×4 field matrix $\hat{F}$

$$\hat{F} = \begin{bmatrix} E_{y1}^+ & E_{y1}^- & E_{y2}^+ & E_{y2}^- \\ H_{z1}^+ & H_{z1}^- & H_{z2}^+ & H_{z2}^- \\ E_{z1}^+ & E_{z1}^- & E_{z2}^+ & E_{z2}^- \\ H_{y1}^+ & H_{y1}^- & H_{y2}^+ & H_{y2}^- \end{bmatrix}. \tag{2.25}$$

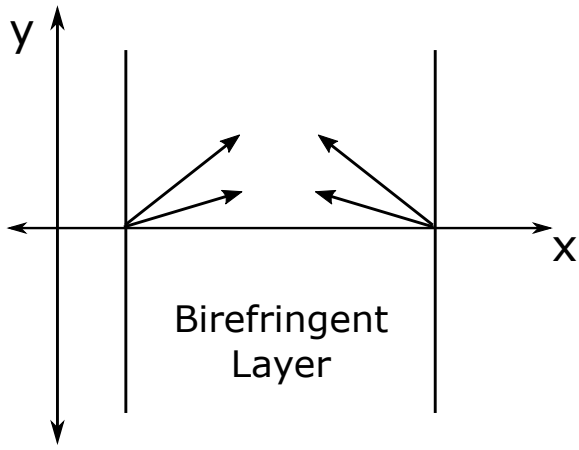

Fig. 2.1: Schematic of a planar layer of birefringent material showing light propagating in the $x-y$ plane. The birefringent material supports four waves - two propagating forward in x and two propagating backward in x.

The total field in the birefringent layer can be understood as a linear combination of the four basis vectors described above. Each basis wave can be multiplied by a complex amplitude which serves as a field coefficient

$$\begin{aligned} \vec{m} &= a_1^+ \vec{F}_1^+ + a_1^- \vec{F}_1^- + a_2^+ \vec{F}_2^+ + a_2^- \vec{F}_2^- \\ \implies \vec{m} &= \begin{bmatrix} a_1^+ E_{y1}^+ + a_1^- E_{y1}^- + a_2^- E_{y2}^+ + a_2^- E_{y2}^- \\ a_1^+ H_{z1}^+ + a_1^- H_{z1}^- + a_2^- H_{z2}^+ + a_2^- H_{z2}^- \\ a_1^+ E_{z1}^+ + a_1^- E_{z1}^- + a_2^- E_{z2}^+ + a_2^- E_{z2}^- \\ a_1^+ H_{y1}^+ + a_1^- H_{y1}^- + a_2^+ H_{y2}^+ + a_2^- H_{y2}^- \end{bmatrix}, \end{aligned} \tag{2.26}$$

where $a_{1/2}^{+/-}$ are the complex amplitudes of the basis waves and $\vec{m}$ is the total field. Arranging the complex amplitudes in the form of a column vector we can write

$$\vec{a} = \begin{bmatrix} a_1^+ \\ a_1^- \\ a_2^+ \\ a_2^- \end{bmatrix}. \tag{2.27}$$

We can use eqs. 2.25 and 2.27 to write the total field $\vec{m}$ as a matrix product

$$\vec{m} = \hat{F}\vec{a}. \tag{2.28}$$

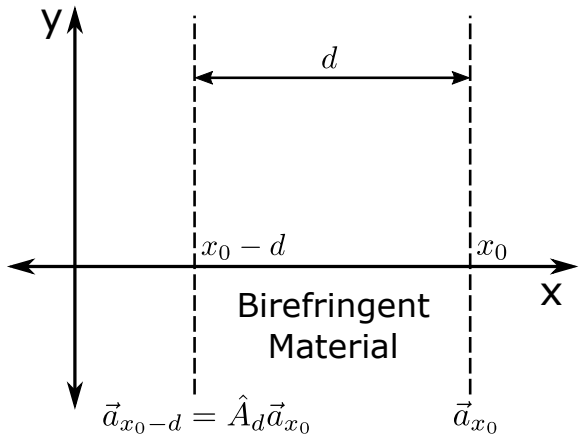

Fig. 2.2: The phase matrix $\hat{A}_d$ transforms the basis wave amplitudes a_{x_0} at a point $x = x_0$ to the basis wave amplitudes at the point $x = x_0 - d$.

From eq. 2.28 we can see that it is possible to obtain the amplitudes of the basis waves from the total field $\vec{m}$ by inverting the field matrix $\hat{F}$

$$\vec{a} = \hat{F}^{-1}\vec{m}. \tag{2.29}$$

As the waves propagate in the birefringent material, they accumulate phase depending on the wave vector and the distance propagated. Since we study modes that propagate along the y-direction, all four basis waves have the same propagation constant κ_y along that direction. We shall therefore focus only on the phase accumulated by the waves as they travel along the x-direction right now. The accumulation of phase by each basis wave can be represented by the multiplication of the the basis wave amplitude a with an exponential term, $e^{-ik_0\kappa_x d}$, where d is the distance travelled by the wave along the x-direction in the birefringent layer. We can write this in terms of a phase matrix $\hat{A}_d$

$$\hat{A}_d = \begin{bmatrix} e^{-ik_0\kappa^+_{x1}d} & 0 & 0 & 0 \\ 0 & e^{-ik_0\kappa^-_{x1}d} & 0 & 0 \\ 0 & 0 & e^{-ik_0\kappa^+_{x2}d} & 0 \\ 0 & 0 & 0 & e^{-ik_0\kappa^-_{x2}d} \end{bmatrix} \tag{2.30}$$

such that $\hat{A}_d$ acting on the basis wave amplitude vector a_{x_0} at a point $x = x_0$ transforms the vector to a_{x_0-d} at the point $x = x_0 - d$ within

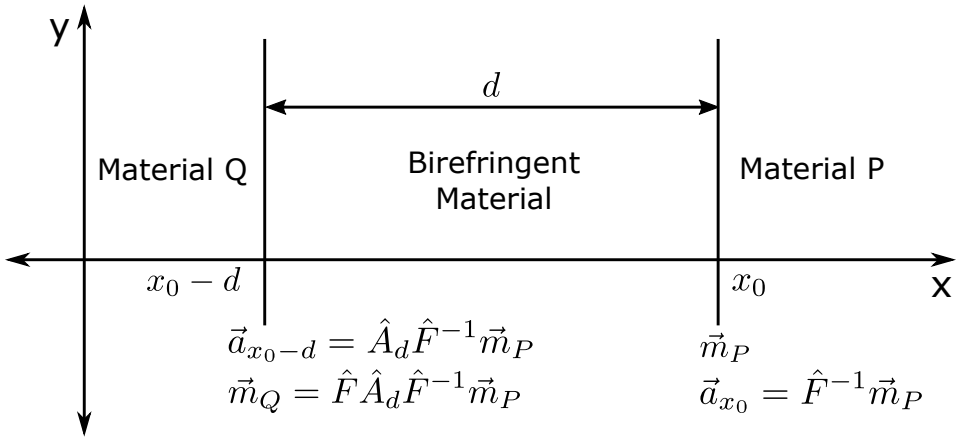

Fig. 2.3: The apparatus of the transfer matrix method involving the field matrices and the phase matrices can be deployed to transform the electric and magnetic fields from one side of a birefringent layer to another by defining a characteristic matrix for the layer.

the same medium

$$\vec{a}_{x_0-d} = \hat{A}_d \vec{a}_{x_0}. \tag{2.31}$$

Now we consider a birefringent material with thickness d as shown in Fig. 2.3 that is sandwiched between two materials P and Q. The interfaces of this material are located at $x = x_0$ and at $x = x_0 - d$. We know the total field in the material P just to the right of the interface at $x = x_0$ and this is given by $\vec{m}_P$. We are now going to use the apparatus described above to calculate the total field $\vec{m}_Q$ in material Q just to left of the interface at $x = x_0 - d$ (note that the matrices translate fields in the $-x$ direction). We assume that we know the wave vector component in the y-direction, κ_y, that is common for all the waves propagating in the system and therefore we can calculate the eigenvectors and eigenvalues of $\hat{L}$ (see eq. 2.24). In other words, we know the field matrix $\hat{F}$ and the wave vector components in the x-direction for the four basis waves $\kappa_{x1}^+, \kappa_{x1}^-, \kappa_{x2}^+$ and κ_{x2}^-.

The total field $\vec{m}$ contains the components $E_y, \tilde{H}_z, E_z$, and $\tilde{H}_y$ that are parallel to the interfaces in our geometry as shown in fig. 2.3 and those components are continuous across the interface. Therefore, in a transformation across any interface parallel to the $y-z$ plane, the total field $\vec{m}$ is conserved. Therefore since the total field $\vec{m}_P$ in material P just to the right of the interface is known, the total field just to the left of the interface would be the same. Using eq. 2.29, we can calculate

the amplitude of the basis waves in the birefringent material just to the left of the interface at $x = x_0$

$$\vec{a}_{x_0} = \hat{F}^{-1}\vec{m}_P. \tag{2.32}$$

We can then combine eqs. 2.31 and 2.32 to calculate the amplitude vector just to the right of the interface at $x = x_0 - d$ at the other end of the birefringent material

$$\vec{a}_{x_0-d} = \hat{A}_d\hat{F}^{-1}\vec{m}_P. \tag{2.33}$$

Multiplying $\vec{a}_{x_0-d}$ with the field matrix $\hat{F}$ gives us the fields at the point just to the right of the interface at $x = x_0 - d$ and since the total field is conserved across the interface, this field is equal to the field just to the left of the interface and we can write

$$\vec{m}_Q = \hat{F}\hat{A}_d\hat{F}^{-1}\vec{m}_P. \tag{2.34}$$

We can define a matrix

$$\hat{M} = \hat{F}\hat{A}_d\hat{F}^{-1}, \tag{2.35}$$

to write eq. 2.34 as

$$\vec{m}_Q = \hat{M}\vec{m}_P \tag{2.36}$$

which transforms the total fields across the birefringent layer from the right hand interface at $x = x_0$ to the left hand interface at $x = x_0 - d$. $\hat{M}$ is the characteristic matrix of the birefringent layer. It is important to note that when calculating the characteristic matrix $\hat{M}$ for a birefringent layer, the order in which the basis wave eigenvectors are arranged as the columns of the field matrix $\hat{F}$ for that layer does not matter. The arrangement of the basis wave eigenvectors for the field matrix $\hat{F}$ only matters for the cover and substrate when we want to calculate modes propagating in the y-direction and not for any of the layers in between.

When dealing with a stack comprising multiple layers of birefringent materials, as shown in Fig. 2.4, we have to calculate the fields across each of the layers. If the total field at one end of the stack is known, we can calculate the field at the other end by repeating, for each layer, the operation described in eq. 2.34 in order to convert the fields from the right to the left of each layer. This operation can be

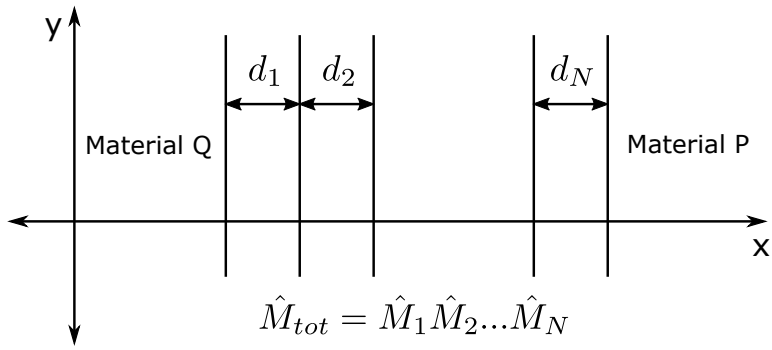

Fig. 2.4: Characteristic matrix for a stack of birefringent layers.

achieved simply by repeated multiplication of the characteristic matrix for each layer such that

$$\begin{aligned}\vec{m}_Q &= (\hat{F}_1\hat{A}_{d_1}\hat{F}_1^{-1})(\hat{F}_2\hat{A}_{d_2}\hat{F}_2^{-1})...(\hat{F}_N\hat{A}_{d_N}\hat{F}_N^{-1})\vec{m}_P,\\ \vec{m}_Q &= \hat{M}_1\hat{M}_2\ ...\hat{M}_N\vec{m}_P,\\ \vec{m}_Q &= \hat{M}_{tot}\vec{m}_P,\end{aligned} \tag{2.37}$$

where d_i is the thickness of the i-th layer of the birefringent material. Thus the characteristic matrix of the entire stack $\hat{M}_{tot}$ can be calculated by multiplying the characteristic matrix $\hat{M}_i$ of each individual layer.

Thus, in this section we have described an apparatus that allows us to calculate the fields in single or multiple planar layers of birefringent materials. This method can be employed to calculate the waves across these layers or the reflection from and transmission through these planar structures which may serve as polarizers, wave plates, filters or displays [139–142]. However, we are interested in using the Berreman transfer matrix method to calculate the modes propagating along the y-direction through these planar structures comprising uniaxial materials. We use the Berreman method for boundary condition matching and thus derive a dispersion equation whose solutions give us the discrete values of κ_y for which modes are supported by the structure. For more accurate calculations we analytically solve for the eigenvalues κ_x and the corresponding eigenvectors which give us the field matrix $\hat{F}$ for each material. The method and the relevant analytic results for uniaxial materials are described at the beginning of the next chapter.

2.2 Complex Root Finding Method

In the course of our calculations, we encounter various transcendental equations. The dispersion equations for the leaky modes supported by the structures we study as well as the equations arising from the auxiliary condition whose solutions give us BICs are transcendental equations that have complex solutions. We apply Newton's method to these transcendental equations in order to obtain their roots numerically.

Newton's method uses a guess for the root as a starting point and then iterates in order to improve that guess and arrive at the correct root of the equation [143]. Given a function $f(x)$ and an initial guess for a root x_0 we can expand the function about x_0 using the Taylor expansion

$$f(x) = f(x_0) + f'(x_0)(x - x_0) + \frac{1}{2}f''(x_0)(x - x_0)^2 + ..., \tag{2.38}$$

where $f'(x)$ gives the first derivative and $f''(x)$ gives the second derivative of the function $f(x)$. If we keep terms only to the first order, then we have

$$f(x) = f(x_0) + f'(x_0)(x - x_0), \tag{2.39}$$

which is the equation of the tangent to f(x) at x_0. Let the point at which this tangent crosses the x-axis be given by x_1. Then we get

$$f(x_0) + f'(x_0)(x_1 - x_0) = 0. \tag{2.40}$$

From eq. 2.40 we can calculate that

$$x_1 = x_0 - \frac{f(x_0)}{f'(x_0)}. \tag{2.41}$$

The value of x_1 given in eq. 2.41 would be the adjusted value of x that the Newton method would use in it's following iteration. This process would then be repeated where the value of x_2 would be obtained from x_1 and so on. Thus, generally, given x_n, obtained after n iterations of Newton's method, an adjusted value x_{n+1} would be obtained as

$$x_{n+1} = x_n - \frac{f(x_n)}{f'(x_n)}. \tag{2.42}$$

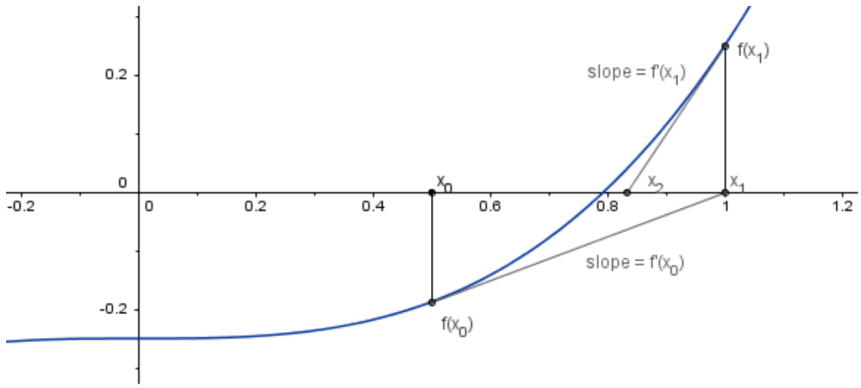

Fig. 2.5: Graphical demonstration of the first two steps of the Newton method for $f(x) = 0.5x^3 - 0.24$. Image obtained from Ref. [144].

Newton's method stops iterating when the adjustment to the value of x after an iteration is below a certain threshold. Therefore, the stopping condition is given by

$$|x_{n+1} - x_n| < th, \tag{2.43}$$

where th gives the stopping threshold.

Since the guess provides Newton's method with a starting point, it plays an extremely important role. Depending on the starting point provided, the Newton method may converge to the desired root, oscillate or even diverge instead of converging [145]. In fact, given a real starting point, the Newton method remains confined to the real line and cannot find complex solutions that have a non-zero imaginary part [144]. Since we are sometimes interested in starting from a real guess and reaching a complex solution, we implement a variation of Newton's method wherein we calculate the gradient of our function in the complex plane instead of simply the derivative along the real line and this allows us to obtain the desired complex roots of our function. We define our function by putting all the terms of our transcendental equations on one side of the equation and leaving the other side equal to zero so that finding the roots of this function would give us the solutions of the transcendental equation.

2.3 The Finite Difference Time Domain Method

The study of the propagation of light in any structure requires the solution of Maxwell's equations in that structure. There are, however, only a handful of systems where Maxwell's equations can be solved analytically. Therefore, we have to resort to numerical methods to solve Maxwell's equations and study the propagation of light in various structures. The finite difference time domain (FDTD) method is one such numerical method to calculate propagation of light [133, 146].

2.3.1 Derivative as Finite Difference

The derivative of a function f of a single variable x is defined as

$$\frac{d}{dx}f(x) = \lim_{h\to 0}\frac{f(x+h)-f(x)}{h}. \tag{2.44}$$

However, if we want to calculate this derivative numerically, we have to use a finite, non-zero value of h. An expression for the numerical value of the derivative can be obtained using the Taylor expansion [146]. We can use the Taylor expansion to expand the function $f(x)$ about $x_0+\delta/2$ and $x_0-\delta/2$. We thus obtain

$$f(x_0+\frac{\delta}{2}) = f(x_0)+f'(x_0)\frac{\delta}{2}+\frac{1}{2!}f''(x_0)\left(\frac{\delta}{2}\right)^2+\frac{1}{3!}f'''(x_0)\left(\frac{\delta}{2}\right)^3+..., \tag{2.45}$$

and

$$f(x_0-\frac{\delta}{2}) = f(x_0)-f'(x_0)\frac{\delta}{2}+\frac{1}{2!}f''(x_0)\left(\frac{\delta}{2}\right)^2-\frac{1}{3!}f'''(x_0)\left(\frac{\delta}{2}\right)^3+..., \tag{2.46}$$

where $f'(x)$ indicates the first derivative, $f''(x)$ indicates the second derivative and so on and the $n!$ indicates the factorial of n. Subtracting eq. 2.46 from eq. 2.45, we get

$$\begin{aligned} f(x_0+\frac{\delta}{2})-f(x_0-\frac{\delta}{2}) &= \delta f'(x_0)+\frac{2}{3!}f'''(x_0)\left(\frac{\delta}{2}\right)^3+..., \\ \implies \frac{f(x_0+\delta/2)-f(x_0-\delta/2)}{\delta} &= f'(x_0)+\frac{1}{24}\delta^2 f'''(x_0)+... \end{aligned} \tag{2.47}$$

Therefore from eq. 2.47 we get a definition for $f'(x_0)$ in terms of the values of $f(x)$ at two neighbouring points

$$f'(x_0) = \frac{f(x_0 + \delta/2) - f(x_0 - \delta/2)}{\delta} + O(\delta^2), \tag{2.48}$$

where $O(\delta^2)$ indicates the terms that are not shown and δ^2 indicates that the lowest order of δ contained in those terms is δ^2. Since we expect δ to be small when calculating the numerical value of the derivative, we can ignore terms containing higher orders of delta in order to arrive at a reasonable approximation for the value of the derivative. Therefore, we get

$$f'(x_0) \approx \frac{f(x_0 + \delta/2) - f(x_0 - \delta/2)}{\delta}. \tag{2.49}$$

This finite difference expression is said to have second order accuracy since terms having δ^2 and higher powers of δ have been ignored. The approximation becomes exact in the limit $\delta \to 0$. An important point to note is that the calculation of the derivative at x_0 does not require the computation of the value of the function at x_0 and knowing the value at two neighbouring points is sufficient.

We have calculated an approximate expression for the derivative at the point x_0 based on the value of $f(x)$ at two neighbouring points that is second order accurate. It is possible to calculate expressions with higher orders or accuracy but that would require the use of more points. It is also possible to calculate finite difference expressions for higher derivatives.

2.3.2 The FDTD algorithm

The FDTD algorithm that was proposed by Kane Yee solves the curl equations from Maxwell's equations (see eq. 2.5) using finite difference expressions for the derivatives [133, 146]. The algorithm can be summarised as follows:

- Discretize space and time so that the electric and magnetic fields are staggered.
- Replace all the derivatives in the curl equations of Maxwell's equations with finite difference equations.

- Solve the finite difference equations to obtain the update equations to get the values of the fields in the future from the fields in the past.

- Evaluate the magnetic fields in the future. This is half a time step.

- Evaluate the electric fields in the future. This is another half time step and taken with the previous step, completes a full time step.

- Repeat the previous two time steps till the desired duration in time has been reached.

We can understand this using a dry run where we apply this algorithm to a concrete example where we consider only one dimension in space (x) and then study the electric and magnetic fields as they evolve in time. We assume that only the z-component of the electric field is non-zero ($E_z \neq 0, E_x = E_y = 0$). Therefore, from the curl equation of the electric field, we get

$$\begin{aligned} \nabla \times \mathbf{E} = -\hat{\mathbf{y}} \frac{\partial E_z}{\partial x} &= -\mu \frac{\partial \mathbf{H}}{\partial t}, \\ \implies \frac{\partial E_z}{\partial x} &= \mu \frac{\partial H_y}{\partial t}, \end{aligned} \tag{2.50}$$

where $\hat{\mathbf{y}}$ is the unit vector in the y-direction and $\mu = \mu_0 \mu_r$ is the magnetic permeability. Therefore, we find that only the y component H_y of the magnetic field $\mathbf{H}$ varies with time. H_x and H_z may have non-zero values but they must be static since their time derivative is zero and since we are only interested in time varying quantities for FDTD simulations, we will ignore them. Considering only $H_y \neq 0$ and applying it to the curl equation of the magnetic field, we get

$$\begin{aligned} \nabla \times \mathbf{H} = \hat{\mathbf{z}} \frac{\partial H_y}{\partial x} &= \epsilon \frac{\partial \mathbf{E}}{\partial t}, \\ \implies \frac{\partial H_y}{\partial x} &= \epsilon \frac{\partial E_z}{\partial t}, \end{aligned} \tag{2.51}$$

where $\hat{\mathbf{z}}$ is the unit vector in the z-direction and $\epsilon = \epsilon_0 \epsilon_r$ is the dielectric permittivity.

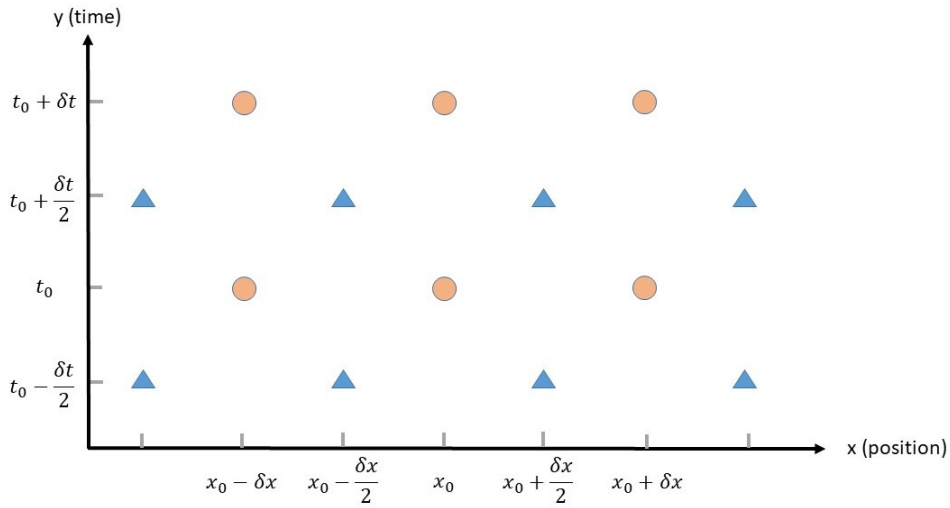

Fig. 2.6: Staggered electric (circles) and magnetic (triangles) field nodes at discretized points in space and time for a 1D system. Time serves as the second dimension for the purpose of visualization.

Now we have to discretize space and time in order to write the differential equations obtained in eqs. 2.50 and 2.51 as finite difference equations. We see that the time derivative of the electric field component depends only on the spatial derivative of the magnetic field component and the time derivative of the magnetic field component depends only on the spatial derivative of the electric field component. We have seen from the finite difference expression given in eq. 2.49 that in order to calculate the derivative of a function at a point x_0, we need to know the value of the function at two different points in its vicinity ($x_0 - \delta/2$ and $x_0 + \delta/2$), but not at the point x_0 itself. Therefore, to know the magnetic (electric) field at a point, we need to know the electric (magnetic) field at two points in its vicinity and not at the very same point. Therefore, we can have staggered grids for the electric and magnetic fields so that at every point where we know the magnetic (electric) field, we know the electric (magnetic) field at two points around it. Therefore if we know the electric field at every value of $x = x_0 + n\delta x$, we must know the magnetic field values at every $x = x_0 + \left(n + \frac{1}{2}\right)\delta x$ where n can take any integer value. The staggered grid that satisfies this requirement for a one dimensional system is shown in Fig. 2.6.

We assume that we know the electric and magnetic fields at every

point for all time $t \leq t_0$. Now we want to calculate the magnetic field at the next step in time $t = t_0 + \delta t/2$ at the point $x = x_0 + \delta x/2$. Then, converting eq. 2.50 to a difference equation using the expression derived in eq. 2.49, we get

$$\begin{aligned} \mu \frac{H_y(x+\delta x/2, t+\delta t/2) - H_y(x+\delta x/2, t-\delta t/2)}{\delta t} = \\ \frac{1}{\delta x}[E_z(x_0+\delta x, t_0) - E_z(x_0, t_0)], \\ \implies H_y(x+\delta x/2, t+\delta t/2) = H_y(x+\delta x/2, t-\delta t/2) + \\ \frac{\delta t}{\mu \delta x}[E_z(x_0+\delta x, t_0) - E_z(x_0, t_0)] \end{aligned} \tag{2.52}$$

The second line of eq. 2.52 is known as the update equation for the magnetic field since it calculates the updated field using the knowledge of the past fields. These update equations move us forward in time by half a time step. We can apply this equation to calculate the value of the magnetic field at at $t = t_0 + \frac{\delta t}{2}$ for every grid point $x = x_0 + \left(n + \frac{1}{2}\right)\delta x$ where the magnetic field is stored.

Now that we know the values of the magnetic field at $t = t_o + \delta t/2$, we can calculate the values of the electric field at $t = t_0 + \delta t$. As an example we want to solve for the electric field at $x = x_0$ at time $t = t_0 + \delta t$. For this we convert the differential equation in eq. 2.51 to a difference equation

$$\begin{aligned} \epsilon \frac{E_z(x_0, t_0+\delta t) - E_z(x_0, t_0)}{\delta t} = \\ \frac{1}{\delta x}[H_y(x_0+\delta x/2, t_0+\delta t/2) - H_y(x_0-\delta x/2, t_0+\delta t/2)], \\ \implies E_z(x_0, t_0+\delta t) = E_z(x_0, t_0) + \\ \frac{\delta t}{\epsilon \delta x}[H_y(x_0+\delta x/2, t_0+\delta t/2) - H_y(x_0-\delta x/2, t_0+\delta t/2)] \end{aligned} \tag{2.53}$$

Eq. 2.53 gives us the update equations for the electric field and advances us by half a time step from $t = t_0 + \delta t/2$ to $t = t_0 + \delta t$. This update equation can be applied to every point $x = x_0 + n\delta x$ to calculate the electric field there. Now these update equations can be repeatedly applied in order to calculate the electric and magnetic fields at more advanced values of time t till we reach the desired duration.

We have shown that it suffices to have a staggered grid with alternate locations storing the values of the electric and magnetic fields to

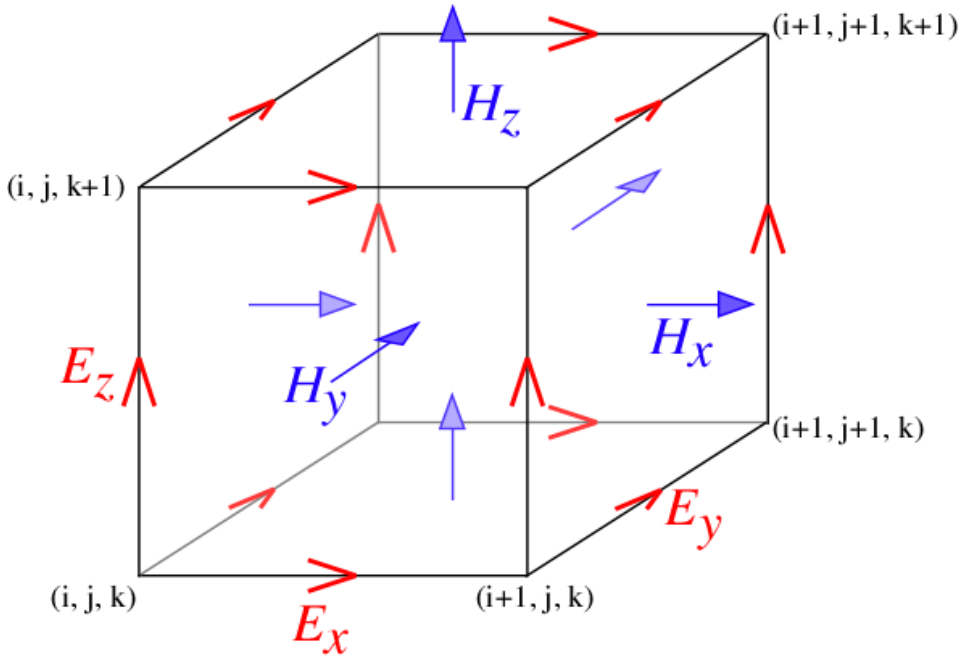

Fig. 2.7: The generalisation of the Yee grid to three dimensions with i, j and k indicating the indices of the grid points in space. The red and the blue arrows indicate the positions at which values of the electric and magnetic fields are stored, respectively. Image from MEEP documentation [147].

calculate the evolution of the fields in time. The structure of Maxwell's equations means that even the generalisation of the FDTD method to higher dimensions and with more field components allows us to maintain this staggered grid, which is known as the Yee lattice, named after the scientist who first proposed this scheme. Fig. 2.7 shows the generalisation of the Yee grid to a three dimensional cell.

We have presented the very fundamentals of the FDTD algorithm in this section. There are several other aspects that require consideration in order to build a full-featured program. There are several open source and commercial programs that implement the FDTD algorithm. Over the course of research carried out for this thesis, we have made use of the open source MEEP package [148] to study the propagation of light in structures of our interest.

Since FDTD simulations are run over a finite area of space, the region of simulation must be terminated using appropriate boundary

conditions. MEEP incorporates three such boundary conditions [147]. Firstly there are metallic boundary conditions which require that the fields are zero at the boundary. Therefore, any fields arriving at the boundary are reflected back into the area of simulation due to the metallic boundary conditions. Then there are Bloch-periodic boundary conditions that are useful for simulating periodic structures such as arrays of waveguides, photonic crystals, etc. This boundary condition requires that $f(x + L) = e^{ik_x L} f(x)$ where L is the period of the structure being simulated and $\mathbf{k}$ is the Bloch wavevector. Finally, there are perfectly matched layer (PML) boundary conditions that absorb all waves incident on them without any reflection. Therefore, they are useful in simulating open boundary conditions. PML layers actually comprise a non-physical material placed at the boundary with some finite thickness, which is designed to have no reflection at the interface and absorbs all the light incident on it. We use the PML boundary conditions from MEEP when we run FDTD simulations. More information about MEEP can be found in Ref. [147].

In this chapter we have provided a short introduction to the various methods employed to carry out the calculations that we have undertaken over the course of research for this thesis. In the following chapters we shall see the results of these calculations.

Chapter 3

BICs in Anisotropic Waveguides with a Single Radiation Channel

As discussed in the introduction, planar anisotropic waveguides comprising uniaxial materials can support two kinds of BICs on leaky modes above the light line:

- pure TE/TM BICs arising from polarisation separation of the mode and the radiation channel (PS BICs),
- hybrid INT BICs arising from destructive interference (INT BICs).

The existence of anisotropy induced BICs was reported in [117] and that opened the pathway for the exploration of the rich parameter space of these anisotropic waveguide structures. In this chapter we will present the results of our investigations on the existence of PS and INT BICs in anisotropic planar waveguides under variation of various structure parameters. In this chapter we will restrict ourselves to studying modes in structures which couple to continuum modes in the substrate via a single radiation channel.

In the first section of this chapter we will present analytic calculations for ordinary and extraordinary waves in uniaxial materials by calculating the eigenvalues and eigenvectors of the auxiliary matrix $\hat{L}$ (see eq. 2.24) and then derive the dispersion equation for the structures being studied using the Berreman transfer matrix method. In the second section we will focus on the impact of the variation of optic

axis orientation on the existence of BICs in these structures. The third section will be focusing on the impact of variation of refractive indices in the structure on BIC existence.

3.1 Theory

In this section, we will derive the dispersion equation for the anisotropic planar waveguide structures that we want to study. We shall use the Berreman transfer matrix method to implement the boundary conditions and calculate the fields across the structures. The dispersion equation will give us the leaky modes that we are interested in studying but in order to find the BICs we have to find the zeroes of the radiation channel amplitude. These zeroes of the radiation channel amplitude are found using the auxiliary condition and we shall also derive that in this section.

3.1.1 Ordinary and Extraordinary Basis Waves

First we shall focus on deriving analytic expressions for the ordinary and extraordinary fields and propagation constants for a uniaxial material. We repeat here the eigenvalue equation 2.24 derived in the previous chapter

$$\hat{L}\vec{F} = \kappa_x \vec{F}. \tag{3.1}$$

The eigenvalues and eigenvectors of the 4×4 matrix $\hat{L}$ represent the x-component of the normalised propagation constant of the travelling basis waves in a general birefringent material. In the case of a uniaxial birefringent material, the four basis waves correspond to two forward and two backward propagating waves, where one of each is the ordinary wave and the other is the extraordinary wave. The values of κ_x and the basis waves can be calculated numerically using an eigenvalue solver however analytic expressions would improve both speed and accuracy. Therefore we calculate analytic expressions for them.

In order to calculate analytic expressions for the eigenvalues of $\hat{L}$ it is essential to know each component of the dielectric tensor. We therefore start with a dielectric tensor for a uniaxial material which, when propagation is along one of the principal axes, is a diagonal matrix and comprises two equal elements which represent the ordinary permittivity while the other element represents the extraordinary permittivity.

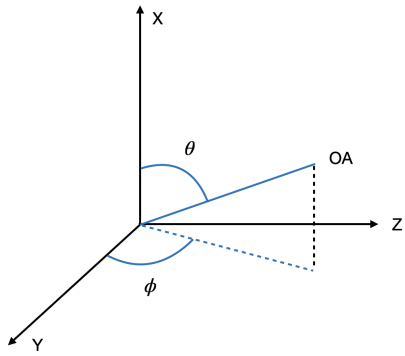

Fig. 3.1: Optic axis in blue and the angles required to specify its orientation. θ is the polar angle and gives the rotation about the z-axis. ϕ is the azimuthal angle and gives the rotation about the x-axis.

We start with the optic axis pointing along the x-axis, perpendicular to the interfaces in our structure, resulting in the following dielectric tensor in the principal axis frame

$$\hat{\epsilon}_r^{OA} = \begin{bmatrix} \epsilon_e & 0 & 0 \\ 0 & \epsilon_o & 0 \\ 0 & 0 & \epsilon_o \end{bmatrix} \tag{3.2}$$

As shown in Fig. 3.1, we arrive at the required orientation of the optic axis first by a rotation about the z axis by the polar angle θ. This is followed by a rotation about the x-axis by the azimuthal angle ϕ. The effect of these rotations on the permittivity tensor can be calculated using the appropriate rotation matrices

$$\hat{R}_x(\phi) = \begin{bmatrix} 1 & 0 & 0 \\ 0 & \cos(\phi) & -\sin(\phi) \\ 0 & \sin(\phi) & \cos(\phi) \end{bmatrix}, \hat{R}_z(\theta) = \begin{bmatrix} \cos(\theta) & -\sin(\theta) & 0 \\ \sin(\theta) & \cos(\theta) & 0 \\ 0 & 0 & 1 \end{bmatrix}. \tag{3.3}$$

Consequently the permittivity tensor in the propagation frame can be obtained as

$$\hat{\epsilon}_r = \hat{R}_x(\phi)\hat{R}_z(\theta)\hat{\epsilon}_r^{OA}\hat{R}_z(-\theta)\hat{R}_x(-\phi). \tag{3.4}$$

Rotation matrices acting on a diagonal matrix according to eq. 3.4 results in a symmetric matrix with only 6 independent elements. We

list the expressions for these elements below

$$\epsilon_{xx} = \epsilon_e \cos^2(\theta) + \epsilon_o \sin^2(\theta) \tag{3.5}$$
$$\epsilon_{xy} = (\epsilon_e - \epsilon_o) \sin(\theta) \cos(\theta) \cos(\phi) \tag{3.6}$$
$$\epsilon_{xz} = (\epsilon_e - \epsilon_o) \sin(\theta) \cos(\theta) \sin(\phi) \tag{3.7}$$
$$\epsilon_{yy} = \epsilon_e \sin^2(\theta) \cos^2(\phi) + \epsilon_o[\sin^2(\phi) + \cos^2(\phi) \cos^2(\theta)] \tag{3.8}$$
$$\epsilon_{yz} = (\epsilon_e - \epsilon_o) \sin^2(\theta) \sin(\phi) \cos(\phi) \tag{3.9}$$
$$\epsilon_{zz} = \epsilon_e \sin^2(\theta) \sin^2(\phi) + \epsilon_o[\cos^2(\phi) + \cos^2(\theta) \sin^2(\phi)]. \tag{3.10}$$

Now that we know the expressions for each element of the permittivity tensor, we can plug these in to the expression for the matrix $\hat{L}$ as given in eq. 2.22 and set about calculating expressions for the eigenvalues of $\hat{L}$

$$\begin{aligned} \hat{L}\vec{F} &= \kappa_x \vec{F}, \\ \implies (\hat{L} - \kappa_x \mathbf{I})\vec{F} &= 0, \end{aligned} \tag{3.11}$$

where $\mathbf{I}$ is a 4×4 identity matrix. Given that we are not interested in the trivial solution where $\vec{F} = 0$, we obtain an expression for the characteristic equation by imposing the only other condition under which the above equation might hold,

$$|\hat{L} - \kappa_x \mathbf{I}| = 0. \tag{3.12}$$

The roots of the characteristic equation above give us the eigenvalues $\kappa_x = k_x/k_0$. For the permittivity tensor of a uniaxial material described above, after some algebra, we can arrive at analytic expressions for κ_x

$$\kappa_x^o = \pm\sqrt{\epsilon_o - \kappa_y^2}, \tag{3.13}$$

$$\kappa_x^e = \frac{1}{\epsilon_{xx}} \left[-\epsilon_{xy}\kappa_y \pm \sqrt{\epsilon_o \left(\epsilon_{xx}\epsilon_e + \kappa_y^2 \left(\epsilon_{zz} - \epsilon_e - \epsilon_o \right) \right)} \right], \tag{3.14}$$

where κ_x^o and κ_x^e are the x-components of the normalised wave propagation vector for the ordinary wave and extraordinary waves, respectively. The $+$ and $-$ signs correspond to waves propagating forward and backward in x. In addition to depending on the permittivity tensor, κ_x also depends on κ_y, the y-component of the normalised wave propagation vector.

Once the analytic expressions for κ_x are known, with some further algebra, we can derive analytic expressions for the eigenvectors $\vec{F}$. The ordinary eigenvector is

$$\overrightarrow{F}_o = \begin{bmatrix} \kappa_x^o \sin(\phi) \sin(\theta) \\ \epsilon_o \sin(\phi) \sin(\theta) \\ -\kappa_x^o \sin(\theta) \cos(\phi) + \kappa_y \cos(\theta) \\ \kappa_x^o \left(\kappa_x^o \sin(\theta) \cos(\phi) - \kappa_y \cos(\theta)\right) \end{bmatrix}, \tag{3.15}$$

and the extraordinary eigenvector is

$$\overrightarrow{F}_e = \begin{bmatrix} -\kappa_x^e \kappa_y \cos(\theta) + \kappa_x^{o2} \sin(\theta) \cos(\phi) \\ \epsilon_o \left(\kappa_x^e \sin(\theta) \cos(\phi) - \kappa_y \cos(\theta)\right) \\ \epsilon_o \sin(\phi) \sin(\theta) \\ -\epsilon_o \kappa_x^e \sin(\phi) \sin(\theta) \end{bmatrix}. \tag{3.16}$$

The appropriate expression for the forward or backward $\kappa_x^{o/e}$ from eqs. 3.13 and 3.14 must be substituted in eqs. 3.15 and 3.16.

We can now write the field matrix $\hat{F}$ in analytic terms as a function of the dielectric tensor and κ_y as

$$\hat{F} = [\vec{F_o^+} \quad \vec{F_o^-} \quad \vec{F_e^+} \quad \vec{F_e^-}], \tag{3.17}$$

where $\hat{F}$ is a 4×4 matrix comprising 4 column vectors.

Isotropic Materials

When we are dealing with an isotropic material, $\epsilon_o = \epsilon_e = \epsilon_r$, and the permittivity can be written as a scalar value, meaning there is no optic axis and $\phi = \theta = 0°$ and $\kappa_x^o = \kappa_x^e = \kappa_x = \sqrt{\epsilon_r - \kappa_y^2}$. The expressions for the fields given in eqs. 3.15 and 3.16 then reduce to

$$\vec{F}_o = \begin{bmatrix} 0 \\ 0 \\ \kappa_y \\ -\kappa_x \kappa_y \end{bmatrix}, \tag{3.18}$$

and

$$\vec{F}_e = \begin{bmatrix} -\kappa_x \kappa_y \\ \epsilon_r \kappa_y \\ 0 \\ 0 \end{bmatrix}. \tag{3.19}$$

Thus, we see that the ordinary and extraordinary basis waves become transverse electric (TE) and transverse magnetic (TM) waves, respectively, when working with isotropic materials.

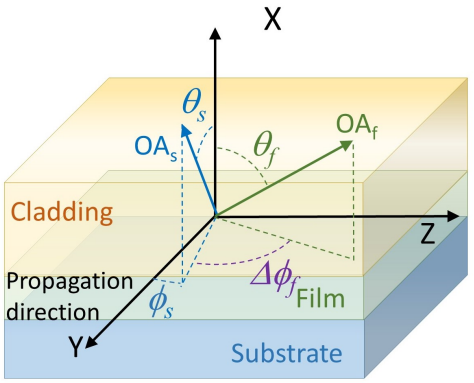

Fig. 3.2: Geometry: a layered waveguide system comprising isotropic cover, and uniaxial film/core and substrate with light propagating along the y-axis. The green and the blue arrows indicate the substrate and film optic axis , respectively. The angles θ_f and θ_s give the polar orientations of the film and substrate optic axes. The azimuthal angle ϕ_f indicates the angle the projection of the film optic axis in the interface plane makes with the direction of light propagation. The azimuthal detuning of the substrate optic axis with respect to the film optic axis is given by $\Delta\phi = \phi_s - \phi_f$.

3.1.2 Dispersion Equation

In this chapter we will study structures where the cover is isotropic, while the core and the substrate are uniaxial as shown in Fig. 3.2. Any valid solution of Maxwell's equations for this structure must simultaneously satisfy the boundary conditions at the film-substrate and the film-cover interfaces. We enforce these boundary conditions using the Berreman transfer matrix method as described in the previous chapter.

The substrate and the cover are semi-infinite in that they extend from their respective interfaces with the film to $-\infty$ and $+\infty$, respectively. Since they are semi-infinite, there are no reflected waves coming back from the direction where they are unbounded. Therefore, when calculating the eigenmodes of the structure without any driving term, we would only consider two basis waves each in the cover and the substrate.

Most commonly, the modes considered are guided waveguide modes below the light line of the structure. The mode propagation constant of the guided modes is higher than the ordinary and extraordinary indices of the cover and the substrate. Therefore, they have evanescent tails

in the cover and the substrate and the two basis waves that have to be selected are obvious: we must select the ones which are exponentially decaying in the cover and the substrate as we move away from the interface.

However, in our work, we are primarily interested in leaky modes. Leaky modes are improper modes that occur above the light line. They are coupled to the continuum via radiation channels. In this chapter we will be focusing on structures where the radiation channel corresponds to one of the basis waves in the substrate. The leaky mode loses energy from the core/film via radiation to the substrate through this channel. This loss of energy can be approximated by adding an imaginary part with a proper sign to the mode propagation constant. Therefore, as this leaky mode with a complex propagation constant propagates, it would decay exponentially. Flux conservation considerations mean that this exponential decay in the direction of propagation has to be compensated by exponential growth in the transverse direction, particularly in the radiation channel via which the radiation leaks [8, 107]. Therefore, when selecting the waves in the cover or the substrate for the leaky mode calculation, we must select the wave that is exponentially growing for the polarisation corresponding to the radiation channel.

Equipped with this knowledge we shall attempt to derive the dispersion equation for the leaky modes in the layered waveguide system shown in Fig. 3.2. We do this by fixing our materials, their optic axes orientations and the thickness of the core in units of wavelength and then solving for the values of the mode propagation constant κ_y (= the mode propagation constant N) where boundary conditions at both interfaces are satisfied.

Since the cover is isotropic and we choose a material with its refractive index below the mode indices of our interest, in the cover we simply have to choose the basis waves that are exponentially decaying as x increases. On the other hand, we will choose a material for the substrate where only one of the ordinary or extraordinary refractive indices is greater than the mode index N and the corresponding polarisation serves as the radiation channel ($n_{es} < N < n_{os}$ or $n_{os} < N < n_{es}$). The basis wave with the polarisation corresponding to the other refractive index, which is lesser than the mode index remains evanescent or confined. The schematic of the transverse section of a leaky mode is shown in Fig. 3.3.

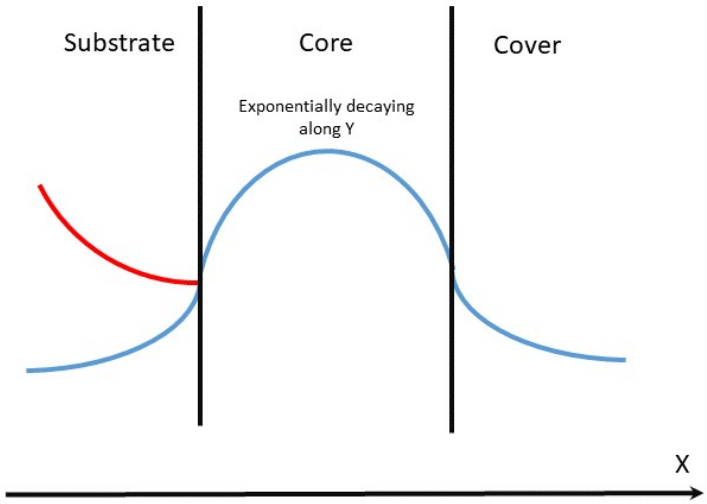

Fig. 3.3: Leaky mode: Schematic of the transverse profile of a leaky mode. The exponentially growing basis wave in the radiation channel in the substrate is shown in red.

Given that we know which waves to select in the cover and in the substrate, we can write the total field at the interfaces. The total field in the cover just to the right of the cover-film interface would be

$$\begin{aligned}\vec{m}_{cover-film} &= a_c^{TE}\vec{F}_c^{TE} + a_c^{TM}\vec{F}^{TM}, \\ &= a_c^{TE}\begin{bmatrix} E_{yc}^{TE} \\ \tilde{H}_{zc}^{TE} \\ E_{zc}^{TE} \\ \tilde{H}_{yc}^{TE} \end{bmatrix} + a_c^{TM}\begin{bmatrix} E_{yc}^{TM} \\ \tilde{H}_{zc}^{TM} \\ E_{zc}^{TM} \\ \tilde{H}_{yc}^{TM} \end{bmatrix},\end{aligned} \tag{3.20}$$

Similarly the total field in the substrate just to the left of the film-substrate interface can be written as

$$\begin{aligned}\vec{m}_{film-substrate} &= a_s^o\vec{F}_s^o + a_s^e\vec{F}_s^e, \\ &= a_s^o\begin{bmatrix} E_{ys}^o \\ \tilde{H}_{zs}^o \\ E_{zs}^o \\ \tilde{H}_{ys}^o \end{bmatrix} + a_s^e\begin{bmatrix} E_{ys}^e \\ \tilde{H}_{zs}^e \\ E_{zs}^e \\ \tilde{H}_{ys}^e \end{bmatrix},\end{aligned} \tag{3.21}$$

where the subscripts c and s indicate the cover and the substrate respectively, the superscripts TE, TM, o and e represent the choice of

polarisation of the basis wave (transverse electric, transverse magnetic, ordinary and extraordinary), $a_{c/s}^{TE/TM/o/e}$ is the scalar amplitude of the corresponding basis wave and $\vec{F}_{c/s}^{TE/TM/o/e}$ is a 4×1 column vector which represents the basis wave vector for the cover or the substrate containing the four tangential field components: $E_y, \tilde{H}_z, E_z$ and $\tilde{H}_y$. Since the cover being considered is isotropic, we classify the basis waves as TE or TM while for the uniaxial substrate we classify the basis waves as ordinary or extraordinary.

Since we consider the 4 tangential components, the total field $\vec{m}$ is continuous across the interface. Therefore the field in the film just to the left of the cover-film interface would be the same as the field in the cover just to the right of the interface. The same applies to the field being the same just to the left and right of the film-substrate interface.

Since we have derived analytic expressions for the field matrix $\hat{F}$ for a uniaxial layer in the previous section, we can calculate the characteristic matrix

$$\hat{M} = \hat{F}^{-1}\hat{A}_d\hat{F} \tag{3.22}$$

for any layer of thickness d where $\hat{A}_d$ is the phase matrix for the layer as defined in eq. 2.30. If there are multiple layers of material in between the cover and the substrate, we can multiply the characteristic matrix of each layer to calculate a total transfer matrix $\hat{M}_{tot}$ for the system as shown in eq. 2.37.

Now we know that in the Berreman transfer matrix formalism, the characteristic matrix for a layer translates the total fields across a layer. Therefore, we can use the characteristic matrix for the film to relate the fields given in eqs. 3.20 and 3.21 as

$$a_s^o\vec{F}_s^o + a_s^e\vec{F}_s^e = a_c^{TE}\hat{M}\vec{F}_c^{TE} + a_c^{TM}\hat{M}\vec{F}_c^{TM}. \tag{3.23}$$

This gives us four equations, one for each field component contained in $\vec{F}_{c/s}^{TE/TM/o/e}$. We can re-write this as

$$\begin{aligned} &a_c^{TE}\hat{M}\vec{F}_c^{TE} + a_c^{TM}\hat{M}\vec{F}_c^{TM} - a_s^o\vec{F}_s^o - a_s^e\vec{F}_s^e = 0, \\ \implies &\begin{bmatrix}\hat{M}\vec{F}_c^{TE} & \hat{M}\vec{F}_c^{TM} & -\vec{F}_s^o & -\vec{F}_s^e\end{bmatrix}\begin{bmatrix}a_c^{TE}\\ a_c^{TM}\\ a_s^o\\ a_s^e\end{bmatrix} = \begin{bmatrix}0\\0\\0\\0\end{bmatrix}. \end{aligned} \tag{3.24}$$

Since $\hat{M}$ is a 4×4 matrix and $\vec{F}_c^{TE/TM}$ is a 4×1 column vector, their multiplication yields another 4×1 column vector. Therefore, eq. 3.24

can be written as

$$\hat{R} \begin{bmatrix} a_c^{TE} \\ a_c^{TM} \\ a_s^o \\ a_s^e \end{bmatrix} = 0, \tag{3.25}$$

where $\hat{R} = \begin{bmatrix} \hat{M}\vec{F}_c^{TE} & \hat{M}\vec{F}_c^{TM} & -\vec{F}_s^o & -\vec{F}_s^e \end{bmatrix}$ is a 4×4 matrix. We therefore have a homogeneous system of 4 equations where the amplitudes $a_{c/s}^{TE/TM/o/e}$ serve as the four unknown variables. This system of equations always supports a trivial solution but we are interested only in non-trivial solutions. A system of homogeneous linear equations can have a non-trivial solution only if the determinant of the coefficient matrix, $\hat{R}$, is zero. This requirement gives us the dispersion condition

$$|\hat{R}| = 0. \tag{3.26}$$

Once the materials, the dimensions of the structure and the orientation of the optic axes in the uniaxial layers is fixed, $|\hat{R}|$ only depends on κ_y. However this is a transcendental equation since several elements of $\hat{R}$ contain expressions involving κ_y but under a square root. Thus, while it is not possible to obtain closed form expressions for κ_y, we can solve for it numerically to obtain the values of $\kappa_y (= N)$ where $|\hat{R}| = 0$.

3.1.3 Auxiliary Condition

The dispersion equation given by eq. 3.26 only gives us the values of N where the mode exists. While the imaginary part of N approximates the losses of leaky modes, the dispersion equation cannot definitively tell us about the existence of BICs, particularly INT BICs.

BICs exist when the coupling to the radiation channel is entirely cancelled. In the case of PS BICs which are the analogues of symmetry protected BICs in our system, this occurs because the radiation channel and the mode have orthogonal polarisations (TE mode and TM radiation channel or vice versa). These PS BICs can only occur at specific directions with propagation along the principal axes of the uniaxial structure. INT BICs occur when the amplitude of the basis wave in the radiation channel becomes zero. This is a consequence of the boundary conditions inducing mixing of the basis waves in the different layers and resultant destructive interference. Therefore, INT BICs occur when the amplitude of the radiation channel becomes zero.

We have been working with the scenario where either the ordinary or the extraordinary polarisation in the substrate is the radiation channel while the other polarisation corresponds to an evanescent of confinement channel. In this scenario, we can write eq. 3.24 as

$$a_c^{TE}\hat{M}\vec{F}_c^{TE} + a_c^{TM}\hat{M}\vec{F}_c^{TM} - a_s^{rad}\vec{F}_s^{rad} - a_s^{conf}\vec{F}_s^{conf} = 0, \tag{3.27}$$

where the superscripts rad and $conf$ indicate the radiation and confinement channels in the substrate, respectively. They can be either the ordinary or the extraordinary wave depending on whether the uniaxial material used in the substrate is positive birefringent ($n_{es} > n_{os}$) or negative birefringent ($n_{es} < n_{os}$). For BIC existence the requirement is that the amplitude of the radiation channel go to zero, i.e., $a_s^{rad} = 0$. Given that, we can write eq. 3.27 as

$$\begin{aligned} &a_c^{TE}\hat{M}\vec{F}_c^{TE} + a_c^{TM}\hat{M}\vec{F}_c^{TM} - a_s^{conf}\vec{F}_s^{conf} = 0, \\ \implies &\begin{bmatrix}\hat{M}\vec{F}_c^{TE} & \hat{M}\vec{F}_c^{TM} & -\vec{F}_s^{conf}\end{bmatrix}\begin{bmatrix}a_c^{TE}\\ a_c^{TM}\\ a_s^{conf}\end{bmatrix} = \begin{bmatrix}0\\0\\0\\0\end{bmatrix}. \end{aligned} \tag{3.28}$$

This is an overdetermined, homogeneous system of linear equations since there are four equations for the four field components while there are only 3 unknown amplitudes.

Given that there are only 3 unknown amplitudes, if all 4 of the equations are linearly independent, then the system would be inconsistent. Moreover, the system is homogeneous, and therefore the trivial solution where all amplitudes are 0 always exists. Again, since there are only 3 unknown variables, if any three of the equations are linearly independent then there can only be one solution. And since the trivial solution always exists for a homogeneous system, then it is the only solution. Therefore, we find that non-trivial solutions can only exist if at most two of the equations are linearly independent. We can define a matrix $\hat{Z}_{4\times3}$ from eq. 3.28 such that

$$\hat{Z}_{4\times3} = \begin{bmatrix}\hat{M}\vec{F}_c^{TE} & \hat{M}\vec{F}_c^{TM} & -\vec{F}_s^{conf}\end{bmatrix}. \tag{3.29}$$

Since non-trivial solutions to eq. 3.28 can only exist if at most two of the equations are linearly independent, we must check if this holds. If two of the equations are linear combinations of the other two equations,

then the determinant of any 3×3 sub-matrix, which we call $\hat{Z}_{3\times3}$, selected from $\hat{Z}_{4\times3}$ would be zero. There are four different ways we can select three rows from $\hat{Z}_{4\times3}$ to make distinct 3×3 sub-matrices. Therefore the auxiliary condition for the radiation channel amplitude (a_s^{rad}) to be zero can be formulated as the requirement that

$$|\hat{Z}_{3\times3}| = 0 \; \forall \; \hat{Z}_{3\times3} \subset \hat{Z}_{4\times3} \tag{3.30}$$

Therefore we can conclude that INT BICs occur wherever the auxiliary condition and the dispersion equation both hold. In other words INT BICs can be found wherever the same value of κ_y or N solves both eqs. 3.26 and 3.30.

3.2 Variation of Optic Axis Orientation

BICs can broadly be classified into two categories. BICs belonging to the first category, symmetry protected BICs are extremely sensitive to perturbations that break the required symmetry and under those perturbations those BICs cease to exist, typically resulting in high Q-factor resonances that are often referred to as quasi-BICs [68, 71, 73, 74]. The other category of BICs arise as a result of parameter tuning and occur at specific points in the parameter space where leakage to a radiation channel is cancelled. Since these BICs arise as a result of parameter tuning and therefore occur at specific points on the parameter space, they may not survive under variation of parameters. The exceptions to this are those parameter tuned BICs that are topologically protected and therefore robust under the variation of parameters. BICs that are topologically protected are characterised by phase or polarisation singularities and have been reported in a variety of photonic systems [20, 58–61].

We have discussed the existence of BICs in anisotropic planar waveguides as reported in [117] in Chapter 1. However, while the existence of anisotropy induced BICs had been reported in [117], there was no information about the properties of these BICs or their robustness to perturbation of system parameters. In this section we shall present the results of our investigation on the effect of variation of the orientation of the optic axes of the uniaxial layers on the anisotropy induced BICs supported by the layered waveguide structure shown in Fig. 3.2.

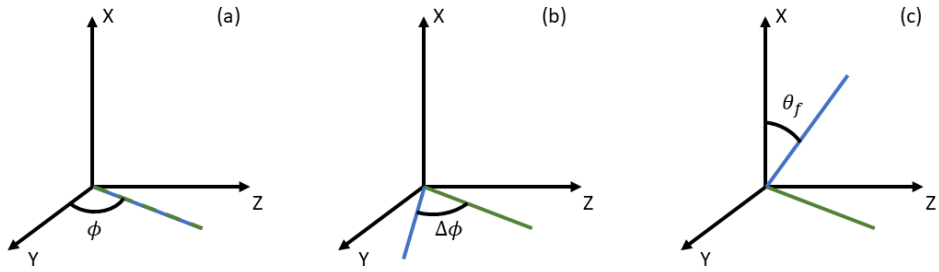

Fig. 3.4: The optic axes of the film (blue) and substrate (green) in different configurations. (a) Full anisotropy-symmetry with both optic axes parallel to each other and lying in the interface $(y-z)$ plane. (b) Azimuthal anisotropy-symmetry breaking with both optic axes in the interface plane but not parallel to each other. (c) Polar anisotropy-symmetry breaking where the film optic axis has been moved out of the interface plane ($\theta_f \neq 90°$).

3.2.1 Anisotropy-symmetry

We must first define here the concept of anisotropy-symmetry which becomes relevant when studying structures with multiple birefringent layers. Since we consider structures with a uniaxial core and a uniaxial substrate, we are dealing with a total of two optic axes. The orientation of these optic axes relative to one another and with respect to the interface plane are important parameters. While the structure shown in Fig. 3.2 is geometrically asymmetric, we shall talk of the various combinations of optic axes orientations in terms of anisotropy-symmetry.

The different scenarios that may arise are shown in Fig. 3.4 and are as follows:

- **Full anisotropy-symmetry** is maintained when both optic axes are parallel to the interface plane and to each other, i.e., $\theta_f = \theta_s = 90°$ and $\Delta\phi = \phi_s - \phi_f = 0°$. In this scenario it is possible to define a set of coordinate axes which coincides with both the principal axes of the film and the substrate while keeping the interface perpendicular to one axis. When light propagates along one of these axes, the permittivity tensor of both the film and the substrate is diagonal and there can be TE/TM solutions for the modes of the structure.

- **Azimuthal anisotropy-symmetry breaking** occurs when the optic axes of the film and the substrate are both parallel to the interface plane ($\theta_f = \theta_s = 90°$) but not to each other. They are offset by an angle $\Delta\phi \neq 0°$. In this scenario, as long as $\Delta\phi \neq 90°$, there can be no coordinate axes that coincides with the principal axes of both the film and the substrate. Therefore, for no direction of propagation can both permittivity tensors be diagonal and therefore no TE/TM modes are supported. More importantly, for the geometry shown in Fig. 3.2, for azimuthal anisotropy-symmetry breaking, the permittivity tensor for the two layers takes the form

$$\hat{\epsilon}_r = \begin{bmatrix} \epsilon_{xx} & 0 & 0 \\ 0 & \epsilon_{yy} & \epsilon_{yz} \\ 0 & \epsilon_{yz} & \epsilon_{zz} \end{bmatrix}, \tag{3.31}$$

  meaning that only two off-diagonal terms are introduced. Moreover, because the permittivity tensor is symmetric they are identical. This is true for at least one of the layers even if light propagates along one of the principal axes of the other layer.

- **Polar anisotropy-symmetry breaking** occurs when one or both the optic axes of the film or the substrate are taken out of the interface plane, i.e., they are no longer parallel to the interface plane ($\theta_f \neq 90°$ and/or $\theta_s \neq 90°$). Even here there is no choice of coordinate axes which coincides with the principal axes of the film and substrate while keeping the interface perpendicular to one axis. Therefore, the permittivity tensor cannot be diagonal for any propagation direction. For any general propagation direction, with polar anisotropy-symmetry breaking we have to consider the full 3×3 permittivity tensor with 3 unique off diagonal elements.

In the following sections we shall inspect how anisotropy-symmetry affects the existence of BICs in different anisotropic layered waveguides.

3.2.2 Positive Uniaxial Core, Negative Uniaxial Substrate

We shall now focus on a structure with a positive uniaxial core/film whose ordinary and extraordinary refractive indices are $n_{of} = 1.5, n_{ef} =$

1.75 and a negative uniaxial substrate whose indices are $n_{of} = 2, n_{ef} = 1.25$. We consider that the cover is isotropic air with $n_c = 1$. This is an anti-guiding structure since the highest refractive index is the ordinary index in the cladding and since the ordinary index is independent of the direction of propagation, this structure always has a radiation channel that is available for the light in the core/film to couple to the continuum of ordinary waves in the substrate. Therefore this structure cannot support any guided modes. However, it can support leaky modes where the radiation leaks to the substrate via the channel provided by the ordinary basis wave in the substrate whereas the extraordinary wave in the substrate is evanescent. This waveguide structure with full anisotropy-symmetry was analysed in [117] and it was found that the aforementioned leaky modes can support both polarization separable (PS) and interference (INT) BICs. The fundamental leaky mode only supports PS BICs while the first order leaky mode supports both PS and INT BICs. We shall therefore focus exclusively on the first order leaky mode in our study.

The modes of this structure can be studied in a three dimensional dispersion plot involving ω, k_y and k_z. Now if one takes the projection of the film optic axis in the interface $y - z$ plane as a reference, the angle ϕ gives us the angle between that projection and the propagation direction. Given that, it would be possible to collapse the three dimensional dispersion plot to a two dimensional plot by using the relation $\phi = arctan(k_z/k_y)$. D/λ is a dimensionless ratio but it can be linked to the frequency ω by the relation $\omega \cdot D = \frac{2\pi cD}{\lambda}$ where λ is the free space wavelength. Therefore, the mode plots in the $\phi - D/\lambda$ space are 2D projections of the 3D dispersion plots though instead of the mode index, the colour indicates the propagation length L, which is a measure of the radiative losses of the leaky mode.

We fix the propagation direction in the y-direction. In this situation, rotation of the entire geometry about the x-axis, which is normal to the interface plane, would mean that the film and the substrate optic axes are rotating concurrently. Therefore, while we vary $\phi(= \phi_f)$ in our calculations, it is more useful to consider the offset $\Delta_s = \phi_s - \phi_f$ as an independent variable instead of treating ϕ_s as the independent variable. Therefore we broadly have two scenarios: (a) film and substrate optic axes (or their projections in the interface plane when the axes are taken out of the plane) are either aligned ($\Delta_s = 0°$) or (b) not aligned($\Delta_s \neq 0°$). These correspond to the scenarios where azimuthal

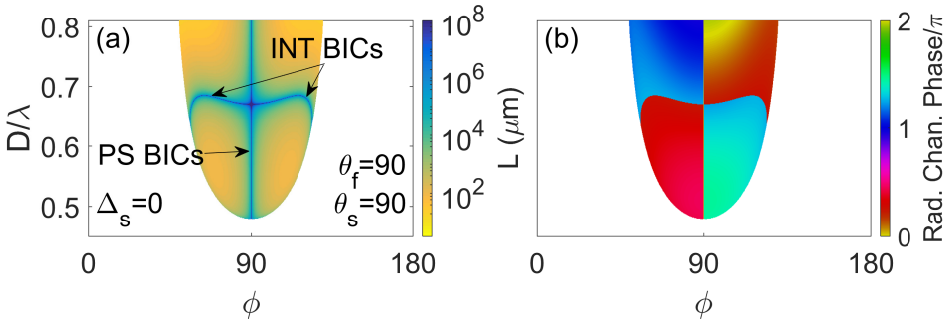

Fig. 3.5: Full anisotropy-symmetry: (a) First order leaky mode for a structure with an isotropic cover ($n_c = 1$), positive uniaxial core/film ($n_{of} = 1.5, n_{ef} = 1.75$), and a negative uniaxial substrate $n_{os} = 2, n_{es} = 1.25$ in the $\phi - D/\lambda$ space. The film and substrate optic axes are aligned ($\Delta_s = 0°$) and lie in the interface plane ($\theta_f = \theta_s = 90°$). The colour indicates the propagation length L that the mode travels before suffering $1/e$ attenuation. Blue lines indicate BICs. The white area indicates the area beyond the leaky mode cut-off. (b) Phase of the radiation channel (ordinary) amplitude measured with respect to the confinement channel (extraordinary) for the mode in (a).

anisotropy-symmetry is either maintained or broken, respectively.

Fig. 3.5(a) shows the aforementioned projection of the dispersion plot for first order leaky mode supported by the structure when full anisotropy-symmetry is maintained, i.e, the film and substrate optic axes are aligned ($\Delta_s = 0°$) and the optic axes of the film and the substrate lie in the interface plane ($\theta_f = \theta_s = 90°$). The colour shows the propagation length L that the mode can travel before it is attenuated by a factor $1/e$. The transition from the coloured sheet to the white space denotes the leaky mode cut-off. The BIC lines of existence on this leaky mode are denoted by the blue lines where L diverges to infinity. We have put a finite colour scale only because our calculations are limited by numerical resolution. This is the mode B1 that we saw in the full three dimensional dispersion plot in Fig. 1.5. We see that when full anisotropy-symmetry is maintained, the structure supports both PS and INT BICs. The blue line at $\phi = 90°$ comprises the PS BICs that occur because the polarisation of the mode is orthogonal to the polarisation of the radiation channel. With $\theta_s = \theta_f = 90°$ and $\phi_s = \phi = 90°$, the ordinary and extraordinary waves in the substrate and the film reduce to TM and TE waves, respectively (see eq. 3.15).

Therefore, at $\phi = 90°$ we can talk of TE and TM modes when full anisotropy-symmetry is maintained. Since the ordinary wave in the substrate, which is the TM wave at $\phi = 90°$, provides the radiation channel in the structure we are considering, the TE mode supported by the structure at that point cannot access the TM radiation channel and this gives rise to the PS BIC. However, this BIC can only occur at $\phi = 90°$ and that too only when full anisotropy-symmetry is maintained since the ordinary and extraordinary waves do not correspond to TE/TM waves when anisotropy-symmetry is broken. This is why we consider PS BICs in anisotropic planar waveguiding structures as analogous to symmetry protected BICs in periodic structures. The lateral, curved line corresponds to hybrid (TE dominant) INT BICs that occur because the mixing of waves at the interfaces due to birefringence leads to destructive interference and the amplitude of the radiation channel being zero. Since full anisotropy-symmetry is maintained the distribution of the BIC lines of existence on the leaky mode is symmetric about $\phi = 90°$.

As outlined in subsection 3.1.3, INT BICs occur when the zeroes of the radiation channel amplitude coincide with the solutions of the dispersion condition. The radiation channel amplitude is typically complex and therefore carries a phase. When the magnitude of the radiation channel amplitude is zero, the phase is undefined. Therefore, we inspect the phase map of the radiation channel amplitude. In this geometry the wave with ordinary polarisation in the substrate serves as the radiation channel. Fig. 3.5(b) shows the phase of the radiation channel amplitude for the leaky mode in Fig. 3.5(a). The phase is measured with respect to the confinement channel, which is the extraordinary wave. We see that the blue lines indicating BICs correspond to discontinuities of $\pm\pi$ radians in the phase map.

We now consider the case when $\Delta_s = 2°$, i.e, the substrate optic axis is no longer aligned with the film optic axis. Whenever the film optic axis makes an angle ϕ with the direction of propagation y, the substrate optic axis would make an angle $\phi_s = \phi + \Delta_s$. Both optic axes remain in the interface plane ($\theta_f = \theta_s = 90°$) which means polar anisotropy-symmetry is maintained. As mentioned before, since azimuthal anisotropy-symmetry is broken and $\phi_s = 92°$ when $\phi = 90°$, the ordinary and extraordinary waves in the film and substrate do not simultaneously become TM/TE waves at any value of ϕ and therefore the structure does not support any purely TE or TM modes. This

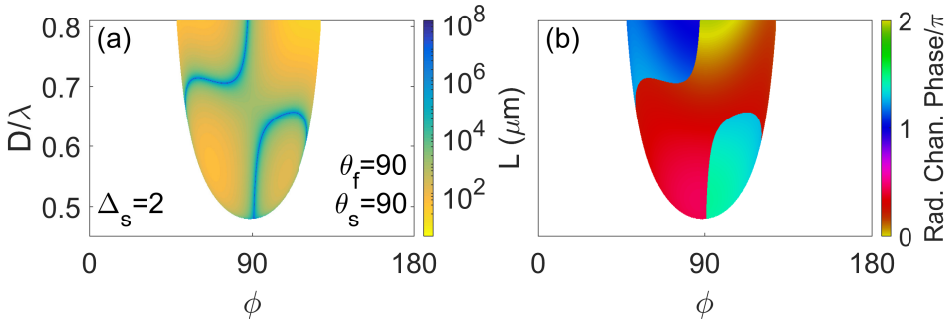

Fig. 3.6: Azimuthal anisotropy-symmetry breaking: (a) First order leaky mode for in the $\phi - D/\lambda$ space. The film and substrate optic axes are offset by an angle ($\Delta_s = 2°$). Both optic axes lie in the interface plane ($\theta_f = \theta_s = 90°$). (b) Phase of the radiation channel (ordinary) amplitude measured with respect to the confinement channel (extraordinary) for the mode in (a).

precludes the existence of PS BICs. Therefore, any BICs supported by this structure would have to be INT BICs. Fig. 3.6(a) shows the first order leaky mode when azimuthal anisotropy-symmetry is broken. With the azimuthal anisotropy-symmetry broken, we find in Fig. 3.6(a) that the BIC lines of existence seen in Fig. 3.5 are now distorted. The distribution of the BIC lines of existence on the leaky mode is no longer symmetric about $\phi = 90°$. The TE PS BICs become hybrid (TE dominant) INT BICs. Moreover, the crossing of the PS and INT BIC lines in Fig. 3.5(a) becomes an anti-crossing in Fig. 3.6(a) when azimuthal anisotropy-symmetry is broken. There are two separate lines of INT BICs embedded on the leaky mode. There is one line of INT BICs at higher values of ϕ and lower values of D/λ and another line of INT BICs at lower values of ϕ and higher values of D/λ.

Fig. 3.7(a) shows the leaky mode when we have the opposite azimuthal anisotropy-symmetry breaking, i.e., $\Delta_s = -2°$. In this scenario, there are again no PS BICs and the the crossing between the lines of INT BICs and PS BICs (see Fig. 3.5(a)) is transformed into an anti-crossing between two lines of INT BICs. However, the position of the BIC lines of existence on the leaky mode in Fig. 3.7(a) is swapped about the $\phi = 90°$ line when compared to Fig. 3.6(a). There is one BIC line of existence at lower values of ϕ and low D/λ and another BIC line of existence at higher values of ϕ and low D/λ. It is important to note from Fig. 3.6(b) and 3.7(b), which show the phase maps of the

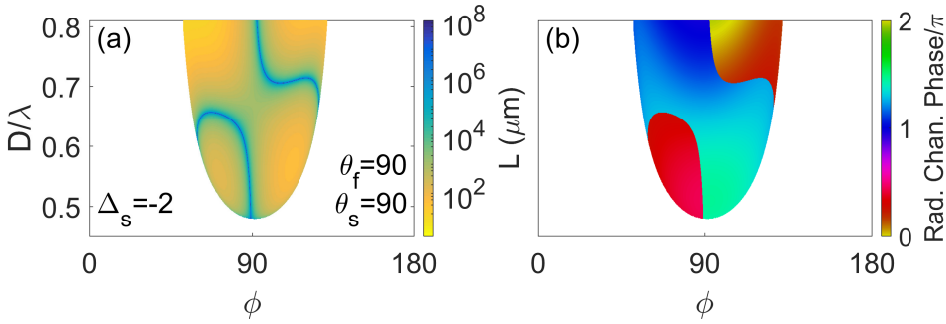

Fig. 3.7: Same as Fig. 3.6 but with opposite azimuthal anisotropy-symmetry breaking with $\Delta_s = -2°$.

radiation channel amplitude for the corresponding leaky mode, that the BIC lines of existence continue corresponding to discontinuities of $\pm\pi$ in the phase maps. Since azimuthal anisotropy-symmetry breaking leads to smooth distortions of the BIC lines of existence on the leaky mode sheet, we shall refer to it as weak anisotropy-symmetry breaking. That azimuthal anisotropy-symmetry breaking leads to the conversion of lines of PS BICs to INT BICs is analogous to the situation reported in Ref. [66] where the breaking of certain symmetries in a photonic crystal slab leads to a symmetry protected BIC being converted to a BIC arising due to parameter tuning.

We shall now consider the case where polar anisotropy-symmetry is broken. Fig. 3.8 shows the leaky mode when polar anisotropy-symmetry is broken by taking the film optic axis out of the interface plane. The optic axis of the film is no longer parallel to the interface $(y-z)$ plane and makes an angle $\theta_f = 85°$ with the x-axis. Azimuthal anisotropy-symmetry is not broken. This means that $\Delta_s = 0°$ and the projection of the film optic axis is parallel to the substrate optic axis which lies in the interface plane ($\theta_s = 90°$). As in the case with azimuthal anisotropy-symmetry breaking, PS BICs cannot exist in this geometry since no purely TE/TM modes are supported. Remarkably, we find that in this scenario, the BIC lines of existence on the leaky mode sheet seen in Fig. 3.5(a) collapse to BIC points in Fig. 3.8(a). Each segment of the BIC lines of existence collapse to an isolated BIC point and the distribution of the points is symmetric about $\phi = 90°$. Therefore, the INT BICs now exist only at isolated points in the $\phi - D/\lambda$ space. Families of BICs as represented by the lines of BIC existence embedded on the leaky mode sheet no longer exist under

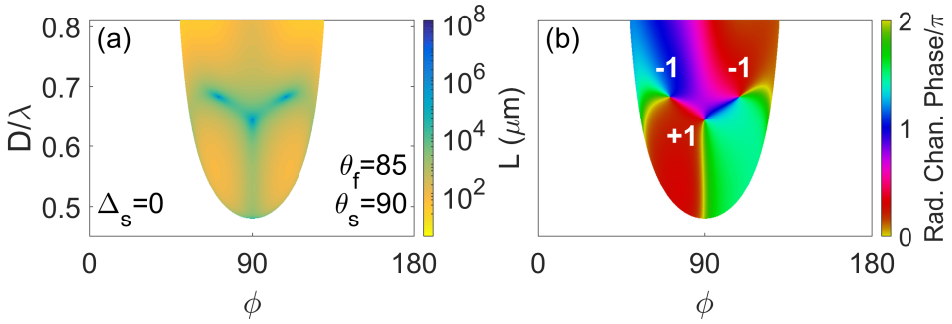

Fig. 3.8: Polar anisotropy-symmetry breaking: (a) First order leaky mode in the $\phi - D/\lambda$ space. The film optic axis is moved out of the interface plane ($\theta_f = 85°$ with respect to the normal to the interface) while the substrate optic axis remains in the interface plane ($\theta_f = 90°$). The projection of the film optic axis in the interface plane is parallel to the substrate optic axis ($\Delta_s = 0°$). (b) Phase of the radiation channel (ordinary) amplitude measured with respect to the confinement channel (extraordinary) for the mode in (a).

polar anisotropy-symmetry breaking. Thus adding a degree of freedom by allowing the optic axis to move out of the interface plane, leads to a collapse of the BIC solutions from lines to isolated points. This arises as a consequence of the interplay of the solutions of the dispersion equation (eq. 3.26) and the auxiliary condition (eq. 3.30) and will be explored in more detail later in this chapter. The breaking of a symmetry usually leads to symmetry protected BICs being converted to quasi BICs in photonic systems [68, 73]. However we find that in this system that instead of BICs disappearing altogether, breaking polar anisotropy-symmetry leads to a reduction in the dimension of the BIC solution on the leaky mode sheet.

The collapse of the BIC lines of existence to isolated BIC points brings about a drastic change in the phase map as shown in Fig. 3.8(b). While the BIC lines of existence had been characterised by discontinuities of $\pm\pi$ in the phase map, the BIC points are characterised by screw phase dislocations that are indicative of branch point singularities in the phase of the radiation channel amplitude. Therefore the BIC points can now be assigned winding numbers. In Fig. 3.8(b), the BIC point originating from the line of PS BICs has a winding number of $+1$ (clockwise increase) and the two BIC points arising from the lines of INT BICs have a winding number of -1 (counter-clockwise

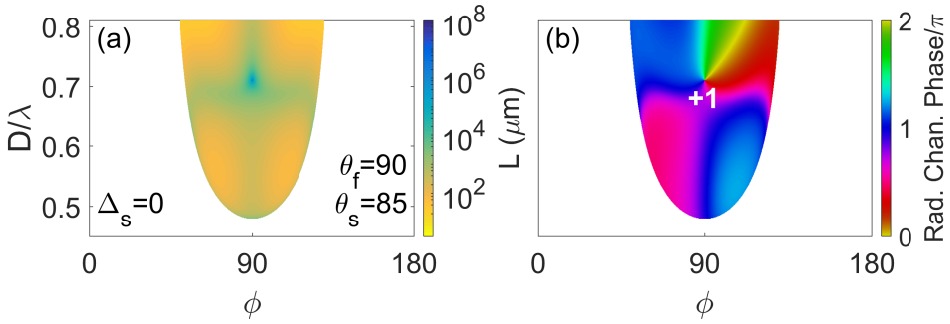

Fig. 3.9: Same as Fig. 3.8 but with the film optic axis in the interface plane ($\theta_f = 90°$) and the substrate optic axes taken out of the interface plane.($\theta_s = 85°$).

increase). The signs of the winding numbers are reversed for the BICs that exist in the range $180° < \phi < 360°$ (not shown in the figure). That BICs are characterised by either polarisation or phase singularities has been theoretically predicted and experimentally observed [20, 58–61] but the transition from phase discontinuities to screw phase dislocations was observed for the first time in this system and was reported in Ref. [134]. Because polar anisotropy-symmetry breaking causes the collapse of BIC lines of existence to BIC points, we shall refer to it as strong anisotropy-symmetry breaking. Note that strong/weak does not indicate the magnitude of the angle by which the optic axis has been moved but rather the anisotropy-symmetry that has been broken: polar or azimuthal.

Polar anisotropy-symmetry was broken for the mode in in Fig. 3.8 by moving the film optic axis out of the interface plane ($\theta_f \neq 90°$) while leaving the substrate optic axis in the interface plane ($\theta_s = 90°$). Polar anisotropy-symmetry can also be broken by doing the opposite, i.e, leaving the film optic axis in the interface plane ($\theta_f = 90°$) and moving the substrate optic axis out of the interface plane ($\theta_s \neq 90°$). The mode supported by this latter structure is shown in Fig. 3.9(a). We find that there is only a single INT BIC point that is embedded on the leaky mode sheet at $\phi = 90°$. Though there are no BIC lines of existence, there remain echoes of those BICs in the form of areas of low losses corresponding to those lines. Inspecting the corresponding phase map, shown in Fig. 3.9(b) shows us that the screw phase dislocation involves a clockwise increase and thus a winding number of +1 can be assigned to it. Since the INT BIC point arising from the PS BIC

carried a +1 winding number in the previous case (see Fig. 3.8), we can say that this INT BIC point also emerges from the the PS BIC. Note that the regions of low loss on the leaky mode sheet in Fig. 3.9(b) corresponding to the areas supporting lines of BIC existence in the fully anisotropy-symmetric case do not correspond to any phase singularities and therefore there are no discontinuities here.

Another configuration that results in polar anisotropy-symmetry breaking is the situation when both the film and the substrate optic axes are moved out of the interface plane. Fig. 3.10(a) shows the leaky mode for the configuration where both the film and substrate interface have been moved out of the interface plane. However, the two optic axes are parallel to each other ($\theta_f = \theta_s = 70° \neq 90°$). In this configuration we find that the lines of BIC existence again collapse to BIC points like it did in the previous cases with polar anisotropy-symmetry breaking. However, now the point BICs occur very close to the cut-off of the leaky mode. They are still distributed symmetrically about $\phi = 90°$. The phase map in Fig. 3.10(b) shows that the screw phase dislocations for both INT BICs involve counter-clockwise increase and therefore can be assigned a winding number -1.

After studying a structure with polar anisotropy-symmetry breaking where the optic axes were moved out of the interface plane but parallel to each other, we now focus on a structure where they are moved out of the interface plane and are no longer parallel. The mode shown in Fig. 3.11(a) is for the configuration where the film optic axis makes an angle of 70° and the substrate optic axis makes an angle of 89° with the x-axis, respectively. We find that there are three INT

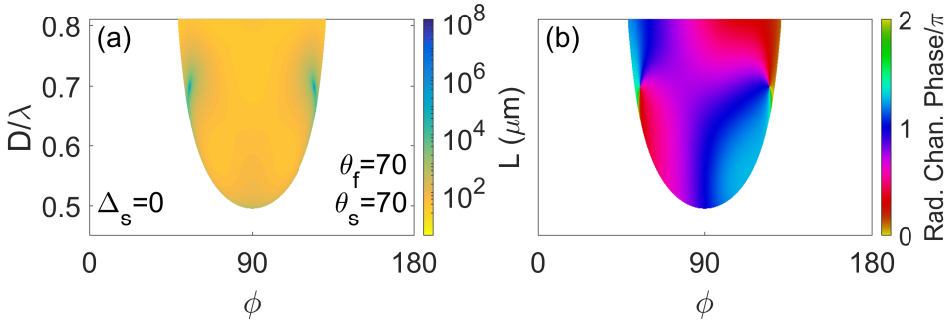

Fig. 3.10: Same as Fig. 3.8 but with both the film and substrate optic axes moved out of the interface plane and parallel. ($\theta_f = \theta_s = 70°$).

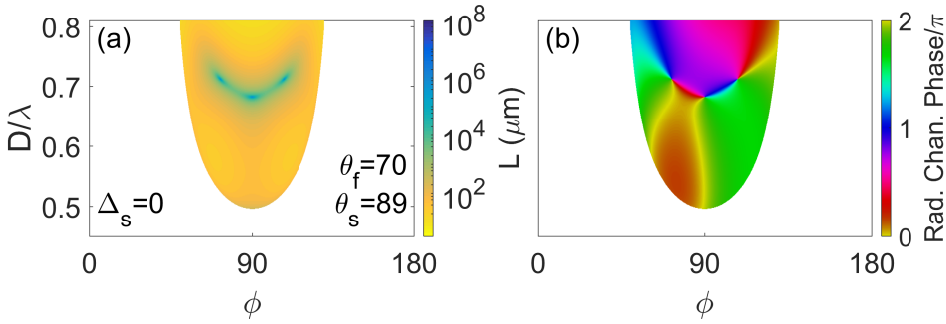

Fig. 3.11: Same as Fig. 3.8 but with both the film and substrate optic axes moved out of the interface plane however they are no longer parallel to each other ($\theta_f = 70°$ while $\theta_s = 89°$).

BIC points embedded on the leaky mode sheet for this structure which are connected by a region of low loss. There is one BIC at $\phi = 90°$ and two others distributed symmetrically about $\phi = 90°$. The phase map of the radiation channel amplitude shown in Fig. 3.11(b) shows that once again the screw phase dislocation at the BIC point at $\phi = 90°$ arising from the PS BIC is characterised by a clockwise increase and therefore can be assigned a winding number $+1$ while the two BIC points arising from the lateral curved line of INT BICs (see Fig. 3.5) are characterised by screw phase dislocations that increase counter-clockwise and so can be assigned a winding number -1. This situation is quite similar to the situation shown in Fig. 3.8 where the two optic axes were also not parallel but the substrate optic axis was left in the interface plane ($\theta_s = 90°$) and therefore the leaky mode sheet, the BICs embedded on it, and the phase map in Fig. 3.11 look similar to it.

We have studied various configurations for this anisotropic layered waveguide with a positive uniaxial core and a negative uniaxial substrate. We have found that when full anisotropy-symmetry is maintained, the first order leaky mode supports lines of INT BICs. Azimuthal anisotropy-symmetry breaking results in the lines of BIC existence being distorted while polar anisotropy-symmetry breaking results in the collapse of the BIC lines to BIC points and a transition from phase discontinuities to screw phase dislocations with winding numbers. In both cases the BICs appear to be fairly robust under the variation of system parameters. Now we shall see the effect of combining the two kinds of anisotropy-symmetry breaking.

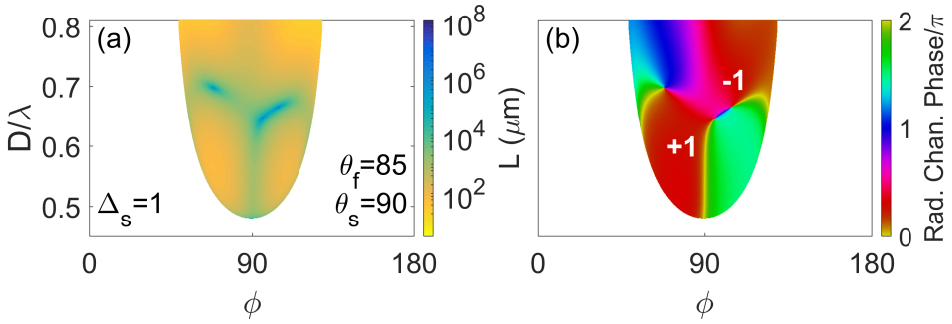

Fig. 3.12: Both azimuthal and polar anisotropy-symmetry breaking: (a) Leaky mode sheet for a configuration with breaking of both polar ($\theta_f = 85°$) and azimuthal ($\Delta_s = 1°$) anisotropy-symmetry. (b) Phase map of the radiation channel amplitude for the leaky mode sheet in (a) showing phase singularities at the three BIC points.

Fig. 3.12(a) shows the first order leaky mode in a situation where both polar and azimuthal anisotropy-symmetry are broken. The film optic axis is taken out of the interface plane ($\theta_f = 85°$) while the substrate optic axis remains in the interface plane ($\theta_s = 90°$). Additionally, the substrate optic axis is offset from the projection of the film optic axis in the interface plane by $\Delta_s = 1°$. Once again, as a consequence of polar anisotropy-symmetry breaking, the BIC lines of existence collapse to BIC points. However, comparing this to Fig. 3.8, which had the same polar orientations of the optic axes but maintained azimuthal anisotropy-symmetry, we note that the distribution of BIC points is no longer symmetric about $\phi = 90°$. The BICs placed at $\phi = 90°$ and $\phi > 90°$ have come closer to each other while the BIC at $\phi < 90°$ has moved away from the other two BICs. They are still connected by regions of low loss on the mode but the losses are even lower between the two BIC points that are closer to each other on the leaky mode sheet. The reduction of losses when BICs are brought closer in parameter space has been reported in [62]. Another point to be noted is that the BICs that have come closer to each other have opposite winding numbers.

We explore this further by varying the degree of azimuthal anisotropy-symmetry breaking. Fig. 3.13(a) shows the mode when the offset of the substrate optic axis with the projection of the film optic axis in the film is $\Delta_s = 2°$. We maintain the same polar anisotropy-symmetry breaking as in Fig. 3.12, i.e, $\theta_f = 85°$ and $\theta_s = 90°$. In this scenario,

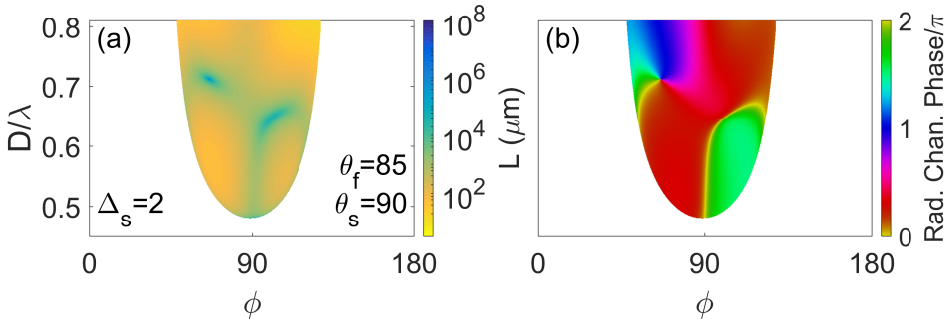

Fig. 3.13: Same as Fig. 3.12 but with $\Delta_s = 2°$.

we find that the increase in the value of Δ_s results in the two BIC points that were close to each other in the $\phi > 90°$ area for $\Delta_s = 1°$ merging. They merge and cancel each other out since they had opposite winding numbers. There is a residual area of low loss on the leaky mode sheet as a remnant of the BICs that existed but there is no BIC point in that area. The other BIC point in the $\phi < 90°$ area continues existing. Therefore we find that, under tuning of suitable parameters, BIC points with opposite winding numbers can merge and cancel each other out.

We have studied the leaky modes and BICs supported by the system under various optic axes configurations and found that the BIC lines can be distorted or collapsed to BIC points under different regimes of anisotropy-symmetry breaking. We have so far considered only snapshots at different optic axes configurations and would like to focus on the evolution of the BICs under continuous variation of parameters. However, before that we shall study the BICs in a different kind of waveguide.

3.2.3 Negative Uniaxial Core, Positive Uniaxial Substrate

Now we shall consider an anisotropic planar waveguide with a negative uniaxial core ($n_{of} = 1.75, n_{ef} = 1.5$) and a positive uniaxial substrate ($n_{os} = 1.25, n_{es} = 2$). As cover, we simply use air ($n_c = 1$). Therefore, the extraordinary wave in the substrate provides the radiation channel to leaky modes in this waveguide, since it is the highest index in the structure. However, even though $n_{es} = 2$, the actual extraordinary refractive index, is a function of the orientation of the optic axis and,

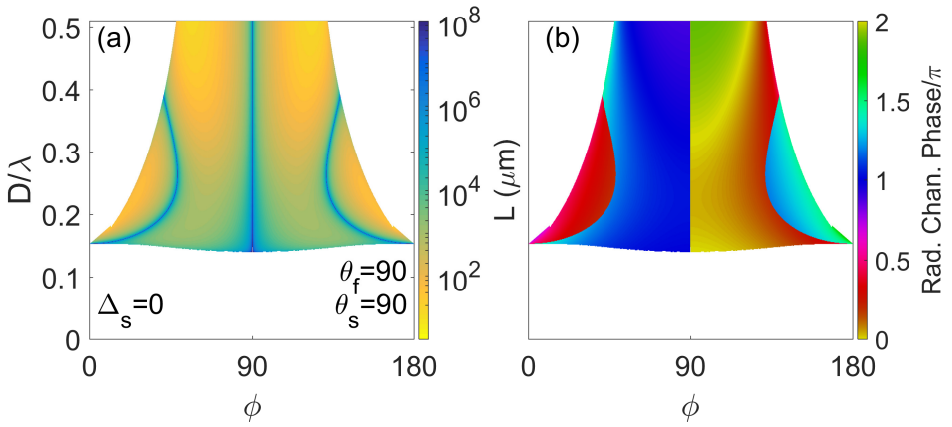

Fig. 3.14: (a) Fundamental leaky mode in a structure maintaining full anisotropy-symmetry ($\Delta_s = 0°, \theta_f = \theta_s = 90°$) with isotropic air as cover ($n_c = 1$), negative uniaxial core/film ($n_{of} = 1.75, n_{ef} = 1.5$), and positive uniaxial substrate ($n_{os} = 1.25, n_{es} = 2$). (b) Phase of the radiation channel (extraordinary) amplitude measured with respect to the confinement channel (ordinary) for the mode in (a).

therefore, of both θ and ϕ. This can be written generally for any uniaxial material as

$$n_e(\theta,\phi) = \sqrt{\frac{\epsilon_e(\epsilon_e \cos^2\theta + \epsilon_o \sin^2\theta)}{\epsilon_e + \epsilon_o - \epsilon_e \sin^2\theta \sin^2\phi - \epsilon_o[\cos^2\phi + \cos^2\theta \sin^2\phi]}}. \tag{3.32}$$

The effective extraordinary index varies and therefore, the extraordinary wave in the substrate provides a radiation channel to the mode in the waveguide only for a certain range of angles. Outside of that range of angles, the waveguide can therefore support guided modes. BICs in this structure were first studied in Ref. [117]. In our study we shall focus exclusively on the leaky mode which radiates via the extraordinary wave in the substrate and ignore the guided parts of the dispersion and study the impact of variation of the optic axis orientation on the existence of BICs embedded on the leaky mode sheets supported by this structure.

Fig. 3.14(a) shows the fundamental leaky mode for the structure described above when full anisotropy-symmetry is maintained, i.e, both optic axes lie in the interface place ($\theta_s = \theta_f = 90°$) and are aligned ($\Delta_s = 0°$). The white area below the coloured leaky mode sheet corresponds to where the single channel leaky mode cuts off. In other

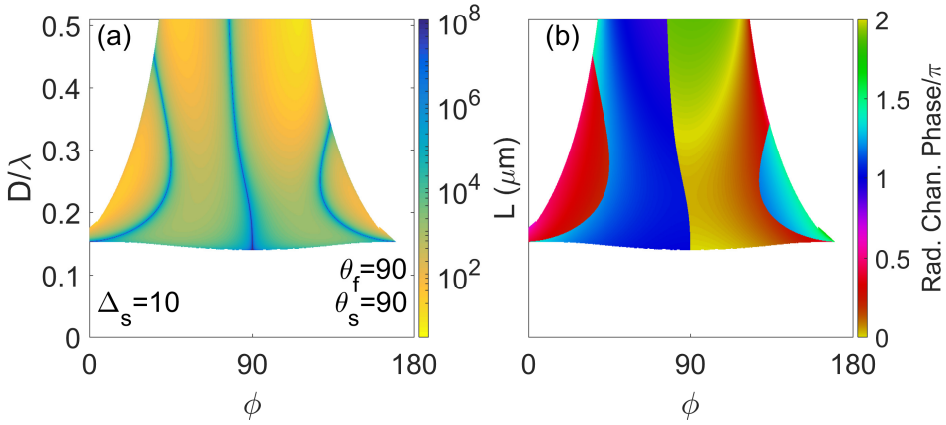

Fig. 3.15: Same as Fig. 3.14 but with azimuthal anisotropy-symmetry broken since the substrate optic axis is offset from the film optic axis by $\Delta_s = 10°$.

words, a second radiation channel becomes available to the mode since the mode propagation constant $N < max(n_c, n_{os})$. The white area to the sides of the coloured leaky mode sheet, however, contains the fundamental guided mode that is supported by the structure at those values of ϕ (see Fig. 1(b) in Ref. [117]). We do not show this guided mode as we want to focus exclusively on the BICs supported by the guided mode. Therefore the leaky mode transitions to the guided mode here at the point where the mode propagation constant $N > n_{es}(\phi_s, \theta_s)$ and there are no available radiation channels.

As in the previous waveguide (see section 3.2.2), the structure supports PS BICs at $\phi = 90°$. However, since it is the extraordinary wave in the substrate that serves as the radiation channel, at $\phi = 90°$, it corresponds to the TE wave. Therefore the TM mode supported by the waveguide at $\phi = 90°$ is orthogonal to the radiation channel and corresponds to the line of PS BICs. The curved blue lines that are symmetrically distributed about $\phi = 90°$ are INT BICs. Therefore, unlike the previous waveguide, this structure supports INT BICs on the fundamental leaky mode. Fig. 3.14(b) shows the phase map of the radiation channel amplitude for the corresponding mode. We see that once again, lines of existence of BICs on the leaky mode sheet correspond to discontinuities of $\pm\pi$ on the phase map.

We study the effect of anisotropy-symmetry breaking in this structure. Fig. 3.15(a) shows the impact of breaking azimuthal anisotropy-

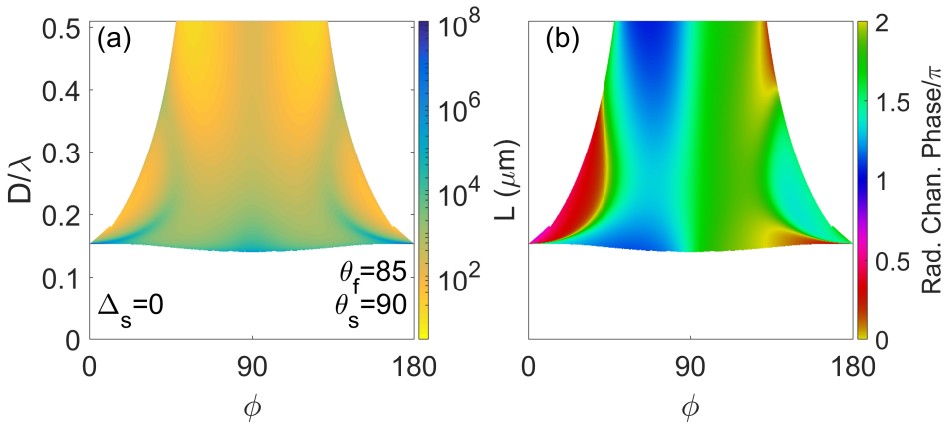

Fig. 3.16: Same as Fig. 3.14 but with polar anisotropy-symmetry broken since the film optic axis is moved out of the interface plane and makes an angle $\theta_f = 85°$ with the normal to the interface.

symmetry. The substrate optic axis is offset from the film optic axis by $\Delta_s = 10°$. This leads to a change in the leaky-mode cut-off that is obvious compared to the case with full anisotropy-symmetry (see Fig. 3.14(a)). Like in the previous waveguide with azimuthal anisotropy-symmetry breaking, the BIC lines of existence continue to exist though they are distorted. The line of PS BICs is converted to INT BICs since there is no longer any point in the parameter space where the structure supports TE/TM modes. Also, the distribution is no longer symmetric about $\phi = 90°$ (or any value of ϕ). The phase map in Fig. 3.15(b) shows that once again, BIC lines of existence correspond to discontinuities of $\pm\pi$.

Fig. 3.16(a) shows the fundamental leaky mode when polar anisotropy-symmetry is broken by moving the film optic axis out of the interface plane ($\theta_f = 85°$). The substrate optic axis remains in the interface plane ($\theta_s = 90°$) and it is aligned with the projection of the film optic axis in the interface plane ($\Delta_s = 0°$), thereby maintaining azimuthal anisotropy-symmetry. Since azimuthal anisotropy-symmetry is maintained, the leaky mode is symmetric about $\phi = 90°$. The BIC lines disappear in this configuration of the optic axes. There are low loss areas on the mode, particularly close to the mode cut-off but no BIC points. This is confirmed by the phase map shown in Fig. 3.16(b) where we do not see any screw phase dislocations.

As we have seen before, there are other ways to break polar anisotropy-

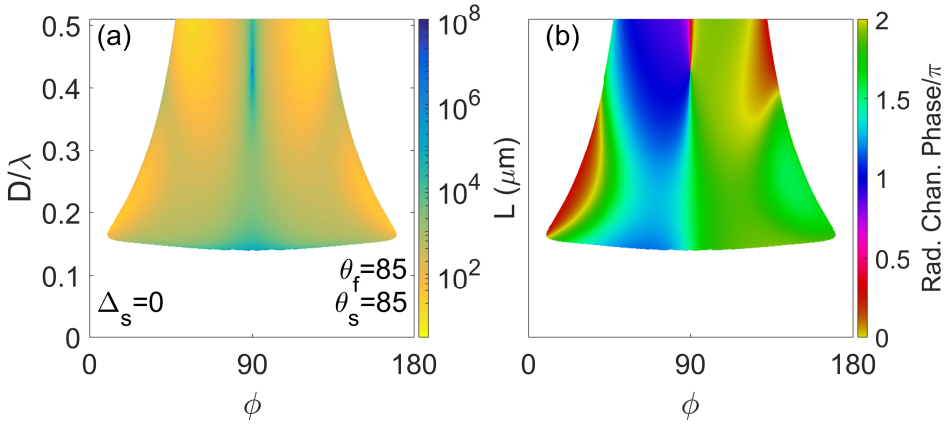

Fig. 3.17: Same as Fig. 3.14 but with polar anisotropy-symmetry broken since both the film and substrate optic axes are moved out of the interface plane ($\theta_f = \theta_s = 85°$).

symmetry and Fig. 3.17(a) shows the fundamental leaky mode when both the film and the substrate optic axes are moved out of the interface plane and are parallel to each other ($\theta_f = \theta_s = 85°$). In this scenario, the central line of PS BICs (see Fig. 3.14) collapses to a single INT BIC point at $\phi = 90°$, while the lines of INT BICs disappear entirely. There remain areas of low loss on the leaky mode sheet in the areas where BICs existed under full anisotropy-symmetry. Since polar anisotropy-symmetry is broken, there is no point in the parameter space where the structure supports TE/TM modes and so there is no possibility of PS BICs being supported. Fig. 3.17(b) shows the phase map where the INT BIC corresponds to a screw phase dislocation with the phase increasing in the counter clockwise direction, meaning a winding number of -1.

Fig. 3.18 shows a structure where both the film and substrate optic axis are moved out of the plane. However, they are no longer parallel to each other. While the film optic axis makes an acute angle with the normal to the interface ($\theta_f = 85°$), the substrate optic axis makes an obtuse angle ($\theta_s = 95°$). The projection of the optic axes in the interface plane remains aligned and so azimuthal anisotropy-symmetry is maintained. In this scenario, we find that the two lines of INT BICs collapse to two individual BIC points that are symmetrically distributed about $\phi = 90°$ while the line of PS BICs simply disappears. Fig. 3.18(b) shows the phase map featuring screw phase dislocations,

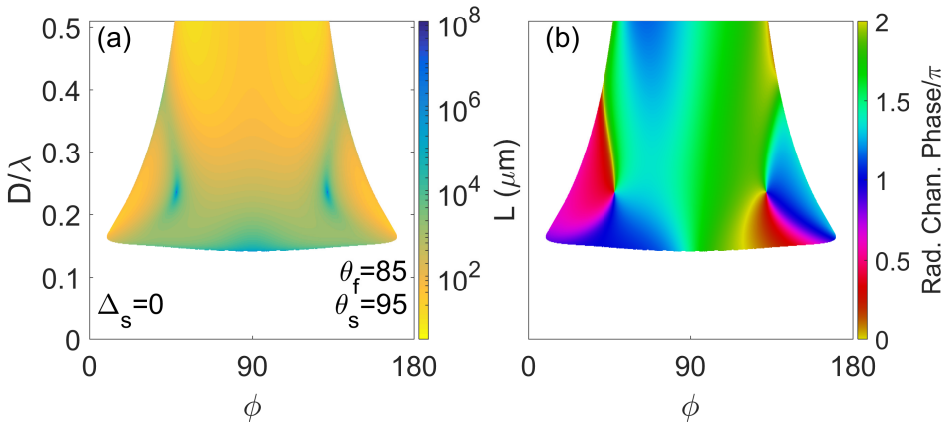

Fig. 3.18: Same as Fig. 3.14 but with polar anisotropy-symmetry broken since both the film and substrate optic axes are moved out of the interface plane. However, they are not parallel. The film and substrate optic axes make acute and obtuse polar angles with the normal to the interface, respectively ($\theta_f = 85°, \theta_s = 95°$).

both of which are increasing anti-clockwise and therefore have winding numbers -1.

So far we have studied three cases in this waveguide where the film optic axis made an acute angle with the normal to the interface. Now we shall study cases where the film optic axis makes an obtuse angle with the x-axis. Fig. 3.19(a) shows the case where both the film and substrate optic axes are moved out of the interface plane and are oriented at the same obtuse angle with respect to the x-axis ($\theta_f = \theta_s = 95°$). The result is similar to the scenario when we had $\theta_f = \theta_s = 85°$ (see Fig. 3.17) as the PS BIC line collapses to a single BIC point whereas the lines of INT BICs disappear. However, unlike in Fig. 3.17(b), the phase map in Fig. 3.19(b) shows that the screw phase dislocation now increases clockwise and therefore the winding number associated with the BIC is $+1$.

Fig. 3.20(a) shows the mode when polar anisotropy-symmetry is broken with the film and the substrate optic axes in opposite quadrants with respect to the polar angle. The film optic axis makes an obtuse angle ($\theta_f = 95°$) and the substrate optic axis makes an acute angle ($\theta_s = 85°$) with the normal to the interface. In this scenario, the two INT BIC lines collapse to two BIC points while the PS BIC line disappears entirely. The phase map in Fig. 3.20 shows that both the

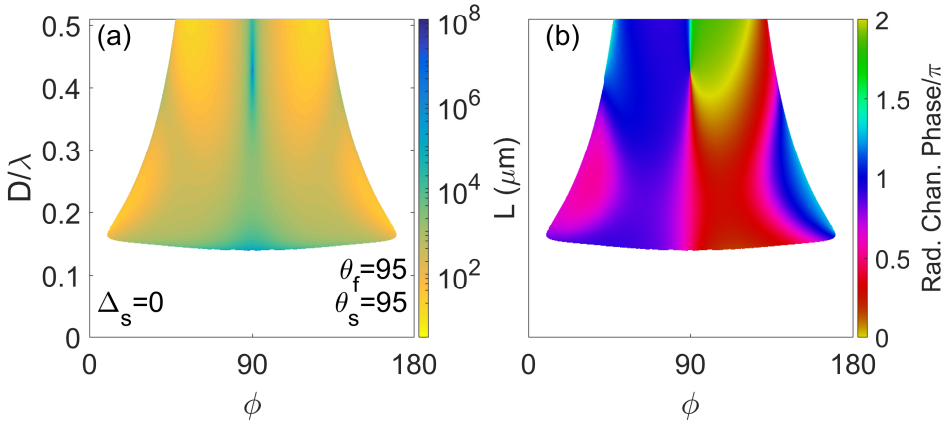

Fig. 3.19: Same as Fig. 3.17 with both optic axes parallel and moved out of the interface plane but making an obtuse angle with the normal to the interface ($\theta_f = \theta_s = 95°$).

BICs correspond to screw phase dislocations, as expected. Moreover, both screw phase dislocations feature clockwise increase, meaning both BIC points can be assigned a winding number of +1.

We find that for the waveguide with a negative uniaxial film and a positive uniaxial substrate, BIC points exist when polar anisotropy-symmetry is broken only if both film and substrate optic axes are

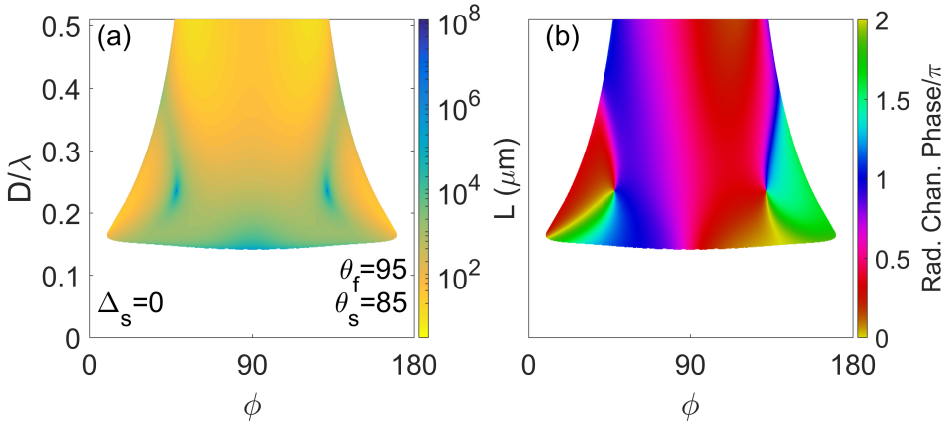

Fig. 3.20: Same as Fig. 3.18 with both optic axes moved out of the interface plane and not parallel to each other. Here the film optic axis makes an obtuse angle with the normal to the interface and the substrate optic axis makes an acute angle ($\theta_f = 95°, \theta_s = 85°$).

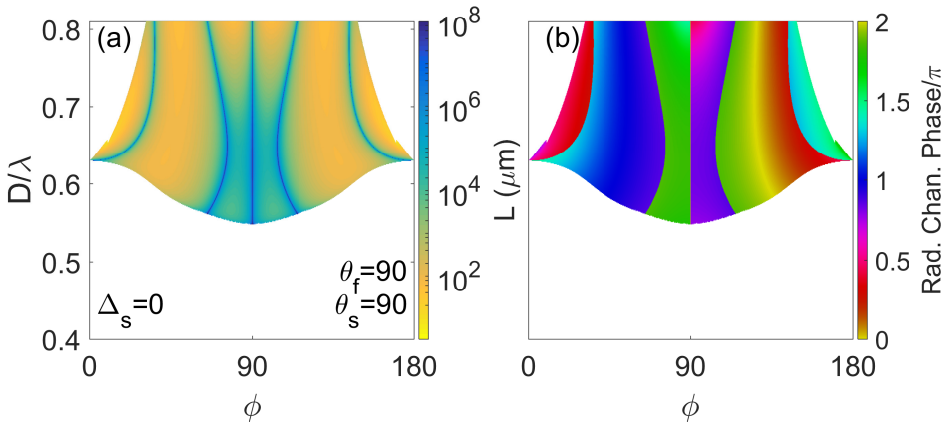

Fig. 3.21: Same as Fig. 3.14 with both optic axes aligned and placed in the interface plane but showing the first order leaky mode instead of the fundamental leaky mode.

moved out of the interface plane. Moreover, we find that when polar anisotropy-symmetry is broken with both optic axes in the same quadrant in terms of the polar angle they make with the normal to the interface, only the PS BIC line collapses to a BIC point while the two INT BIC lines disappear. On the other hand, when the two optic axes are in opposite quadrants, the two INT BIC lines collapse to BIC points while the PS BIC line disappears. Unlike the waveguide discussed in the previous section, the sign of the winding number that can be assigned to the BIC points upon polar anisotropy-symmetry breaking does not depend on which BIC line the BIC point arises from. Rather the sign of the winding number appears to depend on the polar angle made by the film optic axis. When the polar angle the film optic axis makes with the normal to the interface is acute ($\theta_f < 90°$), the BIC points on the leaky mode sheet carry a winding number of -1 regardless of the polar orientation of the substrate optic axis or the line of BICs from which the BIC point originates. Similarly, the BIC points are characterised by a positive winding number on the phase map when the polar angle the film optic axis makes with the normal to the interface is obtuse ($\theta_f > 90°$). The fact that in the cases where there are two BIC points on the leaky mode sheet, they have the same winding number, precludes the possibility of the BIC points merging and cancelling each other out.

We have so far focused exclusively on the fundamental leaky mode

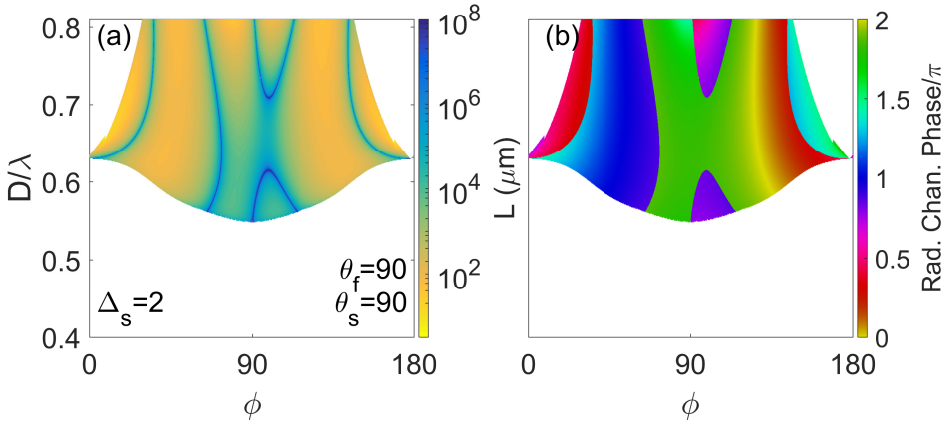

Fig. 3.22: Same as Fig. 3.21 but with azimuthal anisotropy-symmetry breaking with the substrate optic axis offset from the film optic axis by $\Delta_s = 2°$.

supported by this waveguide. We shall now consider the first order leaky mode supported by this waveguide and the BICs embedded on it. Fig. 3.21(a) shows the first order leaky mode supported by this waveguide when full anisotropy-symmetry is maintained. This leaky mode is even richer in BICs compared to the fundamental leaky mode. In addition to the PS BICs at $\phi = 90°$, this mode supports four lines of INT BIC existence. Two of the INT BIC lines are in the area where $\phi < 90°$ and the two others are in the area where $\phi > 90°$. The distribution of the BIC lines is symmetric about $\phi = 90°$ since azimuthal anisotropy-symmetry is maintained ($\Delta_s = 0°$). Obviously, the first order mode has a higher cutoff in D/λ as opposed the fundamental (around $D/\lambda = 0.55$ as opposed to around $D/\lambda = 0.15$). Generally we have found that higher order modes which typically occur at higher values of D/λ are richer in terms of INT BICs and this is borne out in both waveguides we have studied so far (there are more INT BICs in the first order mode than in the fundamental). The phase map in Fig. 3.21(b) shows that each BIC line of existence corresponds to a phase discontinuity of $\pm\pi$.

Fig. 3.22(a) shows the first order mode supported by the structure under azimuthal anisotropy-symmetry breaking with the substrate optic axis offset from the film optic axis by $\Delta_s = 2°$. Firstly, we note that the distribution of BICs on the leaky mode is no longer symmetric about $\phi = 90°$ now that azimuthal anisotropy-symmetry is broken.

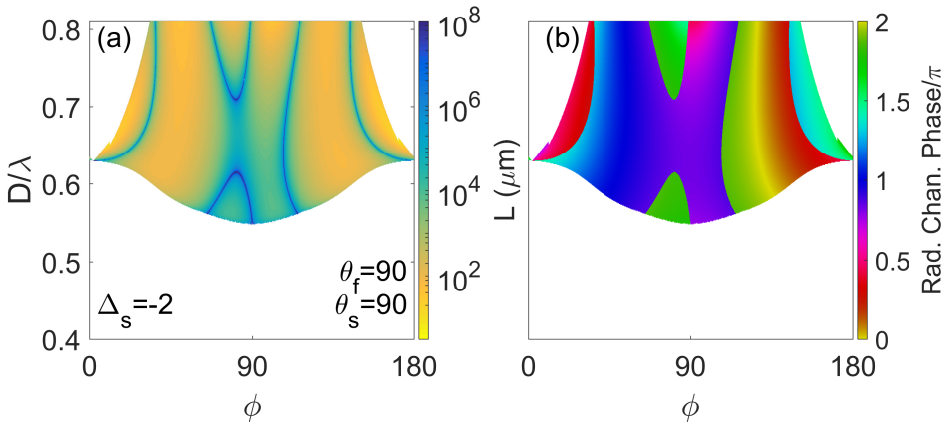

Fig. 3.23: Same as Fig. 3.21 but with azimuthal anisotropy-symmetry breaking with the substrate optic axis offset from the film optic axis by $\Delta_s = -2°$.

Further, in this scenario the line of PS BICs and a line of INT BICs, in the area with $\phi > 90°$ that was closer to the the PS BICs, merge. Initially, with full anisotropy-symmetry, the two BIC lines of existence are separated in ϕ (see Fig. 3.21). As Δ_s is increased from 0° to 2°, the lines approach in ϕ till they merge at a specific point and then starting from that point, they separate in D/λ as shown in Fig. 3.22(a). As Δ_s is increased further, the lower line of INT BICs moves below the cutoff while the upper line of INT BICs moves to progressively higher values of D/λ. The three remaining lines of BICs are distorted as Δ_s increases but they do not intersect. The phase map shown in Fig. 3.22 (b) shows that the BIC lines of existence are again characterised by phase discontinuities of $\pm\pi$. More relevant, however, is the fact that the merger of the two BIC lines in ϕ and their subsequent separation in D/λ leads to the joining of two spaces where the phase evolves continuously as represented by the area in green on the phase map. Inspecting the phase map in the fully anisotropy-symmetric case (Fig. 3.21(b)), we find that there is another possible merger and separation of BIC lines that could create a similar area of continuous evolution of phase on the phase map and that would be if the line of PS BICs and the line of INT BICs that is nearest to it in the $\phi < 90°$ zone were to merge. We see in Fig. 3.23 that this is precisely what happens when the azimuthal anisotropy-symmetry is broken with opposite sign of $\Delta_s(= -2°)$. The merger of the BIC lines in ϕ and their subsequent

separation in D/λ creates an area of continuous evolution of the phase represented by the purple/blue area in Fig. 3.23(b).

We have so far studied the leaky modes and BICs supported by two different waveguides with various configurations of their optic axes. However, these are snapshots which can only hint at how the BICs evolve under continuous variation of optic axes orientation. In the next section we shall focus on the evolution of the existence loci of BICs under continuous variation of the optic axes configurations.

3.2.4 Existence Loci of BICs under Continuous Variation of Optic Axes Orientation

In this section we will study the existence loci of BICs supported by these waveguides under variation of the orientation of the optic axes. We shall do this by plotting the orientation of the film optic axis (θ_f and ϕ) on a hemisphere while orientation of the substrate optic axis is fixed, i.e., both the in-plane offset Δ_s and the polar orientation θ_s remain fixed. This would therefore correspond to the situation where each spherical representation corresponds to a structure with a fixed optic axis orientation for the substrate, typically a crystal, and a film made of, e.g., a liquid crystal, where the film optic axis polar angle θ_f can be controlled by a DC electric field and ϕ_f could be varied by the physical rotation of the sample for a fixed propagation direction.

We plot six of these hemispheres in Fig. 3.24. We focus only on the hemisphere in the range $\phi_f \in [0°, 180°]$ since the vertical axis of the sphere, $\theta_f = 0°$ is a symmetry axis. We also note the winding numbers that can be assigned to the BICs whenever we have BIC points. Each cut along a parallel of these hemispheres would correspond to a fixed value of θ_f while ϕ was being varied. Therefore, each cut corresponds to one of the dispersion plots that we have shown so far. However, in Fig. 3.24 we focus exclusively on the BIC loci and not the losses of the rest of the leaky mode surface to glean further insight into the existence of the BICs.

The first four hemispheres, Fig. 3.24(a-d), show the existence loci of BICs supported by the first order mode for the waveguide with positive uniaxial core/film and negative uniaxial substrate discussed in section 3.2.2. Fig. 3.24(a) depicts the BIC existence loci, which appear as lines, and winding number (labelled as ± 1) for a structure with the substrate optic axis in the interface plane ($\theta_s = 90°$) and

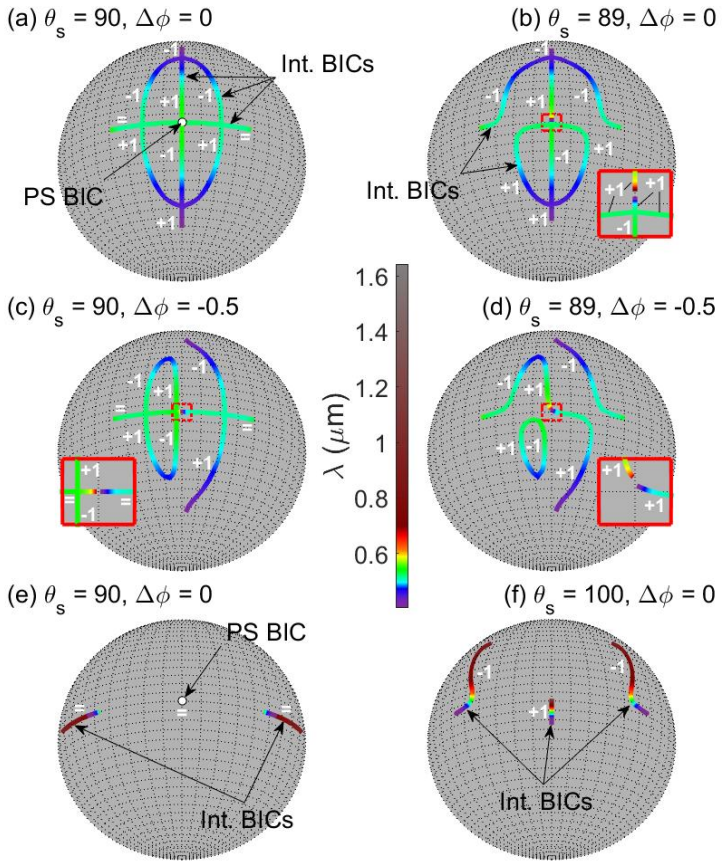

Fig. 3.24: Spherical representation of the BIC existence loci as a function of the optical axis orientation in the guiding film. The film optic axis orientation is given by the azimuthal angle ϕ_f and the polar angle θ_f in spherical coordinates, while the parameters for the substrate (θ_s, and $\Delta\phi$) are kept constant in each plot. Film thickness is $d = 0.35\mu m$. Hence, the colours of the BIC existence lines indicate the value of the wavelength. Winding numbers are labeled as '+1' or '-1' and lines of phase discontinuity are labeled with '='. Spherical representation of the BIC loci with different orientations of the substrate optic axis for the waveguide in section 3.2.2 with positive uniaxial core and negative uniaxial substrate in (a-d) and for the structure in section 3.2.3 with negative uniaxial core and positive uniaxial substrate) in (e-f).

where azimuthal anisotropy-symmetry is maintained ($\Delta_s = 0°$). Since $\Delta_s = 0°$ and $\theta_s = 90$, the cut along the parallel at $\theta_f = 90°$ corresponds

to the case with full anisotropy-symmetry. The leaky mode sheet in this case was shown in Fig. 3.5(a), and shows that INT BICs exist for a broad range of values of ϕ_f and and a narrow range of wavelengths which corresponds to the light green line along the equator of the sphere in Fig. 3.24(a). The polarization separable BIC shown in Fig. 3.24(a) appears here as a white dot at the symmetry point $\theta_f = \phi_f = 90°$, where the white colour indicates that the polarization separable BICs exist for all values of the wavelength above the mode cut-off. The BIC lines of existence are characterised by discontinuities on the phase map and this is indicated on the sphere by the white '=' sign. Any point that is not on the equator corresponds to a case where polar anisotropy-symmetry is broken. A cut along the parallel at $\theta_f = 85°$ in Fig. 3.24(a) corresponds to the leaky mode sheet shown in Fig. 3.8. Since there are only three BIC points supported on that leaky mode, we find the BIC existence loci at only three points, with different wavelengths falling in the green-blue region of the spectrum. The BIC points are characterised by screw phase dislocations that allow us to assign them winding numbers and we find that the winding number assigned to the BIC on each loci is conserved as film optic axis orientation is varied. The allowed wavelength for the three INT BICs to exist varies when the film optic axis is taken out of the interface plane. In addition, the loci of the BICs grow closer as the film optic axis moves further away from the interface plane, until the three BICs join near $\theta_f = 46°$ and $\theta_f = 134°$ in the northern and southern hemisphere, respectively. Then, two BICs with opposite winding numbers are cancelled. The cancellation of BICs featuring winding numbers with opposite signs also occurs when the INT BICs reach the equator. The winding numbers reverse their sign in the range $\phi_f = [180°, 360°]$ (i.e., in the reverse of the sphere), thus the total topological charge in the full range of orientations ϕ_f for each value of θ_f is always null. We find using this representation that the existence loci of the BICs are symmetrically distributed in the northern and southern hemispheres and in the eastern and western hemispheres. The winding numbers change sign with respect to the equatorial plane.

Taking the substrate optic axis out of the interface plane while azimuthal anisotropy-symmetry is maintained results in different configurations for the northern and southern hemispheres in the spherical representation. This is shown in Fig. 3.24(b) for $\theta_s = 89°$. The symmetry of the BIC existence lines in the spherical representation between the northern and southern hemispheres is broken, but the symmetry

of the eastern and western hemispheres is preserved. Now, the cut at the equator ($\theta_f = 90°$) no longer corresponds to a structure with full anisotropy-symmetry, but rather it corresponds to a case where polar anisotropy-symmetry is broken. The crossings that appear in Fig. 3.24(a) at the equator ($\theta_f = 90°$, $\phi_s \neq 90°$) corresponding to INT BICs, now transform into anti-crossings and the lines of BIC existence are pulled out from the equator. In addition, the polarization separable BIC existence line at $\phi_s = 90°$ (shown as a white dot in Fig 3.24(a)) transforms into two separate lines of INT BICs, and a gap in wavelength appears in the polar direction as shown in the inset. The lower section of the BIC existence line crosses the equator (inset of Fig. 5b) for a given wavelength, resulting in a dot in the dispersion diagram that is the only BIC that survives at $\theta_f = 90°$ when the substrate optic axis is out-of-plane. This is similar to the case shown in Fig. 3.9 where there is only one BIC at $\theta_f = 90°$. When $\theta_f \neq 90°$, three isolated INT BICs may exist, one of them always at $\phi_f = 90°$ and two which are at symmetric orientations with respect to the former. This symmetry arises from the fact that azimuthal anisotropy-symmetry is maintained ($\Delta_s = 0°$) and we have concluded earlier that the placement of BICs on the leaky mode sheet is symmetric about $\phi = 90°$ as long as $\Delta_s = 0°$. Taking the substrate optic axis out-of-plane in the opposite direction, i.e., $\theta_s = 91°$, results in a representation where the BIC existence lines are mirror images with respect to the equatorial plane of those shown in Fig. 3.24(b), but the sign of the winding numbers of the INT BICs is maintained. Again, we find that BICs featuring opposite winding numbers cancel at crossings of BIC existence lines.

Fig. 3.24(c) shows the case where the substrate optic axis is kept in the interface plane ($\theta_s = 90°$) but azimuthal anisotropy-symmetry is broken by introducing an offset between the projection of the film optic axis in the interface plane and the substrate optic axis ($\Delta_s = -0.5°$). We see on the hemisphere that this breaks the plane mirror symmetry at the meridian plane, $\phi_f = 90°$ while the mirror symmetry between northern and southern hemispheres is maintained. This is an expected consequence of the breaking of azimuthal anisotropy-symmetry since we have seen before that it leads to asymmetric distribution of BICs about $\phi = 90°$ on the leaky mode sheet. Under such conditions, the lines of INT BICs existing at the equator for the cut with $\theta_f = 90°$ are preserved (as shown in Figs. 3.6 and 3.7). However, no BIC can exist at the meridian $\phi_f = 90°$ plane. The crossings that appear at

the top and the bottom on the sphere, $\phi_s = 90°$ and $\theta_f \neq 90°$, in Fig. 3.24(a), where 3 BIC loci cross, become anti-crossings in Fig. 3.24(c) where the BIC existence loci at $\phi > 90°$ is separated while the other two loci which have opposite signs of the winding number merge and disappear. The polarization separable BIC existence line breaks into two existence lines of INT BICs (shown in inset), opening a gap of existence in wavelength and azimuthal angle. Note that the transition to anti-crossings is a combined effect of the azimuthal and polar symmetry-breaking, as $\theta_f \neq 90°$ at those points.

When in addition to azimuthal anisotropy-symmetry breaking ($\Delta_s = -0.5°$), the substrate optic axis is taken out of the interface plane ($\theta_s = 89°$), the mirror-symmetries of the BIC loci between the north-south and the east-west hemispheres are broken as shown in Fig. 3.24(d). Therefore, we find that there are no points at all where three BIC loci cross. There remain places however, where BIC loci characterised by opposite winding numbers merge and disappear as the film optic axis orientation is varied. Existence lines of BICs then appear as closed lines or as disconnected lines that cease to exist at the leaky mode cut-off. The topological charge switches sign at structures located at a maximum or minimum in θ_f of a line. If the polar symmetry-breaking increases, the closed BIC existence line may cease to exist as they collapse to a single point and thus the corresponding winding numbers cancel each other. Open BIC existence lines cease also to exist for structures where they would fall beyond the leaky mode cut-off edge, resulting in structures where no BICs exist for any orientation of the film OA.

The last two hemispheres, Fig. 3.24(e-f), show the BIC existence loci for the fundamental mode of the waveguide with negative uniaxial film and positive uniaxial substrate discussed in section 3.2.3 and they show a map of BIC existence loci that is substantially different compared to Fig. 3.24(a-d). The most remarkable property, shown in Fig. 3.24(e), is that BICs exist only at the equator when the substrate optic axis is lying in the interface plane ($\theta_s = 90°$). Therefore, when only one optic axis is taken out of the interface plane, no BICs are supported by the fundamental mode of this system. As a result, breaking the polar anisotropy-symmetry by taking the film optic axis out of the interface plane results in no BICs. This has been shown in Fig. 3.16 where there are no BICs on the leaky mode sheet with $\theta_s = 90°$ and $\theta_f = 85°$. When the substrate optic axis is taken out of

the interface plane ($\theta_s = 100°$), a number of features similar to those described above occur as shown in Fig. 3.24(f). Firstly, all BIC existence lines are pulled out of the equator. Therefore, at each cut along a parallel, the leaky mode sheet only supports BIC points and not BIC lines. This is so because the polar anisotropy-symmetry is always broken with $\theta_s = 100°$. The polarization separable BICs cease to exist and the resulting INT BICs only exist at given orientations of the film optic axis and wavelengths and feature screw phase dislocations in the radiated field near the BIC. Secondly, the winding number of the BIC originating from the polarization separable BIC ($\phi_f = 90°$) exhibits a sign opposite to the winding number corresponding to the BICs originating from INT BICs. The sign of the winding number changes sign in the reverse of the sphere, $\phi_f = [180°, 360°]$, so that the total topological charge in the full range of orientations ϕ_f for each value of θ_f is null. Finally, though not shown in the spherical representation, breaking the azimuthal anisotropy-symmetry ($\Delta_s \neq 0°$) only deforms the BIC existence lines in the west-east direction, avoiding the existence of polarization separable BICs. The leaky mode corresponding to such a cut is shown in Fig. 3.15.

We therefore learn that BICs cease to exist when BIC points with opposite winding numbers merge or the BIC is moved beyond the leaky mode cutoff where a second radiation channel opens up. These are the same conditions for the destruction of BICs that were reported in the case of topologically protected BICs in arrays of dielectric spheres [20]. The hemispheres in Fig. 3.24 help us visualise easily the impact of varying optic axis orientation on the existence loci of BICs and see the impact of breaking various anisotropy-symmetries on the distribution of the BICs in the parameter space. We can now easily relate polar anisotropy-symmetry with the north-south hemispheres and azimuthal anisotropy-symmetry with the east-west hemispheres.

3.2.5 Impact of the Auxiliary Condition

We have seen that polar anisotropy-symmetry breaking leads to the transition from BIC lines of existence to only BIC points being supported on the leaky mode sheets. We have attributed this collapse to the degree of freedom being added by the ability to freely orient an optic axis outside the interface plane. In this section we will explore the interplay of the solutions of the dispersion equation and the auxiliary

condition to gain a better understanding of this phenomenon.

The solution of the dispersion equation given in Eq. 3.26 gives us the mode index. Since we are dealing with leaky modes, the mode index is complex and the imaginary part approximates the loss due to energy radiated away from the mode via the radiation channels. Therefore, one method for detecting BICs is to focus on the imaginary part of the complex mode propagation constant. However, a more reliable method is provided by the auxiliary condition (eq. 3.30). As outlined in section 3.1.3, the auxiliary condition is obtained using the Berreman transfer matrix method after setting the amplitudes of the waves corresponding to the radiation channel to be equal to zero. Since we are dealing with a structure where there is only one radiation channel, this leads to a system of 4 linear equations and 3 unknowns. Therefore, the condition that there exists a non-trivial solution of this system of equations is satisfied only when the determinant of any 3×3 matrix built by selecting the coefficients of any three out of the four equations is zero. There are four ways to select three out of four equations and therefore, we have four determinants. We calculate the values of the mode propagation constant where these determinants are zero and if there is a point where all four of the determinants go to zero which is also a solution of the dispersion equation, then we have a BIC. We explicitly plot the solution of the dispersion equation and the four determinants arising from the auxiliary condition in the subsequent figures to gain a clearer understanding of the distribution of BICs on the leaky mode sheet.

Fig. 3.25(a) shows the first order leaky mode sheet for the waveguide with positive uniaxial film and negative uniaxial substrate that was discussed in section 3.2.2 when full anisotropy-symmetry is maintained ($\theta_f = \theta_s = 90°$ and $\Delta_s = 0°$). This case has been shown in Fig. 3.5 and we know that with this configuration of the optic axes, the structure supports lines of INT BICs. Here, we focus on the area of the leaky mode sheet where these BICs are supported. We fix the value of D/λ and calculate the values of the mode propagation constant where the dispersion equation and auxiliary conditions are satisfied at different values of ϕ. This is shown in Fig. 3.25(b) for $D/\lambda = 0.68$. The real value of the mode propagation constant N that is obtained as a solution of the dispersion equation is given by the dashed black line and that corresponds to a cut of the leaky mode sheet. The four coloured lines correspond to the values of N where the four determinants arising

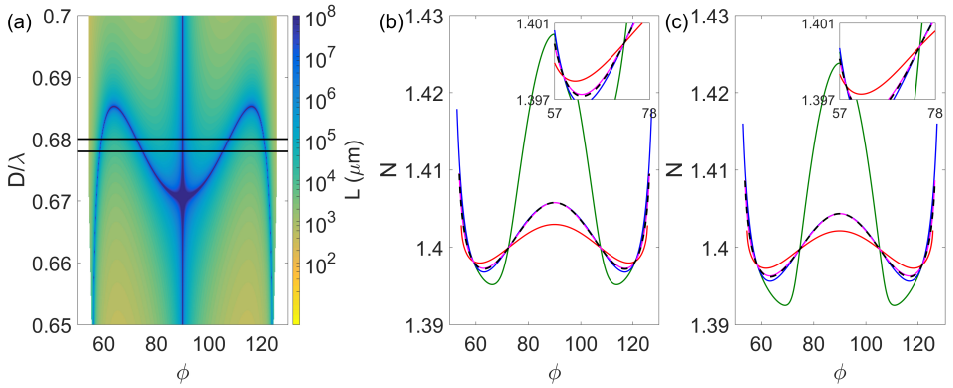

Fig. 3.25: (a) The first order leaky mode for the waveguide discussed in section 3.2.2 when full anisotropy-symmetry is maintained. The black lines indicate the values of D/λ for which the solutions of the dispersion equation and auxiliary condition are calculated. (b) Real part of the value of the mode index N where the dispersion equation and auxiliary condition are fulfilled as a function of ϕ for a fixed value of $D/\lambda = 0.68$. The dashed black line gives the dispersion equation while the four solid coloured lines correspond to the zeroes of the four determinants of the auxiliary condition. The points where all lines intersect correspond to BICs. The inset magnifies the area where the lines intersect to confirm that indeed all 5 solutions intersect at a particular value of ϕ. (c) Same as (b) but for $D/\lambda = 0.678$.

from the auxiliary condition are zero. The auxiliary condition is only satisfied when all four of the coloured lines intersect and a BIC only exists if the four coloured lines intersect at the same point with the solution of the dispersion equation. We see four points where all five lines intersect and this corresponds to the four points where the solid black line intersects the line of INT BICs as shown in Fig. 3.25(a). The inset in Fig. 3.25(b) serves to confirm that indeed all the five lines intersect at the points where the BIC occurs. Fig. 3.25(c) shows the result of the same calculation but with $D/\lambda = 0.678$. As expected from Fig. 3.25(a) once again there are four BIC points but at different values of ϕ compared to Fig. 3.25(b). Therefore, we conclude that when D/λ is varied with all the optic axes lying in the interface plane, the solutions of the dispersion equation and the auxiliary condition coincide at different, but adjacent, values of ϕ and therefore, continuous lines of INT BIC existence can be supported on the leaky mode sheet. It is also interesting to note that though PS BICs are present

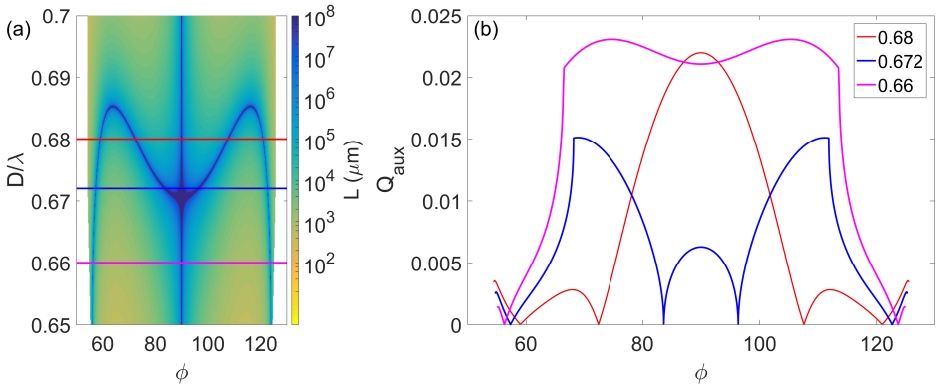

Fig. 3.26: (a) Same as Fig. 3.25(a) with full anisotropy-symmetry maintained. (b) Line plots showing Q_{aux} as a function of ϕ for $D/\lambda = 0.68$ (red), $D/\lambda = 0.672$ (blue) and $D/\lambda = 0.66$ (magenta). The coloured lines in (a) serve as visual guides for the values of D/λ for which Q_{aux} is calculated.

at $\phi = 90°$, the auxiliary condition is not satisfied there and indeed the coloured lines do not intersect with the dashed black line of the dispersion equation at $\phi = 90°$. This further serves to confirm that the mechanism underlying PS BICs is distinct from that which gives rise to INT BICs.

Fig. 3.25(b) and (c) explicitly show five lines corresponding to the real parts of the solutions of the dispersion equation and the four determinants arising from the auxiliary condition. However, we are only interested in the BIC existence condition, i.e., whether the five lines intersect at a single point, meaning that the solution of the dispersion equation and the auxiliary condition coincide. This can be represented better by defining a metric Q_{aux} such that

$$Q_{aux} = \sqrt{\sum_{i=1}^{4} |N_{disp} - N_{aux}^{i}|^2}, \tag{3.33}$$

where N_{disp} refers to the solution of the dispersion equation and N_{aux}^{1-4} refers to the zeroes of the four determinants arising from the auxiliary condition. The metric Q_{aux} measures the total distance between the five solutions. Therefore wherever $Q_{aux} = 0$, the five solutions intersect and we have an INT BIC. An added advantage of this metric is that while Fig. 3.25(b) and (c) only showed the real parts of the solutions

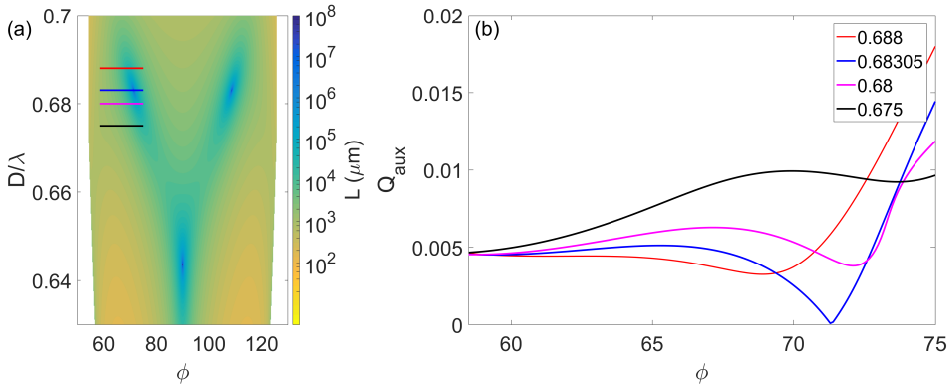

Fig. 3.27: (a) Same as Fig. 3.26(a) but with polar anisotropy-symmetry broken as the substrate optic axis is moved out of the interface plane with $\theta_s = 89°$. (b) Line plots showing Q_{aux} as a function of ϕ for $D/\lambda = 0.688$ (red), $D/\lambda = 0.68305$ (blue), $D/\lambda = 0.68$ (magenta) and $D/\lambda = 0.675$ (black).

of the dispersion equation and the auxiliary condition, the metric Q_{aux} also includes the imaginary part of the solution and only goes to zero when both the real and imaginary part of all 5 solutions coincide.

Fig. 3.26 shows the same mode that we have plotted in Fig. 3.25 for the structure with full anisotropy-symmetry, but now instead of plotting the five solutions separately, we plot the metric Q_{aux} for different values of D/λ in Fig. 3.26(b). The coloured lines in Fig. 3.26(a) correspond to the values of D/λ for which we calculate Q_{aux}. We note that just as all five lines in Fig. 3.25(b) and (c) intersect wherever there is an INT BIC, the plots of Q_{aux} go to zero in Fig. 3.26(b) wherever there is an INT BIC. If we compare the plots for $D/\lambda = 0.68$ (red) and $D/\lambda = 0.672$ (blue) we see that both feature four zeroes of Q_{aux} corresponding to the four INT BICs and the zeroes shift in ϕ in keeping with the position of the BICs at that D/λ as shown in Fig. 3.26(a). Shifting to an even lower value of $D/\lambda = 0.66$, we find that instead of four, there are only two INT BICs and therefore we see $Q_{aux} = 0$ at only two values of ϕ. The BICs closer to $\phi = 90°$ have now merged and we see much higher values of Q_{aux} around $\phi = 90°$.

We now focus on the situation when polar anisotropy-symmetry is broken and the BIC lines collapse to isolated BIC points. We study two different cases here. One where the polar anisotropy-symmetry is broken by moving the film optic axis out of the interface plane ($\theta_f \neq$

90°) and another where the polar anisotropy-symmetry is broken by taking the substrate optic axis out of the interface plane ($\theta_s \neq 90°$). Fig. 3.27(a) shows the leaky mode sheet in the case when the film optic axis has been moved out of the interface plane ($\theta_f = 85°$) while the substrate optic axis remains in the interface plane ($\theta_s = 90°$). Azimuthal anisotropy-symmetry is maintained ($\Delta_s = 0°$). This case has been shown earlier in Fig. 3.8 and we know that the leaky mode sheet supports three isolated INT BIC points: one at $\phi = 90°$ two other INT BIC points at a different value of D/λ that are symmetrically distributed about $\phi = 90°$. The coloured lines indicate the values of D/λ and the range of ϕ where we calculate the solutions of the dispersion equation and the auxiliary condition. We focus on the area where in the case with full anisotropy-symmetry (Fig. 3.25) we had seen two BICs. Fig. 3.27(b) shows the plots of the value of Q_{aux} as a function of ϕ for different values of D/λ. We note that Q_{aux} is zero only for a specific value of ϕ for $D/\lambda = 0.68305$. That point corresponds to a BIC. However, shifting the value of D/λ to higher or lower values (red, magenta and black lines) leads to the loss of the BIC solution entirely since $Q_{aux} \neq 0$ for any value of ϕ for these other values of D/λ. This can be seen in Fig. 3.27(a) from the losses which show that of the four coloured lines, only the one at $D/\lambda = 0.68305$ touches a single BIC point. We conclude that with polar anisotropy-symmetry breaking, shifting in D/λ from a BIC results in a shift to a situation where there are no BICs since the solutions of the dispersion equation and the auxiliary condition do not intersect any more. This is distinct from the case with full anisotropy-symmetry, shown in Fig. 3.26, where shifting in D/λ resulted in the points of intersection of the solution simply shifting continuously in ϕ. This is the reason why in the case with full anisotropy-symmetry, lines of BICs are supported on the leaky mode sheet in the $\phi - D/\lambda$ space, whereas with polar anisotropy-symmetry broken, there are only isolated BIC points on the leaky mode sheet. In other words, we see that when polar anisotropy-symmetry is maintained, Q_{aux} touches zero at different values of ϕ for different values of D/λ unless the BICs merge or fall off the leaky mode sheet at the cutoff. But breaking polar anisotropy results in all the curves of Q_{aux} departing immediately from zero except at a specific value of D/λ.

Fig. 3.28(a) shows the leaky mode sheet when the substrate optic axis is moved out of the interface plane ($\theta_s = 89°$) while the film

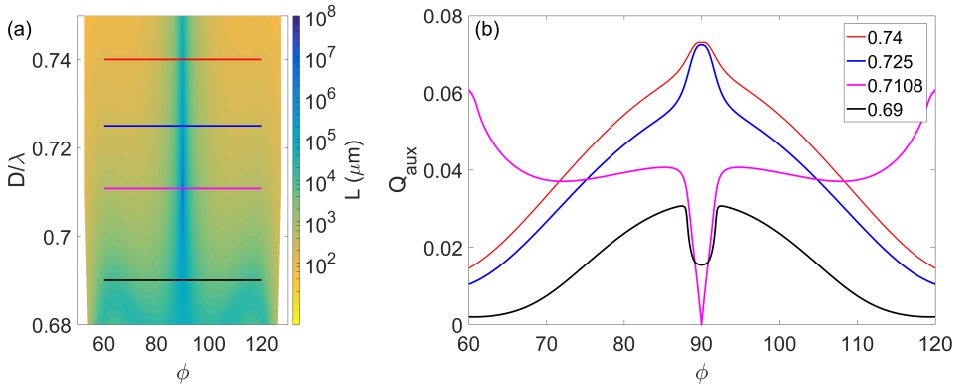

Fig. 3.28: (a) Same as Fig. 3.26(a) but with polar anisotropy-symmetry broken as the substrate optic axis is moved out of the interface plane with $\theta_s = 89°$. (b) Line plots showing Q_{aux} as a function of ϕ for $D/\lambda = 0.74$ (red), $D/\lambda = 0.725$ (blue), $D/\lambda = 0.7108$ (magenta) and $D/\lambda = 0.69$ (black).

optic axis remains in the interface plane ($\theta_f = 90°$). In this situation, there is a single INT BIC point supported on the leaky mode sheet at $D/\lambda = 0.7108$. Fig. 3.28(b) shows Q_{aux}, calculated from solutions of the dispersion equation and the auxiliary condition, as a function of ϕ for different values of D/λ. We see that $Q_{aux} = 0$ at $\phi = 90°$ for $D/\lambda = 0.7108$, and this corresponds to a BIC as shown in Fig. 3.28(a). However, moving to other values of D/λ once again leads to a loss of the BIC solution since $Q_{aux} \neq 0$ for all values of ϕ.

This serves to confirm that polar anisotropy-symmetry breaking affects the interplay of the solutions of the auxiliary condition and the dispersion equation in such a way that moving away from a BIC point in D/λ results in the BIC solution, characterised by the intersection of all five lines ($Q_{aux} = 0$), entirely disappearing. On the other hand, when polar anisotropy-symmetry is maintained, moving in D/λ results in the BIC solution merely being shifted in ϕ (unless BICs merge or fall of the leaky mode cutoff) giving rise to lines of BIC existence on the leaky mode sheet in the $\phi - D/\lambda$ space.

We have so far studied the impact of variation of optic axes orientation on the existence of BICs. We have shown that there exist various regimes of anisotropy-symmetry breaking and they determine whether we have lines of BIC existence or just isolated points. Variation of the optic axes orientation can also shift the BIC solutions on the leaky

mode. However, we have so far only studied waveguides with fixed constitutive parameters. In the following section we shall study the impact of the variation of refractive indices on the existence of BICs.

3.3 Variation of the Refractive Indices of Waveguide Materials

BICs in photonic systems occur only when certain conditions are fulfilled. These conditions are functions of the system parameters. Therefore the position of BICs in the parameter space is often dependent on the various system parameters, including the refractive indices. The sensitivity of photonic BICs to refractive indices has been harnessed to design sensors on various photonic platforms such as photonic crystal slabs [89], all-dielectric photonic crystal metasurfaces [90–93], and dielectric gratings [94, 95]. In this section we will study the impact of the variation of the different refractive indices of the anisotropic waveguides on the existence of BICs supported by them. For ease of understanding, we will restrict ourselves to the the simplest scenario where full anisotropy-symmetry is maintained, with both film and substrate optic axes lying in the interface plane ($\theta_f = \theta_s = 90°$) and aligned ($\Delta_s = 0°$). As discussed in the previous section, in this configuration, leaky mode sheets support lines of BIC existence. We shall follow the evolution of these lines as individual refractive indices are varied.

3.3.1 Positive Uniaxial Core, Negative Uniaxial Substrate

First we shall consider the waveguide with a positive uniaxial core and a negative uniaxial substrate that we had studied in section 3.2.2. The default values we use for the refractive indices are as follows: $n_c = 1; n_{of} = 1.5, n_{ef} = 1.75; n_{os} = 2, n_{es} = 1.25$. We shall vary only one of these indices at a time and study the impact of its variation on the existence of BICs. We shall focus only on the first order leaky mode, which supports both PS and INT BICs.

Fig. 3.29 shows the first order leaky mode sheet for three different values of the cover refractive index n_c. Fig. 3.29(a) shows the mode for $n_c = 1$ and therefore is the same as the plot seen previously in

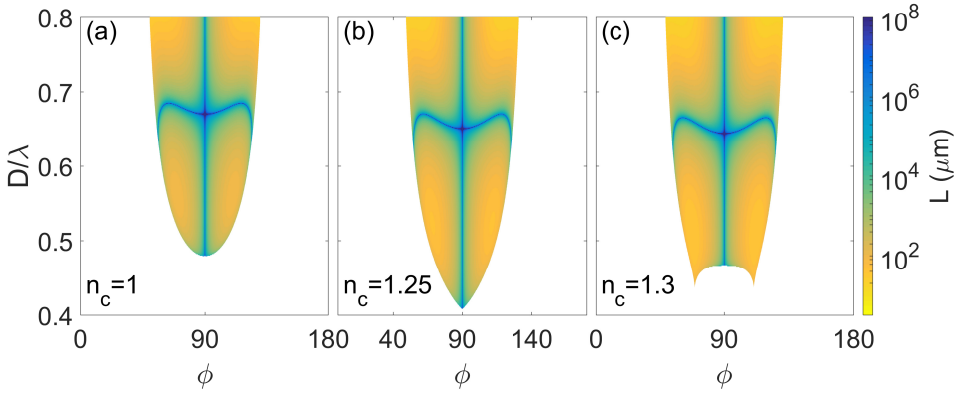

Fig. 3.29: First order leaky mode sheet for a waveguide with positive uniaxial core and negative uniaxial substrate for different values of the cover refractive index (n_c): (a) $n_c = 1$, (b) $n_c = 1.25$, and (c) $n_c = 1.3$. The colour shows the propagation length $L(\mu m)$ that the mode travels before $1/e$ attenuation. Blue lines correspond to BICs.

Fig. 3.5. As we move to higher values of $n_c = 1.25$ and $n_c = 1.3$ in Fig. 3.29(b) and (c), respectively, we see that the mode changes substantially. This is because the cutoff of the mode in this case is determined by whichever is higher among n_c and $n_{es}(\theta_s, \phi_s)$. Whenever, the mode propagation constant N is lesser than whichever is the higher of the two ($N < max(n_c, n_{es}(\theta_s, \phi_s))$), the mode is able to access another radiation channel and therefore becomes different from the leaky mode with a single radiation channel that we are interested in studying. Therefore, varying n_c varies the cutoff of the mode substantially, particularly when $n_c > n_{es}(\theta_s, \phi_s)$. The mode cutoff shifts to lower values of D/λ till $n_c = n_{es} = 1.25$ and then moves to higher values as n_c is increased beyond that. However, the effect of the variation of n_c on the line of INT BICs is much less pronounced. Inspection of the modes shown in the three subplots in Fig. 3.29 reveals that the line of INT BICs shifts to marginally lower values of D/λ as we increase from $n_c = 1$ to $n_c = 1.3$. However, the shape of the line remains almost identical in the three cases shown in Fig. 3.29.

Another interesting point has to do with the existence of PS BICs. As we have seen in the previous section, waveguides with full anisotropy-symmetry support PS BICs at $\phi = 90°$ at all wavelengths as long as one set of refractive indices provides a guiding configuration, i.e., either the ordinary or the extraordinary index of the film material is

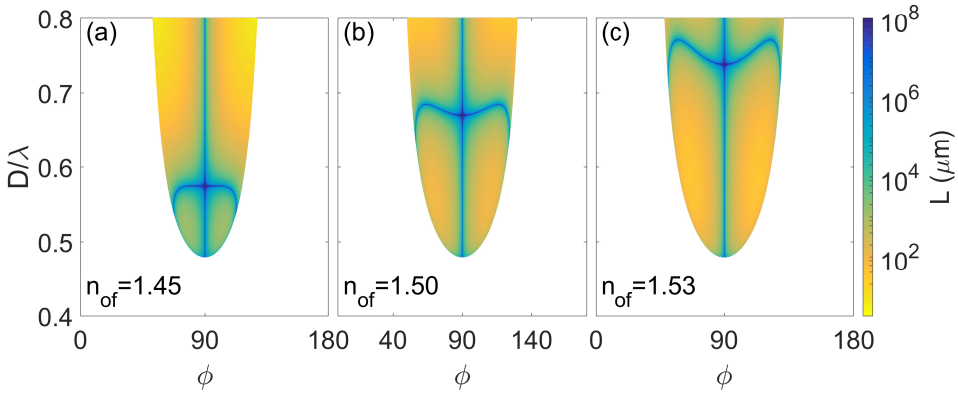

Fig. 3.30: Same as Fig. 3.29 but for variation of the ordinary refractive index of the film with values (a) $n_{of} = 1.45$, (b) $n_{of} = 1.50$, (c) $n_{of} = 1.53$.

higher than the corresponding index of the substrate. PS BICs arise due to orthogonal TE/TM polarisations of the mode and the radiation channel arising from the geometry of the configuration, i.e., the principal axes of the material being along or orthogonal to the propagation axes. Therefore, the PS BICs are not substantially affected by continuous variation of the refractive indices of the waveguide materials. PS BICs are only affected insofar as they exist above the leaky mode cutoff and this cutoff itself varies under variation of the refractive indices of the materials making up the waveguide. Therefore, we see that the PS BIC exists at $\phi = 90°$ for all values above the mode cutoff in all the three cases shown in Fig. 3.29.

Fig. 3.30 shows the impact of the variation of the ordinary refractive index of the film (n_{of}) on the existence of INT BICs. The first thing we note is that variation of n_{of} does not have a substantial impact on the mode cutoff. This can be attributed to the fact that n_{of} has no direct impact on the determination of the cutoff though it has some indirect impact via the mode propagation constant $N(= k_y/k_0)$. However, compared to n_c, n_{of} has a much greater impact on the line of INT BICs supported on the leaky mode. Fig. 3.30(b) shows the familiar case with $n_{of} = 1.5$. Lower values of n_{of}, as shown in Fig. 3.30(a) for $n_{of} = 1.45$, lead to the line of INT BICs existing at lower values of D/λ. In fact, further lowering the value of n_{of} leads to the scenario where the line of INT BICs moves below the cutoff and stops existing (not shown here). On the other hand, increasing the value of

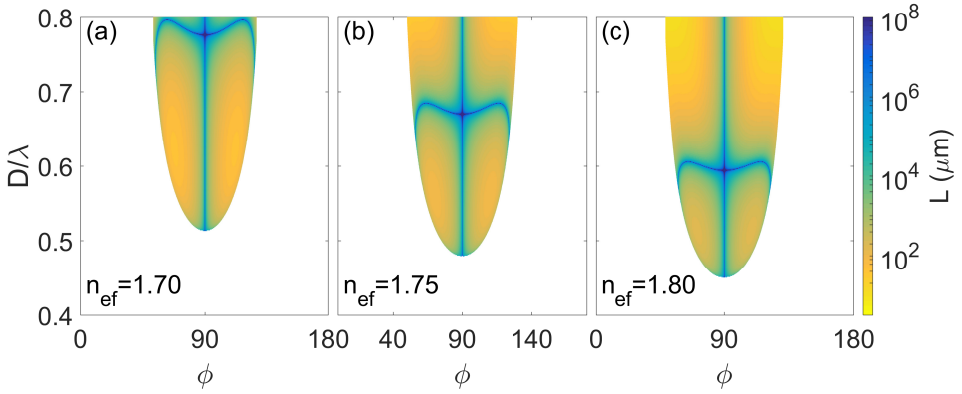

Fig. 3.31: Same as Fig. 3.29 but for variation of the extraordinary refractive index of the film with values (a) $n_{ef} = 1.70$, (b) $n_{ef} = 1.75$, (c) $n_{ef} = 1.80$.

n_{of}, as shown in Fig. 3.30(c) for $n_{of} = 1.53$, leads to the line of INT BICs shifting to higher values of D/λ. As the value of of n_{of} tends to the value of n_{ef}, the position of the line of INT BICs in D/λ tends to infinity. This is in agreement with the knowledge that an isotropic film, sandwiched between an isotropic cover and an anisotropic substrate cannot support INT BICs [117]. Therefore, we can conclude that increasing the value of n_{of} leads to the line of INT BICs being shifted to higher values of D/λ.

Fig. 3.31 shows the impact of the variation of the extraordinary refractive index of the film (n_{ef}) on the INT BICs. Comparing Fig. 3.31 to Fig. 3.30, we note that variation of the extraordinary refractive index of the film has a greater impact on the mode cutoff than the variation of the ordinary index. Increasing the value of n_{ef} brings the mode cutoff to lower values of D/λ. Once again, Fig. 3.31(b) shows the familiar figure with $n_{ef} = 1.75$. Reducing the value of of the film extraordinary index to $n_{ef} = 1.70$, as shown in Fig. 3.31(a), results in the line of INT BICs being shifted to higher values of D/λ. As seen previously in the case where n_{of} was varied, when one index approaches the other, i.e., $|n_{ef} - n_{of}| \to 0$, the line of INT BICs moves towards $D/\lambda \to \infty$. On the other hand, increasing the value of n_{ef} moves the line of INT BICs to lower values of D/λ, shifting them towards to mode cutoff as shown for $n_{ef} = 1.80$ in Fig. 3.31(c). Therefore, we conclude that increasing the value of n_{ef} leads to the line of BICs being shifted to lower values of D/λ. This is opposite to the effect that increasing

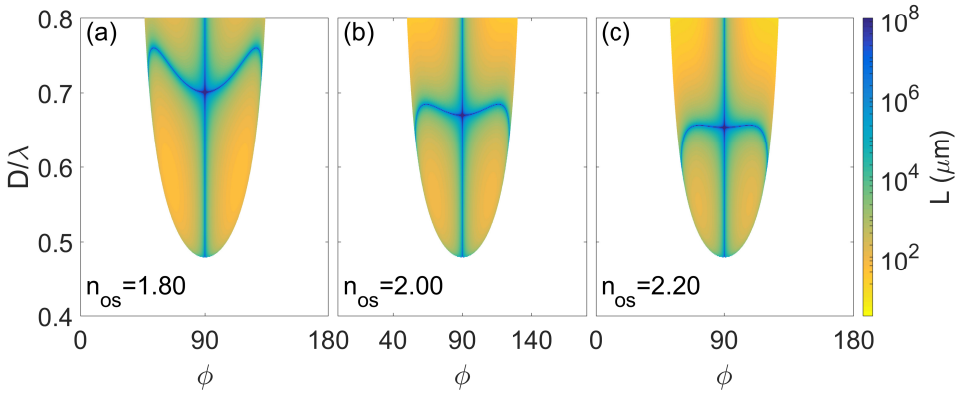

Fig. 3.32: Same as Fig. 3.29 but for variation of the ordinary refractive index of the substrate with values (a) $n_{os} = 1.80$, (b) $n_{os} = 2.00$, (c) $n_{os} = 2.20$.

the film ordinary index n_{of} had on the line of INT BICs.

Fig. 3.32 shows the impact of the variation of the ordinary index of the substrate (n_{os}) on the leaky mode. Since the substrate is a negative uniaxial material ($n_{os} > n_{es}$) in this structure, the leaky mode cutoff depends more on the extraordinary index of the substrate rather than the ordinary index and this is obvious from Fig. 3.32 where we see that a substantial change in the value of n_{os} has little impact on the leaky mode cutoff. We note from Figs. 3.32(a)-(c) that an increase in the value of n_{os} leads to the line of INT BICs shifting to lower values of D/λ. However, compared to the variation of the indices of the film, the effect of the variation of n_{os} is much less pronounced. We see a more muted effect upon varying n_{os} by 0.4 compared to when we varied n_{of} by 0.08 (see Fig. 3.30) and n_{ef} by 0.1 (see Fig. 3.31).

Fig. 3.33 shows the impact of the variation of the extraordinary index of the substrate (n_{es}) on the leaky mode. Since the substrate is a uniaxial negative material with $n_{es} < n_{os}$, it is n_{es} that plays a major role in determining the leaky mode cutoff. This is clearly shown in Fig. 3.33 as increasing the value of n_{es} leads to the mode cutoff being shifted to higher values of D/λ. At the same time, increasing the value of n_{es} also leads to the line of INT BICs being shifted to lower values of D/λ. Again we note that the effect of the variation of n_{es} on the line of INT BICs is relatively muted compared to variation of the film indices since a variation of n_{es} by 0.2 produces an effect that is comparable to variations of n_{of} by 0.08 and of n_{ef} by 0.1.

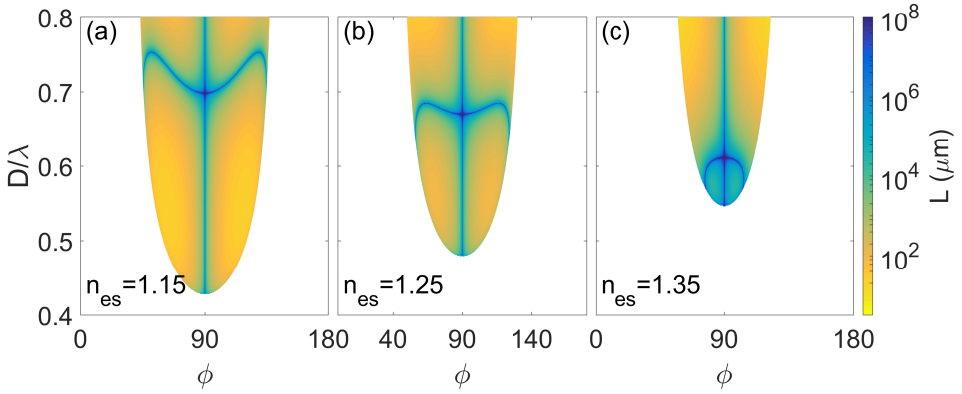

Fig. 3.33: Same as Fig. 3.29 but for variation of the extraordinary refractive index of the substrate with values (a) $n_{es} = 1.15$, (b) $n_{es} = 1.25$, (c) $n_{es} = 1.35$.

Therefore, we find that for this waveguide, the variation of the refractive indices of the waveguide varies the position of the line of INT BICs on the leaky mode sheet. The effect is most pronounced upon the variation of the film refractive indices, n_{of} and n_{ef}. The increase of n_{of} leads to the line of INT BICs shifting to higher values of D/λ while the increase of n_{ef} leads to the line of INT BICs being shifted to lower values of D/λ. The effect of variation of the cover and substrate refractive indices is relatively muted but n_c and n_{es} have substantial impact on the leaky mode cutoff. This can be attributed to the fact that the indices of the cladding materials only contribute to the phase difference needed for destructive interference via the phase accumulated upon reflection of the waves at that interface. The variation of the refractive indices of the materials constituting the waveguide only impact the pure TE-polarised PS BICs via their impact on the leaky mode cutoff since the PS BICs exist at $\phi = 90°$ for all values of D/λ above the mode cutoff.

3.3.2 Negative Uniaxial Core, Positive Uniaxial Substrate

Next, we focus on the other waveguide that we had studied in section 3.2.3 with a negative uniaxial core/film and a positive uniaxial substrate. The default values we use for this waveguide are as follows: $n_c = 1; n_{of} = 1.75, n_{ef} = 1.5; n_{os} = 1.25, n_{es} = 2$. Once again we shall

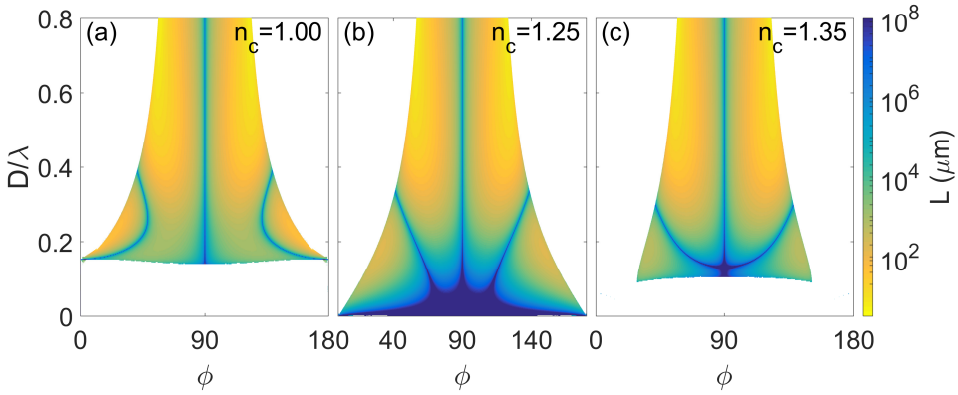

Fig. 3.34: Fundamental leaky mode supported by a waveguide with a negative uniaxial core and a positive uniaxial substrate for different values of the cover refractive index (n_c): (a) $n_c = 1$, (b) $n_c = 1.25$, (c) $n_c = 1.35$. The colour shows the leaky mode propagation length $L(\mu m)$ that the mode travels before $1/e$ attenuation. The blue lines correspond to BICs.

study the impact of the variation of each refractive index on the existence of INT BICs on the fundamental leaky mode supported by this waveguide. As in the previous case, we shall study the waveguide with full anisotropy-symmetry. Therefore, we will see at $\phi = 90°$, there is always a blue line indicating a pure TM-polarised PS BIC.

Fig. 3.34 shows the fundamental leaky mode supported by this waveguide under variation of the cover refractive index, n_c. As expected, we see from the three figures that varying the cover refractive index has substantial impact on the mode cutoff since the leaky mode cutoff in this waveguide is determined by the points where the mode propagation constant N becomes lower than whichever is the greater of the cover index (n_c) or the substrate ordinary index (n_{os}) and thus accesses another radiation channel. We find that as the value of n_c is increased from 1 (see Fig. 3.34(a)), the leaky mode cutoff moves to lower values of D/λ till we reach the point where $n_c = n_{os} = 1.25$ and there the fundamental mode has no cutoff since for the ordinary wave (see Fig. 3.34(b)), the waveguide becomes symmetric. Then as the value of n_c is increased further to 1.35 (see Fig. 3.34(c)), the mode cutoff moves to higher values of D/λ. At the same time, the lines of INT BICs that are well separated in ϕ when $n_c = 1$ (see Fig. 3.34(a)), move closer to the line of PS BICs at $\phi = 90°$ as the value of n_c is

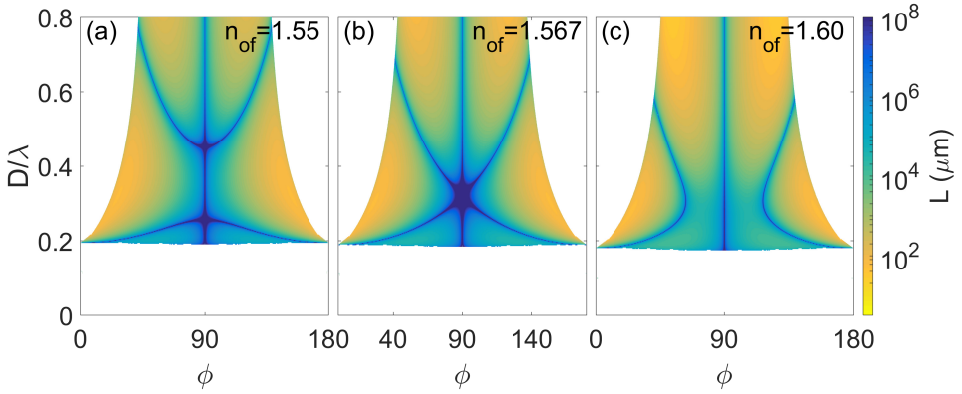

Fig. 3.35: Same as Fig. 3.34 but for variation of the ordinary refractive index of the film with values (a) $n_{of} = 1.55$, (b) $n_{of} = 1.567$, (c) $n_{of} = 1.60$.

increased. When $n_c = 1.25$ the lines of INT BICs touch at $\phi = 90°$ via an area of very low loss at the lower values of D/λ as shown in Fig. 3.34(b). Then, as n_c increases further, and the cutoff increases with it, the two lines of INT BICs, which are now joined at $\phi = 90°$ to form a single line moves to higher values of D/λ on the leaky mode sheet. Therefore we see that as n_c increases, the separation between the two lines of INT BICs in ϕ reduces and they also move to lower vales of D/λ, reaching a minimum as $n_c = n_{os}$. The lines of INT BICs join at $\phi = 90°$ as n_c increases and then as we reach values where $n_c > n_{os}$, the line of INT BICs, while still joined at $\phi = 90°$ moves to higher values of D/λ. In other words, the lines of INT BICs that can broadly be described as vertically oriented in the $\phi - D/\lambda$ space, merge and then become horizontally oriented as n_c increases.

Fig. 3.35 shows the impact of the variation of the ordinary refractive index of the film, n_{of}, on the leaky mode and INT BICs. The first thing we note is that the variation of the film ordinary index does not have any substantial impact on the mode cutoff. This is because the cutoff is primarily determined by the indices of the cladding layers, which in this case are the cover index n_c and the substrate ordinary index n_{os}. The film indices only affect the mode cutoff via their impact on the mode propagation constant N and we see that as n_{of} increases the mode cutoff shifts to marginally lower values of D/λ. The film ordinary index, however, has a drastic impact on the INT BICs supported by the mode. We find that with $n_{of} = 1.55$ there are two

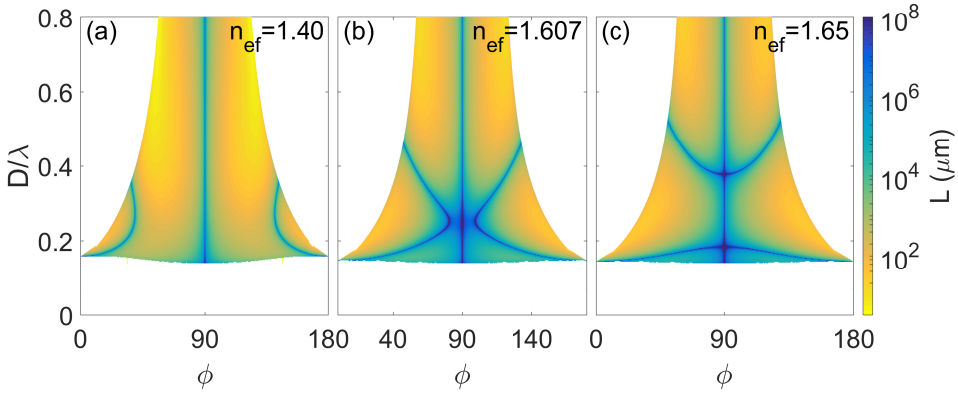

Fig. 3.36: Same as Fig. 3.34 but for variation of the extraordinary refractive index of the film with values (a) $n_{ef} = 1.40$, (b) $n_{ef} = 1.607$, (c) $n_{ef} = 1.65$.

lines of INT BICs that are separated in D/λ as shown in Fig. 3.35(a). Upon increasing the value of n_{of}, the lines of INT BICs approach each other in D/λ and at $n_{of} = 1.567$, the two line of INT BICs meet at $\phi = 90°$ as shown in Fig. 3.35(b). There is a region of low loss in the area where the INT BIC lines merge. As the value of n_{of} is further increased, the lines of INT BICs now separate in ϕ as shown in Fig. 3.35(c) for $n_{of} = 1.60$. Thus we see that increase of n_{of} brings lines of INT BICs that are initially separated in D/λ closer together till they merge at $\phi = 90°$ and then separate in ϕ. The lines of BICs that can initially be described as being horizontally oriented in the $\phi - D/\lambda$ space become vertical as n_{of} increases.

Fig. 3.36 shows the impact of the variation of the extraordinary index of the film, n_{ef}, on the leaky mode and the INT BICs it supports. Once again, we see that variation of the film index does not have much impact on the mode cutoff: increasing n_{ef} only shift the mode cutoff to marginally lower values of D/λ. However, just like the ordinary index, variation of the extraordinary index has substantial impact on the INT BICs. Fig. 3.36(a) shows the mode when $n_{ef} = 1.40$ and we see that there are two lines of INT BICs that are separated in ϕ. They can be described as being vertically oriented in the $\phi - D/\lambda$ space. As n_{ef} increases the modes move closer to each other in ϕ as shown in Fig. 3.36(b) for $n_{ef} = 1.607$. The figure shows the line of INT BICs just before they merge at $\phi = 90°$. Fig. 3.36(c) shows the mode when $n_{ef} = 1.65$ and we see that the lines of INT BICs have

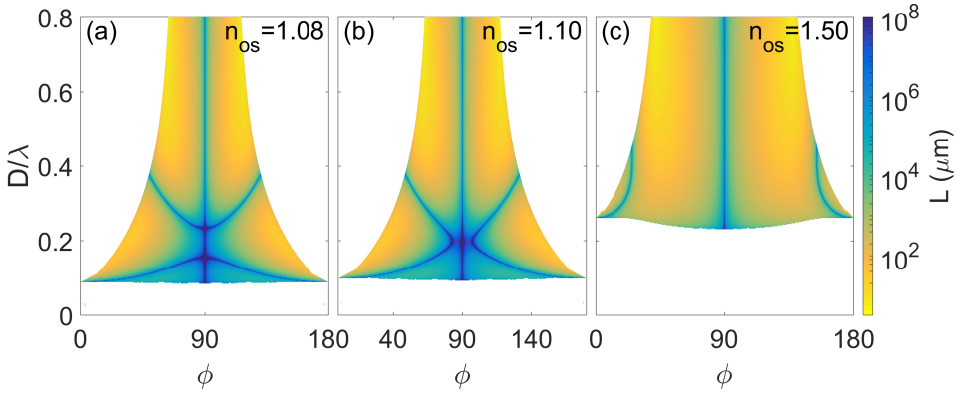

Fig. 3.37: Same as Fig. 3.34 but for variation of the ordinary refractive index of the substrate with values (a) $n_{os} = 1.08$, (b) $n_{os} = 1.10$, (c) $n_{os} = 1.5$.

now separated in D/λ and may now be described as being horizontally oriented. Therefore, as n_{ef} increases, the lines of INT BICs that are initially separated in ϕ, come closer to each other on the leaky mode sheet, merge and then separate in D/λ. The effect of the increase of the extraordinary film index is the reverse of the effect of the increase of the ordinary film index.

Fig. 3.37 shows the impact of the variation of the ordinary refractive index of the substrate, n_{os}, on the leaky mode sheet and the lines of INT BICs. Firstly, we see that variation of n_{os} has a substantial effect on the leaky mode cutoff. This is because the substrate is a uniaxial positive material and $n_{os} < n_{es}$, thereby being the determining factor in terms of deciding the leaky mode cutoff by determining the point at which a second radiation channel opens up. The cutoff increases to higher values of D/λ as n_{os} increases. Increasing n_{os} also has an impact on the line of INT BICs that is similar to the effect that increasing n_{of} had. Fig. 3.37(a) shows the leaky mode when $n_{os} = 1.08$ when the lines of INT BICs are horizontally oriented in the $\phi - D/\lambda$ space and are separated in D/λ. A slight increase in the value of n_{os} leads to the lines of INT BICs merging and then beginning to separate in ϕ as shown in Fig. 3.37(b) for $n_{os} = 1.10$. Further increasing the value of n_{os} leads to the lines of INT BICs that have more of a vertical orientation in the $\phi - D/\lambda$ space separating further in ϕ as shown in Fig. 3.37(c) for $n_{os} = 1.5$.

Fig. 3.38 shows the impact of the variation of the extraordinary

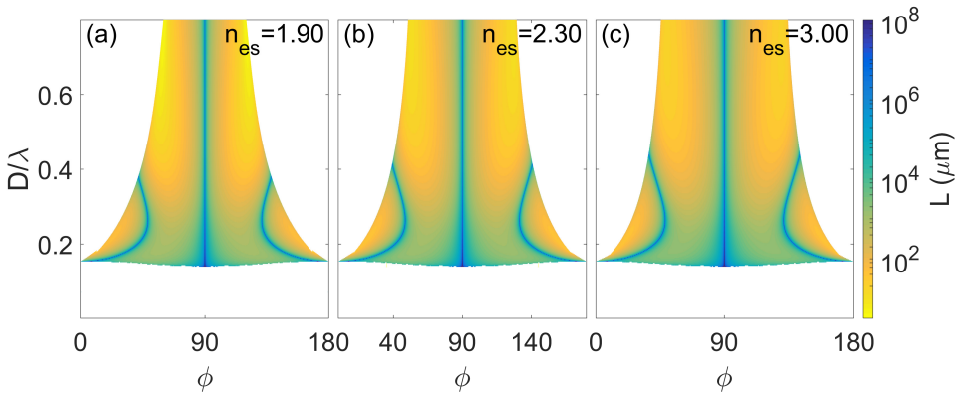

Fig. 3.38: Same as Fig. 3.34 but for variation of the extraordinary refractive index of the substrate with values (a) $n_{es} = 1.90$, (b) $n_{es} = 2.30$, (c) $n_{es} = 3.00$.

refractive index of the substrate, n_{es}, on the leaky mode. Since this is the higher of the refractive indices of the substrate, the corresponding extraordinary wave serves as the radiation channel and therefore variation of n_{es} has almost no impact on the mode cutoff. The impact of the variation of n_{es} on the lines of INT BICs is also muted. Increasing the value of n_{es} from 1.90 to 3.00, we see very little change in the lines of INT BICs. They remain largely vertically oriented in the $\phi - D/\lambda$ space for the entire range of values of n_{es}. However, increasing the value of n_{es} changes the curvature of the line of INT BICs slightly and results in INT BICs being supported at slightly higher values of D/λ.

As expected, we find that the two indices that have maximum impact on the leaky mode cutoff are the ones that determine whether the mode can access another radiation channel: namely n_c and n_{os}. More importantly, we have seen that changing the refractive indices of the various materials constituting this waveguide has a substantial impact on the lines of INT BICs. Unlike for the INT BICs discussed in the previous section (sec. 3.3.1), changing the values of the refractive indices of this waveguide leads to the orientation of the line of INT BICs changing. The lines of INT BICs also merge for specific values of the refractive indices and give rise to areas of very low loss on the leaky mode. The merger of BICs leading to lower loss is an effect that has also been seen for BICs on other photonic platforms [62]. The existence of a region of very low losses on the leaky mode sheet is important for practical applications such as a band pass filter in both wavelength

and direction.

3.3.3 Bands of INT BICs

Since INT BICs exist for a range of values of D/λ and this range varies as various refractive indices of the waveguide are varied, we can plot these ranges as bands which are functions of the refractive indices. In this section we will plot such bands for a few of the refractive indices whose variation we have studied in the previous two sections. As earlier, we maintain full anisotropy-symmetry.

First we focus on the variation of the cover refractive index n_c in the waveguide studied in section 3.3.2 with a negative uniaxial core ($n_{of} = 1.75, n_{ef} = 1.5$) and a positive uniaxial substrate($n_{os} = 1.25, n_{es} = 2$). We focus once again on the fundamental leaky mode. The geometry is shown again in Fig. 3.39(a) for convenience. Fig. 3.39(b) is a schematic showing the layout of the refractive indices. The radiation channel is provided by the extraordinary wave in the substrate since n_{es} is the highest refractive index in the structure. The red arrow shows the refractive index being varied and the dashed grey line gives an indication of the mode propagation constant N which is constrained as $max(n_c, n_{os}) < N < n_{of}$ so that there is only one radiation channel available at a time. The colored lines in Fig. 3.39(c) show how the INT BICs at specific values of ϕ move to different values of D/λ as n_c is varied. The collection of these loci for all possible values of ϕ allows us to construct the grey band in Fig. 3.39(c) which shows the range of existence for INT-BICs in D/λ for all values of ϕ as n_c is varied. The upper BIC cutoff, which decreases monotonically with n_c, corresponds to the transition from leaky to guided modes. This occurs when the mode propagation constant N is greater than $n_{es}(\phi)$ leading to the radiation channel becoming a confinement channel. The lower BIC cutoff decreases up to the point where $n_c = n_{os}$. At $n_c = n_{os}$ the structure becomes symmetric for the non-leaking polarization and like the fundamental guided mode in symmetric waveguides, the leaky mode has no lower frequency cutoff. The lower BIC cutoff for the case when $n_c < n_{os}$ corresponds to the leaky mode cutoff to the substrate continuum of ordinary radiation waves, where a second radiation channel opens up. For $n_c > n_{os}$, the leaky mode cutoff is dictated by the coupling to the continuum of the TE and TM radiation waves into the cover when $N < n_c$. However, BICs now do not extend to the lower

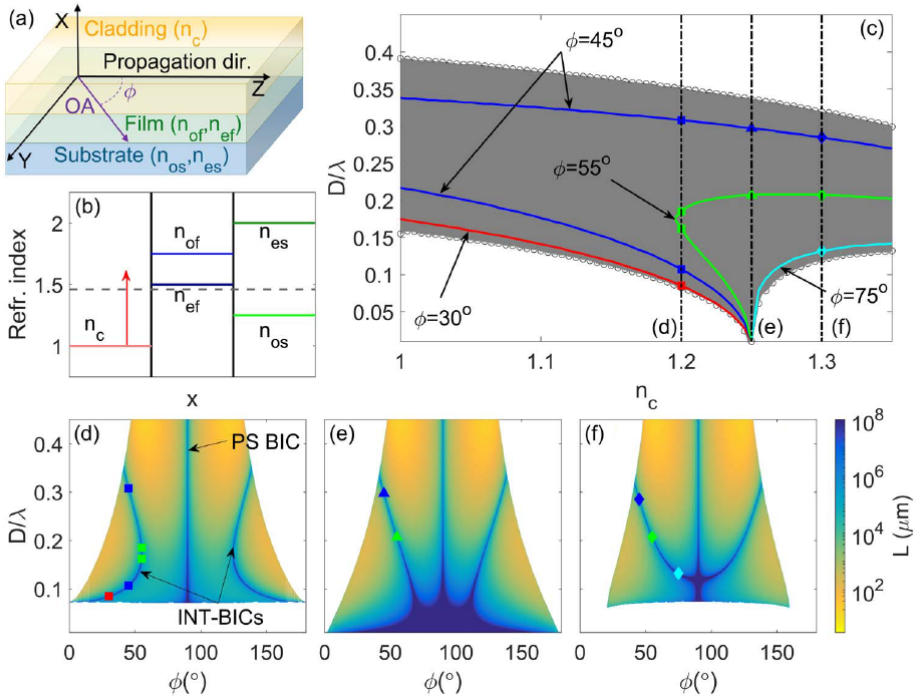

Fig. 3.39: Impact of the variation of n_c on the existence of INT BICs in a waveguide with an isotropic cover, a negative uniaxial core and a positive uniaxial substrate. (a) Geometry of the structure. (b) Schematic of the refractive indices of the structure. The red arrow shows that n_c varies. The dashed grey line is an indication of the mode index N. (c) The colored lines show the loci of INT BICs at specific values of ϕ in the $\phi - D/\lambda$ space. The grey band shows the range of existence of the INT BICs for all ϕ. The three vertical dashed lines in (c) indicate the values of n_c for which the leaky mode in the $\phi - D/\lambda$ space is shown in (d) $n_c = 1.2$, (e) $n_c = 1.25$ and (f) $n_c = 1.3$. The colored point-markers serve as visual guides for the BICs lines shown by the colored curves in (c).

cutoff of the leaky mode as shown in Fig. 3.39(f) for $n_c = 1.3$, and therefore the lower limit in the range of existence of INT-BICs in Fig. 3.39(c) corresponds to the minimum value of D/λ at which INT-BICs exist. Fig. 3.39(d)-(f) are similar to Fig. 3.34 and show the leaky mode with different values of n_c which are indicated in Fig. 3.39(b) using the dashed black lines. The coloured markers in theses figures serve as visual guides to observe the loci of the INT BICs under variation of

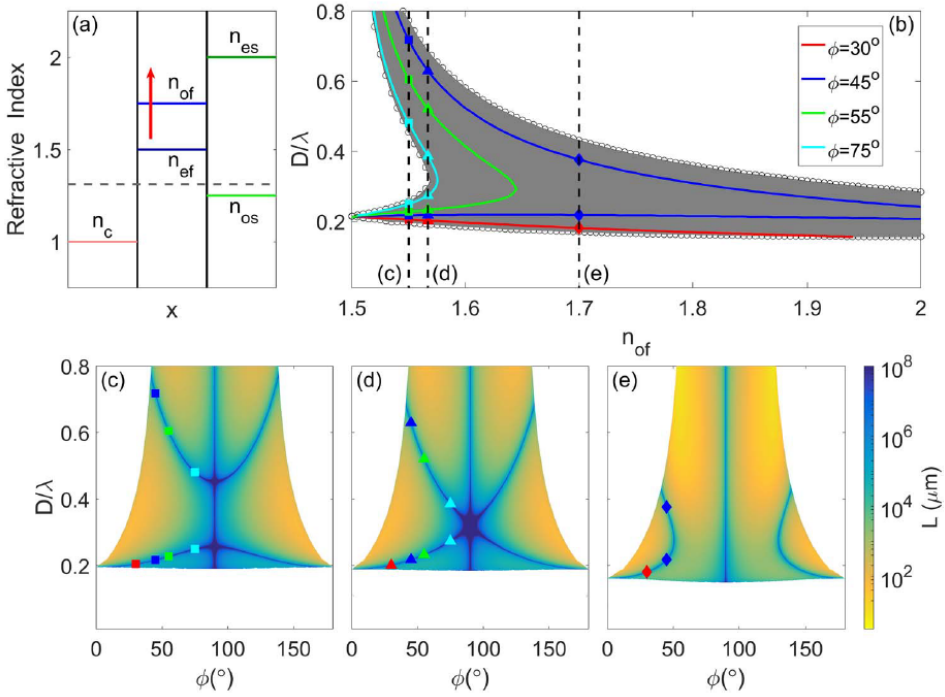

Fig. 3.40: Impact of the variation of n_{of} on the existence of INT BICs in a waveguide with an isotropic cover, a negative uniaxial core and a positive uniaxial substrate. (a) Schematic of the refractive indices of the structure. The red arrow shows that n_{of} is varied. The dashed grey line is an indication of the mode index N. (b) The colored lines show the loci of INT BICs at specific values of ϕ in the $\phi - D/\lambda$ space. The grey band shows the range of existence of the INT BICs for all values of ϕ. The three vertical dashed lines in (b) indicate the values of n_{of} for which the leaky mode in the $\phi - D/\lambda$ space is shown in (c) $n_{of} = 1.55$, (d) $n_{of} = 1.567$ and (e) $n_{of} = 1.7$. The colored point-markers serve as visual guides for the BIC lines shown by the colored curves in (b).

n_c.

Figure 3.40 shows the impact of the variation of n_{of} for the same waveguide as in the previous case, but now with a fixed value of $n_c = 1$. When $n_{of} = n_{ef} = 1.5$, the core is an isotropic material, thus existence of INT-BICs is no longer possible and only PS-BICs may exist [117]. When the value of n_{of} increases and $n_{of} > n_{ef}$, providing a uniaxial positive film, INT-BICs exist. The existence loci of the INT BICs

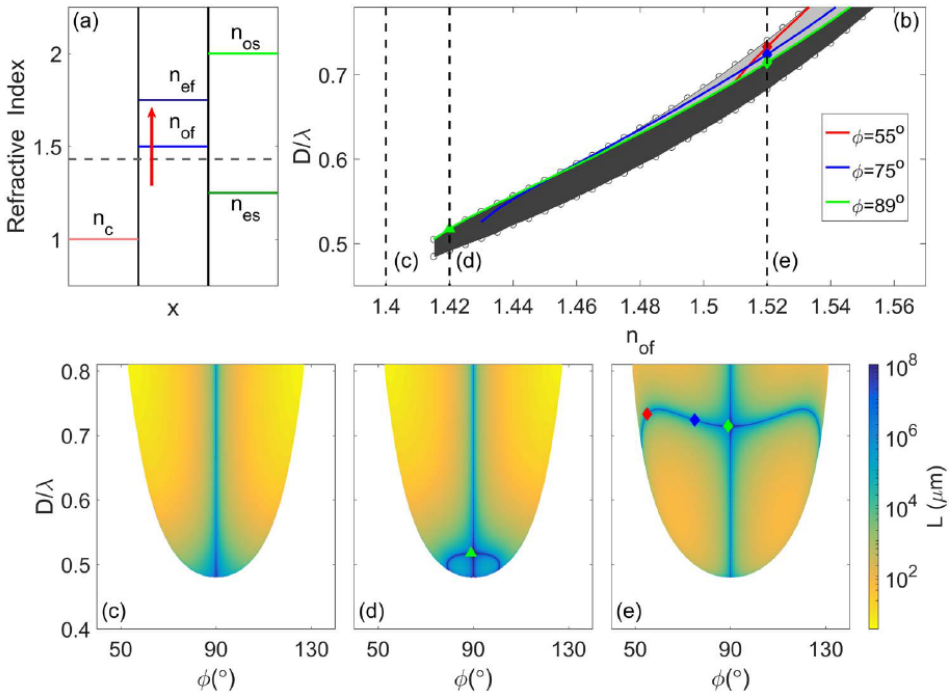

Fig. 3.41: Impact of the variation of n_{of} on the existence of INT BICs in a waveguide with an isotropic cover, a positive uniaxial core and a negative uniaxial substrate. (a) Schematic of the refractive indices of the structure. The red arrow shows that n_{of} is varied. The dashed grey line is an indication of the mode index N. (b) The colored lines show the loci of INT BICs at specific values of ϕ in the $\phi - D/\lambda$ space. The grey band shows the range of existence of the INT BICs for all values of ϕ. The three vertical dashed lines in (b) indicate the values of n_{of} for which the leaky mode in the $\phi - D/\lambda$ space is shown in (c) $n_{of} = 1.4$, (d) $n_{of} = 1.42$ and (e) $n_{of} = 1.52$. The colored point-markers serve as visual guides for the BICs lines shown by the colored curves in (b).

bends and forms two bands separated in D/λ, as shown in 3.40(b). One band starts at the lower D/λ cutoff, and the other approaches from $D/\lambda >> 1$, as n_{of} increases. A case from this regime is shown in Fig. 3.40(c) for $n_{of} = 1.55$, where a lower BIC line is visible, ascending from the lower cutoff, while an upper BIC line is seen approaching from infinity. Fig. 3.40(d) shows the case when $n_{of} = 1.567$, where all BIC lines merge at $\phi = 90°$ and $D/\lambda = 0.325$, resulting in a large region of

very low loss on the leaky mode sheet around the point of intersection of the BIC lines. Upon increasing n_{of} further, the lines of INT-BICs stop intersecting with the PS-BIC and separate in ϕ as shown in Fig. 3.40(e) for $n_{of} = 1.7$. Therefore, we see that the two bands that had been separated in D/λ now merge and there is a single grey band showing the continuous values of D/λ where INT BICs may be found at different values of ϕ.

We shall now shift our focus to the waveguide studied in section 3.3.1 and study the band structure of INT BICs on the first order leaky mode upon the variation of one of the refractive indices of the waveguide. The waveguide has an isotropic cover with $n_c = 1$, a positive uniaxial core/film with $n_{ef} = 1.75$ and n_{of} being varied, and a negative uniaxial substrate with $n_{os} = 2$ and $n_{es} = 1.25$. Fig. 3.41(a) shows the schematic of refractive indices with the red arrow marking the refractive index being varied. The grey dashed line is an approximate indicator of the value of the mode propagation constant N which lies in the range $n_{es}(\phi) < N < n_{ef}(\phi)$ for this waveguide. Fig. 3.41, shows only one band of INT BICs that appear above a particular value $n^c_{of} = 1.415$. Below n^c_{of}, only PS-BICs exist as shown in Fig. 3.41(c). Just above n^c_{of}, a line of INT-BICs appears at the lower frequency cut-off as shown in Fig. 3.41(d). As the value of n_{of} is increased this line of INT BICs moves to higher values of D/λ, as shown in Fig. 3.41(e). This results in a band of BICs that ascends in D/λ until $n_{of} = n_{ef}$, the point at which INT-BICs cannot exist, and so their position in D/λ diverges. As shown in Fig. 3.41(d), at low values of n_{of}, the line of INT-BICs on the leaky mode sheet increases monotonically in D/λ within the range $0° \leq \phi \leq 90°$. As a consequence, at a given value of D/λ there is only one INT-BIC. At higher values of n_{of}, the line of existence of INT-BICs on the leaky mode sheet is not monotonic, and therefore this can result in more than one BIC propagating in different directions, for a given value of D/λ as shown in Fig. 3.41(e). This situation is shown in Fig. 3.41(b), where the dark and light grey colour correspond to one and two INT-BICs in the range $0° \leq \phi \leq 90°$, respectively.

3.3.4 Refractive Index Sensing

Changes of the refractive indices of photonic structures leads to shifts in the position of BICs in some parameter space and this has led to

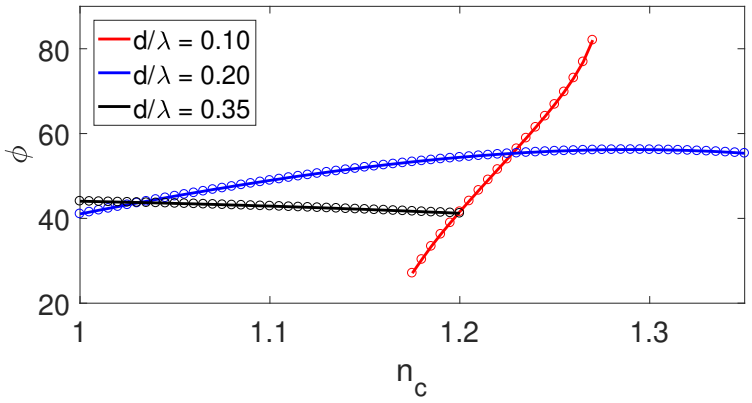

Fig. 3.42: Loci of existence of the INT-BICs as a function of the refractive index of the cover n_c, for the waveguide in Fig. 3.39

applications of BICs in sensing as mentioned earlier [89–95]. Since we have found that the INT BICs in anisotropic planar structures are sensitive to changes in the refractive indices of the materials constituting the waveguide, they have the potential to be used in sensing. The most obvious application as a sensor would involve observing the shift in BIC position as the refractive index of the cover is varied and the core and the substrate remain unchanged. Since the effect of the variation of n_c was more pronounced for the waveguide with a negative uniaxial core and positive uniaxial substrate, that is the one we study.

Figure 3.42 shows how the angular position of the INT BIC varies as a function of the refractive index of the isotropic cover, n_c, for specific values of D/λ in the range $0° \leq \phi \leq 90°$. The plot shows that the INT BIC can have different sensitivities and tendencies in ϕ depending on the value of D/λ. The highest sensitivity is obtained at low values of D/λ. We see that at for $D/\lambda = 0.1$, a change in n_c from 1.175 to 1.27 corresponds to a monotonic change in ϕ from 27° to 82°. Of course, the range of values of n_c for which INT BICs exist depends on the other parameters of the waveguide and can be seen from the band diagram in Fig. 3.39(c). For $D/\lambda = 0.2$, the sensitivity of the angular loci of existence of the BIC as a function of n_c is much reduced. However, BICs exist for all values of n_c in the range we have studied since its existence is not affected by the lower cutoff in Fig. 3.39(c). At an even higher values of D/λ, the

sensitivity remains low, but now the BIC reaches the upper cutoff in Fig. 3.39(c) at $n_c = 1.2$. These results show that INT BICs in anisotropic planar waveguides show promise for sensing devices where mode losses change under variation of external parameters, such as the cover refractive index. Fig. 3.42 shows that higher sensitivities to changes in n_c can be obtained at lower values of D/λ. Therefore, it would be possible to fabricate waveguides for the range of values of n_c that are of interest, having high sensitivity to changes in n_c by varying the different waveguide parameters. Besides, the sensitivity of the INT-BICs to the direction of propagation relative to the optic axis orientation suggests their use as spatial angular filters as only light propagating along the direction around a BIC can propagate with low-losses [149].

Chapter 4

BICs and UGRs in Anisotropic Waveguides with Two Radiation Channels

So far we have focused on anisotropic planar waveguide structures with a single radiation channel. We shall now shift our focus to anisotropic planar waveguide structures with two radiation channels. It is not immediately obvious whether structures with two radiation channels can even support BICs. Most studies of BICs in photonic structures remain restricted to structures where radiation is cancelled in a single radiation channel using various mechanisms [9, 12]. Away from photonic platforms, two channel structures have been studied in quantum systems and they report only quasi BICs which are resonances with a long, but finite, lifetime [150]. We shall explore the existence and properties of BICs in anisotropic planar waveguides in this chapter.

A structure with two radiation channels also offers the possibility of cancelling radiation in only one channel while the mode leaks to the continuum via the other channel. The existence of BICs in single radiation channel structures has shown us that is possible to cancel radiation into a channel. The mechanisms underlying BICs have then been applied to create directional resonances with control over how light radiates from a mode [130]. More recently, this understanding has been applied to photonic crystal structures to create perfectly unidirectional radiation into a single radiation channel even when multiple radiation channels are available and these modes have been termed unidirectional guided resonances (UGRs) [120, 131]. In this chapter we

shall also explore if anisotropic planar waveguides with two channels can support unidirectional guided resonances. Though the existence of BICs in single radiation channel anisotropic planar waveguides shows us that radiation through a single radiation channel may be cancelled, it is not immediately obvious this cancellation of radiation in a single channel would be possible in a situation where two radiation channels are available since the amplitudes of the various basis waves are mixed by the boundary conditions at the interfaces.

The structure that we have studied in the previous chapter has an isotropic cover, a uniaxial core/film and a uniaxial substrate. We studied modes that had only one radiation channel in the substrate. This radiation channel was provided by the wave in the substrate corresponding to whichever was the higher of two indices of the uniaxial substrate - the ordinary wave for a negative uniaxial substrate and the extraordinary wave for a positive uniaxial substrate. We ensure that the leaky mode can access only one radiation channel by constraining the mode propagation index, N, such that $max(n_c, min(n_{os}, n_{es})) < N < max(n_{os}, n_{es})$. Relaxing this constraint would allow the mode to access another radiation channel. If we allow $N < max(n_c, min(n_{os}, n_{es})$ it would mean that the mode can access the radiation continuum in the cover or of both the polarisations in the substrate. It is possible to obtain leaky mode solutions for these situations with two radiation channels in this structure, but without exception such leaky modes have very high losses and support neither PS nor INT BICs. Therefore, this structure is unsuitable for the study of BICs when the mode can access more than one radiation channel and we must explore other structures.

We have seen that a uniaxial core/film along with a uniaxial substrate is essential for INT BICs to be supported by the waveguide [117] and therefore these are essential. Therefore, the obvious modification is to change the cover material from an isotropic to a uniaxial material so that there would be one evanescent and one radiating wave in the cover for an appropriate range of mode indices. Thus the new structure would have a uniaxial cover, a uniaxial core/film and a uniaxial substrate. Such a structure would have a leaky mode with two radiation channels, one each in the substrate and the cover. Given that the framework we had developed to study leaky modes and BICs in section 3.1 only applied to structures with an isotropic cover, we need to modify that framework to deal with a uniaxial material in the cover.

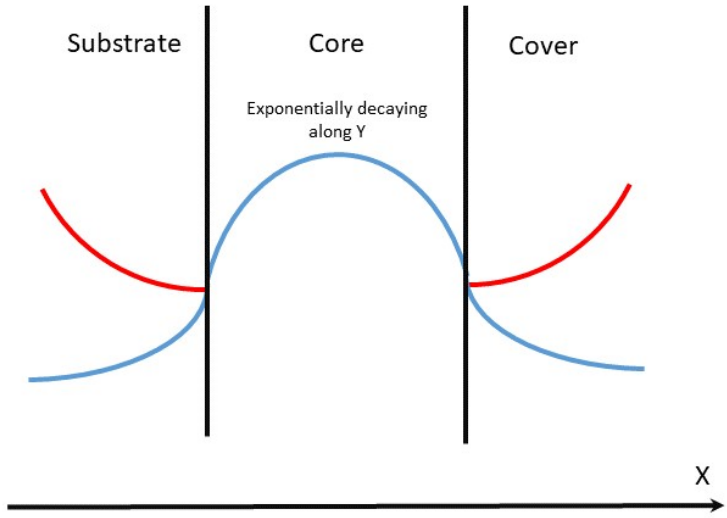

Fig. 4.1: Semi-leaky mode: Schematic of the transverse section of a leaky mode. The exponentially growing basis waves in the radiation channels in the substrate and the cover are shown in red.

In the following section we shall study the required modifications to the theoretical framework.

4.1 Theory

We developed a theoretical framework in section 3.1 involving a dispersion equation to find the leaky modes and an auxiliary condition which works in conjunction with the dispersion equation to find BICs. This framework can be extended to the structure with a uniaxial cover, uniaxial film and uniaxial substrate with some modification. Given that the cover material is now uniaxial instead of isotropic, we will classify the waves travelling along $\pm x$ as ordinary and extraordinary instead of TE or TM as we did in section 3.1.2 and 3.1.3 for the waveguide with isotropic cover. This will lead to changes in the dispersion equation and the auxiliary conditions.

4.1.1 Dispersion Equation

Once again the prescription to arrive at the dispersion equation is to simultaneously apply the boundary conditions at the cover-film and the film-substrate interfaces. We will use the Berreman transfer matrix, $\hat{M}$, defined in eq. 2.35, to translate the fields across the core/film and thus relate the fields at the two interfaces. Since we now have radiation channels in both the cover and the substrate, the prescription that had been applied only to the substrate in section 3.1.2 must now be applied to both the cover and the substrate in this structure when selecting the proper basis waves.

We propagate the mode along the y-axis and the x-axis is perpendicular to the interface. We are interested in improper leaky mode solutions which decay along the direction of propagation, y, but due to flux considerations, must have exponentially growing waves in the transverse direction as energy leaks away from the mode [8, 107]. For a given value of the mode propagation constant $\kappa_y (= N)$, from the four basis waves (2 ordinary, 2 extraordinary) propagating in $\pm x$, we have to choose one ordinary wave and one extraordinary wave each in the substrate and in the cover. For the polarisation that corresponds to the confinement channel, we must choose the wave that is exponentially decaying away from the interface whereas for the polarisation corresponding to the radiation channel, we must choose the wave that is exponentially growing away from the interface. Now that we know the waves to select in the cover and the substrate, we can write the total field in the cover just to the right of the cover-film interface as

$$\begin{aligned} \vec{m}_{cover-film} &= a_c^o \vec{F}_c^o + a_c^e \vec{F}^e, \\ &= a_c^o \begin{bmatrix} E_{yc}^o \\ \tilde{H}_{zc}^o \\ E_{zc}^o \\ \tilde{H}_{yc}^o \end{bmatrix} + a_c^e \begin{bmatrix} E_{yc}^e \\ \tilde{H}_{zc}^e \\ E_{zc}^e \\ \tilde{H}_{yc}^e \end{bmatrix}. \end{aligned} \tag{4.1}$$

Similarly the film just to the left of the film-substrate interface can be written as

$$\begin{aligned} \vec{m}_{film-substrate} &= a_s^o \vec{F}_s^o + a_s^e \vec{F}_s^e, \\ &= a_s^o \begin{bmatrix} E_{ys}^o \\ \tilde{H}_{zs}^o \\ E_{zs}^o \\ \tilde{H}_{ys}^o \end{bmatrix} + a_s^e \begin{bmatrix} E_{ys}^e \\ \tilde{H}_{zs}^e \\ E_{zs}^e \\ \tilde{H}_{ys}^e \end{bmatrix}, \end{aligned} \tag{4.2}$$

where the subscripts c and s indicate the cover and the substrate respectively, the superscripts o (ordinary) and e (extraordinary) represent the choice of polarisation of the basis wave in the uniaxial media, $a_{c/s}^{o/e}$ is the scalar amplitude of the corresponding basis wave and $\vec{F}_{c/s}^{o/e}$ is a 4×1 column vector which represents the basis wave vector for the cover or the substrate containing the four tangential field components: $E_y, \tilde{H}_z, E_z$ and $\tilde{H}_y$. Since the total field given in eqs. 4.1 and 4.2 only contains the tangential field components, which are continuous across any interface, we know that the film to the just to the right of either interface is the same as the field just to the left of that interface.

Since we have analytical expressions for the field vectors $\vec{F}$ as a function of the propagation index κ_y, we can calculate the field matrix $\hat{F}$ as given in eq. 2.25. Moreover, since we know the values of the propagation constants in the x direction, we can calculate the the phase matrix $\hat{A}_d$ for a film of thickness d as given in eq. 2.30. Using these, we can calculate the characteristic matrix $\hat{M} = \hat{F}\hat{A}_d\hat{F}^{-1}$ (see eq. 2.35).

The characteristic matrix for a layer translates the total fields across a layer. Therefore, we can use the characteristic matrix for the film to relate the fields given in eqs. 4.1 and 4.2 and thus apply the boundary conditions at both interfaces simultaneously. This gives us

$$a_s^o\vec{F}_s^o + a_s^e\vec{F}_s^e = a_c^o\hat{M}\vec{F}_c^o + a_c^e\hat{M}\vec{F}_c^e. \tag{4.3}$$

This gives us four equations for the four tangential field components. We can re-write this as

$$\begin{aligned} a_c^o\hat{M}\vec{F}_c^o + a_c^e\hat{M}\vec{F}_c^e - a_s^o\vec{F}_s^o - a_s^e\vec{F}_s^e &= 0, \\ \implies \begin{bmatrix} \hat{M}\vec{F}_c^o & \hat{M}\vec{F}_c^e & -\vec{F}_s^o & -\vec{F}_s^e \end{bmatrix} \begin{bmatrix} a_c^o \\ a_c^e \\ a_s^o \\ a_s^e \end{bmatrix} &= \begin{bmatrix} 0 \\ 0 \\ 0 \\ 0 \end{bmatrix}, \\ \implies \hat{R}\vec{a}_{c+s} &= 0, \end{aligned} \tag{4.4}$$

where $\vec{a}_{c+s}$ is a 4×1 vector containing the amplitudes of the basis waves in the cover and the substrate. $\hat{M}$ is a 4×4 matrix and $\vec{F}_{c/s}^{o/e}$ is a 4×1 column vector. Therefore, $\hat{R} = \begin{bmatrix} \hat{M}\vec{F}_c^o & \hat{M}\vec{F}_c^e & -\vec{F}_s^o & -\vec{F}_s^e \end{bmatrix}$ is a 4×4 matrix.

We therefore have a homogeneous system of four equations where the amplitudes $a_{c/s}^{o/e}$ serve as the four unknown variables. We are only

interested in non-trivial solutions of this system of equations and a system of homogeneous linear equations can have a non-trivial solutions only if the determinant of the coefficient matrix, $\hat{R}$, is zero. This gives us the dispersion condition

$$|\hat{R}| = 0. \tag{4.5}$$

Once the materials and the dimensions of the waveguide and the orientation of the optic axes in the uniaxial layers is fixed, $|\hat{R}|$ only depends on κ_y. However, eq. 4.5 is a transcendental equation and we have to solve it numerically to find the complex propagation constants of the leaky modes supported by this structure with two radiation channels.

4.1.2 Auxiliary Condition

The complex solutions of the dispersion equation gives us the mode propagation index, N, for the leaky mode. However, while the imaginary part of N approximates the loss of the leaky mode, we cannot definitively determine the existence of BICs from it. Moreover, now that we have two radiation channels, the imaginary part of N will not give us any information as to the ratio of radiation in the two channels or the existence of UGRs. BICs and UGRs exist when the coupling of the leaky mode to the continuum is cancelled due to some mechanism. For PS BICs this means that the polarisation of the mode is orthogonal to that of the radiation channel and they occur due to the geometry of the structure at specific orientations of the optic axes. UGRs or INT BICs in this structure will arise due to cancellation of the radiation in only one or both the channels, respectively. This would occur due to the mixing of the waves when applying the boundary conditions at the interface. In this section we will define auxiliary conditions where we explicitly study the cancellation of radiation in the required radiation channel(s) in order to study the existence of UGRs and BICs in this structure with two radiation channels.

We are interested in studying leaky modes that are coupled to two radiation channels, one radiating to the substrate and the other radiating to the cover. The cover and the substrate would each have one radiation channel and one confinement channel. In this situation we can write eq. 4.4 as

$$a_c^{rad}\hat{M}\vec{F}_c^{rad} + a_c^{conf}\hat{M}\vec{F}_c^{conf} - a_s^{rad}\vec{F}_s^{rad} - a_s^{conf}\vec{F}_s^{conf} = 0, \tag{4.6}$$

where the superscript *rad* and *conf* indicate the radiation and confinement channels respectively. For a UGR to be supported, radiation into only one of the two radiation channels would have to be cancelled. This would require that the amplitude of the basis wave that corresponds to that radiation channel would have to be zero. If we want to study the UGR that radiates only towards the cover, for instance, we would require that the amplitude of the substrate radiation channel be zero. Applying this to eq. 4.6 we would get

$$\begin{aligned} & a_c^{rad}\hat{M}\vec{F}_c^{rad} + a_c^{conf}\hat{M}\vec{F}_c^{conf} - a_s^{conf}\vec{F}_s^{conf} = 0, \\ \implies & \begin{bmatrix}\hat{M}\vec{F}_c^{rad} & \hat{M}\vec{F}_c^{conf} & -\vec{F}_s^{conf}\end{bmatrix} \begin{bmatrix} a_c^{rad} \\ a_c^{conf} \\ a_s^{conf}\end{bmatrix} = \begin{bmatrix}0\\0\\0\\0\end{bmatrix}, \\ & \implies \hat{Z}^c_{4\times 3}\vec{a} = 0. \end{aligned} \tag{4.7}$$

For the UGR which would radiate only to the substrate, the requirement would be that the amplitude of the wave corresponding to the cover radiation channel would have to be zero. Applying this to eq. 4.6, we would get

$$\begin{aligned} & a_c^{conf}\hat{M}\vec{F}_c^{conf} - a_s^{rad}\vec{F}_s^{rad} - a_s^{conf}\vec{F}_s^{conf} = 0, \\ \implies & \begin{bmatrix}\hat{M}\vec{F}_c^{conf} & \hat{M}\vec{F}_s^{rad} & -\vec{F}_s^{conf}\end{bmatrix} \begin{bmatrix} a_c^{conf} \\ a_s^{rad} \\ a_s^{conf}\end{bmatrix} = \begin{bmatrix}0\\0\\0\\0\end{bmatrix}, \\ & \implies \hat{Z}^s_{4\times 3}\vec{a} = 0. \end{aligned} \tag{4.8}$$

Eqs. 4.7 and 4.8 give us the auxiliary conditions for the existence of UGRs radiating to the cover and the substrate, respectively. Essentially, both of these are systems of linear equations with four equations corresponding to the four tangential field components contained in $\vec{F}^{o/e}_{c/s}$ and three unknown amplitudes $a^{conf/rad}_{c/s}$. $\hat{Z}^{c/s}_{4\times 3}$ is a 4×3 matrix that contains the coefficients and $\vec{a}$ is a 3×1 column vector containing the three unknown amplitudes. Therefore, we again have overdetermined, homogeneous sets of linear equations which can only have non-trivial solutions if at most two of the equations are linearly independent. This translates into the requirement that the determinant calculated by selecting any 3 of the rows of $\hat{Z}^{c/s}_{4\times 3}$ must be zero. This condition applied

to the appropriate $\hat{Z}^{c/s}_{4\times3}$ in conjunction with the dispersion equation would give us the UGR radiating to the cover or the substrate.

While UGRs radiate through one of the two available radiation channels, a BIC would require that there is no radiation through any of the channels. Therefore, both a_s^{rad} and a_c^{rad} would have to be zero for the BIC to exist in a structure with two radiation channels. This is the same as requiring that both eq. 4.7 and eq. 4.8 are satisfied at the same time. For BICs in a single radiation channel structure, there was a single auxiliary condition, which in addition with the dispersion condition, gave us the locations of INT BIC solutions. However, in a structure with two radiation channels, there is an extra constraint that is placed on the existence of BICs in the form of an added auxiliary condition.

The two auxiliary conditions can be combined and written as

$$\begin{aligned} & a_c^{conf}\hat{M}\vec{F}_c^{conf} - a_s^{conf}\vec{F}_s^{conf} = 0, \\ \implies & \begin{bmatrix}\hat{M}\vec{F}_c^{conf} & -\vec{F}_s^{conf}\end{bmatrix}\begin{bmatrix}a_c^{conf}\\ a_s^{conf}\end{bmatrix} = \begin{bmatrix}0\\0\\0\\0\end{bmatrix}, \\ & \implies \hat{Z}^{BIC}_{4\times2}\vec{a} = 0. \end{aligned} \tag{4.9}$$

Thus, for BICs, we would require that there exist non-trivial solutions to eq. 4.9 in conjunction with the leaky mode dispersion equation given in eq. 4.5.

Now that we are equipped with the theoretical framework required to study leaky mode solutions in structures with two radiation channels, we shall proceed to study the existence of BICs and UGRs in them.

4.2 Waveguide with Negative Uniaxial Materials

The structure that we will study first will be an anti-guiding structure comprising three uniaxial negative materials. For simplicity, we consider identical materials in the cover and substrate. We then choose the material of the core/film so that the refractive indices are situated between the refractive indices of the cover and the substrate

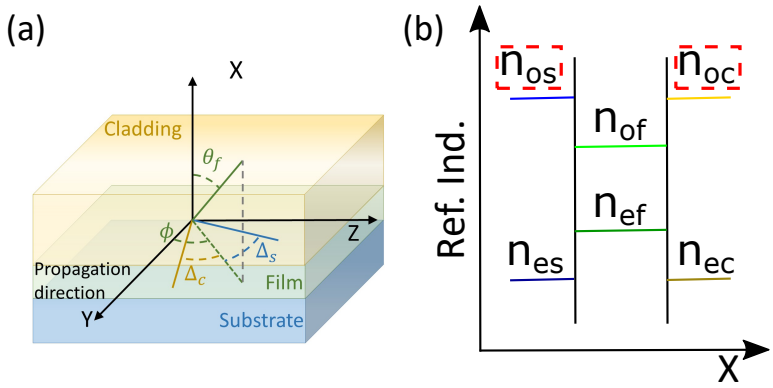

Fig. 4.2: (a) Waveguide comprising three negative birefringent materials whose optical axis orientations are assumed to be varied independently. (b) Schematic of the refractive indices of the structure. The dashed red boxes indicate the index/polarisation corresponding to the radiation channel.

($n_{oc} = n_{os} > n_{of} > n_{ef} > n_{ec} = n_{es}$). We assume that the optic axes orientations can be varied independently for the three materials. The highest refractive indices in the structure are the ordinary indices in the cover and the substrate. Therefore, the two radiation channels will be provided by the ordinary waves in the cover (n_{oc}) and the substrate (n_{os}). Since the ordinary index does not vary upon variation of optic axis orientation relative to propagation direction, modes in this structure will always have access to the radiation channels in the cover and the substrate. Therefore, the structure will not be able to support any conventional guided modes. The only bound modes that this structure could support would have to be BICs.

The structure that we study is shown in Fig. 4.2(a). D is the thickness of the film though we present our results in terms of the normalized dimensionless thickness or operating wavelength D/λ. As always, we consider propagation along the y-axis. The x-axis is normal to the interfaces of the waveguide materials. The angle ϕ denotes the azimuthal angle in the interface plane between the propagation direction and the projection of the film optic axis in the interface plane. Δ_c and Δ_s give the offset of the optic axes of the cover and the substrate with respect to the film optic axis in the interface ($y-z$) plane, such that $\Delta_{c/s} = \phi - \phi_{c/s}$. θ_s, θ_f and θ_c are the polar angles of the substrate, film and cover optic axes with respect to the normal to the interface

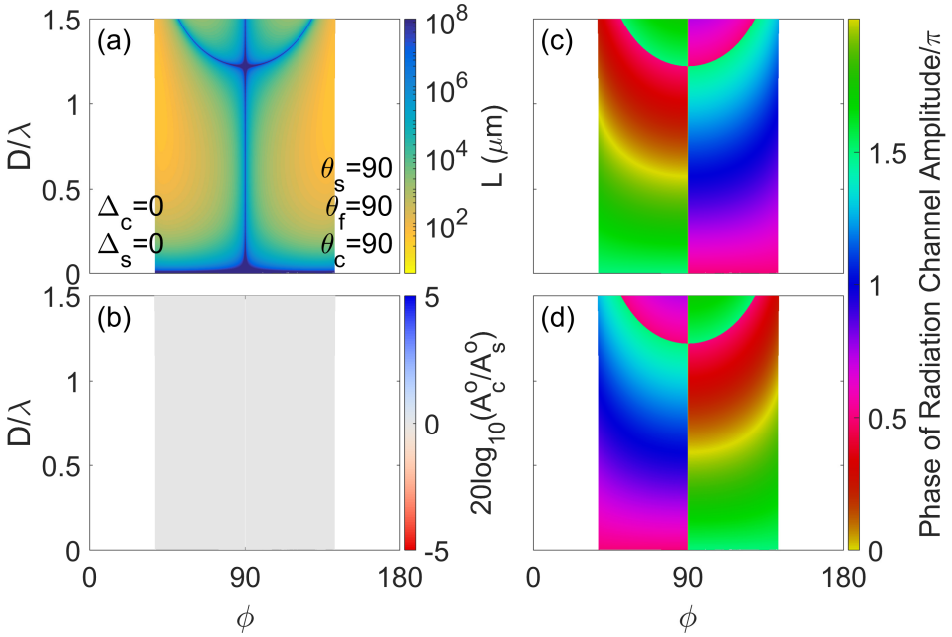

Fig. 4.3: (a) Fundamental leaky mode supported by a structure with full anisotropy-symmetry ($\Delta_c = \Delta_s = 0°$ and $\theta_c = \theta_f = \theta_s = 90°$). (b) Ratio of radiation channel amplitudes in dB for the mode in (a). (c) Phase of the radiation channel (ordinary wave) amplitude in the cover, measured with respect to the phase of the extraordinary confined wave. (d) Same as (c) but for the substrate radiation channel amplitude.

plane. Without loss of generality, unless otherwise specified, we choose the values for the refractive indices in the substrate and the cover as $n_{os} = n_{oc} = 1.7 > n_{es} = n_{ec} = 1.3$. The refractive indices of the material of the film situated between those of the cover and the substrate are $n_{of} = 1.6 > n_{ef} = 1.4$. A schematic of the refractive index layout is shown in Fig. 4.2(b) with the indices corresponding to the radiation channels in the red boxes.

The two radiation channels in the cover and the substrate are equivalent when the structure is mirror-symmetric about the $x = 0$ (or $y-z$) plane. Since having two equivalent radiation channels would be similar to having a single radiation channel, which is the case that is familiar to us from Chapter 3, we start our study with a structure that is mirror-symmetric about the $x = 0$ plane. Fig. 4.3(a) shows the fundamental leaky mode supported by the structure when, in addition to mirror symmetry about $x = 0$, full anisotropy-symmetry is also main-

tained, i.e., the optic axes of the cover, film, and substrate lie in the interface plane ($\theta_c = \theta_f = \theta_s = 90°$) and are aligned ($\Delta_c = \Delta_s = 0°$). Since the structure is a symmetric, planar waveguide the fundamental leaky mode has no cutoff in D/λ. The leaky mode supports a line of PS BICs at $\phi = 90°$ which arises due to the guiding profile provided by the extraordinary indices. The structure also supports INT BICs as shown by the curved blue line on the leaky mode. Since azimuthal anisotropy-symmetry is maintained, the distribution of the INT BICs is symmetric about $\phi = 90°$. Fig. 4.3(b) shows the ratio of the radiation channel amplitudes in the two channels in dB for the mode shown in Fig. 4.3(a). The symmetric structure has equivalent radiation channels and therefore, the radiation into the two channels is identical at all points on the mode. Fig. 4.3(c) and (d) shows the phase of the ordinary radiation channel amplitude in the cover and substrate, respectively, measured with respect to the extraordinary confined wave. Once again, we find that the lines of BIC existence correspond to a phase discontinuity of $\pm\pi$. Note that the discontinuity in the phase of the radiation channel amplitude carries opposite sign in the cover and the substrate.

4.2.1 Azimuthal Anisotropy-Symmetry Breaking

We now study another structure that maintains mirror symmetry about $x = 0$ but with azimuthal anisotropy-symmetry breaking. We offset the cover and the substrate optic axis from the film optic axis by the same amount so that $\Delta_c = \Delta_s = -5°$. Polar anisotropy-symmetry is maintained. Fig. 4.4(a) shows the fundamental leaky mode supported by this structure. Once again we see that fundamental mode has no cutoff in D/λ since the structure is symmetric. Moreover, as expected we find that the azimuthal anisotropy-symmetry breaking leads to the distortion of the lines of BICs which are no longer distributed symmetrically about $\phi = 90°$. This structure no longer supports pure TE/TM modes for any value of ϕ and consequently, there are no PS BICs. There are, however, two separate lines of INT BICs - one that occurs at low values of ϕ and high values of D/λ above 1.4 and another vertical line that occurs at relatively higher values of ϕ and for all values of D/λ that we study. Since the structure is symmetric and the radiation channels are equivalent, the radiation escaping via each channel is the same as shown in Fig. 4.4(b). Fig. 4.4(c) and (d) show the phase of

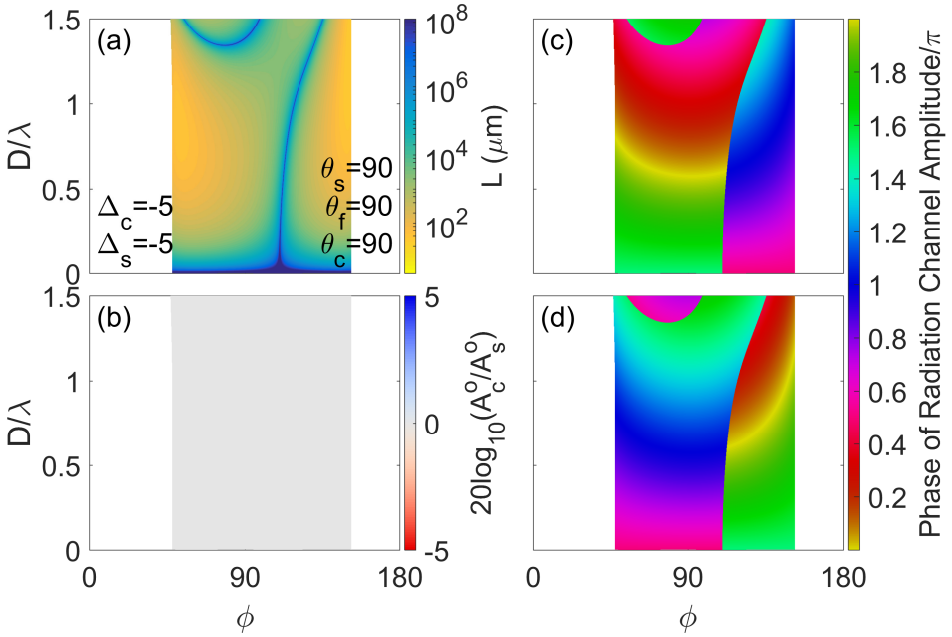

Fig. 4.4: Same as Fig. 4.3 but for a structure with azimuthal anisotropy-symmetry breaking with both the cover and substrate optic axes offset from the film optic axis by $\Delta_c = \Delta_s = -5°$.

the radiation channel amplitude in the cover and the substrate, respectively. Once again, we see that the lines of BIC existence correspond to discontinuities of $\pm\pi$ in the phase of the radiation channel amplitude and the discontinuity for a specific BIC line has opposite signs in the cover and substrate radiation channel amplitudes.

Next we study a structure where azimuthal anisotropy-symmetry is broken but the offset in the cover and the substrate is not equal ($\Delta_c \neq \Delta_s$). Fig. 4.5(a) shows the fundamental leaky mode supported by such a structure with the cover optic axis offset from the film optic axis by $\Delta_c = -5°$ while the substrate optic axis is aligned with the film optic axis ($\Delta_s = 0°$). Polar anisotropy-symmetry is maintained. The mode cutoff is determined by the points where the mode propagation constant N drops below the extraordinary index of either the cover ($n_{ec}(\phi_c = \phi + \Delta_c)$) or the substrate ($n_{es}(\phi_s = \phi)$). This structure is no longer mirror symmetric about $x = 0$ and therefore the radiation channels are now distinct. Therefore in order for a BIC to exist, two separate auxiliary conditions, corresponding to the two distinct radiation channels, have to be fulfilled. We find that with this additional

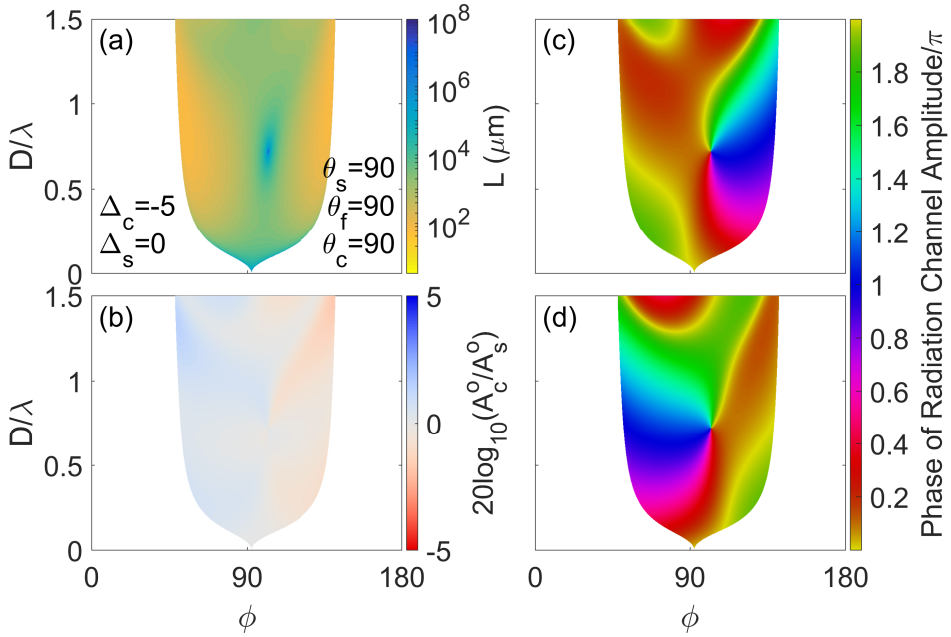

Fig. 4.5: Same as Fig. 4.3 but for a structure with azimuthal anisotropy-symmetry breaking in the cover. The cover optic axis is offset from the film optic axis by $\Delta_c = -5°$. The substrate optic axis is aligned with the film optic axis, i.e., $\Delta_s = 0°$.

constraint, the mode no longer supports lines of BICs but a single BIC point. Finding the BIC point for this structure with two radiation channels is not the same as solving for the point of intersection of the BIC lines of existence in structures containing the individual radiation channels. This is because the radiation channels are coupled via the reflections occurring at the film interface and encapsulated in the characteristic matrix of the film. Thus we find that adding a constraint leads to the collapse of BIC lines to a single BIC point. Since this is an anti-guiding structure, this discrete BIC point is the only bound mode that this structure can support at that value of ϕ. The BIC appears as an isolated, needle-like spectrally-discrete state in the dispersion diagram in the $\phi - D/\lambda$ space and thus it resembles the discrete resonances that occur in closed systems. Therefore, going forward, we shall refer to these isolated, discrete BICs as needles. Moreover, since the radiation channels are no longer equivalent, the radiation escaping via each channel is no longer identical. This is shown in Fig. 4.5(b) where we find that at lower values of ϕ the radiation channel in the cover

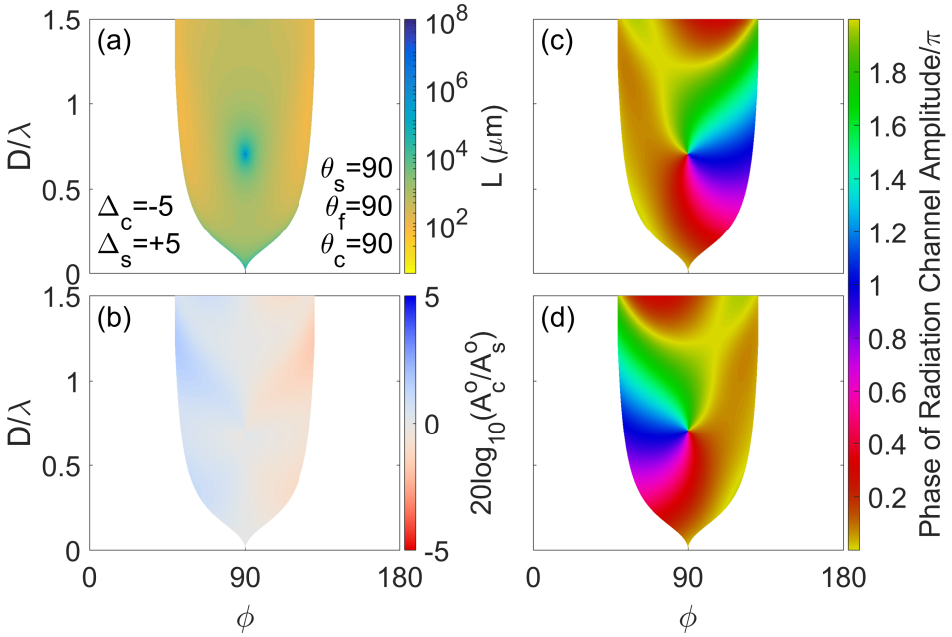

Fig. 4.6: Same as Fig. 4.3 but for a structure with opposite azimuthal anisotropy-symmetry breaking in the cover and the substrate. The cover optic axis is offset from the film optic axis by $\Delta_c = -5°$. The substrate optic axis is offset from the film optic axis $\Delta_s = +5°$.

dominates whereas at higher values of ϕ, radiation escapes mostly via the radiation channel in the substrate. The BIC point corresponds to a zero of the radiation channel amplitude in both the substrate and the cover. This leads to a phase singularity and a screw phase dislocation around the BIC point in the phase map of the radiation channel amplitudes as shown in Fig. 4.5(c) and (d). We can assign the phase singularity due to the BIC in the cover radiation channel a winding number -1 since the phase increases counter clockwise. The singularity in the substrate radiation channel can be assigned a winding number with the opposite sign $+1$ since the phase increases clockwise.

Since the discrete BIC points or needles are characterised by phase singularities that can be assigned winding numbers, we expect them to be robust under variation of parameters. We verify this by studying another structure that is not symmetric about the $x = 0$ plane. Fig. 4.6(a) shows the mode of a structure with opposite offsets of the optic axes in cover and substrate from the film optic axis ($\Delta_s = -\Delta_c = 5°$). Polar anisotropy-symmetry is maintained. Once again, since the two

radiation channels are distinct, two separate auxiliary conditions have to be fulfilled. As a consequence we see that the leaky mode supports only a single, isolated BIC point just like in the previous case that was studied. However, the BIC point or needle has shifted on the leaky mode sheet compared to the previous case and is now situated as $\phi = 90°$. This is because $\Delta_c = \Delta_s$. Though the needle exists at $\phi = 90°$, it is an INT BIC. This structure does not support any pure TE/TM modes and therefore, cannot support any PS BICs. With the radiation channels no longer being equivalent due to the asymmetry of the structure, radiation into the channels is not identical as shown in Fig. 4.6(b). As in the previous case, as lower values of ϕ, the cover radiation channel dominates while at higher values of ϕ, the dominant radiation channel is the one in the substrate. The phase map of the cover and substrate radiation channel amplitudes is shown in Fig. 4.6(c) and (d), respectively. The BIC point corresponds to phase singularities in both phase maps and is characterised by a screw phase dislocation around the singularity. The singularity in the cover radiation channel can again be assigned a winding number -1 (counter clockwise increase of phase) and the one in the substrate radiation channel can be assigned a winding number $+1$ (clockwise increase of phase).

Locus of the Needle

We have seen from Figs. 4.5 and 4.6 that the isolated, discrete BIC points are robust under variation of optic axes orientation. The needle merely shifts its position on the leaky mode sheet upon the variation of the offset. We study the impact of the variation of optic axis orientation on the position of the needle systematically in Fig. 4.7. Fig. 4.7(a) and (b) show how the mode and the BIC evolve when Δ_c is varied while keeping Δ_s fixed. We find that changing from $\Delta_c = -20°$ in Fig. 4.7(a) to $\Delta_c = +20°$ in Fig. 4.7(b) while we maintain $\Delta_s = 0°$ results in the mode as well as the position of the needle on the mode being reflected about $\phi = 90°$. However, for the same change in value of Δ_c but now with $\Delta_s = 10°$, as shown in Fig. 4.7(c) and (d), the mode cutoff and the needle BIC point are both shifted but the change now is no longer just a simple reflection about $\phi = 90°$. In general, we find that greater the difference between Δ_c and Δ_s, the narrower the ϕ-range of existence of leaky modes. The leaky mode cutoff largely determines

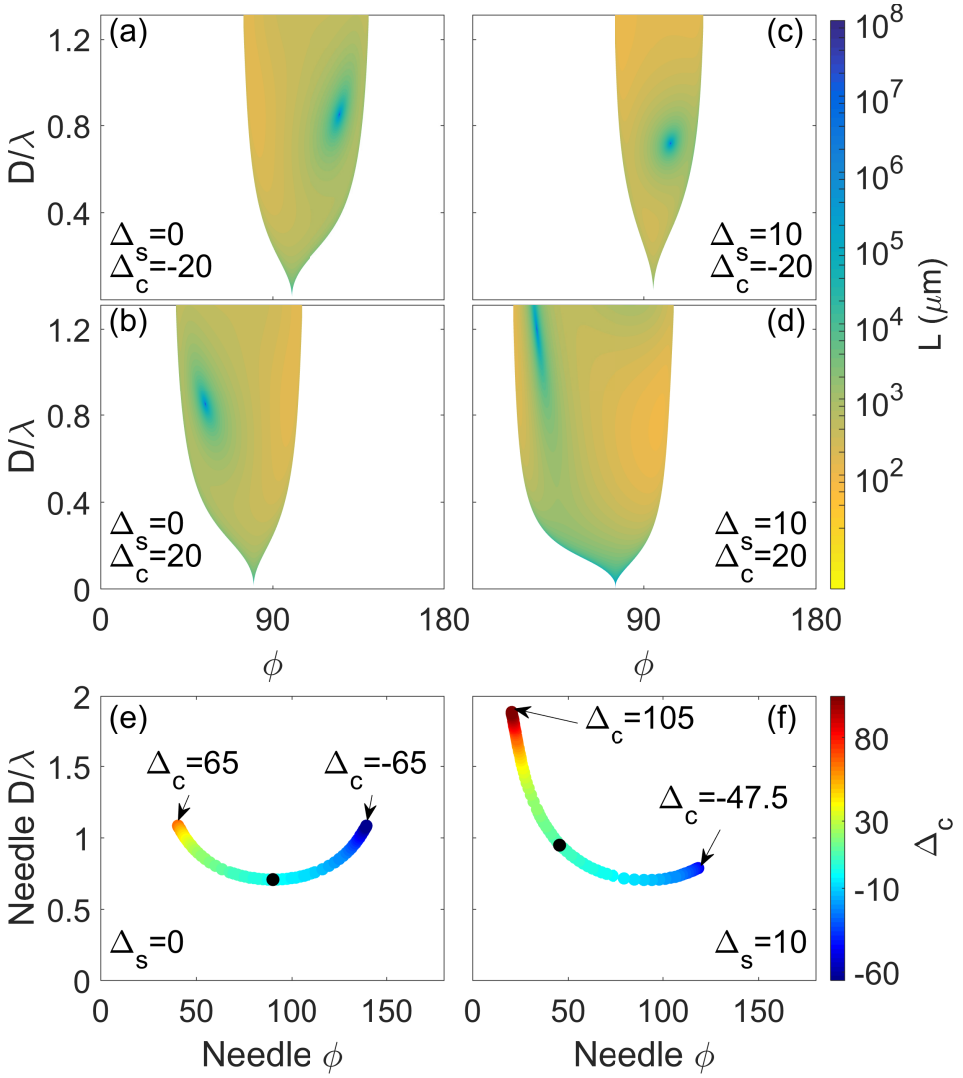

Fig. 4.7: Leaky mode sheet for $\Delta_s = 0°$ and (a) $\Delta_c = -20°$ (b) $\Delta_c = +20°$. The leaky mode sheet in (c) and (d) has the same values of Δ_c but with $\Delta_s = 10°$. Locus of the needle in the $\phi - D/\lambda$ space under variation of Δ_c for fixed values of (e) $\Delta_s = 0°$ and (f) $\Delta_s = 10°$. The color of the dots in (e) and (f) indicate the value of Δ_c. The black dot on each plot corresponds to the scenario $\Delta_c = \Delta_s$ where the radiation channels are equivalent and instead of the needle the structure supports BIC lines of existence.

the range of ϕ for which the needle exists since under variation of optic axes orientation, the needle BIC point keeps existing unless it falls off

the mode cutoff. Note that in the four cases shown in Fig. 4.7(a)-(d), the BIC position is never symmetric about $\phi = 90°$ since azimuthal anisotropy symmetry is broken and $\Delta_c \neq \Delta_s$. It is obvious from these plots that the needle can exist for a large range of values of ϕ and D/λ. Fig. 4.7(e) shows the locus of the needle in the $\phi - D/\lambda$ space as a function of variation of Δ_c with $\Delta_s = 0°$. The locus of the BIC is symmetric about $\phi = 90°$ as the substrate optic axis remained aligned with the film optic axis. Fig. 4.7(f) shows the locus when we set a value of $\Delta_s = 10° \neq 0°$. The symmetry of the locus is broken, allowing us to tune the needle locus for a greater range of D/λ when Δ_c is changed. The needle only stops existing when it moves beyond the cutoff of the fundamental semi-leaky mode on which it exists (extreme values of Δ_c in the figures), showing its robustness against perturbations.

We should note that there are other needles that occur at different values of ϕ and D/λ, both on the fundamental semi-leaky mode and on higher order leaky modes. However, these other needles can be found at much higher values of D/λ, often more than 2 octaves beyond. Therefore, the needle shown is the only bound mode supported by the structure for any practical operation range of wavelengths.

Asymmetry due to Refractive Indices

We began our study of BICs in structures with two radiation channels by selecting a symmetric anti-guiding waveguide with identical materials in the cover and the substrate. We have seen that when the structure is mirror symmetric about $x = 0$, the radiation channels are identical and the structure supports leaky modes with lines of BIC existence on those leaky mode sheets (see Figs. 4.3 and 4.4). Breaking the mirror symmetry of the structure by having different optic axes orientations in the cover and the substrate lead to the BIC lines collapsing to a single BIC point that we term a needle (see Figs. 4.5, 4.6, and 4.7).

We shall now make a short detour to study the result of breaking the symmetry in another way. It is also possible to break the mirror symmetry about $x = 0$ by having different materials in the cover and the substrate even if the optic axes orientations in the cover and substrate are identical ($\Delta_c = \Delta_s$). We consider the scenario where we have different materials in the cover and the substrate ($n_{ec} = 1.3 \neq n_{es} = 1.25; n_{os} = n_{oc} = 2$). With full anisotropy-

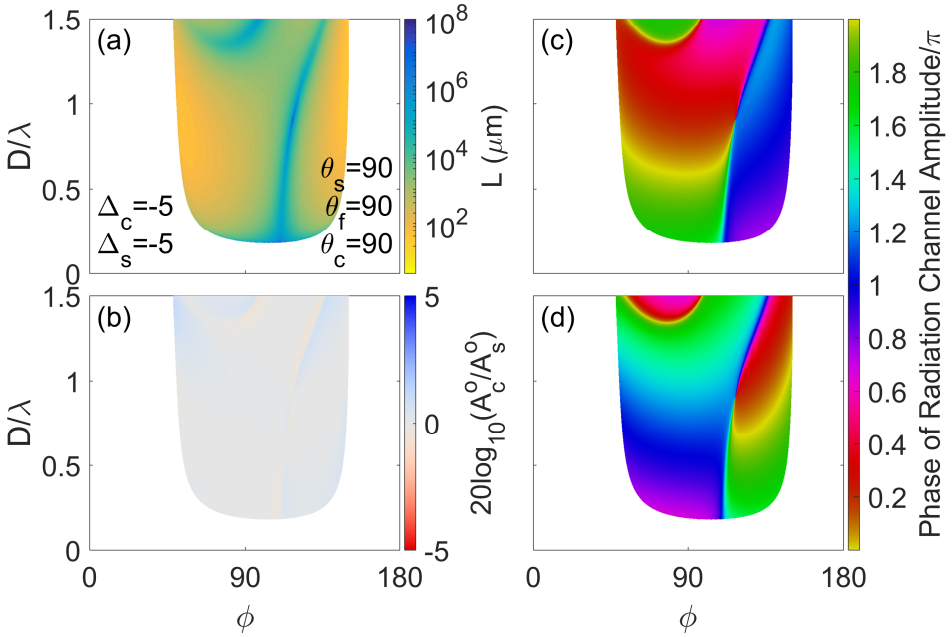

Fig. 4.8: Same as Fig. 4.5 but for a structure with different materials in the cover and substrate ($n_{ec} = 1.3 \neq n_{es} = 1.25$).

symmetry ($\Delta_c = \Delta_s = 0°$ and $\theta_c = \theta_f = \theta_s = 90°$), this structure supports only a line of PS BICs at $\phi = 90°$ and no INT BICs. Therefore we consider a case where azimuthal anisotropy-symmetry has been broken but with identical offsets for the cover and substrate optic axes($\Delta_c = \Delta_s = -5°$). The optic axes orientations are the same as in the case studied in Fig. 4.4 but the radiation channels in the cover and the substrate are distinct due to different materials used. Consequently an added auxiliary condition has to be satisfied to obtain a BIC solution. Fig. 4.8(a) shows the fundamental leaky mode supported by the structure. We find that the BIC lines shown in Fig. 4.4(a) have collapsed to BIC points in Fig. 4.8(a). Echoes of the BIC lines of existence remain in the form of areas of low loss. Since the radiation channels are no longer equivalent, the energy leaking from the mode is unequal in the two channels and this is shown in Fig. 4.8(b). Compared to the cases shown in Figs. 4.5(b) and 4.6(b) where asymmetry arises due to optic axis orientation, the asymmetry of radiation in the two channels is much lesser in this case where the asymmetry arises due to different materials being used in the cover and the substrate.

Figs. 4.8(c) and (d) shows the phase maps of the radiation channel amplitudes in the cover and substrate, respectively. Once again, we see that the BIC point is characterised by screw phase dislocations in both channels and opposite winding numbers can be assigned to the phase singularity in the cover (+1, clockwise increase) and substrate (−1, counter clockwise increase).

Thus we have seen that in general, having two distinct radiation channels leads to the reduction in dimension of the BIC solutions from lines to isolated, discrete points on the leaky mode sheet. This can be explained by the requirement that an additional auxiliary condition, corresponding to the additional channel, has to be satisfied in order that a BIC may exist. We also find that distinct radiation channels results in different amounts of radiation leaking from the mode in the different radiation channels.

4.2.2 Polar Anisotropy-Symmetry Breaking

We have so far only studied azimuthal anisotropy-symmetry breaking in this structure. However, we know from our study of structures with a single radiation channel that polar anisotropy-symmetry breaking can also introduce interesting features. In this section, therefore, we will study the impact of polar anisotropy-symmetry breaking in this anti-guiding structure. We start by moving the film optic axis out of the interface plane. Fig. 4.9(a) shows the fundamental semi-leaky mode for the structure when the film optic axis makes a polar angle $\theta_f = 85°$ with the normal to the interface. The other optic axes remain parallel to the interface plane ($\theta_c = \theta_s = 90°$) and azimuthal anisotropy-symmetry is not broken ($\Delta_c = \Delta_s = 0°$). Though the materials and the optic axis orientation in the cover and substrate are identical, the structure is no longer mirror symmetric about the $x = 0$ plane since the optic axis of the film is no longer parallel to that plane ($\theta_f = 85°$). We find in Fig. 4.9(a) that the fundamental leaky mode only supports an isolated INT BIC point at $\phi = 90°$ and $D/\lambda \approx 1.434$ and not lines of BICs. This is in keeping with what we have learnt in the previous section. The structure also supports other BIC points at higher values of D/λ.

As expected, the radiation into the two channels is distinct, but we now see a qualitative difference in the ratio of the radiation channel amplitudes shown in Fig. 4.9(b). The blue and red lines indicate

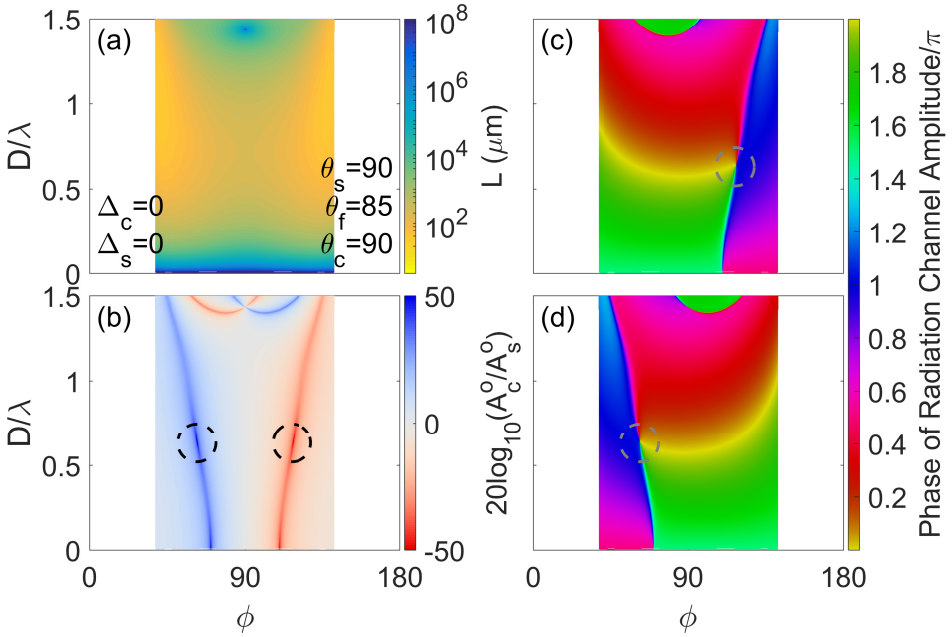

Fig. 4.9: Same as Fig. 4.3 but for a structure with polar anisotropy-symmetry breaking since the film optic axis is moved out of the interface plane ($\theta_f = 85°; \theta_c = \theta_s = 90°$). The dashed circles mark the UGRs. Note the change in color scale in (b).

strongly asymmetric radiation (note the change in limits of the color scale) to the cover and the substrate, respectively. Moreover, there are specific points in the $\phi - D/\lambda$ space, marked by dashed black circles in Fig. 4.9(b), where the ratio of the radiation channel amplitudes diverges. This is because at these points radiation into one channel is entirely canceled while all radiation escapes via the other channel. Such points have been termed unidirectional guided resonances [120]. Because $\Delta_c = \Delta_s = 0°$ in this case, the two UGRs occur at the same value of $D/\lambda = 0.643$, and at symmetric locations about $\phi = 90°$. The UGRs at $\phi = 62.09°$ and $\phi = 117.91°$ radiate to the cover and the substrate, respectively. From the color scale of Fig. 4.9(a) which indicates the $1/e$ propagation length of the mode, L, we can see that radiation losses do not decrease at the UGRs. Therefore, the UGR in one radiation channel results in the deviation of all the radiation to the opposite channel on the leaky mode.

Fig. 4.9(c) and (d) show the phase maps of the radiation channel amplitudes in the cover and the substrate. The discrete BIC point at

$\phi = 90°$ and $D/\lambda \approx 1.434$ corresponds to opposite screw phase dislocations in the cover and the substrate radiation channel amplitudes. This is however, only obvious upon zooming in and has not been shown in Fig. 4.9(c) and (d). We focus instead on a more interesting feature in these plots. The grey dashed circles in (c) and (d) show points on the leaky mode sheet in the $\phi - D/\lambda$ space where there is a phase singularity and a screw phase dislocation in only one of the radiation channels and not in the other. We know that the phase singularity arises due to a zero in the radiation channel amplitude. Therefore, we now see that there are zeroes of the radiation channel amplitude at different points in the $\phi - D/\lambda$ space for the two radiation channels. Therefore, at these points the leaky mode loses energy only via one radiation channel. These points correspond to the UGRs marked by the dashed black circles in Fig. 4.9(b). The phase singularity in the cover radiation channel in Fig. 4.9(c) at $D/\lambda = 0.643$ and $\phi = 117.91°$ means that there is no radiation to the cover at that point and therefore we have a UGR radiating exclusively to the substrate at the point on the leaky mode sheet. The phase singularity in the substrate radiation channel at $D/\lambda = 0.643$ and $\phi = 62.09°$ shown in Fig. 4.9(d) means there is no radiation to the substrate at that point and therefore we have a UGR radiating exclusively to the cover. This is confirmed by the plot of the ratio of the radiation channel amplitudes shown in 4.9(b). The singularities in the cover and the substrate can be assigned opposite winding numbers because the phase of the radiation channel amplitude on the leaky mode sheet grows clockwise $(+1)$ in the cover and counter clockwise (-1) in the substrate.

We have studied the BICs and UGRs supported by the structure using leaky modes. Leaky modes are improper modes in that they are not proper solutions of Maxwell's equations. They are a convenient approximation and are only accurate in the vicinity of the waveguide. However, UGRs are modes that have energy radiating from the waveguide. Therefore, to verify our results we study UGRs using the FDTD method [133] using the open source implementation of the FDTD method contained in the MEEP package [148]. This FDTD calculation demonstrating the dynamics of the UGR is shown in Fig. 4.10 for the structure with polar anisotropy-symmetry breaking that we have just studied with $\theta_f = 85°$ (see Fig. 4.9). The UGR radiating only to the cover with $\phi = 62.09°$ and $D/\lambda = 0.643$ (left circle in Fig. 4.9(b)) is shown in Fig. 4.10(a), resulting in radiation to the cover. Fig.

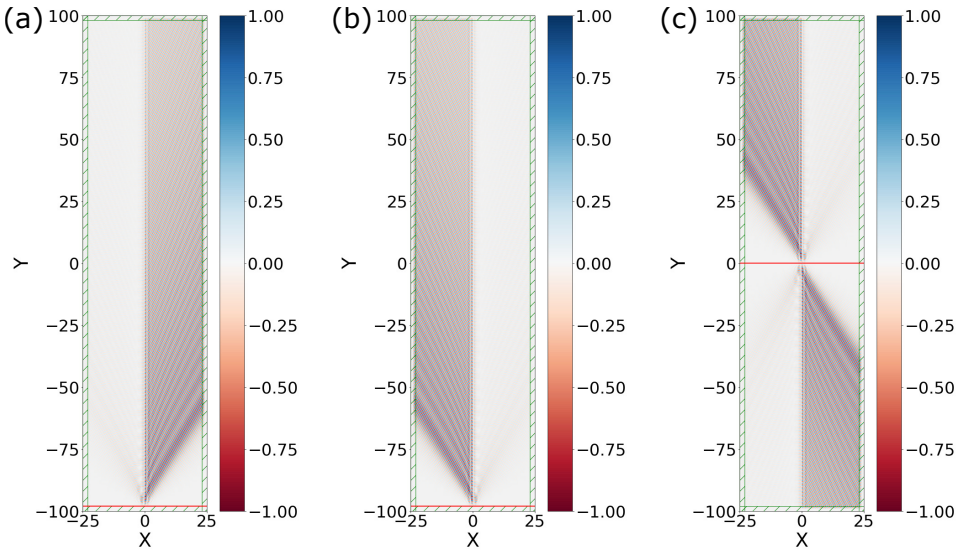

Fig. 4.10: FDTD calculation of UGRs, showing the z-component of the magnetic field (H_z), in a structure with only polar anisotropy symmetry breaking ($\theta_f = 85°; \theta_c = \theta_s = 90°$ and $\Delta_c = \Delta_s = 0°$) for $D/\lambda = 0.643$ and (a) $\phi = 62.09°$ and (b-c) $\phi = 117.91°$. (a) and (b) correspond to forward propagation with radiation into the cover and substrate, respectively. (c) Simultaneous forward and backward propagation. The Y propagation distance is normalized relative to the wavelength.

4.10(b) shows the UGR radiating only to the substrate at $\phi = 117.91°$. Fig. 4.10(c) shows the scenario where the structure is excited in the centre with both forward and backward propagation with $\phi = 117.91°$. For forward propagation, in the $+y$ direction, the situation does not change, and radiation goes to the substrate, as in Fig. 4.10(b). A change of propagation direction to $-y$ results in radiation going to the cover, as the situation is equivalent to having $\phi = 62.09°$ or orienting the film OA at $\theta_f = 95°$. This ease of switching the radiation direction is a characteristic of UGRs in anisotropic planar structures. Moreover, while leaky waveguides can also have perfectly unidirectional radiation, they forbid radiation in the other direction using total internal reflection (arising from the refractive index constrast) and therefore cannot allow switching of the radiation direction without flipping the entire system. Note that in the FDTD calculations, we use the eigenmode source provided by MEEP, which does not exactly match the improper

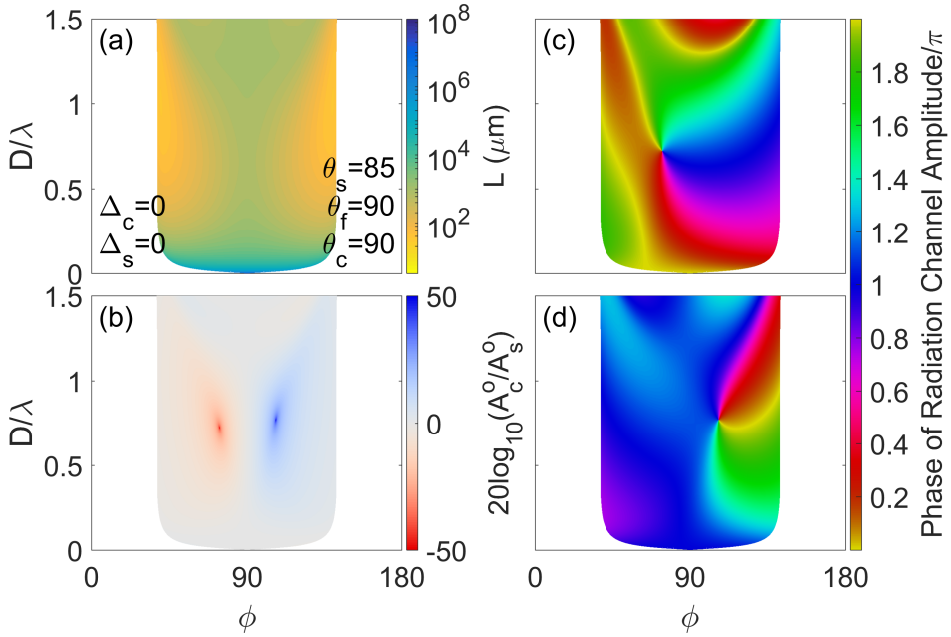

Fig. 4.11: Same as Fig. 4.9 but for a structure where polar anisotropy-symmetry is broken by moving the substrate optic axis out of the interface plane ($\theta_s = 85°; \theta_c = \theta_f = 90°$).

leaky mode, resulting in some reshaping during propagation.

Since the structure being studied has three optic axes, there are multiple other ways that polar anisotropy-symmetry can be broken. We shall now study a few of these cases. Fig. 4.11(a) shows the fundamental leaky mode in the scenario where only the substrate optic axis has been moved out of the interface plane ($\theta_s = 85°$) while the film and cover optic axes remain in the interface ($\theta_c = \theta_f = 90°$). Azimuthal anisotropy-symmetry is maintained ($\Delta_c = \Delta_s = 0°$). In this scenario we see that while there are low loss areas on the fundamental leaky mode that are reminiscent of the lines of BICs in Fig. 4.3, there are no BICs at any point. The radiation channels are distinct since the structure is not symmetric about the $x = 0$ plane and we find that UGRs do exist in this configuration as shown in Fig. 4.11(b). We see though, that the distribution of the UGRs is no longer symmetric about $\phi = 90°$ even though azimuthal anisotropy-symmetry is maintained. The unidirectional radiation is concentrated around the UGRs and we do not have areas of largely unidirectional radiation compared to the case shown in Fig. 4.9. As before, we find that the UGRs correspond

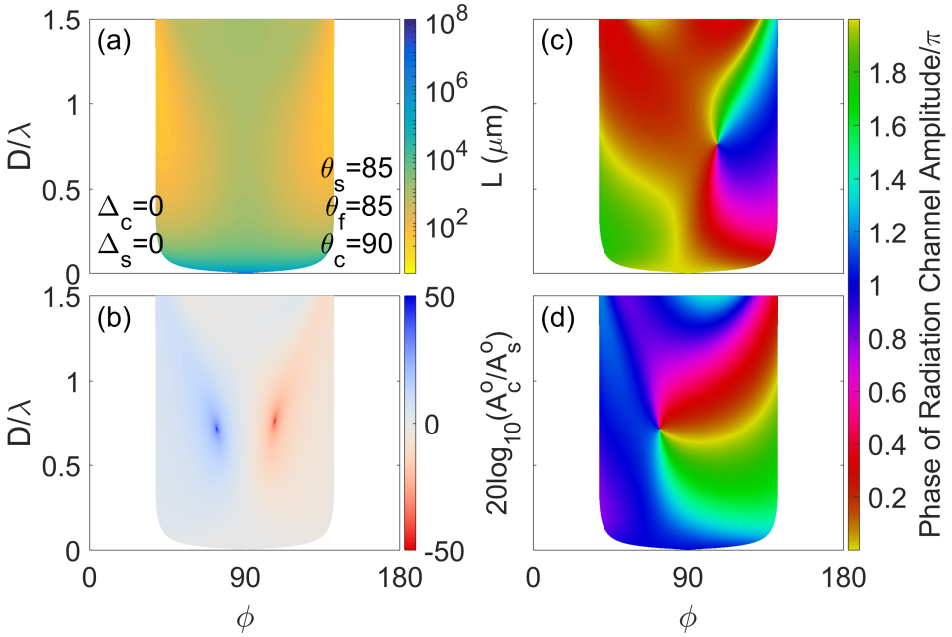

Fig. 4.12: Same as Fig. 4.9 but for a structure where polar anisotropy-symmetry is broken by moving the film and the substrate optic axes out of the interface plane while keeping them parallel ($\theta_s = \theta_f = 90°$).

to zeroes of the radiation channel amplitude in only one channel while radiating in the other channel. Therefore, the UGR radiating to the substrate (at $\phi < 90°$) corresponds to a phase singularity and a screw phase dislocation in the cover radiation channel shown in Fig. 4.11(c). The other UGR, radiating to the cover at $\phi > 90°$ corresponds to a phase singularity in the substrate radiation channel shown in Fig. 4.11(d). Since the cover and the substrate materials are identical, the impact of moving only the cover optic axis out of the interface plane ($\theta_c \neq 90°$) while keeping the core and substrate optic axis in the interface plane would have a similar impact, but the position of the UGRs radiating to the cover and the UGR radiating to the substrate would be swapped. The singularities in the cover and the substrate can be assigned the same winding number -1 due to counter clockwise phase increase.

Thus far we have studied polar anisotropy-symmetry breaking in structures with only one optic axis moved out of the interface plane. However, it would also be possible to move more than one optic axis

out of the interface plane simultaneously. Fig. 4.12(a) shows the fundamental leaky mode in such a configuration where both the film and the substrate optic axes are moved out of the interface plane ($\theta_f = \theta_s = 85°$) while the cover refractive index remains in the interface plane ($\theta_c = 90°$). Azimuthal anisotropy-symmetry is maintained. There are no BICs supported on the fundamental leaky mode as shown on Fig. 4.12(a). The profile of losses is the same as what we saw in Fig. 4.11(a) but this is because the relative orientations of the optic axes are similar. However, since now the film optic axis has been moved out of the interface plane, we find that the positions of the UGRs are swapped in Fig. 4.12(b) compared to Fig. 4.11(b). The UGR radiating to the cover is now located at $\phi < 90°$ while the UGR radiating to the substrate is located at $\phi > 90°$. The UGRs correspond to phase singularities in the phase maps of the radiation channels into which they do not radiate as shown in Figs. 4.12(c) and (d). The singularities in the cover and the substrate can be assigned the same winding number -1 due to counter clockwise phase increase.

In Fig. 4.12 we studied the case where the film and substrate optic axes are both taken out of the interface plane but they were parallel. Now we shall study the scenario where they are oriented in different directions. Fig. 4.13(a) shows the fundamental leaky mode in such a configuration where both the film and the substrate optic axes are moved out of the interface plane ($\theta_f = 85°, \theta_s = 95°$) while the cover refractive index remains in the interface plane ($\theta_c = 90°$). Azimuthal anisotropy-symmetry is maintained. We see once again that there are no BICs on the fundamental leaky mode. The low loss areas are also not as pronounced. We see in Fig. 4.13(b) that once again, polar-anisotropy symmetry breaking leads to the formation of UGRs on the leaky mode sheet. Here we see that the UGR at $\phi < 90°$ radiates to the cover while the UGR at $\phi > 90°$ radiates to the substrate. There are also regions of highly unidirectional radiation adjacent to the UGR. We see in Figs. 4.13(c) and (d) that, as expected, the UGRs correspond to phase singularities with integer winding numbers in the radiation channel in which they do not radiate. The singularities in the cover and the substrate can be assigned the same winding number $+1$ due to clockwise phase increase.

We now shift our focus to a scenario where the cover and the substrate optic axes are moved out of the interface plane while the film optic axis remains in the interface plane ($\theta_f = 90°$). First we

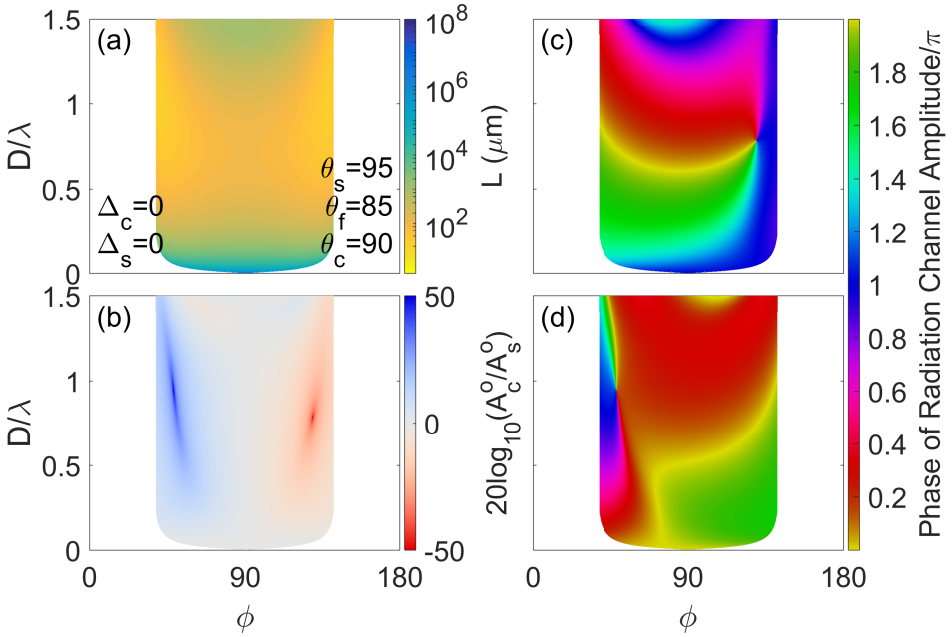

Fig. 4.13: Same as Fig. 4.12 but for a structure where polar anisotropy-symmetry is broken by moving the substrate and the film optic axes out of the interface plane and they are no longer parallel ($\theta_f = 85°; \theta_s = 95°$).

study a structure where the film and substrate optic axes are parallel ($\theta_s = \theta_c = 85°$). Fig. 4.14(a) shows the leaky mode supported by the structure with a discrete point BIC. This is identical to the leaky mode shown in Fig. 4.9(a). This is again because the relative orientations of the structures are similar. However, unlike the case studied in Fig. 4.9 it is now only the film optic axis that remains parallel to the interface plane and therefore we find that the positions of the UGR radiating to the cover and the UGR radiating to the substrate are swapped in Fig. 4.14(b) compared to Fig. 4.9(b). Again, each UGR corresponds to a phase singularity due to zero amplitude in the phase map of the radiation channel where radiation is cancelled. The singularities in the cover and the substrate can be assigned opposite winding numbers.

Fig. 4.15 shows the case when polar anisotropy-symmetry is broken by taking the cover and the substrate optic axes out of the interface plane with different orientations. In fact, the orientations of the cover and substrate optic axes are such that the structure is mirror symmetric ($\theta_s = 90° - 5°; \theta_c = 90° + 5°$). Azimuthal anisotropy-symmetry is

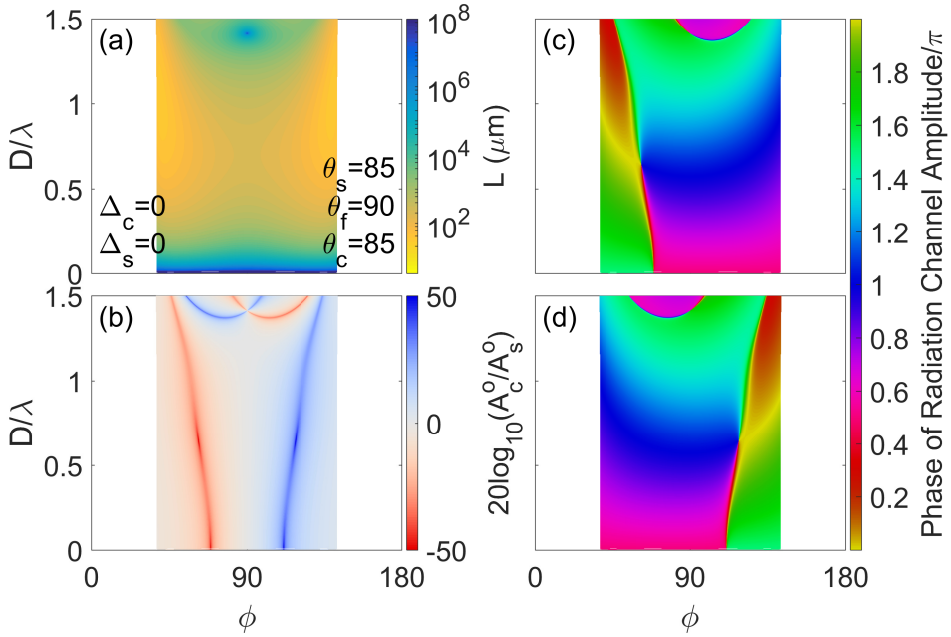

Fig. 4.14: Same as Fig. 4.9 but for a structure where polar anisotropy-symmetry is broken by moving the substrate and the cover optic axes out of the interface plane and keeping them parallel ($\theta_c = \theta_s = 95°$).

maintained. In such a scenario we find that the fundamental leaky mode supports only a discrete BIC point instead of lines of BICs as shown in Fig. 4.15(a). However, this is because polar anisotropy-symmetry is broken and this leads to the collapse of BIC lines to BIC points (as seen in section 3.2) and not due to the added constraint of an extra auxiliary condition due to a second radiation channel. Since the radiation channels are symmetric, the radiation into the two channels is identical throughout the leaky mode sheet and this is shown in Fig. 4.15(b). We see from the phase maps in Fig. 4.15(c) and (d) that the BIC corresponds to zeroes of radiation and corresponding phase singularities in the radiation channel amplitudes of the cover and the substrate. The singularities in the cover and the substrate can be assigned the same winding numbers (-1) since the phase grows counter clockwise both in the cover and in the substrate.

We now focus on a scenario where all three optic axes have been moved out of the interface plane. Fig. 4.16 shows the scenario where polar anisotropy symmetry has been broken and all three optic axes

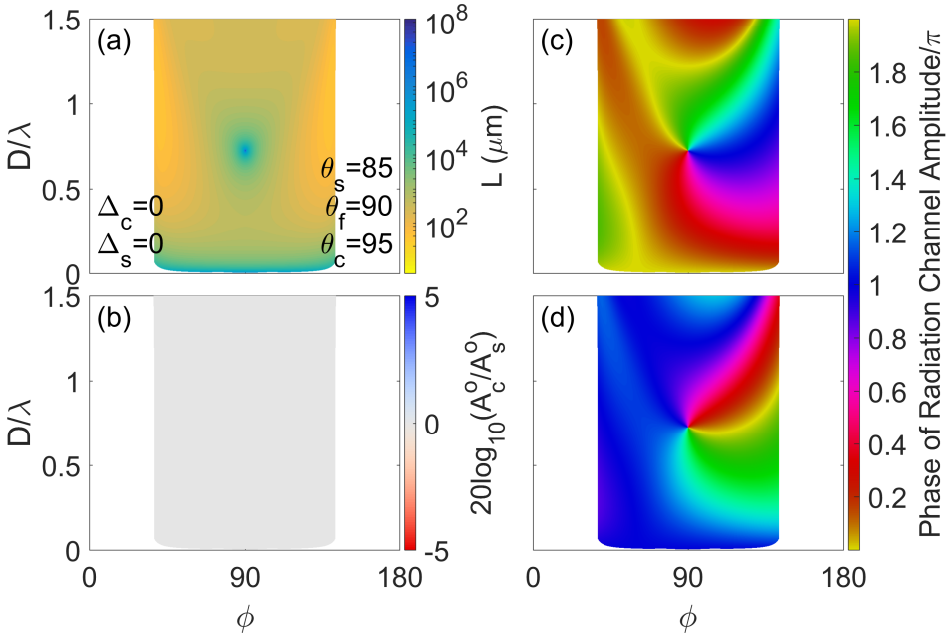

Fig. 4.15: Same as Fig. 4.9 but for a structure where polar anisotropy-symmetry is broken by moving the substrate and the cover optic axes out of the interface plane but they are no longer parallel ($\theta_s = 85°; \theta_c = 95°$). Note the change in scale in (b).

have been moved out of the interface while keeping them parallel to each other ($\theta_c = \theta_f = \theta_s = 85°$). Azimuthal anisotropy symmetry is maintained. In this scenario, the radiation channels are not equal. We see in Fig. 4.16(a) that the BIC lines have collapsed to a single discrete BIC point. There are areas of low loss on the leaky mode sheet that are reminiscent of the BIC lines from Fig. 4.3(a). In Fig. 4.16(b) we see that there are lines of strongly unidirectional radiation that appear. In fact, the lines of strongly unidirectional radiation trace paths that are adjacent to the BIC lines from the fully anisotropy-symmetric case shown in 4.3(a). However, the entirety of these lines does not correspond to zeroes of radiation since polar anisotropy-symmetry has been broken. Therefore, there are zeroes of radiation in both channels at the BIC point and there are zeroes of radiation in individual channels at discrete UGR points. The UGR radiating to the substrate is located near the bottom of the red curve at high values of D/λ and $\phi < 90°$. The UGR radiating to the cover is located near the bottom of the blue curve at high values of D/λ and $\phi > 90°$. The phase map of the ra-

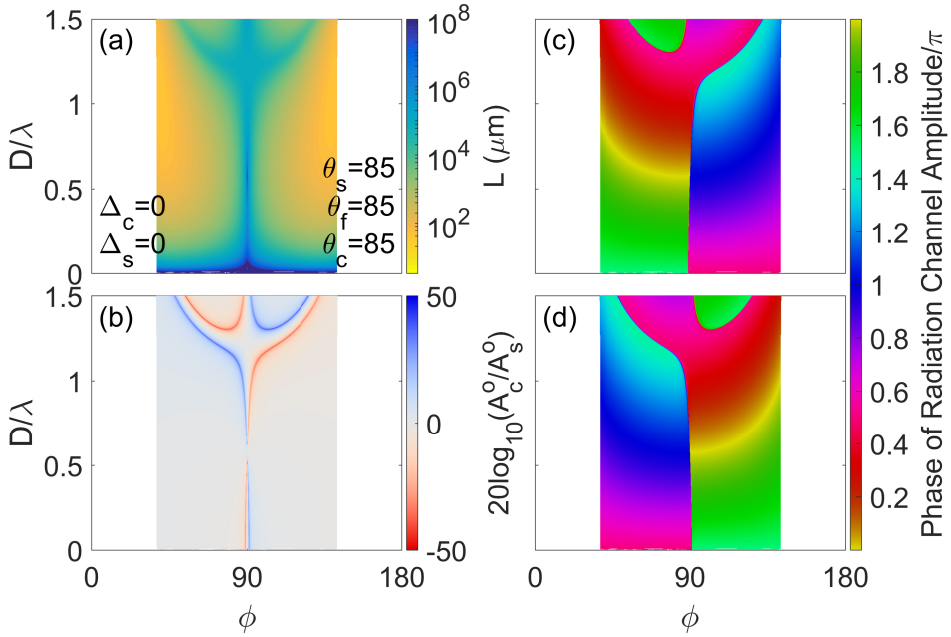

Fig. 4.16: Same as Fig. 4.9 but for a structure where polar anisotropy-symmetry is broken by moving moving all three optic axes out of the interface plane while keeping them parallel to each other ($\theta_c = \theta_f = \theta_s = 85°$).

diation channel amplitudes in the cover and the substrate are shown in 4.16(c) and (d), respectively. We see that the phase singularity at the BIC point can be assigned opposite winding numbers in the cover ($+1$, clockwise increase) and the substrate (-1, counter clockwise increase). The phase singularities corresponding to the UGRs are only visible upon zooming in (not shown).

Fig. 4.17 shows the scenario where the configuration is changed so that while all three optic axes are outside the interface plane, all three are no longer parallel to each other. The cover and the substrate optic axis remain parallel to each other ($\theta_c = \theta_s = 85°$), while the film optic axis is inclined at a different angle ($\theta_f = 89°$). Azimuthal anisotropy-symmetry is maintained. We see that the mode shown in Fig. 4.17(a) resembles the mode shown in Fig. 4.9(a). This is due to the fact that the relative orientations of the optic axes are similar, even though in this case the optic axes have been moved out of the interface. The structure is no longer mirror symmetric about $x = 0$, meaning the radiation channels are distinct and this leads to the BIC

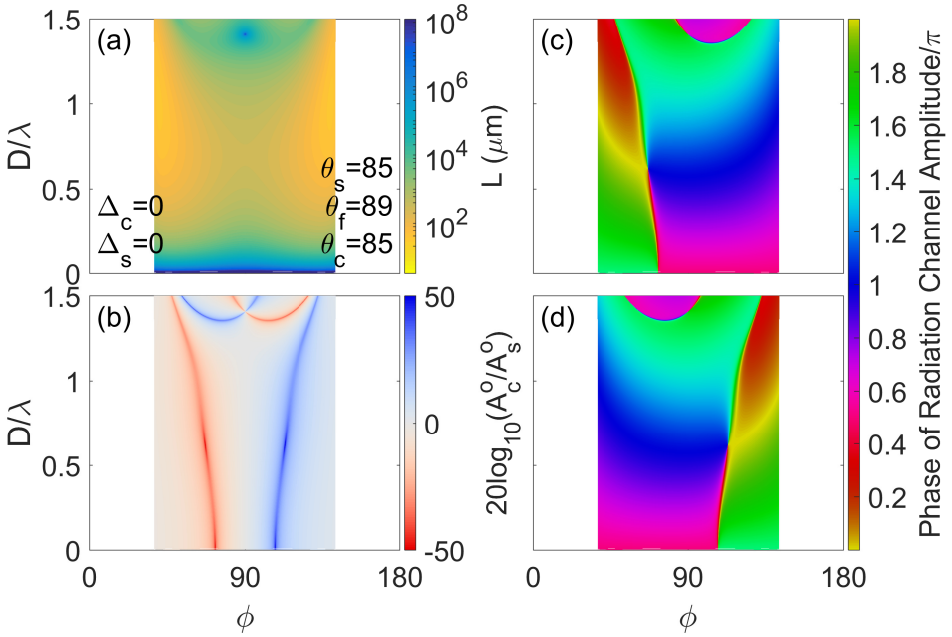

Fig. 4.17: Same as Fig. 4.9 but for a structure where polar anisotropy-symmetry is broken by moving all three optic axes out of the interface plane. The cover and substrate optic axis remain parallel to each other ($\theta_c = \theta_s = 85°$), while the film optic axis is oriented at a different polar angle ($\theta_f = 89°$).

line collapsing to a discrete BIC point due to the added constraint of a second auxiliary condition. Fig. 4.17(b) shows that there are lines of strongly unidirectional radiation on the leaky mode sheet, and there are specific points, the UGRs, where the ratio of radiation diverges. The placement of the UGRs in this case is opposite to what we saw in Fig. 4.9(b) where only the film optic axis had been moved out of the interface plane. We find in Fig. 4.17(b) that the UGR radiating to the substrate is located in the region where $\phi < 90°$ while the UGR radiating to the cover is located in the region where $\phi > 90°$. The phase maps of the radiation channel amplitudes in the cover and the substrate shown in Fig. 4.17(c) and (d) show that the UGRs correspond to phase singularities that can be assigned opposite winding numbers. The BIC also corresponds to phase singularities that are only visible upon zooming in (not shown).

Finally, we study the case where all three optic axes have been moved out of the interface plane and none of them are parallel to each

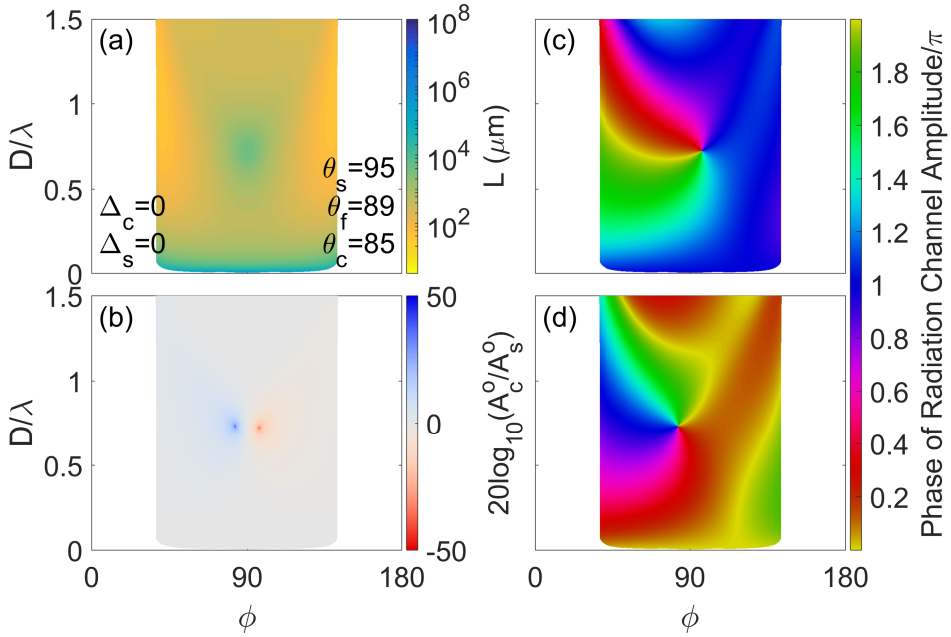

Fig. 4.18: Same as Fig. 4.9 but for a structure where polar anisotropy-symmetry is broken by moving all three optic axes out of the interface plane. The optic axes are all oriented at different polar angles ($\theta_c = 85° \neq \theta_f = 89° \neq \theta_s = 95°$).

other ($\theta_c = 85° \neq \theta_f = 89° \neq \theta_s = 95°$). Azimuthal anisotropy-symmetry is maintained. The structure is not symmetric about $x = 0$ and therefore the radiation channels are distinct. In such a scenario, we see in Fig. 4.18(a) that the fundamental leaky mode does not support any BICs at all. We see in Fig. 4.18(b) that the structure does support UGRs radiating to the cover and the substrate. However, there are no lines of strongly unidirectional radiation that we have seen previously. These UGRs correspond to zeroes of radiation in only one radiation channel and we see that there are phase singularities at the corresponding position in the phase map of the radiation channel amplitude. The UGR radiating to the cover exists at $\phi < 90°$ and corresponds to a singularity in the phase of the substrate radiation channel amplitude which can be assigned a winding number +1 since the phase increases clockwise. The UGR radiating to the substrate, on the other hand, exists at $\phi > 90°$ and corresponds to a singularity in the phase of the cover radiation channel amplitude which can also be assigned the same winding number since the phase increases clockwise

here as well.

In this section, as in the previous section, we have seen that breaking the mirror symmetry about $x = 0$ leads to distinct radiation channels and a reduction in the dimension of the BIC solution from lines to points. In addition, we have seen that breaking polar anisotropy-symmetry leads to the formation of UGRs where radiation is only cancelled in one of the two available channels. The only exception is the case shown in Fig. 4.14 where polar anisotropy-symmetry is broken but the structure remains mirror symmetric about $x = 0$ and therefore, there are no UGRs. However, even though the radiation channels are identical, the polar anisotropy-symmetry breaking results in the BIC lines collapsing to a single discrete point just as we have seen in section 3.2. At the UGRs energy is radiated away from the mode via one channel while there is a zero of the radiation channel amplitude in the other channel. This zero in the radiation channel amplitude corresponds to a phase singularity in the phase map of that amplitude and it can be assigned a winding number based on how the phase increases around the singularity. Thus far, we have always seen the UGRs occur on the leaky mode sheet in pairs, one radiating to the substrate and the other to the channel. The UGRs are characterised by phase singularities with opposite winding numbers in the cover and substrate singularities when the substrate and cover optic axes are parallel ($\theta_c = \theta_s$). They have the same winding number when those optic axes are not parallel ($\theta_c \neq \theta_s$).

4.2.3 Both Polar and Azimuthal Anisotropy-Symmetry Breaking

We shall now focus on the scenario where both polar and azimuthal anisotropy-symmetry are simultaneously broken for the waveguide that we have been studying. Fig. 4.19(a) shows the mode when polar anisotropy-symmetry has been broken by moving only the film optic axis out of the interface plane ($\theta_f = 85°$, $\theta_c = \theta_s = 90°$). Azimuthal anisotropy-symmetry has also been broken with opposite offsets for the cover and the substrate optic axes with respect to the projection of the film optic axis in the interface plane ($\Delta_s = -\Delta_c = 5°$). We have already studied these two exact methods of anisotropy-symmetry breaking earlier in the chapter. This way of breaking polar anisotropy-symmetry has been studied in Fig. 4.9 and this way of breaking the

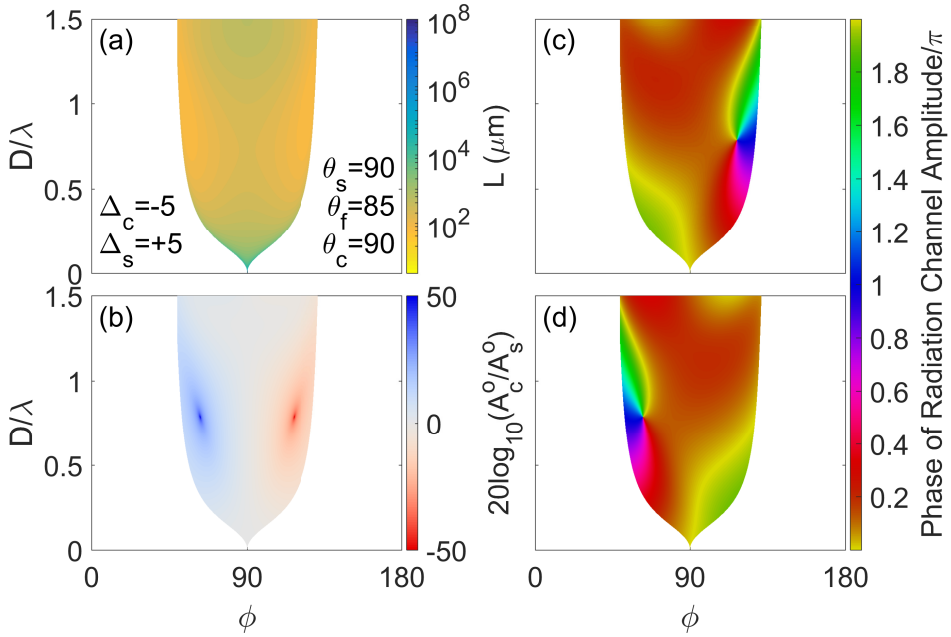

Fig. 4.19: Same as Fig. 4.9 but for a structure where in addition to polar anisotropy-symmetry breaking ($\theta_f = 85$), azimuthal anisotropy symmetry is also broken ($\Delta_s = -\Delta_c = 5°$).

azimuthal anisotropy-symmetry has already been studied in Fig. 4.6. We shall now study the situation when both of these are combined. We find in Fig. 4.19(a) that the fundamental leaky mode does not support any BICs. This is distinct from what we have seen in Figs. 4.6 and 4.9. Therefore, combining the two methods of anisotropy-symmetry breaking leads to the BIC disappearing. However, we see in Fig. 4.19(b) that the mode does support UGRs. While there are no lines of strongly unidirectional radiation to be found on the leaky mode sheet, we find a UGR radiating to the cover and another radiating to the substrate that are distributed symmetrically about $\phi = 90°$ on the leaky mode sheet at the same value of D/λ. In fact, changing the value from $\theta_f = 85°$ to $\theta_f \to 90°$ results in the two UGRs approaching each other till at $\theta_f = 90°$, with polar anisotropy-symmetry restored, they coincide in D/λ at $\phi = 90°$ and result in the BIC that is shown in Fig. 4.6(a). We see in the phase map shown in Fig. 4.19(c) and (d) that the UGRs correspond to phase singularities with opposite winding number in the cover and substrate radiation channel amplitudes.

Thus we find that combining polar and azimuthal anisotropy-symmetry

breaking leads to the BIC disappearing while the UGRs survive. The UGRs can be characterised by the phase singularities and are robust.

4.2.4 Impact of the Auxiliary Condition

We have studied this structure with two radiation channels that can support both BICs and UGRs. As outlined in section 4.1.2, we analyse this structure using auxiliary conditions that require that radiation into one of the radiation channels is cancelled. When the solution of only one auxiliary condition and the dispersion equation coincides, we obtain a UGR. When the solution of both auxiliary conditions and the dispersion equation coincides, we obtain a BIC. In this section we shall study the interplay of these solutions.

The auxiliary conditions for the two radiation channels of this waveguide have been defined in section 4.1.2 in eqs. 4.7 and 4.8. Each condition involves a homogeneous system of four linear equations with only three unknown variables. Since we are only interested in the non-trivial solution, it requires that the determinant of any 3×3 sub-matrix of the 4×3 coefficient matrix of the auxiliary condition system of equations must be zero. There are four possible determinants that can be selected and therefore the solution of the auxiliary condition corresponds to points where the roots of these determinants intersect in the $N-\phi$ space, where $N = k_y/k_0$ is the normalised mode propagation constant. Since we are interested in the points where the solutions of the auxiliary condition and the dispersion equation coincide, we define a metric Q_{aux} such that

$$Q_{aux} = \sqrt{\sum_{i=1}^{4} |N_{disp} - N_{aux}^{i}|^2}, \tag{4.10}$$

where N_{disp} refers to the solution of the dispersion equation and N_{aux}^{1-4} refers to the zeroes of the four determinants arising from one of the auxiliary conditions. The metric Q_{aux} measures the total distance between the five solutions. Since we have two auxiliary conditions corresponding to the two radiation channels, we would have two metrics Q_{aux}^{sub} and Q_{aux}^{cov} where the superscript indicates the radiation channel into which radiation is cancelled. Thus, the points where $Q_{aux}^{sub} = 0$, we would have radiation in the substrate radiation channel being cancelled whereas when $Q_{aux}^{cov} = 0$, radiation in the cover radiation channel would

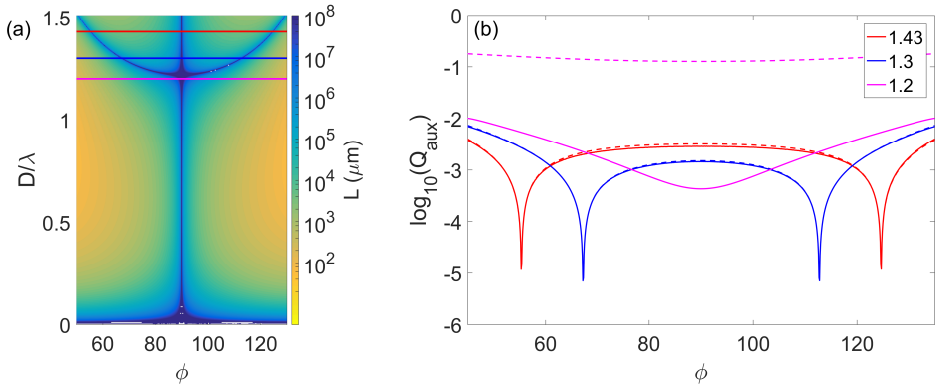

Fig. 4.20: (a) The fundamental leaky mode for the waveguide discussed in section 4.1 when full anisotropy-symmetry is maintained. (b) Line plots showing Q_{aux} as a function of ϕ for $D/\lambda = 1.43$ (red), $D/\lambda = 1.30$ (blue) and $D/\lambda = 1.20$ (magenta). The solid line corresponds to Q_{aux}^{sub} whereas the dashed line corresponds to Q_{aux}^{cov}. The coloured lines in (a) serve as visual guides for the values of D/λ for which Q_{aux} is calculated.

be cancelled. When both both $Q_{aux}^{sub} = 0$ and $Q_{aux}^{cov} = 0$, we would have radiation in both cover and substrate radiation channels being cancelled, leading to BICs.

Fig. 4.20(a) shows the mode for the waveguide structure with full anisotropy-symmetry that we have seen previously in Fig. 4.3(a). The colored lines show the values of D/λ at which we study the interplay of the dispersion equation and auxiliary conditions. Fig. 4.20(b) shows the values of Q_{aux} at those values of D/λ for this structure. The solid lines show Q_{aux}^{sub} whereas the dashed lines show Q_{aux}^{cov}. We find that at $D/\lambda = 1.43$ (red lines), both $Q_{aux}^{sub} = 0$ and $Q_{aux}^{cov} = 0$ at $\phi = 55.3°$ and at $\phi = 124.7°$. Therefore we expect to find INT BICs at those points and that is what we find in Fig. 4.20(a). Shifting to $D/\lambda = 1.3$ (blue lines), we find that once again the zeroes of Q_{aux}^{sub} and Q_{aux}^{cov} coincide but now these points have shifted closer to each other at $\phi = 67.2°$ and $\phi = 112.8°$, and we see exactly the same in Fig. 4.20(a). Moving to an even lower value of $D/\lambda = 1.2$ (magenta lines), we see that there is no value of ϕ at which either Q_{aux}^{sub} or Q_{aux}^{cov} equal zero and therefore we do not expect to find any INT BICs at that value of D/λ. This is borne out in Fig. 4.20(a) since there is only a PS BIC at $\phi = 90°$ at $D/\lambda = 1.2$ and that arises due to geometric considerations leading to

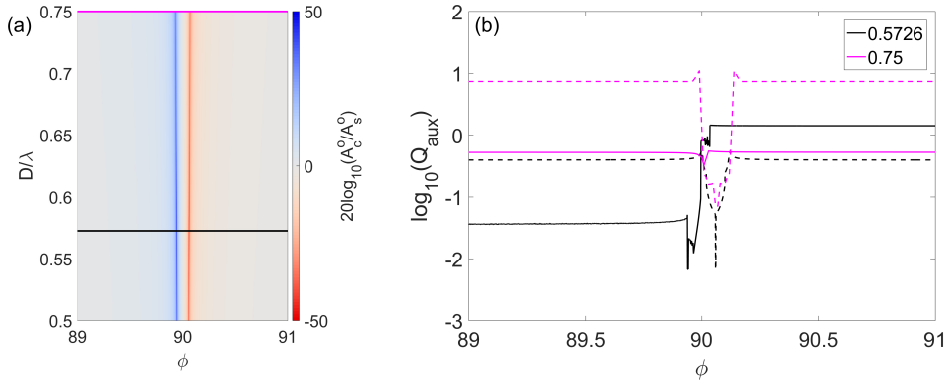

Fig. 4.21: (a) The ratio of radiation channel amplitudes in dB for a waveguide where polar anisotropy symmetry is broken by moving the film optic axis out of the interface plane ($\theta_f = 89.99$). (b) Line plots showing Q_{aux} as a function of ϕ for $D/\lambda = 0.5726$ (black) and $D/\lambda = 0.75$ (magenta). The solid line corresponds to Q_{aux}^{sub} whereas the dashed line corresponds to Q_{aux}^{cov}. The coloured lines in (a) serve as visual guides for the values of D/λ for which Q_{aux} is calculated.

orthogonal polarisations of the mode and the radiation channel and not from cancellation of radiation due to the auxiliary condition. Moreover, since we have studied the structure with full anisotropy-symmetry, the structure is symmetric about $x = 0$ and the radiation channels are equal. Therefore, there is no possibility of a UGR.

Fig. 4.21 shows the results of our study of a structure that is not mirror symmetric about $x = 0$. We now study a structure where polar anisotropy-symmetry is broken by moving the film optic axis out of the interface plane ($\theta_f = 89.99°$). The cover and substrate optic axes remain in the interface plane ($\theta_c = \theta_s = 90°$) and azimuthal anisotropy-symmetry is maintained ($\Delta_c = \Delta_s = 0°$). We find that even this very minor polar anisotropy-symmetry breaking leads to the formation of UGRs and areas of strongly asymmetric radiation on the leaky mode sheet, a part of which is shown in Fig. 4.21(a). The black lines in Fig. 4.21(b) correspond to $D/\lambda = 0.5726$. We find that the solid black line, corresponding to Q_{aux}^{sub}, goes to zero at $\phi = 89.94°$. However, the dashed black line, corresponding to Q_{aux}^{cov} does not go to zero at that value of ϕ. Therefore, at that value of ϕ, only radiation to the substrate is cancelled while radiation to the cover is allowed, meaning that the mode radiates in only the cover radiation channel and we

have a UGR radiating to the cover. This is borne out in Fig. 4.21(a). The dashed black line, on the other hand, goes to zero at $\phi = 90.06°$ and the solid black lines does not go to zero at that value of ϕ and therefore at that point we have radiation to the cover being cancelled and therefore we get a UGR radiating to the substrate. Shifting to $D/\lambda = 0.75$ (magenta lines), we find that neither Q_{aux}^{sub} nor Q_{aux}^{cov} go to zero at any value of ϕ even though there are small dips at some places. Therefore we do not have any UGRs at that value of D/λ. We see that even though we have areas of strongly unidirectional radiation as indicated by the red and blue lines in Fig 4.21(a), the radiation is perfectly unidirectional only at specific points in the $\phi - D/\lambda$ space where either $Q_{aux}^{sub} = 0$ or $Q_{aux}^{cov} = 0$.

Thus, we see in Fig. 4.20 that when polar anisotropy-symmetry and mirror symmetry about $x = 0$ is maintained, we get $Q_{aux}^{sub} = 0$ or $Q_{aux}^{cov} = 0$ at the same values of ϕ, leading to BICs. Moreover, as we change the value of D/λ, we see that the points where $Q_{aux}^{sub/cov}$ goes to zero shifts in ϕ till we get to a point where the BIC points merge at $\phi = 90°$ and then, at lower values of D/λ, there are no more points where $Q_{aux}^{sub/cov} = 0$. On the other hand, we see in Fig. 4.21, that when polar anisotropy-symmetry and mirror symmetry about $x = 0$ are broken in conjunction, it is possible that Q_{aux}^{sub} and Q_{aux}^{cov} can go to zero at different values of ϕ leading to UGRs. And in this scenario, any change in the value of D/λ leads to the value of Q_{aux} no longer going to zero. This same impact of polar anisotropy-symmetry breaking on the interplay of the solutions of the dispersion equation and auxiliary conditions has been seen earlier in section 3.2.5.

Summary

We shall now summarise what we have learnt about the existence of INT BICs and UGRs in waveguide structures comprising negative uniaxial materials with two radiation channels. Table 4.1 summarises the results of what we have studied so far where each row presents information about the symmetry configuration in the first three columns and the existence of INT BICs and UGRs in the two final columns. We find that it is the mirror symmetry about $x = 0$ and polar anisotropy-symmetry that have maximal impact on the existence of INT BICs and UGRs in this structure. The structure supports lines of INT BICs only when both mirror symmetry and polar anisotropy-symmetry are main-

Mirror	Azimuthal	Polar	INT BICs	UGRs
Yes	Yes	Yes	Line	No
No	Yes	Yes	Point	No
Yes	No	Yes	Line	No
No	No	Yes	Point	No
Yes	Yes	No	Point	No
No	Yes	No	Point or none	Yes
No	No	No	None	Yes

Table 4.1: Summary of the existence of INT BICs and UGRs in the waveguide comprising three negative uniaxial materials. The first three columns correspond to mirror symmetry about $x = 0$, azimuthal anisotropy-symmetry and polar anisotropy-symmetry, respectively, and tell us whether each of them is maintained or broken. The two final columns tell us about the existence of INT BICs and UGRs in the structure. Each row corresponds to a different configuration.

tained. If mirror symmetry is maintained, then the radiation channels are identical, and even if polar anisotropy-symmetry is broken, there can be no UGRs. UGRs exist when both mirror symmetry and polar anisotropy-symmetry are broken. When polar anisotropy-symmetry is broken, there are no lines of BIC existence on the leaky mode sheet but only discrete points. We saw the same effect in the previous chapter and understood it using the auxiliary condition in section 3.2.5. In this structure with two radiation channels, we find that with just polar anisotropy-symmetry breaking, we can see a transition from lines of BICs to a single BIC point or even to a leaky mode that does not support any BICs. Combining azimuthal and polar anisotropy-symmetry breaking leads to a situation with an asymmetric structure which does not support any BICs but does contain UGRs.

4.3 Other Waveguide Structures

Till now we have only studied the waveguide structure comprising negative uniaxial materials in this chapter. There are several other combinations of materials that we could select which would lead to waveguide structures which can support leaky modes with two radiation channels. In this section we shall consider a few such structures

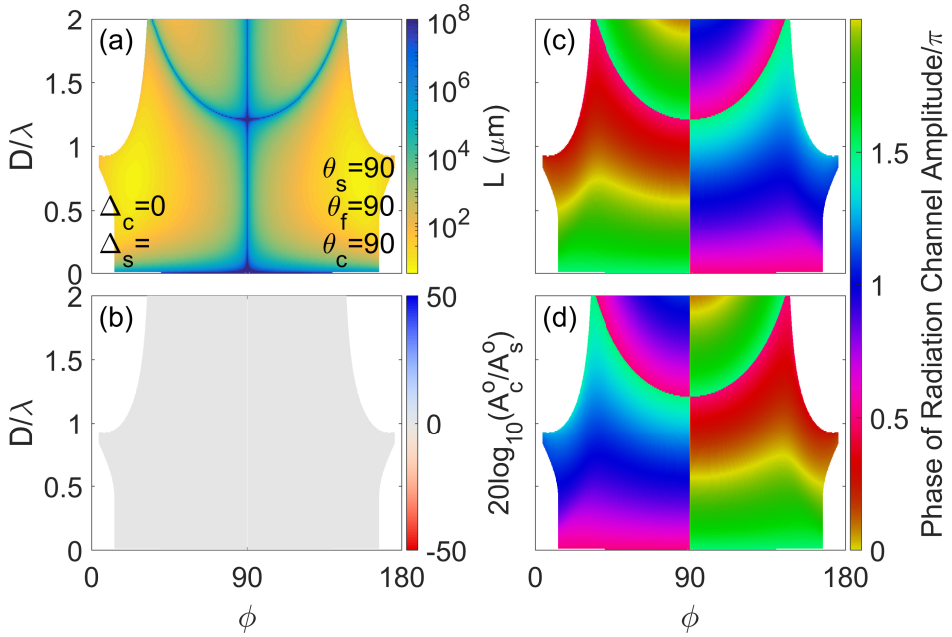

Fig. 4.22: Same as Fig. 4.9 but with full anisotropy-symmetry maintained in a structure with only uniaxial positive materials with $n_{ec} = n_{es} = 1.7, n_{oc} = n_{os} = 1.3$ and $n_{ef} = 1.6, n_{of} = 1.4$.

and study whether they can support BICs and UGRs.

4.3.1 Positive Uniaxial Film, Substrate and Cover

First we study a structure comprising only positive uniaxial materials in the cover, film and substrate. We use the same values of the refractive indices, except we swap the ordinary and extraordinary indices so that $n_{ec} = n_{es} = 1.7, n_{oc} = n_{os} = 1.3$ and $n_{ef} = 1.6, n_{of} = 1.4$. The extraordinary indices being the highest indices in the structure mean that the extraordinary wave in the cover and the substrate provide the radiation channels. However, since the extraordinary index varies as a function of ϕ, this structure would also support guided modes at lower values of ϕ.

Fig. 4.22(a) shows the fundamental leaky mode supported by this structure when full anisotropy-symmetry is maintained. The fundamental mode has no cutoff since the structure is mirror-symmetric about $x = 0$. We see that when full anisotropy-symmetry is maintained, the structure supports lines of BICs. There is a line of PS

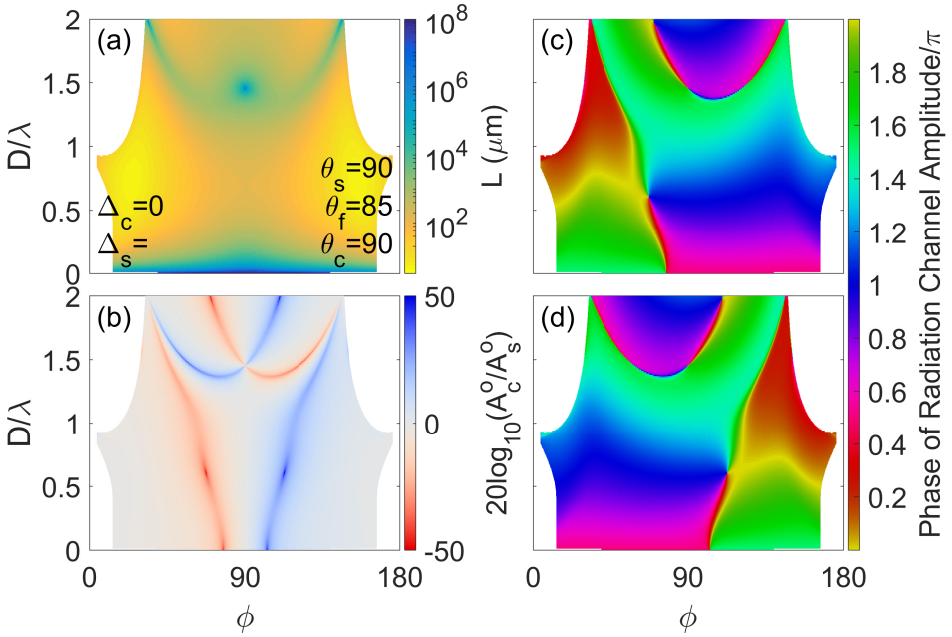

Fig. 4.23: Same as Fig. 4.22 but with polar anisotropy-symmetry broken by moving the film optic axis out of the interface plane ($\theta_f = 85°$).

BICs at $\phi = 90°$ which arise from the guiding profile provided by the ordinary indices. The curved blue lines correspond to INT BICs where radiation is cancelled in both channels. Fig. 4.22(b) shows the radiation channel ratio in dB but since the structure is mirror symmetric about $x = 0$, the radiation into the two channels is identical. Fig. 4.22(c) and (d) show the phase map of the radiation channel amplitude for the cover and substrate radiation channels, respectively. We see that the BIC lines correspond to discontinuities of $\pm\pi$ in the phase. The change in the phase across the BIC line is opposite in the two channels.

Fig. 4.23(a) shows the fundamental leaky mode supported by this waveguide when polar anisotropy-symmetry is broken by taking the film optic axis out of the interface plane ($\theta_f = 85°$). The cover and substrate optic axes remain in the interface plane ($\theta_c = \theta_s = 90°$) and azimuthal anisotropy-symmetry is maintained ($\Delta_c = \Delta_s = 0°$). The structure is no longer mirror symmetric about $x = 0$ and so the added constraint of a second auxiliary condition has to be satisfied in order for BICs to exist. This leads to a collapse of the BIC solution from

lines to a discrete BIC point on the leaky mode sheet as shown in Fig. 4.23(a). Since the structure is no longer mirror symmetric about $x = 0$, we see that the radiation into the two channels is now distinct. Therefore, we have lines of strongly unidirectional radiation as shown in Fig. 4.23(b). Moreover, we find that there are UGRs on the leaky mode sheets where the radiation ratio diverges, i.e., radiation in one channel is cancelled entirely and directed into the other channel. These occur because at these points, the auxiliary condition is satisfied for only one of the channels. Fig. 4.23(c) and (d) show the phase map of the radiation channel amplitude for the cover and substrate radiation channels, respectively. We see that the UGRs correspond to singularities in the phase of the radiation channel amplitude into which radiation is cancelled. We see that the phase singularities corresponding to the UGRs can be assigned opposite winding numbers in the cover and the substrate radiation channel depending on how the phase evolves around the singularity.

4.3.2 Positive Uniaxial Film, Negative Uniaxial Substrate and Cover

We shall now study a structure where the cover and substrate are negative uniaxial media ($n_{ec} = n_{es} = 1.3, n_{oc} = n_{os} = 1.7$) while the core/film comprises a positive uniaxial material ($n_{ef} = 1.6, n_{of} = 1.4$). The fundamental leaky mode supported by this structure when full anisotropy-symmetry is maintained only contains a line of PS BICs at $\phi = 90°$ arising from the guiding profile provided by the extraordinary indices. It does not support any INT BICs. When polar anisotropy-symmetry is broken by moving only one optic axis (either the film or substrate optic axis) out of the interface plane, mirror symmetry about $x = 0$ is broken and there are lines of strongly unidirectional radiation on the leaky mode sheet but there are no UGRs.

Fig. 4.24(a) shows the fundamental leaky mode supported by the structure when polar anisotropy-symmetry is broken by moving both film and substrate optic axes out of the interface plane while keeping them parallel to each other ($\theta_f = \theta_s = 85°$). Azimuthal anisotropy-symmetry is maintained and the cover optic axis remains in the interface plane. We see that in this scenario, there are no BICs supported on the fundamental leaky mode sheet. The radiation channels are not equivalent since the structure is no longer mirror symmetric about

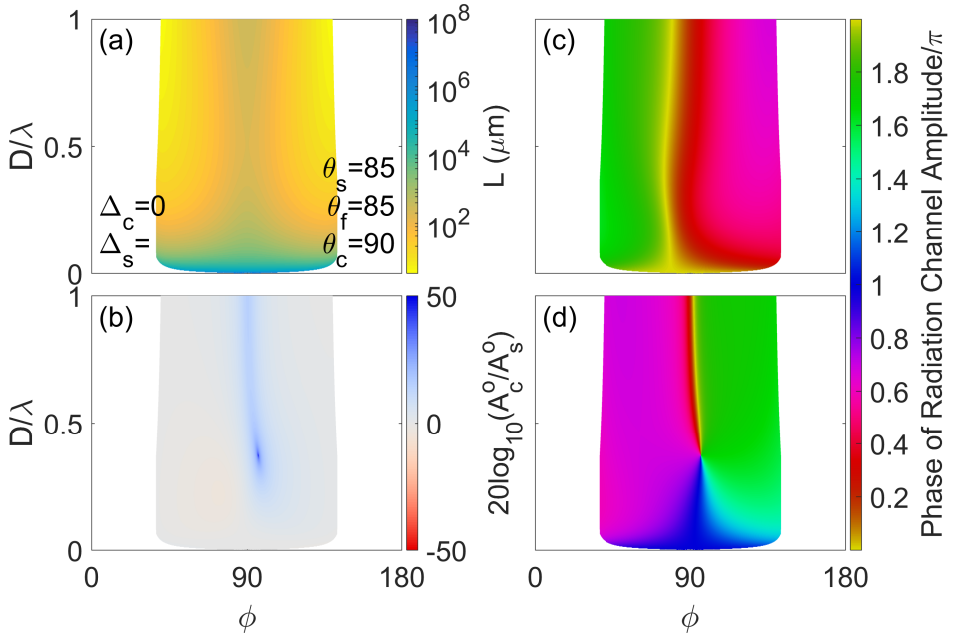

Fig. 4.24: Same as Fig. 4.9 but with polar anisotropy-symmetry broken by moving both the film and substrate optic axis out of the interface plane while keeping them parallel to each other ($\theta_f = \theta_s = 85°$) in a structure with negative uniaxial cover and substrate ($n_{ec} = n_{es} = 1.3, n_{oc} = n_{os} = 1.7$) and a positive uniaxial core ($n_{ef} = 1.6, n_{of} = 1.4$).

$x = 0$ and we see that the leaky mode sheet contains a line of strongly unidirectional radiation to the cover in Fig. 4.24(b). There is also a point on the leaky mode sheet which is a UGR radiating only to the cover. The phase maps in Fig. 4.24(c) and (d) show that the UGR corresponds to a phase singularity in the substrate radiation channel amplitude since radiation to the substrate is cancelled at that point. There is no phase singularity in the phase map of the cover radiation channel amplitude meaning that there is no UGR radiating to the substrate.

This is the first time that we have seen a scenario where the UGRs to the cover and the substrate do not appear in pairs. As stated earlier, when polar anisotropy symmetry is broken by only moving the film optic axis out of the interface plane while leaving the substrate optic axis in the interface plane, there are no UGRs but there are lines of strongly unidirectional radiation to the cover and the substrate at low

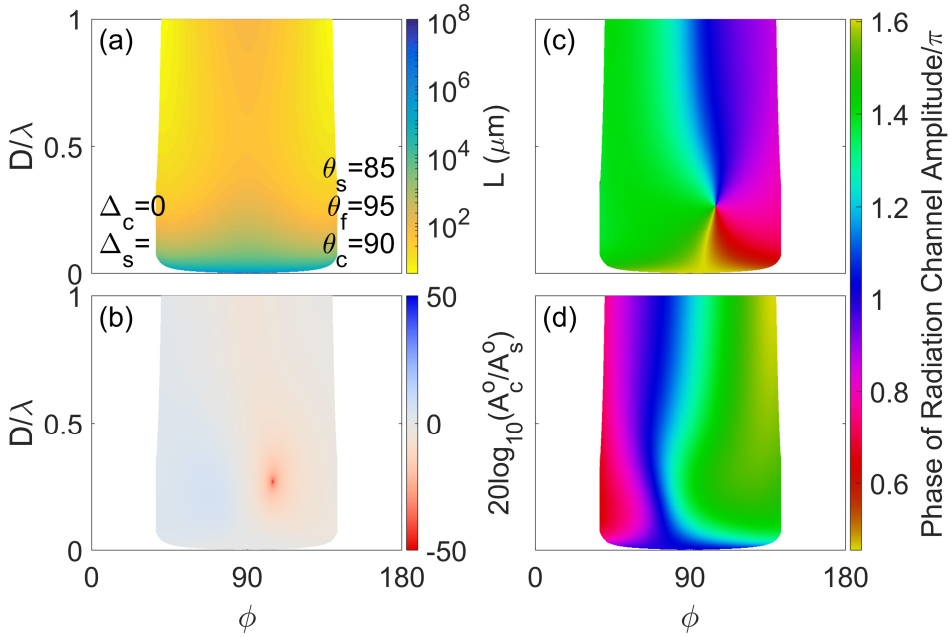

Fig. 4.25: Same as Fig. 4.24 but with different orientations of the film and the substrate optic axes ($\theta_f = 95° \neq \theta_s = 85°$).

values of D/λ. As the substrate optic axis is also moved out, the line of radiation to the substrate disappears while the line of radiation to the cover moves up in D/λ and a UGR radiating to the cover also appears. On the other hand, if we leave the substrate optic axis in the interface plane and move the cover optic axis out of the interface plane to be parallel with the film optic axis, we find a scenario where there is only one UGR radiating to the substrate.

Fig. 4.25(a) shows the fundamental leaky mode supported by the structure when polar anisotropy-symmetry is broken by moving both film and substrate optic axes out of the interface plane but now they have different polar orientations ($\theta_f = 95° \neq \theta_s = 85°$). Azimuthal anisotropy-symmetry is maintained and the cover optic axis remains in the interface plane. We see that in this scenario, once again, there are no BICs supported on the fundamental leaky mode sheet. The structure is not mirror symmetric about $x = 0$ and therefore the radiation channels are not equivalent. We see that there is a point on the leaky mode sheet which is a UGR radiating only to the substrate in Fig. 4.25(b). However, there are no lines of strongly unidirectional

radiation any more. The phase maps in Fig. 4.25(c) and (d) show that the UGR corresponds to a phase singularity in the cover radiation channel amplitude since radiation to the cover is cancelled at that point. There is no phase singularity in the phase map of the substrate radiation channel amplitude and thus there is no UGR radiating to the cover.

Therefore, we have seen that planar waveguide structures with two radiation channels made up of different combinations of uniaxial positive and uniaxial negative materials can support leaky modes that contain BICs and UGRs. The UGRs arise exclusively when polar anisotropy-symmetry and mirror symmetry about $x = 0$ are broken in conjunction and not otherwise. BICs can occur in various regimes of anisotropy-symmetry but there is a reduction in dimension of the BIC solution when we move from a scenario with two identical radiation channels to a scenario with two distinct radiation channels due to added constraint of a new auxiliary condition having to be satisfied. Of course, as seen in the previous chapter, polar anisotropy-symmetry breaking also leads to a collapse of the BIC solution from lines in the $\phi - D/\lambda$ space to discrete points.

Chapter 5

Leaky D'yakanov Surface Waves and DSW BICs

Surface waves in optics are special modes that exist at the interfaces of two unlike materials. There are several examples of such surface waves that exist at the interfaces between different pairs of materials. Some examples of surface waves include surface plasmon polaritons (SPPs) that exist at the interface between dielectrics with positive permittivity ($\epsilon > 0$) and metals with negative permittivity ($\epsilon < 0$) [151], magnetic plasmons that exist at the interface of a dielectric with a material that has negative permeability ($\mu < 0$) [152], and optical Tamm waves that exist at the interfaces of photonic crystals with homogeneous media, which are analogous to the electronic surface states in crystals [153]. Further information about different electromagnetic surface waves can be found in the review article in Ref. [154].

In 1988, D'yakonov theoretically proposed the existence of a new electromagnetic surface wave at the interface of an isotropic dielectric and a positive uniaxial material with the constraint on the constitutive parameters that the refractive index of the dielectric material (n_c) lie between the two indices of the uniaxial material (n_o, n_e) [155]

$$n_o < n_c < n_e. \tag{5.1}$$

Our group referred to these waves as D'yakonov surface waves (DSWs) and the term was subsequently adopted in the community [156]. A feature of particular interest about DSWs is the fact that they occur at the interface between two transparent materials and therefore can theoretically propagate with zero attenuation. They were reported to

exist for a narrow range of propagation directions on the interface. Subsequently, the existence of DSWs were predicted at interfaces involving two positive uniaxial materials with their optic axes oriented in different directions by Averkiev and D'yakonov [157]. Since then there have been many theoretical proposals predicting DSWs at interfaces involving biaxial materials [158, 159], photonic crystals and metamaterials [160, 161], negative index materials [162], magnetic materials [163], van der Waals materials [164, 165] and hyperbolic materials [166–169]. Given their narrow angular range of existence, the experimental demonstration of DSWs was complicated and was first reported by our group a full 20 years after their initial theoretical prediction [170]. More recently, DSWs have been studied at finite interfaces between uniaxial positive materials [171, 172],in cylindrical structures where DSWs transition to guided or leaky modes [173], and also in cylindrical structures comprising metamaterials using transformation optics [174].

DSW mediated guided modes in ultra-thin films below the ordinary waveguide cutoff were theoretically predicted [163, 175] and then experimentally demonstrated in dielectric nano-sheets [149]. These modes could have useful applications in sensing due to their guided-to-leaky mode transitions based on changes in refractive indices. The existence of related waves known as D'yakonov-Tamm waves were predicted at the interface of a dielectric with an anisotropic, periodically non-homogeneous material [176], including chiral materials [177]. These D'yakonov-Tamm waves exist for a greater range of propagation directions and have also been experimentally demonstrated [178]. Theoretical predictions have also been made for another related wave known as a D'yakonov-Voigt wave that only exists for one particular direction at the interface of a dielectric and a positive uniaxial material but with added constraints on the constitutive parameters. This D'yakonov-Voigt wave decays away from the interface with a combination of exponential and linear functions [179].

The constraint equation on the constitutive parameters (eq. 5.1) given in the original paper by D'yakonov has meant that research in the field of DSWs has been focused almost exclusively on positive uniaxial materials. However, there are a few reports on DSWs at interfaces involving materials where the permittivity $\epsilon_e < \epsilon_o$. The existence of a DSW at the interface between an isotropic dielectric and a negative uniaxial crystal has been predicted if and only if both materials are

dissipative [180]. Another study predicts the existence of a hyperbolic surface wave at the interface of an isotropic dielectric with a negative uniaxial metal (both $\epsilon_e < 0$ and $\epsilon_o < 0$ and also $\epsilon_e < \epsilon_o$) [181]. The existence of DSWs at the interface between two non-dissipative negative uniaxial dielectric materials has also been predicted but with the constraint that the interface be finite [182].

In this chapter we shall present the results of our study of DSWs at the interface between a positive uniaxial material and a negative uniaxial material. We study an infinite interface between these two materials and we assume that they are transparent and not dissipative since the potential lossless propagation of DSWs is one of their most attractive features. We find that depending on the relative orientation of the optic axes of the two uniaxial materials, such an interface can support not just a DSW but also a leaky DSW which radiates via the ordinary wave in the negative uniaxial material. Since we study the interface between two uniaxial materials and assume that their optic axes can be independently oriented, our scheme is similar to that in Ref. [157]. However, unlike the scheme in Ref. [157], we assume that one of the materials is a negative uniaxial material. This leads to the existence of a leaky DSW since the ordinary refractive index of the negative uniaxial material is higher than the extraordinary index and it remains constant for different orientations of the optic axis, thereby providing a radiation channel via the ordinary basis wave in that material in certain optic axis configurations. Therefore, this structure supports a guided to leaky surface wave transition. Moreover, in this structure, it is also possible to tune the optic axis parameters to cancel the radiation in the leaky part of the DSW to obtain a surface BIC.

We have seen in Chapter 1 that it is possible for BICs to exist at the interfaces of finite one dimensional arrays of waveguides [54–56] and finite two dimensional photonic crystals [21, 57], localised in the region where the array or photonic crystal ends and a homogeneous bulk material begins. To the best of our knowledge, there have been no reports of surface BICs at a continuous interface of two blocks of homogeneous material. Since we are studying a structure that supports a leaky DSW, we apply the techniques used in the previous chapters to study BICs to this structure and uncover the existence of a DSW BIC in the leaky part of the DSW where the amplitude of the radiation channel in the substrate (ordinary wave) becomes zero and we obtain a surface BIC propagating in a particular direction.

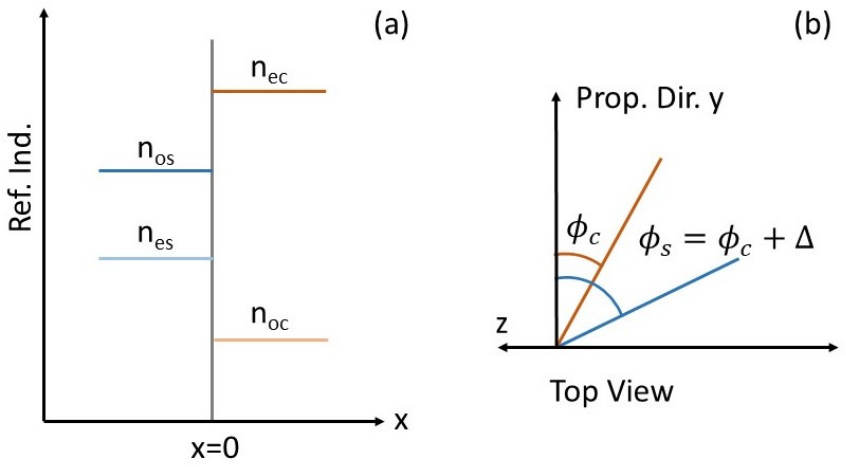

Fig. 5.1: (a) Schematic of the refractive indices of the structure studied with a negative uniaxial material in the substrate and a positive uniaxial material in the cover. The grey line shows the interface at $x = 0$. (b) View from the top showing the arrangement of the optic axes of the cover (brown) and the substrate (blue) in the interface plane.

5.1 Theory

We study a structure, shown in Fig. 5.1(a), where the negative half space ($x < 0$) is filled by a uniaxial negative material ($n_{os} > n_{es}$) which we shall call the substrate, for the sake of consistency of notation. The positive half space ($x > 0$) is filled by a uniaxial positive material ($n_{oc} < n_{ec}$) which we shall call the cover. Once again, we set y as the propagation direction. The angle made by the optic axis of the cover with the direction of propagation is given by ϕ_c. The substrate optic axis is offset from the cover optic axis by the angle Δ so that the angle made by the substrate optic axis with the direction of propagation is given by $\phi_s = \phi_c + \Delta$.

We know from section 2.1 that for a given value of the propagation constant k_y along the y direction, there are four basis waves with different values of the propagation constant along the x direction. There are two ordinary waves and two extraordinary waves, and one of each propagates in the $+x$ direction and the other propagates in the $-x$ direction. Since we consider infinite half spaces, we will only consider two waves in each material, since there are no reflected waves coming back

from $\pm\infty$. Therefore, at the interface, there will be two waves in the substrate and two waves in the cover. For a standard or guided DSW, all four of these waves must decay exponentially as we move away from the interface at $x = 0$. However, for a leaky DSW, we will have only three waves decaying exponentially away from the interface while the fourth wave will serve as the radiation channel, and will therefore be growing exponentially away from the interface within the leaky mode formalism.

We have derived the expressions for the normalized propagation constants k_x/k_0 in the x direction for the ordinary and extraordinary waves in section 3.1.1 in eqs. 3.13 and 3.14. The expressions for the tangential field components of the basis waves in a uniaxial material are given in eqs. 3.15 and 3.16. Based on the sign of the imaginary part of k_x/k_0 we can select the appropriate waves (all four decaying for guided DSWs, and three decaying and one growing for leaky DSWs) for the solution of our interest and apply the boundary conditions at the interface. Using the notation that we have used previously, we can write the total field in the cover just to the right of the interface at $x = 0$ as

$$\begin{aligned} \vec{m}_{cover} &= a_c^o \vec{F}_c^o + a_c^e \vec{F}^e, \\ &= a_c^o \begin{bmatrix} E_{yc}^o \\ \tilde{H}_{zc}^o \\ E_{zc}^o \\ \tilde{H}_{yc}^o \end{bmatrix} + a_c^e \begin{bmatrix} E_{yc}^e \\ \tilde{H}_{zc}^e \\ E_{zc}^e \\ \tilde{H}_{yc}^e \end{bmatrix}. \end{aligned} \tag{5.2}$$

Similarly the total film in the substrate just to the left of the interface can be written as

$$\begin{aligned} \vec{m}_{substrate} &= a_s^o \vec{F}_s^o + a_s^e \vec{F}_s^e, \\ &= a_s^o \begin{bmatrix} E_{ys}^o \\ \tilde{H}_{zs}^o \\ E_{zs}^o \\ \tilde{H}_{ys}^o \end{bmatrix} + a_s^e \begin{bmatrix} E_{ys}^e \\ \tilde{H}_{zs}^e \\ E_{zs}^e \\ \tilde{H}_{ys}^e \end{bmatrix}, \end{aligned} \tag{5.3}$$

where the subscripts c and s indicate the cover and the substrate, the superscripts o and e represent the ordinary and the extraordinary basis waves in the uniaxial media, the scalar coefficient $a_{c/s}^{o/e}$ is the amplitude of the corresponding basis wave and $\vec{F}$ is a 4×1 column

vector containing the four tangential field components: $E_y, \tilde{H}_z, E_z$ and $\tilde{H}_y$.

Since we consider only the four tangential components, the boundary conditions require that the fields be continuous across the interface. This condition can be written as

$$a_s^o \vec{F}_s^o + a_s^e \vec{F}_s^e = a_c^o \vec{F}_c^o + a_c^e \vec{F}_c^e. \tag{5.4}$$

There are four equations, one corresponding to each tangential field component, that arise from eq. 5.4. We can write this as a system of linear equations

$$\begin{aligned} & a_c^o \vec{F}_c^o + a_c^e \vec{F}_c^e - a_s^o \vec{F}_s^o - a_s^e \vec{F}_s^e = 0, \\ \implies & \begin{bmatrix} \vec{F}_c^o & \vec{F}_c^e & -\vec{F}_s^o & -\vec{F}_s^e \end{bmatrix} \begin{bmatrix} a_c^o \\ a_c^e \\ a_s^o \\ a_s^e \end{bmatrix} = \begin{bmatrix} 0 \\ 0 \\ 0 \\ 0 \end{bmatrix}, \\ & \implies \hat{R}\vec{a}_{c+s} = 0, \end{aligned} \tag{5.5}$$

where $\hat{R} = \begin{bmatrix} \vec{F}_c^o & \vec{F}_c^e & -\vec{F}_s^o & -\vec{F}_s^e \end{bmatrix}$ is a 4×4 matrix.

We therefore have a homogeneous system of four equations where the scalar amplitudes $a_{c/s}^{o/e}$ serve as the unknown variables. We are only interested in non-trivial solutions of this system of equations and a system of homogeneous linear equations can have a non-trivial solutions only if the determinant of the coefficient matrix, $\hat{R}$, is zero. This gives us the dispersion condition

$$|\hat{R}| = 0. \tag{5.6}$$

If we restrict the orientation of the optic axes of the two materials so that they always lie in the interface ($x = 0$) plane, we can write an analytic expression for $|\hat{R}|$ using the expressions for the field components of the basis waves in a uniaxial material given in eqs. 3.15 and 3.16. Then eq. 5.6 can be written as

$$\begin{aligned} & 2\epsilon_o^c \epsilon_o^s \kappa_x^{oc} \kappa_x^{os} \left(\kappa_x^{ec} - \kappa_x^{oc}\right)\left(\kappa_x^{es} - \kappa_x^{os}\right) \sin\phi_c \sin\phi_s \cos\phi_c \cos\phi_s \\ & + \epsilon_o^c \epsilon_o^s \left(\kappa_x^{ec} - \kappa_x^{es}\right)\left(\epsilon_o^c \kappa_x^{os} - \epsilon_o^s \kappa_x^{oc}\right) \sin^2\phi_c \sin^2\phi_s \\ & + \epsilon_o^c \kappa_x^{os} \left(\kappa_x^{ec} - \kappa_x^{os}\right)\left(\epsilon_o^c \left(\kappa_x^{os}\right)^2 - \epsilon_o^s \kappa_x^{es} \kappa_x^{oc}\right) \sin^2\phi_c \cos^2\phi_s \\ & + \epsilon_o^s \kappa_x^{oc} \left(\kappa_x^{es} - \kappa_x^{oc}\right)\left(\epsilon_o^s \left(\kappa_x^{oc}\right)^2 - \epsilon_o^c \kappa_x^{ec} \kappa_x^{os}\right) \sin^2\phi_s \cos^2\phi_c \\ & + \kappa_x^{oc} \kappa_x^{os} \left(\kappa_x^{os} - \kappa_x^{oc}\right)\left(\epsilon_o^s \kappa_x^{es} \left(\kappa_x^{oc}\right)^2 - \epsilon_o^c \kappa_x^{ec} \left(\kappa_x^{os}\right)^2\right) \cos^2\phi_c \cos^2\phi_s = 0, \end{aligned} \tag{5.7}$$

where c and s in the superscript or the subscript denote the cladding and the substrate, respectively, $\epsilon_o = n_o^2$ represents the square of the ordinary refractive index of the material indicated in the superscript, κ_x^o and κ_x^e indicates the normalised propagation constant in the x direction of the extraordinary or the ordinary basis wave in the material indicated in the superscript. The expressions for κ_x^o and κ_x^e for a uniaxial material are given in eqs. 3.13 and 3.14, respectively and they depend on κ_y, the normalised propagation constant in the y direction. Once the materials and the dimensions of the waveguide and the orientation of the optic axes in the uniaxial layers is fixed, $|\hat{R}|$ or the expression in eq. 5.7 only depends on κ_y. Eq. 5.7 is a transcendental equation and we have to solve it numerically. When we select the basis waves that decay exponentially away from the interface, we get only real valued solutions of κ_y, which we shall henceforth refer to as N, the mode propagation constant. However, if we select three decaying waves and one exponentially growing wave at the interface, we get complex solutions for N where the imaginary part approximates the energy lost from the surface mode via radiation through the radiation channel available to the mode.

In the original paper by D'yakonov, the bounds of existence of the DSW (the bounds on N) are given by the extraordinary index of the uniaxial material ($n_e(\phi)$) and the refractive index of the isotropic material [155]. The DSW occurs at values of ϕ close to the point where the aforementioned indices cross. We know that the DSW exists at points where $N > n_e(\phi)$ and so the extraordinary index cannot serve as a radiation channel. Therefore, in our structure we select the ordinary wave in the substrate as the radiation channel for the leaky DSW mode.

Given that we have studied structures where it is possible to cancel the radiation in the radiation channel, we want to study that possibility for this geometry as well. To that end, we want to define an auxiliary condition where we set the radiation channel amplitude, $a_s^o = 0$. Applying this condition in eq. 5.4 we get

$$a_s^e \vec{F}_s^e = a_c^o \vec{F}_c^o + a_c^e \vec{F}_c^e. \tag{5.8}$$

This can be written as a system of linear equations like we did for the

dispersion equation

$$
\begin{aligned}
& a_c^o \vec{F}_c^o + a_c^e \vec{F}_c^e - a_s^e \vec{F}_s^e = 0, \\
\implies & \begin{bmatrix} \vec{F}_c^o & \vec{F}_c^e & -\vec{F}_s^o & -\vec{F}_s^e \end{bmatrix} \begin{bmatrix} a_c^o \\ a_c^e \\ a_s^e \end{bmatrix} = \begin{bmatrix} 0 \\ 0 \\ 0 \\ 0 \end{bmatrix}, \\
& \implies \hat{Z}_{4\times 3} \vec{a}_{3\times 1} = 0,
\end{aligned}
\tag{5.9}
$$

Eq. 5.9 gives us an overdetermined, homogeneous set of linear equations. We have encountered such systems earlier and know that they can have a non-trivial solution only if at most two of the linear equations are linearly independent. This translates into the requirement that the determinant of any 3×3 sub-matrix of $Z_{4\times 3}$ must be zero and that is the auxiliary condition. We will obtain a DSW BIC when the solutions of the propagation constant N for the DSW and the solution of the auxiliary condition will coincide. We shall now apply this theoretical framework to study the structure shown in Fig. 5.1.

5.2 Guided DSWs and Leaky DSWs

In order for DSWs to exist we require that there be an overlap between the extraordinary indices of the positive uniaxial cover and the negative uniaxial substrate. Though this is a necessary condition, it is not a sufficient one for the existence of DSWs in the structure. This requirement can be written as

$$
n_{os} > n_{oc} \ \wedge \ n_{ec} > n_{es}. \tag{5.10}
$$

Without loss of generality, we consider a structure with a negative uniaxial substrate with $n_{os} = 1.80$ and $n_{es} = 1.40$, and a positive uniaxial substrate with $n_{oc} = 1.25$ and $n_{ec} = 2$. The schematic of the refractive index layout for this structure is shown in Fig. 5.1(a). We start by considering a structure where the optic axes in the cover and the substrate are aligned ($\Delta = 0^\circ$ or $\phi_s = \phi_c$) and lie in the interface plane ($\theta_c = \theta_s = 90^\circ$). So both polar and azimuthal anisotropy-symmetry are maintained.

Fig. 5.2(a) shows us the DSW mode supported by this structure (red line). We find that the leaky DSW mode exists in the vicinity of

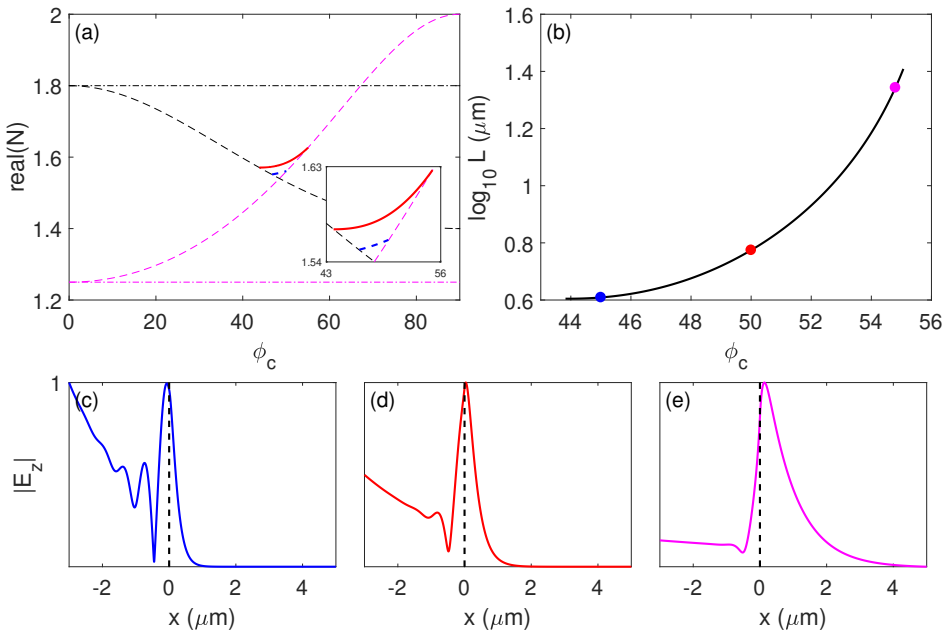

Fig. 5.2: (a) The real part of the DSW mode propagation constant as a function of the cover optic axis orientation (ϕ_c) is shown in red. The dashed blue line shows the solution of the auxiliary condition. The cover and substrate optic axes are aligned ($\Delta = 0°$). The magenta and black lines show the refractive indices of the cover and substrate, respectively. The dashed lines show the extraordinary index while the dot-dashed lines show the ordinary index which does not vary with ϕ_c. The inset shows the area in the vicinity of the DSW. (b) The logarithm of the $1/e$ propagation length of the DSW mode for $\lambda = 0.632\mu m$. The transverse profile of the absolute value of the tangential electric field component, E_z, normalized so the peak is at 1, is shown for the DSW mode at (c) $\phi = 45°$, (d) $\phi = 50°$, and (e) $\phi = 54.8°$. The dashed black line indicates the interface at $x = 0$. The coloured markers in (b) serve as visual guides to show the values of ϕ_c where we plot the fields.

the point where $n_{es}(\phi_s) = n_{ec}(\phi_c)$. The DSW cuts off at the points where $N = n_{es}(\phi_s)$ and $N = n_{ec}(\phi_c)$. The real part of the propagation constant N of the DSW mode is greater than both $n_{es}(\phi_s)$ and $n_{ec}(\phi_c)$ as well as n_{oc}. This means that the three basis waves corresponding to these three refractive indices decay exponentially as we move away from the interface. However, $N < n_{os}$, and this means there will be

radiation away from the surface mode. We select the ordinary basis wave in the substrate so that it grows exponentially as we move away from the interface and acts as the radiation channel via which energy leaks from the mode. In such a scenario, we obtain a complex N for the DSW at all values of ϕ_c^{DSW}, where ϕ_c^{DSW} indicates the range of values of ϕ_c where the DSW solution (either leaky or guided) exists. We see the solution of the auxiliary condition for this structure plotted as the dashed blue line and find that it does not intersect the DSW solution. Therefore, we do not expect to find any BICs. We calculate the propagation length of the leaky DSW for $1/e$ attenuation from the imaginary part of N assuming a wavelength of $\lambda = 0.632\mu m$, and this is shown in Fig. 5.2(b). The DSW is fairly leaky throughout but the losses decrease as we move to higher values of ϕ leading to a higher $1/e$ propagation length.

It might be considered somewhat difficult to determine whether something is a leaky surface mode given that there is no core within which most of the field is confined and from which it leaks [173]. We plot the transverse field profiles for the DSW mode at different values of ϕ_c to determine whether the modes we are studying are indeed surface modes. We see in Fig. 5.2(c), (d), and (e), the absolute value of the transverse profile of the tangential field component E_z (normalized so the maximum near the surface has value 1) when $\phi_c = 45°$, $\phi_c = 50°$, and $\phi_c = 54.8°$. We see in all three cases that even though there is radiation away from the interface, there is substantial localisation at the interface. Besides, we find in Fig. 5.2(c) that at $\phi_c = 45°$, the field profile has its peak in the substrate and more of the field is in the substrate. As expected, we find in Fig. 5.2(d) at $\phi = 50°$ that there is lesser loss by way of radiation, the peak of the field has shifted to the cover, and in general, more of the field is now in the cover. We see in Fig. 5.2(e) that there is even lesser loss and the peak moves further into the cover, while even more of the field, almost it's entirety, is now in the cover. Thus as we traverse the range of ϕ_c^{DSW} from its cutoff at $N = n_{es}(\phi_s)$ to its cutoff at $N = n_{ec}(\phi_c)$, the field distribution of the surface mode shifts from being primarily in the substrate to primarily in the cover and the peak shifts from the substrate to the cover. These are well known properties of DSWs [156] and therefore serve to confirm that this is indeed a leaky DSW. We see that there is an oscillatory part in the field in the substrate because we have complex values of N for the leaky DSW and therefore, the propagation constant in the

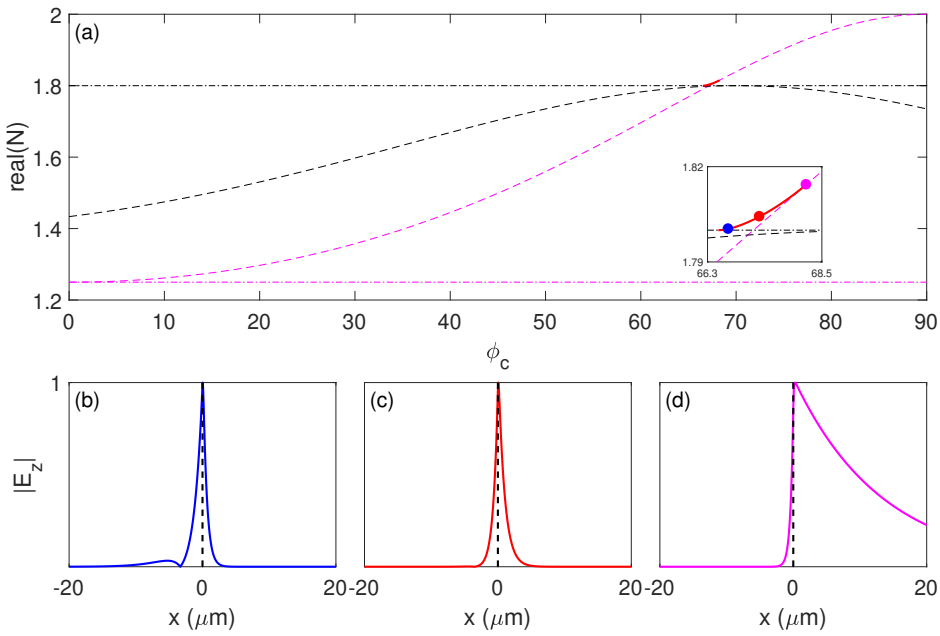

Fig. 5.3: (a) The DSW mode propagation constant as a function of the cover optic axis orientation (ϕ_c) is shown in red. The cover and substrate optic axes are no longer aligned ($\Delta = -70°$). The magenta and black lines show the refractive indices of the cover and substrate, respectively. The dashed lines show the extraordinary index while the dot-dashed lines show the ordinary index. The inset shows the area in the vicinity of the DSW. The transverse profile of the absolute value of the tangential electric field component, E_z, normalized so the peak is at 1, is shown for the DSW mode at (b) $\phi = 66.7°$, (c) $\phi = 67.3°$, and (d) $\phi = 68.2°$. The dashed black line indicates the interface at $x = 0$. The coloured markers in (a) serve as visual guides to show the values of ϕ_c where we plot the fields.

transverse direction k_x is also complex and not purely imaginary. The real part of k_x results in the oscillation and this oscillation is visible in the transverse field profile plots when the oscillation has a shorter spatial period for higher values of k_x, as is the case, for example, in Fig. 5.2(c).

We now study a structure where the cover and substrate optic axes are no longer aligned. The substrate optic axis is offset from the cover optic axis by $\Delta = -70°$. This means that $n_{os} = n_{es}(\phi_s)$ only holds at $\phi_c = -\Delta = 70°$ as shown by the dashed and dot-dashed black lines

in Fig. 5.3(a). We find that the DSW solution in this structure cuts off at $N = n_{os}$ on one side and at $N = n_{es}(\phi_s)$ on the other side. At all points on the DSW solution, N is greater than $n_{es}(\phi_s), n_{os}, n_{ec}(\phi_c)$, and n_{oc} and therefore, the DSW is made up of four basis waves all of which decay exponentially as we move away from the interface. This is therefore a conventional, guided DSW mode being supported at the interface between a positive uniaxial material and a negative uniaxial material. Similar to what we have seen in the previous case, we find in Fig. 5.3(b), (c), and (d) that as we move from a value of ϕ_c near the $N = n_{os}$ cutoff to a value of ϕ_c closer to the $N = n_{ec}(\phi_c)$ cutoff, the field distribution shifts from being more in the substrate to more in the cover and the peak of the field distribution shifts as well. We have found that the structure supports only guided modes if the value of N equals the value of n_{os} at a value of ϕ_c that is less than $-\Delta$. In such a scenario, the DSW solution cuts off at $N = n_{os}$, meaning that for all points on the DSW solution, $N > n_{os}$ and therefore, the ordinary wave in the substrate is confined and not radiative. Therefore, in order for leaky modes to exist, it is a necessary condition that

$$\phi_c(N = n_{os}) > -\Delta \ \vee \ N < n_{os} \ \forall \phi_c \in \phi_c^{DSW}, \tag{5.11}$$

where $\vee$ indicates OR, i.e., leaky modes can exist if either of the two requirements indicated in eq. 5.11 is met.

5.3 DSW BICs

Fig. 5.4 shows the scenario when the offset between the film and substrate optic axis is $\Delta = -56°$. In this scenario the structure supports both purely guided DSW modes as well as leaky DSW modes for different orientations of the optic axis. The guided-to-leaky transition occurs about the point where $N = n_{os}$. The leaky DSW exists in the range of ϕ_c between the points where $N = n_{es}(\phi_s)$ and $N = n_o s$. For these values of ϕ_c, $N < n_{os}$ meaning that the ordinary wave in the substrate serves as the radiation channel and therefore we have leaky mode solutions with complex values of N. The purely guided leaky mode exists for values of ϕ_c between the point where $N = n_{os}$ and where $N = n_{ec}(\phi_c)$. For these values of ϕ_c, N is greater than all the refractive indices in the system and therefore, the four basis waves in the two materials that make up the DSW all decay exponentially as

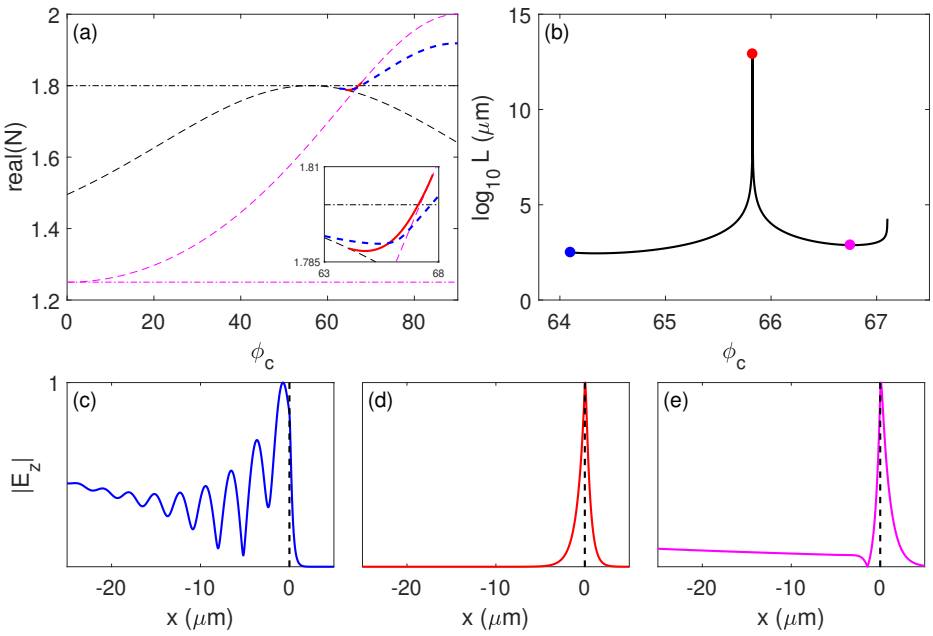

Fig. 5.4: Same as Fig. 5.2 but for an offset between the cover and substrate optic axis of $\Delta = -56°$. The transverse profile of the absolute value of the tangential electric field component, E_z, normalized so the peak is at 1, is shown for the DSW mode at (c) $\phi = 64.1°$, (d) $\phi = 65.8247°$, and (e) $\phi = 66.75°$

we move away from the interface and the imaginary part of N is zero. This coexistence of perfectly guided and leaky DSWs is facilitated by the fact that due to the value of Δ that has been chosen, the point in the $N - \phi_c$ space where n_{os} and $n_{ec}(\phi_c)$ cross and the point where $n_{es}(\phi_s)$ and $n_{ec}(\phi_c)$ cross are close to each other and the DSW solution satisfies the requirement given in eq. 5.11. We have found that for values of Δ where these crossing points are well separated, or the first requirement in eq. 5.11 is not met, we have only guided DSWs or leaky DSWs but not both (see Figs. 5.2 and 5.3). Also note that the DSW propagation constant does not increase monotonically with ϕ_c - it decreases first and then increases as clear from the inset in Fig. 5.4(a).

The dashed blue line in Fig. 5.4(a) shows the real part of the solution of the auxiliary condition. We see in the inset that the solution of the auxiliary conditions intersects the DSW solution at a particular value of ϕ_c. Therefore, at that point, the radiation channel amplitude

must be zero and there should be no radiative loss from the surface mode. The plot of $1/e$ propagation length of the leaky part of the DSW mode, shown in Fig. 5.4(b), confirms this since we see that at the value of ϕ_c where we have the intersection, the $1/e$ propagation length diverges. This is further confirmed in Fig. 5.4(d) where we plot the transverse field profiles and see that at $\phi_c = 65.8247°$ the field resembles a purely guided DSW mode with exponential decay away from the interface even though we are in the leaky part of the DSW. This is therefore a surface BIC and we term this a DSW BIC. We plot the transverse field profile at two other points on the leaky part of the DSW, on either side of the BIC, as shown in Fig. 5.4(c) and (e), at $\phi_c = 64.1°$ and $\phi_c = 66.75°$, respectively. We see that there is radiation into the substrate due to the radiation channel present in the substrate in both those cases. The DSW BIC at $\phi_c = 65.8247°$ is not a PS BIC since there is no question of pure TE/TM modes being supported given the optic axes orientations. BICs that are obtained by parameter tuning, such as INT BICs, invariably involve destructive interference. However, while the DSW BIC is obtained by parameter tuning, we cannot think of it as an INT BIC since this cannot be explained by the interference of waves in the core, or of resonances that are coupled to a channel. In other words, DSW BIC is simply a result of the boundary conditions since, at the point where we have the DSW BIC, it is possible for the field from the confined (extraordinary) wave in the substrate to match the total (ordinary and extraordinary) field in the cover at the interface and thus satisfy the boundary conditions. This is what gives rise to the DSW BIC.

5.4 Variation of the Offset between Optic Axes

We have seen that the offset between the optic axes of the positive uniaxial material and the negative uniaxial material can have substantial impact on the DSW mode that is supported at the interface. We shall therefore focus on a study of the effect of the variation of Δ in this section. We study the impact of the variation of Δ for three different cases. In each of the three cases, we maintain the same values of the refractive index in the cover ($n_{oc} = 1.25$, and $n_{ec} = 2$) and the extraordinary index in the substrate ($n_{es} = 1.4$). We vary the value

of the ordinary index in the substrate, which corresponds to the basis wave that acts as the radiation channel. We study the impact of the variation of Δ for three different structures with values of $n_{os} = 1.7$, $n_{os} = 1.8$, and $n_{os} = 2$ and the results are shown in Fig. 5.5.

Figs. 5.5(a) and (b) show the results for the case with $n_{os} = 1.7$. Fig. 5.5(a) shows the extent of ϕ_c^{DSW}, the range of values of ϕ_c for which the DSW solution exists, as Δ is varied. The red lines show the upper and lower bounds of ϕ_c^{DSW}. The dashed black line shows the extent of the leaky part of the DSW solution in ϕ_c. The colour in the plot shows the $1/e$ propagation length for $\lambda = 0.632\mu m$. Therefore, the blue lines correspond to DSW BICs. The red lines in Fig. 5.5(b) show the upper and lower bounds of the mode propagation constant N of the DSW solution as a function of Δ. Therefore all values of N between the two red lines corresponds to DSW solutions. We see in Fig. 5.5(a) that the DSW solution only exists for a finite range of values of Δ. At very low values of Δ the DSW is purely guided because the DSW cuts off at $N = n_{os} = 1.7$ in this domain. This is confirmed in Fig. 5.5(b) by the flat section of the lower bound where $N = n_{os} = 1.7$. At higher values of Δ, once the requirements given in eq. 5.11 are met, we find that leaky DSW solutions exist. For a small range of values of Δ we find solutions where both guided and leaky DSWs are supported by the structure. The dashed black line shows the value of ϕ_c where we have the guided to leaky DSW transition. This transition can be seen only in cases where $\phi_c(N = n_{os}) > -\Delta$. As we move to even higher values of Δ, we find in Fig. 5.5(b) that $N < n_{os}\ \forall \phi_c \in \phi_c^{DSW}$ and therefore we have purely leaky DSW solutions. We also find that the structure also supports a line of DSW BICs for a particular range of values of Δ shown by the blue line close to the guided-to-leaky DSW mode transition. The leaky DSW becomes more radiative with lower $1/e$ propagation lengths as we move to higher values of Δ.

Figs. 5.5(c) and (d) show the result of the same calculation but for a structure with $n_{os} = 1.8$. We find now that the range of values of Δ for which any DSW solution exists is lesser compared to the case with $n_{os} = 1.7$. Once again we find that the structure supports only guided DSW modes at very low values of Δ. However, these purely guided DSWs exist for a smaller range of values of Δ than in the case with $n_{os} = 1.70$. As we move to higher values of Δ, we find that the structure again supports guided and leaky DSWs simultaneously for different values of ϕ_c. Then, at even higher values of Δ, we reach the

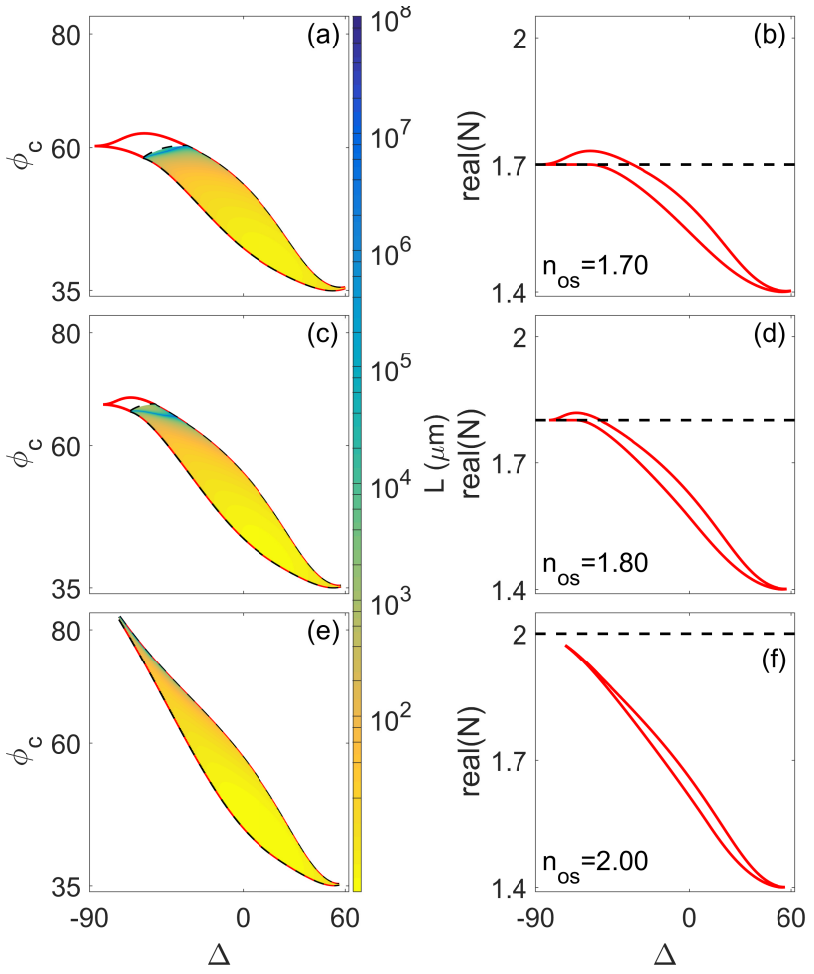

Fig. 5.5: (a) The range of existence of the DSW in ϕ_c as Δ is varied for a structure with $n_{os} = 1.7$, $n_{es} = 1.4$, $n_{oc} = 1.25$, and $n_{ec} = 2$. The red lines show the range of existence of the entire DSW in ϕ_c. The dashed black lines shows the range of existence of only the leaky part of the DSW in ϕ_c. The color in the leaky part of the DSW indicates the length of $1/e$ propagation. The blue line indicates DSW BICs. (b) The range of existence of the DSW in (a) but now the red lines indicate the bounds of the total DSW in terms of the propagation constant N. The dashed black line shows the value of n_{os} below which only leaky DSWs can exist. (c-d) Same as (a-b) but for $n_{os} = 1.8$. (e-f) Same as (a-b) but for $n_{os} = 2$.

regime where the structure supports only leaky DSWs and no guided DSWs. We also find that the structure supports DSW BICs for a range

of values of Δ. The blue line of DSW BICs in Fig. 5.5(c) is oriented so that it is now much farther from the guided-to-leaky DSW mode transition and even exists for values of Δ where we find only leaky DSW solutions. We see in Fig. 5.5(d) that for a fixed value of Δ, the range of values of N for which the DSW solution exists is narrower than in the case with $n_{os} = 1.7$.

Figs. 5.5(e) and (f) show the result of the same calculation but for a structure with $n_{os} = 2$. Now we have $n_{os} = n_{ec}$, i.e. n_{os} is the highest refractive index in the structure and therefore we find that the mode propagation constant of the DSW, $N < n_{os}\ \forall \phi_c \in \phi_c^{DSW}$. Thus this structure only supports leaky DSW solutions and no guided DSW solutions. The range of values of Δ for which we can find DSW solutions is even more restricted than in the case with $n_{os} = 1.8$. Another feature to note is that this structure no longer supports DSW BICs which have moved beyond the cutoff of the DSW. However, the DSW BIC line can be recovered by changing the values of other constitutive parameters of the structure we are studying. In this case lowering the value of n_{es} to 1.2 would restore the line of DSW BICs. We also see in Fig. 5.5(f) that for a fixed value of Δ, the range of values of N for which the DSW solution exists is even narrower than in the case with $n_{os} = 1.8$.

Summary

In conclusion, we have studied a planar interface between a negative uniaxial substrate and a positive uniaxial cover and theoretically shown that when the constitutive parameters satisfy certain requirements (see eq. 5.10), this interface can support D'yakonov surface waves. In addition to guided DSW modes, this structure can also support leaky DSW modes, subject to the requirements in eq. 5.11 being met, where energy is radiated away from the surface mode via the radiation channel provided by the ordinary wave in the substrate. It is also possible to find points where the application of the boundary conditions at the interface results in the amplitude of the radiation channel becoming zero by studying the intersection of the DSW solution with the solution of the auxiliary condition. This leads to the formation of a surface BIC that we term the DSW BIC. This DSW BIC is neither a PS BIC nor an INT BIC. It is a BIC that is obtained by parameter tuning and arises as a consequence of the boundary conditions at the interface.

The DSWs that we have studied exist for different orientations of the optic axes in the substrate and the cover. We have shown in Fig. 5.5 that guided and leaky DSWs exist for various values of the azimuthal offset Δ between the cover and the substrate optic axes. The DSW solutions continue to exist even when one or both optic axes are moved out of the interface plane.

We have thus found a new combination of materials that support guided and leaky DSWs and have shown that an infinite interface involving a negative uniaxial material can support a DSW. We have also related the DSWs that exist at interfaces involving anisotropic materials to BICs that exist in anisotropic planar structures.

Chapter 6

Summary and Conclusions

We have studied the cancellation of radiation from modes in anisotropic planar structures comprising uniaxial materials that exist in the part of the spectrum that corresponds to the radiation continuum. Typically these modes would attenuate as they propagate due to radiative leakage since the modes are above the light line and they would couple to the continuum of radiation modes. We have focused on investigating situations where the coupling to the continuum was cancelled due to different mechanisms. The cancellation of radiative loss from these modes led to the creation of bound states in the continuum (BICs) [9, 10] or unidirectional guided resonances (UGRs) [120] depending on the structure that was studied.

We started by studying structures that couple to the radiation continuum via only one channel in Chapter 3. The structures studied in this chapter comprise a uniaxial core and a uniaxial substrate with an isotropic cover. We have studied modes supported by this structure which radiate energy away from the core to the continuum of radiation modes in the substrate using the leaky mode formalism. The imaginary part of the mode propagation constant approximated the loss from the mode and we found points on the leaky mode sheet where the imaginary part was zero, meaning there was no loss. We used an auxiliary condition to verify that these were the points where the amplitude of the radiation channel was zero. Therefore, these were bound states that exist above the light line, or BICs [117]. These anisotropic planar structures supported two kinds of BICs. They could support polarisation separable (PS) BICs that existed due to the orthogonality of the mode and the radiation channel. Since anisotropic structures

generally support hybrid modes, they were usually not orthogonal to the radiation channel. The question of orthogonality due to a TE (TM) mode and a TM (TE) radiation channel arose only for specific optic axes orientations, when the propagation direction coincided with one of the principal axes of the dielectric tensors of the uniaxial materials. Therefore, the PS BICs were only found at points where both the cover and substrate optic axes made right angles with the direction of propagation. There were also BICs that were found for other optic axis orientations, not along the principal axes. These BICs arose due to the cancellation of radiation in the radiation channel resulting from the mixing of waves at the interfaces. The mixing led to destructive interference of the basis waves so that the amplitude of the basis wave corresponding to the radiation channel was zero. Therefore we called them interference (INT) BICs.

At the beginning of Chapter 3 we derived the analytic expressions for the basis waves in uniaxial materials and then used these waves to derive the dispersion equation and the auxiliary condition which we then used to find the leaky modes and BICs supported by this structure. We applied this theoretical framework to study the impact of the variation of optic axis orientation on the BICs supported by this structure. The structure itself was asymmetric, but beyond the geometric symmetry of the structure, in this section we uncovered the impact of anisotropy-symmetry which was defined by the relative orientations of the optic axes of the core and the substrate. We had full anisotropy-symmetry when both optic axes laid in the interface plane and were aligned. A non-zero offset between the two optic axes or their projections in the interface plane was defined as azimuthal anisotropy-symmetry breaking. Taking either optic axis out of the interface plane was defined as polar anisotropy-symmetry breaking. We studied two different waveguide structures. The first had a positive uniaxial core and a negative uniaxial substrate and the second had a negative uniaxial core and positive uniaxial substrate. In both cases we found that the structures supported lines of INT and PS BICs on the leaky mode sheet when full anisotropy-symmetry was maintained with a symmetric distribution of the INT BICs about the $\phi = 90^\circ$ line. Breaking azimuthal anisotropy-symmetry resulted in a distortion of the BIC lines of existence and the symmetry of the distribution of BICs about the $\phi = 90^\circ$ line on the leaky mode sheet was broken. Since the substrate and cover optic axis could not simultaneously be at right angles to the

direction of propagation in this configuration, azimuthal anisotropy-symmetry breaking led to the disappearance of PS BICs and only INT BICs were supported. Polar anisotropy-symmetry breaking led to the collapse of the BIC lines to discrete INT BIC points. This transition was explained by the interplay of the solutions of the dispersion equation and the auxiliary condition. We found that in the phase map of the radiation channel amplitude the lines of BICs corresponded to discontinuities. Breaking the polar anisotropy-symmetry led to the collapse of these lines of discontinuities to a phase singularity characterised by a screw phase dislocation about the BIC point on the phase map. Depending on whether the phase grew about the singularity of the BIC point in a clockwise or a counter clockwise direction, we assigned a winding number to it. We found that under continuous variation of the optic axes configurations, the discrete BIC points could meet in the parameter space. BICs stopped existing when BICs with opposite winding numbers met in the parameter space or when they moved beyond the leaky mode cutoff. Otherwise, the BIC points were robust to the variation of optic axis orientation. We would like to stress again that all of this occurred due to the breaking of anisotropy-symmetry, not a geometric or a material symmetry. Anisotropy-symmetry had such a drastic impact because different configurations of the optic axes brought different elements of the dielectric permittivity tensor into play and since we were dealing with full vector modes where all three field components had to be considered, the appearance of the new terms had substantial impact on the mixing of the waves at the interfaces. The discrete BIC points on the leaky mode sheet that we obtained upon anisotropy-symmetry breaking could lend themselves for use as tunable spatial and spectral filters providing selective transmission in direction as well as in frequency. The essential points from the work presented in this section can be found in our paper in Ref. [134]. The theoretical framework developed for the study of these structures has also been used to study modes in structures involving hyperbolic materials in Ref. [183].

In the next section of Chapter 3 we studied the impact of the variation of the constitutive parameters on the existence of BICs in the two aforementioned waveguide structures with full anisotropy-symmetry. Variation of the refractive indices changed the cutoff of the leaky mode which was determined by the point at which a second radiation channel became accessible or where the available radiation channel was

closed. The PS BICs arose due to geometric considerations and therefore the variation of the refractive indices of the materials constituting the waveguides only impacted the existence of the PS BICs insofar as they changed the mode cutoff. On the other hand since the existence of the INT BICs depended on the phase accumulated by the various basis waves, the variation of the refractive indices of the materials constituting the waveguide had substantial impact on their existence. We found that the variation of the film indices had the maximum impact on the INT BICs while the impact of the variation of the cover and substrate indices was more muted. We found that, in one of the structures, variation of the indices could bring lines of INT BICs closer in ϕ till they met and then separated in D/λ. For greater understanding of the impact of refractive index variation, we calculated the values of D/λ within which INT BICs existed as a function of some of the indices and plotted them as bands. We found that the widths of the bands could change and the bands could merge or split depending on which refractive index was being varied. We also studied the possibility of using these structures and the BICs they supported as sensors since the BICs existed for different propagation directions depending on the cover refractive index. The most important takeaway from this section was that lines of BICs were continuously transformed by the variation of refractive indices. Therefore we could design real systems which support these BICs and all of the properties being studied would translate to those structures with different materials. Our paper in Ref. [135] provides an overview of the important results from this section.

We moved to the study of structures with two radiation channels in Chapter 4. We studied structures with a uniaxial cover, a uniaxial core and a uniaxial substrate. One of the radiation channels coupled to the continuum of radiation modes in the cover and the other radiation channel coupled to the continuum in the substrate. At the beginning of chapter 4 we made slight modifications to the theory developed in Chapter 3 so that it could be applied to structures with two radiation channels. The first structure we studied comprised identical negative uniaxial materials in the cover and the substrate and and a different negative uniaxial material in the core. We found that the structure supported lines of INT BICs as long as it remained mirror symmetric about the $x = 0$ plane (that was parallel to the interfaces and ran through the midpoint of the core) and polar anisotropy-symmetry was maintained. In this scenario, the two radiation channels were equiv-

alent and radiation into the two channels was identical. The lines of BICs collapsed to discrete points when the mirror symmetry was broken either by having different azimuthal orientations of the cover and substrate optic axes, or by introducing a different material in either the cover or the substrate. The drop in dimension of the BIC solution due to the breaking of the mirror symmetry and the equivalence of the radiation channels could be explained by the additional constraint of another auxiliary condition, corresponding to the second, now distinct, radiation channel, having to be satisfied. These discrete point BICs corresponded to phase singularities in the phase maps of both radiation channels and therefore were robust and could be tuned. The results regarding the existence of BICs in this structure can be found in our paper in Ref. [136]. When mirror symmetry was broken, the radiation channels were distinct and we found that the radiation into the two channels was no longer identical. Breaking polar anisotropy-symmetry resulted in the BIC lines either collapsing to BIC points or disappearing altogether. More importantly, when polar anisotropy-symmetry was broken in conjunction with the mirror symmetry, the structure supported UGRs. These were unbound modes where energy from the core was radiated in only one of the radiation channels while the amplitude of the other radiation channel went to zero. UGRs were characterised by phase singularities that could be assigned a winding number in the phase map of the radiation channel whose amplitude went to zero. These UGRs were robust and existed whenever any one of the three optic axes were moved out of the interface plane and the structure was not mirror symmetric. They existed when the auxiliary condition corresponding to only one of the two radiation channels was met. The results regarding the existence of UGRs in this structure can be found in our paper in Ref. [137]. Finally, we clarified that these properties of structures with two radiation channels were general and also held in waveguides comprising different kinds of uniaxial materials. UGRs in anisotropic planar structures provided the possibility of easy switching of the direction of radiation upon a simple rotation of the sample or optic axis. Unidirectional radiation might have important applications in various devices such as on-chip lasers, directional optical antennas, or directional couplers, and the results of Chapter 4 opened the possibility of their implementation in off-axis anisotropic structures.

Chapter 5 dealt with the study of D'yakonov surface waves (DSWs)

[155, 157] at the interface of a positive uniaxial cover and a negative uniaxial substrate. We developed the theoretical framework needed to study guided and leaky surface waves at this interface and then applied it to study surface modes supported at the interface of this structure. We found that DSWs could be supported at this interface. Moreover, we found that the DSW transitioned to a leaky DSW when the value of the DSW propagation constant was below the ordinary refractive index of the substrate. Though the leaky DSW involved radiation away from the interface as the mode propagated, there was substantial localisation of the field at the interface. We studied the solutions of the auxiliary condition and the points where they intersected with the leaky DSW solution, to find the points where the radiation channel amplitude went to zero. These were the points where we obtained DSW BICs that remained localised at the interface even though a radiation channel was available. Therefore we found a new class of surface BICs. These BICs were neither PS BICs nor INT BICs but BICs that arose at the interface due to the boundary conditions when only one of the basis waves in the substrate, the confined extraordinary wave, matched the field comprising the two basis waves of the cover. We found that the DSW existed for a range of values of the azimuthal offset between the cover and the substrate optic axes. For certain values of the offset the structure only supported guided DSW modes and for certain other values of the offset between the axes, the structure supported only leaky DSW modes. Between these two ranges, the DSW mode featured a guided to leaky mode transition. Varying the constitutive parameters of the interface resulted in the DSW solutions being displaced in the parameter space but they continued to exist, showing that they were robust.

Thus, in this thesis, we explored the cancellation of radiation in anisotropic planar waveguides. We have found that radiation in all available channels could be cancelled to obtain BICs or radiation could be cancelled in all but one channel to obtain UGRs. We studied the fundamental role that anisotropy-symmetry played in the existence of these full vector BICs and UGRs. We also studied the impact of the variation of the constitutive parameters on the BICs. We uncovered a new combination of materials that supported guided and leaky DSWs at their interface and linked the DSW to a fundamentally new kind of anisotropy induced BIC.

List of Publications

- Mukherjee, S., Gomis-Bresco, J., Pujol-Closa, P., Artigas, D., and Torner, L. Topological properties of bound states in the continuum in geometries with broken anisotropy symmetry. Physical Review A 98, 063826 (2018).

- Mukherjee, S., Gomis-Bresco, J., Pujol-Closa, P., Artigas, D., and Torner, L. Angular control of anisotropy-induced bound states in the continuum. Optics Letters 44, 5362 (2019).

- Mukherjee, S., Gomis-Bresco, J., Artigas, D., and Torner, L. Solitary Spectrally-Discrete Bound States in the Continuum in an Open System. arXiv:2010.13869 (2020).

- Mukherjee, S., Gomis-Bresco, J., Artigas, D., and Torner, L. Unidirectional guided resonances in anisotropic waveguides. Optics Letters 46, 2545–2548 (2021).

- Pujol-Closa, P., Gomis-Bresco, J., Mukherjee, S., Gómez-Díaz, J. S., Torner, L., and Artigas, D. Slow light mediated by mode topological transitions in hyperbolic waveguides. Optics Letters 46, 58–61 (2021).

Outlook

Over the course of the investigation undertaken for the purpose of this thesis we have significantly enhanced our understanding of the modes, BICs and UGRs in structures comprising uniaxial guided materials. We can now harness this understanding to spur new directions of research.

- Since PS BICs require a guiding profile for one set of refractive indices, they are standard TE/TM modes of anisotropic waveguides that have been used in various integrated optics settings. However, it was not properly appreciated that they were BICs. The existence of PS BICs in anisotropic planar structures was experimentally demonstrated by our group in Ref. [117]. As discussed in the section 1.4, the existence of minima of leaky-wave losses was also know in special geometries. We have demonstrated that these are INT BICs and a general phenomenon. To the best of

our knowledge, these INT BICs have never been observed experimentally. Thus, a major challenge that is important from a fundamental as well as applied standpoint that remains open is the experimental realization of such BICs in robust integrated-optical structures. Given our understanding of BICs in single channel structures, we can now fabricate a suitable waveguide and attempt to experimentally demonstrate the existence of INT BICs. We have started work on an experiment involving ion-exchanged lithium niobate waveguides to experimentally demonstrate the existence of INT BICs. If that were to be achieved, the experimental line could be pursued further to develop tunable spatial and spectral filters using these INT BICs.

- Another possible experiment would involve the demonstration of the existence of UGRs in anisotropic waveguides.

- We have restricted our theoretical study to waveguides containing only uniaxial materials. Another possible direction of theoretical research would be to extend the study to waveguides containing biaxial materials and to study the existence and properties of BICs and UGRs in them.

- We have also studied structures that are limited only in one spatial dimension while being infinite in the other two directions. It might be interesting to theoretically study finite size effects on the existence of BICs by limiting another spatial dimension. There have already been some studies along these lines for BICs in structures containing only one layer of anisotropic material [101, 102]. We would like to extend this to structures comprising multiple anisotropic materials. We already have some preliminary results in this area but the topic requires further study.

- We have also limited ourselves to linear materials. It would be interesting to explore the impact of nonlinearity on existence of BICs in anisotropic materials, particularly given the proposals for the application of BICs to design high Q-factor cavities for use in nonlinear optics [62, 84].

Therefore, we submit that the work done in this thesis opens up several avenues for both theoretical and experimental research in the future in

the area of of waveguide photonics, from a fundamental as well as an applied viewpoint.

Bibliography

1. Griffiths, D. J. *Introduction to electrodynamics* 4th ed. Re-published by Cambridge University Press in 2017 (Pearson, Boston, MA, 2013).
2. Jackson, J. D. *Classical electrodynamics* 3rd ed. (Wiley, New York, NY, 1999).
3. Landau, L. D., Bell, J., Kearsley, M., Pitaevskii, L., Lifshitz, E. & Sykes, J. *Electrodynamics of continuous media* (Elsevier, 2013).
4. Hondros, D. & Debye, P. Electromagnetic waves in dielectric wires. *Annalen der Physik* **32,** 465 (1910).
5. Kapany, N. S. & Burke, J. J. *Optical Waveguides* 1st ed. (Elsevier, 1972).
6. Dutta Gupta, S., Ghosh, N. & Banerjee, A. *Wave Optics. Basic Concepts and Contemporary Trends* 1st ed. (CRC Press, 2015).
7. Joannopoulos, J. D., Johnson, S. G., Winn, J. N. & Meade, R. D. *Photonic Crystals: Molding the Flow of Light (Second Edition)* 2nd ed. (Princeton University Press, 2008).
8. Hu, J. & Menyuk, C. R. Understanding leaky modes: slab waveguide revisited. *Advances in Optics and Photonics* **1,** 58 (2009).
9. Hsu, C. W., Zhen, B., Stone, A. D., Joannopoulos, J. D. & Soljačić, M. Bound states in the continuum. *Nature Reviews Materials* **1** (2016).
10. Von Neuman, J. & Wigner, E. Uber merkwürdige diskrete Eigenwerte. Uber das Verhalten von Eigenwerten bei adiabatischen Prozessen. *Zeitschrift für Physik* **30,** 467–470 (1929).
11. Stillinger, F. H. & Herrick, D. R. Bound states in the continuum. *Physical Review A* **11,** 446–454 (1975).

12. Friedrich, H. & Wintgen, D. Interfering resonances and bound states in the continuum. *Physical Review A* **32,** 3231–3242 (1985).

13. Parker, R. Resonance effects in wake shedding from parallel plates: Some experimental observations. *Journal of Sound and Vibration* **4,** 62–72 (1966).

14. Kartashov, Y. V., Konotop, V. V. & Torner, L. Bound states in the continuum in spin-orbit-coupled atomic systems. *Physical Review A* **96,** 033619 (2017).

15. Marinica, D. C., Borisov, A. G. & Shabanov, S. V. Bound States in the Continuum in Photonics. *Physical Review Letters* **100,** 183902 (2008).

16. Bulgakov, E. N. & Sadreev, A. F. Bound states in the continuum in photonic waveguides inspired by defects. *Physical Review B* **78,** 075105 (2008).

17. Plotnik, Y., Peleg, O., Dreisow, F., Heinrich, M., Nolte, S., Szameit, A. & Segev, M. Experimental Observation of Optical Bound States in the Continuum. *Physical Review Letters* **107,** 183901 (2011).

18. Hsu, C. W., Zhen, B., Lee, J., Chua, S.-L., Johnson, S. G., Joannopoulos, J. D. & Soljačić, M. Observation of trapped light within the radiation continuum. *Nature* **499,** 188–191 (2013).

19. Cerjan, A., Hsu, C. W. & Rechtsman, M. C. Bound States in the Continuum through Environmental Design. *Physical Review Letters* **123,** 023902 (2019).

20. Bulgakov, E. N. & Maksimov, D. N. Topological Bound States in the Continuum in Arrays of Dielectric Spheres. *Physical Review Letters* **118,** 267401 (2017).

21. Hsu, C. W., Zhen, B., Chua, S.-L., Johnson, S. G., Joannopoulos, J. D. & Soljačić, M. Bloch surface eigenstates within the radiation continuum. *Light: Science and Applications* **2,** e84–e84 (2013).

22. Bulgakov, E. N. & Sadreev, A. F. Bloch bound states in the radiation continuum in a periodic array of dielectric rods. *Physical Review A* **90,** 053801 (2014).

23. Bulgakov, E. N. & Sadreev, A. F. Robust bound state in the continuum in a nonlinear microcavity embedded in a photonic crystal waveguide. *Optics Letters* **39,** 5212 (2014).

24. Bulgakov, E. N. & Sadreev, A. F. Light trapping above the light cone in a one-dimensional array of dielectric spheres. *Physical Review A* **92,** 023816 (2015).

25. Bulgakov, E. N. & Sadreev, A. F. Bound states in the continuum with high orbital angular momentum in a dielectric rod with periodically modulated permittivity. *Physical Review A* **96,** 013841 (2017).

26. Sadrieva, Z. F., Belyakov, M. A., Balezin, M. A., Kapitanova, P. V., Nenasheva, E. A., Sadreev, A. F. & Bogdanov, A. A. Experimental observation of a symmetry-protected bound state in the continuum in a chain of dielectric disks. *Physical Review A* **99,** 053804 (2019).

27. Sidorenko, M. S., Sergaeva, O. N., Sadrieva, Z. F., Roques-Carmes, C., Muraev, P. S., Maksimov, D. N. & Bogdanov, A. A. Observation of an accidental bound state in the continuum in a chain of dielectric disks. *Physical Review Applied* **15,** 034041 (2021).

28. Gansch, R., Kalchmair, S., Genevet, P., Zederbauer, T., Detz, H., Andrews, A. M., Schrenk, W., Capasso, F., Lončar, M. & Strasser, G. Measurement of bound states in the continuum by a detector embedded in a photonic crystal. *Light: Science and Applications* **5,** e16147–e16147 (2016).

29. Li, L. & Yin, H. Bound States in the Continuum in double layer structures. *Scientific Reports* **6,** 26988 (2016).

30. Cerjan, A., Jörg, C., Vaidya, S., Augustine, S., Benalcazar, W. A., Hsu, C. W., von Freymann, G. & Rechtsman, M. C. Creating Bound States in the Continuum using Three-Dimensional Photonic Crystal Environments. *arXiv:2104.09603* (2021).

31. Benalcazar, W. A. & Cerjan, A. Bound states in the continuum of higher-order topological insulators. *Physical Review B* **101,** 161116 (2020).

32. Cerjan, A., Jürgensen, M., Benalcazar, W. A., Mukherjee, S. & Rechtsman, M. C. Observation of a Higher-Order Topological Bound State in the Continuum. *Physical Review Letters* **125,** 213901 (2020).

33. Monticone, F. & Alù, A. Bound states within the radiation continuum in diffraction gratings and the role of leaky modes. *New Journal of Physics* **19,** 093011 (2017).

34. Gao, X., Zhen, B., Soljačić, M., Chen, H. & Hsu, C. W. Bound States in the Continuum in Fiber Bragg Gratings. *ACS Photonics* **6,** 2996–3002 (2019).

35. Azzam, S. I., Shalaev, V. M., Boltasseva, A. & Kildishev, A. V. Formation of Bound States in the Continuum in Hybrid Plasmonic-Photonic Systems. *Physical Review Letters* **121** (2018).

36. Kikkawa, R., Nishida, M. & Kadoya, Y. Polarization-based branch selection of bound states in the continuum in dielectric waveguide modes anti-crossed by a metal grating. *New Journal of Physics* **21,** 113020 (2019).

37. Kikkawa, R., Nishida, M. & Kadoya, Y. Bound states in the continuum and exceptional points in dielectric waveguide equipped with a metal grating. *New Journal of Physics* **22,** 073029 (2020).

38. Kim, S., Kim, K.-H. & Cahoon, J. F. Optical Bound States in the Continuum with Nanowire Geometric Superlattices. *Physical Review Letters* **122,** 187402 (2019).

39. Koshelev, K., Kruk, S., Melik-Gaykazyan, E., Choi, J.-H., Bogdanov, A., Park, H.-G. & Kivshar, Y. Subwavelength dielectric resonators for nonlinear nanophotonics. *Science* **367,** 288–292 (2020).

40. Azzam, S. I., Chaudhuri, K., Shalaev, V. M., Boltasseva, A. & Kildishev, A. V. *High Q-Factor All-Dielectric Metasurface Based on Bound States in the Continuum* in *2019 Conference on Lasers and Electro-Optics (CLEO)* (2019), 1–2.

41. Shi, T., Deng, Z., Tu, Q.-A., Cao, Y. & Li, X. Displacement-mediated bound states in the continuum in all-dielectric superlattice metasurfaces. *PhotoniX* **2** (2021).

42. Koshelev, K., Bogdanov, A. & Kivshar, Y. Meta-optics and bound states in the continuum. *Science Bulletin* **64,** 836–842 (2019).

43. Longhi, S. Bound states in the continuum in PT-symmetric optical lattices. *Optics Letters* **39,** 1697–1700 (2014).

44. Longhi, S. & Della Valle, G. Optical lattices with exceptional points in the continuum. *Physical Review A* **89,** 052132 (2014).

45. Molina, M. I. & Kivshar, Y. S. Embedded States in the Continuum for -Symmetric Systems. *Studies in Applied Mathematics* **133,** 337–350 (2014).

46. Kartashov, Y. V., Milián, C., Konotop, V. V. & Torner, L. Bound states in the continuum in a two-dimensional PT-symmetric system. *Optics Letters* **43,** 575 (2018).

47. Song, Q., Hu, J., Dai, S., Zheng, C., Han, D., Zi, J., Zhang, Z. Q. & Chan, C. T. Coexistence of a new type of bound state in the continuum and a lasing threshold mode induced by PT symmetry. *Science Advances* **6** (2020).

48. Silveirinha, M. G. Trapping light in open plasmonic nanostructures. *Physical Review A* **89,** 023813 (2014).

49. Monticone, F. & Alù, A. Embedded Photonic Eigenvalues in 3D Nanostructures. *Physical Review Letters* **112,** 213903 (2014).

50. Li, L., Zhang, J., Wang, C., Zheng, N. & Yin, H. Optical bound states in the continuum in a single slab with zero refractive index. *Physical Review A* **96,** 013801 (2017).

51. Minkov, M., Williamson, I. A. D., Xiao, M. & Fan, S. Zero-Index Bound States in the Continuum. *Physical Review Letters* **121,** 263901 (2018).

52. Penunuri, D. & Lakin, K. *Leaky Surface Wave Propagation on Si, GaAs, GaP , Al_2O_3 and Quartz* in *1975 Ultrasonics Symposium* (1975), 478–483.

53. Stegeman, G. I. Normal-mode surface waves in the pseudobranch on the (001) plane of gallium arsenide. *Journal of Applied Physics* **47,** 1712–1713 (1976).

54. Molina, M. I., Miroshnichenko, A. E. & Kivshar, Y. S. Surface Bound States in the Continuum. *Physical Review Letters* **108,** 070401 (2012).

55. Corrielli, G., Della Valle, G., Crespi, A., Osellame, R. & Longhi, S. Observation of Surface States with Algebraic Localization. *Physical Review Letters* **111,** 220403 (2013).

56. Weimann, S., Xu, Y., Keil, R., Miroshnichenko, A. E., Tünnermann, A., Nolte, S., Sukhorukov, A. A., Szameit, A. & Kivshar, Y. S. Compact Surface Fano States Embedded in the Continuum of Waveguide Arrays. *Physical Review Letters* **111,** 240403 (2013).

57. Hu, Z. & Lu, Y. Y. Propagating bound states in the continuum at the surface of a photonic crystal. *Journal of the Optical Society of America B* **34,** 1878–1883 (2017).

58. Zhen, B., Hsu, C. W., Lu, L., Stone, A. D. & Soljačić, M. Topological Nature of Optical Bound States in the Continuum. *Physical Review Letters* **113,** 257401 (2014).

59. Bykov, D. A., Bezus, E. A. & Doskolovich, L. L. Bound states in the continuum and strong phase resonances in integrated Gires-Tournois interferometer. *Nanophotonics* **9,** 83–92 (2020).

60. Doeleman, H. M., Monticone, F., den Hollander, W., Alù, A. & Koenderink, A. F. Experimental observation of a polarization vortex at an optical bound state in the continuum. *Nature Photonics* **12,** 397–401 (2018).

61. Zhang, Y., Chen, A., Liu, W., Hsu, C. W., Wang, B., Guan, F., Liu, X., Shi, L., Lu, L. & Zi, J. Observation of Polarization Vortices in Momentum Space. *Physical Review Letters* **120,** 186103 (2018).

62. Jin, J., Yin, X., Ni, L., Soljačić, M., Zhen, B. & Peng, C. Topologically enabled ultrahigh-Q guided resonances robust to out-of-plane scattering. *Nature* **574,** 501–504 (2019).

63. Kang, M., Zhang, S., Xiao, M. & Xu, H. Merging Bound States in the Continuum at Off-High Symmetry Points. *Physical Review Letters* **126,** 117402 (2021).

64. Wang, B., Liu, W., Zhao, M., Wang, J., Zhang, Y., Chen, A., Guan, F., Liu, X., Shi, L. & Zi, J. Generating optical vortex beams by momentum-space polarization vortices centred at bound states in the continuum. *Nature Photonics* **14,** 623–628 (2020).

65. Liu, W., Wang, B., Zhang, Y., Wang, J., Zhao, M., Guan, F., Liu, X., Shi, L. & Zi, J. Circularly Polarized States Spawning from Bound States in the Continuum. *Physical Review Letters* **123,** 116104 (2019).

66. Yoda, T. & Notomi, M. Generation and Annihilation of Topologically Protected Bound States in the Continuum and Circularly Polarized States by Symmetry Breaking. *Physical Review Letters* **125,** 053902 (2020).

67. Ye, W., Gao, Y. & Liu, J. Singular Points of Polarizations in the Momentum Space of Photonic Crystal Slabs. *Physical Review Letters* **124,** 153904 (2020).

68. Sadrieva, Z. F., Sinev, I. S., Koshelev, K. L., Samusev, A., Iorsh, I. V., Takayama, O., Malureanu, R., Bogdanov, A. A. & Lavrinenko, A. V. Transition from Optical Bound States in the Continuum to Leaky Resonances: Role of Substrate and Roughness. *ACS Photonics* **4,** 723–727 (2017).

69. Taghizadeh, A. & Chung, I.-S. Quasi bound states in the continuum with few unit cells of photonic crystal slab. *Applied Physics Letters* **111,** 031114 (2017).

70. Bulgakov, E. N. & Maksimov, D. N. Light enhancement by quasi-bound states in the continuum in dielectric arrays. *Optics Express* **25,** 14134–14147 (2017).

71. Yuan, L. & Lu, Y. Y. Perturbation theories for symmetry-protected bound states in the continuum on two-dimensional periodic structures. *Physical Review A* **101,** 043827 (2020).

72. Hu, Z. & Lu, Y. Y. Resonances and bound states in the continuum on periodic arrays of slightly noncircular cylinders. *Journal of Physics B* **51,** 035402 (2018).

73. Koshelev, K., Lepeshov, S., Liu, M., Bogdanov, A. & Kivshar, Y. Asymmetric Metasurfaces with High-Q Resonances Governed by Bound States in the Continuum. *Physical Review Letters* **121,** 193903 (2018).

74. Han, S., Pitchappa, P., Wang, W., Srivastava, Y. K., Rybin, M. V. & Singh, R. Extended Bound States in the Continuum with Symmetry-Broken Terahertz Dielectric Metasurfaces. *Advanced Optical Materials* **9,** 2002001 (2021).

75. Hu, Z., Yuan, L. & Lu, Y. Y. Bound states with complex frequencies near the continuum on lossy periodic structures. *Physical Review A* **101,** 013806 (2020).

76. Koshelev, K., Tang, Y., Li, K., Choi, D.-Y., Li, G. & Kivshar, Y. Nonlinear Metasurfaces Governed by Bound States in the Continuum. *ACS Photonics* **6,** 1639–1644 (2019).

77. Overvig, A., Yu, N. & Alù, A. Chiral Quasi-Bound States in the Continuum. *Physical Review Letters* **126,** 073001 (2021).

78. Abujetas, D. R., Barreda, Á., Moreno, F., Sáenz, J. J., Litman, A., Geffrin, J.-M. & Sánchez-Gil, J. A. Brewster quasi bound states in the continuum in all-dielectric metasurfaces from single magnetic-dipole resonance meta-atoms. *Scientific Reports* **9,** 16048 (2019).

79. Overvig, A. C., Malek, S. C., Carter, M. J., Shrestha, S. & Yu, N. Selection rules for quasibound states in the continuum. *Physical Review B* **102,** 035434 (2020).

80. Linton, C. M. & McIver, P. Embedded trapped modes in water waves and acoustics. *Wave Motion* **45,** 16–29 (2007).

81. Vallejo, M. L., Guevara, M. L. L. d. & Orellana, P. A. Triple Rashba dots as a spin filter: Bound states in the continuum and Fano effect. *Physics Letters A* **374,** 4928–4932 (2010).

82. Ramos, J. P. & Orellana, P. A. Bound states in the continuum and spin filter in quantum-dot molecules. *Physica B* **455,** 66–70 (2014).

83. Yoon, J. W., Song, S. H. & Magnusson, R. Critical field enhancement of asymptotic optical bound states in the continuum. *Scientific Reports* **5,** 18301 (2015).

84. Rybin, M. V., Koshelev, K. L., Sadrieva, Z. F., Samusev, K. B., Bogdanov, A. A., Limonov, M. F. & Kivshar, Y. S. High-Q Supercavity Modes in Subwavelength Dielectric Resonators. *Physical Review Letters* **119,** 243901 (2017).

85. Carletti, L., Koshelev, K., De Angelis, C. & Kivshar, Y. Giant Nonlinear Response at the Nanoscale Driven by Bound States in the Continuum. *Physical Review Letters* **121,** 033903 (2018).

86. Liu, Z., Xu, Y., Lin, Y., Xiang, J., Feng, T., Cao, Q., Li, J., Lan, S. & Liu, J. High-Q Quasibound States in the Continuum for Nonlinear Metasurfaces. *Physical Review Letters* **123,** 253901 (2019).

87. Minkov, M., Gerace, D. & Fan, S. Doubly resonant $\chi^{(2)}$ nonlinear photonic crystal cavity based on a bound state in the continuum. *Optica* **6,** 1039–1045 (2019).

88. Wang, J., Clementi, M., Minkov, M., Barone, A., Carlin, J.-F., Grandjean, N., Gerace, D., Fan, S., Galli, M. & Houdré, R. Doubly resonant second-harmonic generation of a vortex beam from a bound state in the continuum. *Optica* **7,** 1126–1132 (2020).

89. Liu, Y., Zhou, W. & Sun, Y. Optical Refractive Index Sensing Based on High-Q Bound States in the Continuum in Free-Space Coupled Photonic Crystal Slabs. *Sensors* **17** (2017).

90. Romano, S., Lamberti, A., Masullo, M., Penzo, E., Cabrini, S., Rendina, I. & Mocella, V. Optical Biosensors Based on Photonic Crystals Supporting Bound States in the Continuum. *Materials* **11,** 526 (2018).

91. Yesilkoy, F., Arvelo, E. R., Jahani, Y., Liu, M., Tittl, A., Cevher, V., Kivshar, Y. & Altug, H. Ultrasensitive hyperspectral imaging and biodetection enabled by dielectric metasurfaces. *Nature Photonics* **13,** 390–396 (2019).

92. Romano, S., Zito, G., Torino, S., Calafiore, G., Penzo, E., Coppola, G., Cabrini, S., Rendina, I. & Mocella, V. Label-free sensing of ultralow-weight molecules with all-dielectric metasurfaces supporting bound states in the continuum. *Photonics Research* **6,** 726–733 (2018).

93. Romano, S., Zito, G., Lara Yépez, S. N., Cabrini, S., Penzo, E., Coppola, G., Rendina, I. & Mocellaark, V. Tuning the exponential sensitivity of a bound-state-in-continuum optical sensor. *Optics Express* **27,** 18776 (2019).

94. Maksimov, D. N., Gerasimov, V. S., Romano, S. & Polyutov, S. P. Refractive index sensing with optical bound states in the continuum. *Optics Express* **28,** 38907 (2020).

95. Vyas, H. & Hegde, R. S. Improved refractive-index sensing performance in medium contrast gratings by asymmetry engineering. *Optical Materials Express* **10,** 1616–1629 (2020).

96. Hirose, K., Liang, Y., Kurosaka, Y., Watanabe, A., Sugiyama, T. & Noda, S. Watt-class high-power, high-beam-quality photonic-crystal lasers. *Nature Photonics* **8,** 406–411 (2014).

97. Kodigala, A., Lepetit, T., Gu, Q., Bahari, B., Fainman, Y. & Kanté, B. Lasing action from photonic bound states in continuum. *Nature* **541,** 196–199 (2017).

98. Huang, C., Zhang, C., Xiao, S., Wang, Y., Fan, Y., Liu, Y., Zhang, N., Qu, G., Ji, H., Han, J., Ge, L., Kivshar, Y. & Song, Q. Ultrafast control of vortex microlasers. *Science* **367,** 1018–1021 (2020).

99. Midya, B. & Konotop, V. V. Coherent-perfect-absorber and laser for bound states in a continuum. *Optics Letters* **43,** 607 (2018).

100. Hayran, Z. & Monticone, F. Capturing Broadband Light in a Compact Bound State in the Continuum. *arXiv:2006.03699,* 1–21 (2020).

101. Yu, Z., Xi, X., Ma, J., Tsang, H. K., Zou, C.-L. & Sun, X. Photonic integrated circuits with bound states in the continuum. *Optica* **6,** 1342–1348 (2019).

102. Yu, Z., Tong, Y., Tsang, H. K. & Sun, X. High-dimensional communication on etchless lithium niobate platform with photonic bound states in the continuum. *Nature Communications* **11** (2020).

103. Koshelev, K., Favraud, G., Bogdanov, A., Kivshar, Y. & Fratalocchi, A. Nonradiating photonics with resonant dielectric nanostructures. *Nanophotonics* **8,** 725–745 (2019).

104. Sadreev, A. F. Interference traps waves in an open system: bound states in the continuum. *Reports on Progress in Physics* **84,** 055901 (2021).

105. Suematsu, Y. & Furuya, K. Quasi-Guided Modes and Related Radiation Losses in Optical Dielectric Waveguides with External Higher Index Surroundings. *IEEE Transactions on Microwave Theory and Techniques* **23,** 170–175 (1975).

106. Marcuvitz, N. On field representations in terms of leaky modes or Eigenmodes. *IRE Transactions on Antennas and Propagation* **4,** 192–194 (1956).

107. Monticone, F. & Alu, A. Leaky-Wave Theory, Techniques, and Applications: From Microwaves to Visible Frequencies. *Proceedings of the IEEE* **103,** 793–821 (2015).

108. Barone, S. *Leaky wave contributions to the field of a line source above a dielectric slab* tech. rep. (Microwave Research Institute, Polytechnic Institute of Brooklyn, 1956).

109. Barone, S. & Hessel, A. *Leaky wave contributions to the field of a line source above a dielectric slab—part II* tech. rep. (Microwave Research Institute, Polytechnic Institute of Brooklyn, 1958).

110. Cassedy, E. & Cohn, M. On the Existence of Leaky Waves Due to a Line Source Above a Grounded Dielectric Slab. *IRE Transactions on Microwave Theory and Techniques* **9,** 243–247 (1961).

111. Marcuse, D. & Kaminow, I. Modes of a symmetric slab optical waveguide in birefringent media - Part II: Slab with coplanar optical axis. *IEEE Journal of Quantum Electronics* **15,** 92–101 (1979).

112. Knoesen, A., Gaylord, T. K. & Moharam, M. G. Hybrid guided modes in uniaxial dielectric planar waveguides. *Journal of Lightwave Technology* **6,** 1083–1104 (1988).

113. Torner, L., Canal, F. & Hernandez-Marco, J. Leaky modes in multilayer uniaxial optical waveguides. *Applied Optics* **29,** 2805 (1990).

114. Torner, L., Recolons, J. & Torres, J. P. Guided-to-leaky mode transition in uniaxial optical slab waveguides. *Journal of Lightwave Technology* **11,** 1592–1600 (1993).

115. Lu, M. & Fejer, M. M. Anisotropic dielectric waveguides. *Journal of the Optical Society of America A* **10,** 246 (1993).

116. Shipman, S. P. & Welters, A. T. Resonant electromagnetic scattering in anisotropic layered media. *Journal of Mathematical Physics* **54,** 103511 (2013).

117. Gomis-Bresco, J., Artigas, D. & Torner, L. Anisotropy-induced photonic bound states in the continuum. *Nature Photonics* **11,** 232–236 (2017).

118. Timofeev, I. V., Maksimov, D. N. & Sadreev, A. F. Optical defect mode with tunable Q factor in a one-dimensional anisotropic photonic crystal. *Physical Review B* **97,** 024306 (2018).

119. Pankin, P. S., Wu, B.-R., Yang, J.-H., Chen, K.-P., Timofeev, I. V. & Sadreev, A. F. One-dimensional photonic bound states in the continuum. *Communications Physics* **3** (2020).

120. Yin, X., Jin, J., Soljačić, M., Peng, C. & Zhen, B. Observation of topologically enabled unidirectional guided resonances. *Nature* **580,** 467–471 (2020).

121. Taillaert, D., Bienstman, P. & Baets, R. Compact efficient broadband grating coupler for silicon-on-insulator waveguides. *Optics Letters* **29,** 2749 (2004).

122. Vermeulen, D., Selvaraja, S., Verheyen, P., Lepage, G., Bogaerts, W., Absil, P., Van Thourhout, D. & Roelkens, G. High-efficiency fiber-to-chip grating couplers realized using an advanced CMOS-compatible Silicon-On-Insulator platform. *Optics Express* **18,** 18278 (2010).

123. Yaacobi, A., Sun, J., Moresco, M., Leake, G., Coolbaugh, D. & Watts, M. R. Integrated phased array for wide-angle beam steering. *Optics Letters* **39,** 4575 (2014).

124. Roncone, R. L., Li, L., Bates, K. A., Burke, J. J., Weisenbach, L. & Zelinski, B. J. J. Design and fabrication of a single leakage-channel grating coupler. *Applied Optics* **32,** 4522 (1993).

125. Kim, S.-H., Kim, S.-K. & Lee, Y.-H. Vertical beaming of wavelength-scale photonic crystal resonators. *Physical Review B* **73** (2006).

126. Wade, M. T., Pavanello, F., Kumar, R., Gentry, C. M., Atabaki, A., Ram, R., Stojanović, V. & Popović, M. A. *75% efficient wide bandwidth grating couplers in a 45 nm microelectronics CMOS process* in *2015 IEEE Optical Interconnects Conference (OI)* ISSN: 2376-8665 (2015), 46–47.

127. Wang, K. X., Yu, Z., Sandhu, S. & Fan, S. Fundamental bounds on decay rates in asymmetric single-mode optical resonators. *Optics Letters* **38,** 100 (2013).

128. Ota, Y., Iwamoto, S. & Arakawa, Y. Asymmetric out-of-plane power distribution in a two-dimensional photonic crystal nanocavity. *Optics Letters* **40,** 3372 (2015).

129. Zhou, H., Zhen, B., Hsu, C. W., Miller, O. D., Johnson, S. G., Joannopoulos, J. D. & Soljačić, M. Perfect single-sided radiation and absorption without mirrors. *Optica* **3,** 1079 (2016).

130. Rivera, N., Hsu, C. W., Zhen, B., Buljan, H., Joannopoulos, J. D. & Soljačić, M. Controlling Directionality and Dimensionality of Radiation by Perturbing Separable Bound States in the Continuum. *Scientific Reports* **6,** 33394 (2016).

131. Lee, S.-G., Kim, S.-H. & Kee, C.-S. Bound states in the continuum (BIC) accompanied by avoided crossings in leaky-mode photonic lattices. *Nanophotonics* **9,** 4373–4380 (2020).

132. Berreman, D. W. Optics in Stratified and Anisotropic Media: 4x4-Matrix Formulation. *Journal of the Optical Society of America* **62,** 502–510 (1972).

133. Taflove, A. & Hagness, S. C. *Computational electrodynamics: the finite-difference time-domain method* 3rd ed. (Artech House, Norwood, 2005).

134. Mukherjee, S., Gomis-Bresco, J., Pujol-Closa, P., Artigas, D. & Torner, L. Topological properties of bound states in the continuum in geometries with broken anisotropy symmetry. *Physical Review A* **98,** 063826 (2018).

135. Mukherjee, S., Gomis-Bresco, J., Pujol-Closa, P., Artigas, D. & Torner, L. Angular control of anisotropy-induced bound states in the continuum. *Optics Letters* **44,** 5362 (2019).

136. Mukherjee, S., Gomis-Bresco, J., Artigas, D. & Torner, L. Solitary Spectrally-Discrete Bound States in the Continuum in an Open System. *arXiv:2010.13869* (2020).

137. Mukherjee, S., Gomis-Bresco, J., Artigas, D. & Torner, L. Unidirectional guided resonances in anisotropic waveguides. *Optics Letters* **46,** 2545–2548 (2021).

138. Hodgkinson, I., Kassam, S. & Wu, Q. Eigenequations and Compact Algorithms for Bulk and Layered Anisotropic Optical Media: Reflection and Refraction at a Crystal-Crystal Interface. *Journal of Computational Physics* **133,** 75–83 (1997).

139. McCall, M. W., Hodgkinson, I. J. & Wu, Q. *Birefringent thin films and polarizing elements* 2nd ed. 468 pp. (Imperial College Press, London, 2014).

140. Allia, P., Oldano, C. & Trossi, L. Polarization transfer matrix for the transmission of light through liquid-crystal slabs. *Journal of the Optical Society of America B* **5,** 2452–2461 (1988).

141. Yoon, H. G. & Gleeson, H. F. Accurate modelling of multilayer chiral nematic devices through the Berreman 4×4 matrix methods. *Journal of Physics D: Applied Physics* **40,** 3579–3586 (2007).

142. Stallinga, S. Berreman 4×4 matrix method for reflective liquid crystal displays. *Journal of Applied Physics* **85,** 3023–3031 (1999).

143. Weisstein, E. W. *Newton's Method* From MathWorld - A Wolfram Web Resource.

144. Wiersma, A. G. *The Complex Dynamics of Newton's Method* Bachelor Thesis (Faculty of Mathematics and Natural Sciences, University of Groningen, 2016).

145. Gilbert, W. J. Generalizations of Newton's Method. *Fractals* **9,** 251–262 (2001).

146. Schneider, J. B. *Understanding the Finite-Difference Time-Domain Method* www.eecs.wsu.edu/∼schneidj/ufdtd. 2010.

147. *MEEP documentation* https://meep.readthedocs.io/en/latest/Introduction/. 2010.

148. Oskooi, A. F., Roundy, D., Ibanescu, M., Bermel, P., Joannopoulos, J. & Johnson, S. G. Meep: A flexible free-software package for electromagnetic simulations by the FDTD method. *Computer Physics Communications* **181,** 687–702 (2010).

149. Takayama, O., Artigas, D. & Torner, L. Lossless directional guiding of light in dielectric nanosheets using Dyakonov surface waves. *Nature Nanotechnology* **9,** 419–424 (2014).

150. Nakamura, H., Hatano, N., Garmon, S. & Petrosky, T. Quasibound States in the Continuum in a Two Channel Quantum Wire with an Adatom. *Physical Review Letters* **99,** 210404 (2007).

151. Raether, H. *Surface Plasmons on Smooth and Rough Surfaces and on Gratings* 1st ed. (Springer-Verlag Berlin Heidelberg, 1988).

152. Gollub, J. N., Smith, D. R., Vier, D. C., Perram, T. & Mock, J. J. Experimental characterization of magnetic surface plasmons on metamaterials with negative permeability. *Physical Review B* **71,** 195402 (2005).

153. Yeh, P., Yariv, A. & Cho, A. Y. Optical surface waves in periodic layered media. *Applied Physics Letters* **32,** 104–105 (1978).

154. Takayama, O., Bogdanov, A. A. & Lavrinenko, A. V. Photonic surface waves on metamaterial interfaces. *Journal of Physics: Condensed Matter* **29,** 463001 (2017).

155. D'yakonov, M. I. New type of electromagnetic wave propagating at an interface. *Journal of Experimental and Theoretical Physics (ZhETF)* **94,** 119 (1988).

156. Takayama, O., Crasovan, L.-C., Johansen, S. K., Mihalache, D., Artigas, D. & Torner, L. Dyakonov Surface Waves: A Review. *Electromagnetics* **28,** 126–145 (2008).

157. Averkiev, N. S. & D'yakonov, M. I. Electromagnetic waves localized at the interface of transparent unisotropic media. *Optics and Spectroscopy (USSR)* **68,** 653–655 (1990).

158. Walker, D. B., Glytsis, E. N. & Gaylord, T. K. Surface mode at isotropic–uniaxial and isotropic–biaxial interfaces. *Journal of the Optical Society of America A* **15,** 248–260 (1998).

159. John A. Polo, J., Nelatury, S. R. & Lakhtakia, A. Surface waves at a biaxial bicrystalline interface. *Journal of the Optical Society of America A* **24,** 2974–2979 (2007).

160. Artigas, D. & Torner, L. Dyakonov Surface Waves in Photonic Metamaterials. *Physical Review Letters* **94,** 013901 (2005).

161. Takayama, O., Artigas, D. & Torner, L. Practical dyakonons. *Optics Letters* **37,** 4311–4313 (2012).

162. Crasovan, L.-C., Takayama, O., Artigas, D., Johansen, S. K., Mihalache, D. & Torner, L. Enhanced localization of Dyakonov-like surface waves in left-handed materials. *Physical Review B* **74,** 155120 (2006).

163. Crasovan, L.-C., Artigas, D., Mihalache, D. & Torner, L. Optical Dyakonov surface waves at magnetic interfaces. *Optics Letters* **30,** 3075–3077 (2005).

164. Ma, W., Alonso-González, P., Li, S., Nikitin, A. Y., Yuan, J., Martín-Sánchez, J., Taboada-Gutiérrez, J., Amenabar, I., Li, P., Vélez, S., Tollan, C., Dai, Z., Zhang, Y., Sriram, S., Kalantar-Zadeh, K., Lee, S.-T., Hillenbrand, R. & Bao, Q. In-plane anisotropic and ultra-low-loss polaritons in a natural van der Waals crystal. *Nature* **562,** 557–562 (2018).

165. Li, P., Dolado, I., Alfaro-Mozaz, F. J., Casanova, F., Hueso, L. E., Liu, S., Edgar, J. H., Nikitin, A. Y., Vélez, S. & Hillenbrand, R. Infrared hyperbolic metasurface based on nanostructured van der Waals materials. *Science* **359,** 892–896 (2018).

166. Jacob, Z. & Narimanov, E. E. Optical hyperspace for plasmons: Dyakonov states in metamaterials. *Applied Physics Letters* **93,** 221109 (2008).

167. Zapata-Rodríguez, C. J., Miret, J. J., Vuković, S. & Belić, M. R. Engineered surface waves in hyperbolic metamaterials. *Optics Express* **21,** 19113–19127 (2013).

168. Cojocaru, E. Comparative analysis of Dyakonov hybrid surface waves at dielectric-elliptic and dielectric-hyperbolic media interfaces. *Journal of the Optical Society of America B* **31,** 2558–2564 (2014).

169. Takayama, O., Shkondin, E., Bodganov, A., Aryaee Panah, M. E., Golenitskii, K., Dmitriev, P., Repän, T., Malureanu, R., Belov, P., Jensen, F. & Lavrinenko, A. V. Midinfrared Surface Waves on a High Aspect Ratio Nanotrench Platform. *ACS Photonics* **4,** 2899–2907 (2017).

170. Takayama, O., Crasovan, L., Artigas, D. & Torner, L. Observation of Dyakonov Surface Waves. *Physical Review Letters* **102,** 043903 (2009).

171. Chermoshentsev, D. A., Anikin, E. V., Dyakov, S. A. & Gippius, N. A. Dimensional confinement and waveguide effect of Dyakonov surface waves in twisted confined media. *Nanophotonics* **9,** 4785–4797 (2020).

172. Anikin, E. V., Chermoshentsev, D. A., Dyakov, S. A. & Gippius, N. A. Dyakonov-like waveguide modes in an interfacial strip waveguide. *Physical Review B* **102,** 161113 (2020).

173. Golenitskii, K. Y. & Bogdanov, A. A. Dyakonov-like surface waves in anisotropic cylindrical waveguides. *Physical Review B* **101,** 165434 (2020).

174. Kajorndejnukul, V., Artigas, D. & Torner, L. Conformal transformation of Dyakonov surface waves into bound states of cylindrical metamaterials. *Physical Review B* **100,** 195404 (2019).

175. Torner, L., Torres, J., Ojeda, C. & Mihalache, D. Hybrid waves guided by ultrathin films. *Journal of Lightwave Technology* **13,** 2027–2033 (1995).

176. Lakhtakia, A. & J. Polo, J. Dyakonov–Tamm wave at the planar interface of a chiral sculptured thin film and an isotropic dielectric material. *Journal of the European Optical Society - Rapid publications* **2** (2007).

177. Gao, J., Lakhtakia, A. & Lei, M. On Dyakonov-Tamm waves localized to a central twist defect in a structurally chiral material. *Journal of the Optical Society of America B* **26,** B74–B82 (2009).

178. Pulsifer, D. P., Faryad, M. & Lakhtakia, A. Observation of the Dyakonov-Tamm Wave. *Physical Review Letters* **111,** 243902 (2013).

179. Mackay, T. G., Zhou, C. & Lakhtakia, A. Dyakonov–Voigt surface waves. *Proceedings of the Royal Society A: Mathematical, Physical and Engineering Sciences* **475,** 20190317 (2019).

180. Mackay, T. G. & Lakhtakia, A. Surface waves with negative phase velocity supported by temperature-dependent hyperbolic materials. *Journal of Optics* **21,** 085103 (2019).

181. Repän, T., Takayama, O. & Lavrinenko, A. Hyperbolic surface waves on anisotropic materials without hyperbolic dispersion. *Optics Express* **28,** 33176–33183 (2020).

182. Chermoshentsev, D. A., Anikin, E. V., Dyakov, S. A. & Gippius, N. A. Dyakonov surface waves in dielectric crystals with negative anisotropy. *arXiv:2104.07394v1* (2021).

183. Pujol-Closa, P., Gomis-Bresco, J., Mukherjee, S., Gómez-Díaz, J. S., Torner, L. & Artigas, D. Slow light mediated by mode topological transitions in hyperbolic waveguides. *Optics Letters* **46,** 58–61 (2021).